ugr | Universidad de Granada

SIGNAL PROCESSING-BASED IDENTIFICATION OF PATHOLOGY USING ULTRASONICS

BY:

Nicolas Bochud

A THESIS SUBMITTED TO:

University of Granada

ADVISORS:

Guillermo Rus Carlborg & Ángel M. Gómez García

Department of Structural Mechanics & Hydraulic Engineering ,
University of Granada
Granada (Spain)

January 2014

Editor: Editorial de la Universidad de Granada
Autor: Nicolas Bochud
D.L.: GR 1842-2014
ISBN: 978-84-9083-025-3

Signal processing-based identification of pathology using ultrasonics

Summary

Nondestructive evaluation is an emerging technology that enables to raise the remaining life and reliability of nowadays structures, as well as to characterize advanced materials and biomaterials in medical science. Ultrasound is currently one of the most frequently used nondestructive inspection techniques, since it has been proven to provide effective and reliable results at relatively low cost for the estimation of the quality and general condition of a material, and for the characterization of its mechanical properties. Indeed, ultrasonic nondestructive evaluation is a well-established method to obtain physically relevant parameters to characterize pathologies in isotropic homogeneous materials. Pathologies are here understood as material's defects or consistency change, which altered the linear and/or nonlinear mechanical properties of materials. However, ultrasonic signals obtained from multilayered materials (composites, tissue-engineered products, biomaterials, etc.) require special care in signal interpretation (i.e. multiple and overlapping ultrasonic echoes) due to their structural complexity.

For competitive pathology assessment and quality control of stratified materials, quantitative non-destructive evaluation techniques based on the use of theoretical models of the ultrasonic wave propagation have been developed to extract additional information from experimental measurements. Despite the structural complexity of those materials, relative simple models are required for efficient and real-time monitoring of their structure health. Consequently, the complexity of the signals recorded by the transducers suggests to directly compare the experimental measurements with the theoretical results, with the purpose of extracting quantitative information from damage or consistency changes. A possible approach to solve this problem is provided by the model-based estimation procedure. However, conventional model-based estimation procedure developed in the mechanical engineering community are not attractive from a practical point of view (e.g. imperfections of the acquisition system, excessive computational resources, model uncertainties, etc.). In response to those problems, some procedures have been developed in the information technology community to enhance both the reliability and the quantitative pathology-informational content of ultrasonic signals obtained from conventional nondestructive evaluation systems. Therefore, in this thesis, we intent to unify the grounds implied in both area by developing efficient and novel methods for practical ultrasonic nondestructive evaluation applications

on layered media, facing toward the optimization of the performance of such estimation procedure.

In particular, we present a general framework that relies on an advanced model-based estimation procedure to nondestructively evaluate pathologies using ultrasonics, which incorporates and adapts classical signal processing and modeling techniques to extract relevant features from the ultrasonic signals and enhance the signal interpretation. The main contributions of this dissertation concern the modeling approaches developed within this procedure to cope with the wave propagation in multilayered media. We first revisit a conventional approach known as the Transfer Matrix formalism to review the theoretical grounding for our dissertation and obtain a formulation that offers us the possibility of extending this method to more complex problems. Alternatively, signal modeling has also been proven to be an useful tool to characterize damaged materials under ultrasonic nondestructive evaluation. Consequently, we introduce a novel digital signal model for ultrasonic nondestructive evaluation of multilayered materials. This model borrows concepts from lattice filter theory, and bridges them to the physics involved in the wave-material interactions. In addition, we demonstrate that this digital model has several advantages with respect to purely physics-based models or classical spectral estimation approaches. Finally, we propose an extension of these two models to deal with the classical nonlinear constitutive behavior of such layered materials.

In a further part, the development of consistent optimization strategies and the obtaining of relevant experimental observations necessary to achieve a performant model-based estimation procedure are also contemplated. In particular, we introduce the context and motivation of the employed materials, describing their potential and the challenge that they offer from a structural viewpoint, and focusing on the requirement of efficient ultrasonic nondestructive evaluation techniques to identify their damage mechanisms. In addition, we present the specimens tested and the experimental configurations used to analyze them. Finally, we provide the theoretical background for the inverse problem and system identification approaches used for characterizing the pathologies of the introduced specimens.

The developed models are finally compared and validated with experimental measurements obtained from multilayered media that consist of traditional materials. Once validated, those models are tested using several applications of practical interest, including:

- ▷ The detection and identification of impact and fatigue damages in carbon fiber-reinforced polymers plates. In this case, both contact and immersion measurements are performed.
- ▷ The monitoring of tissue-engineered materials using a embedded ultrasonic system. This novel system is first validated on a gelation process, and then used to characterize a fibrin-agarose based construct for artificial tissue development.
- ▷ The bone damage assessment using nonlinear acoustics. To this end, a nonlinear ultrasonic through-transmission finite-amplitude method was designed.

From a theoretical point of view, the proposed digital signal model opens new perspectives in developing models for ultrasonic nondestructive evaluation, since it represents the material as a digital filter with sparse coefficients by merging concepts both from the mechanics and the signal theory. As a consequence, this model preserves both the strengths of purely physics-based models and (heuristic) parametric signals models. From a practical point of view, this model demonstrates its ability to simulate multilayered materials. In addition, it can be successfully inserted in a model-based estimation procedure to monitor the mechanical properties of relatively complex layered materials.

The presented monitoring technique achieves for the first time the reconstruction of multiple damages in carbon fiber-reinforced polymer plates from a single measurement. In contrast to other studies, the pathologies are not identified by considering the time-of-flight or the broadband ultrasound attenuation, but by reconstructing the complete waveform. Moreover, the damage multiplicity does not only appear at several locations but simultaneously in different forms. The other encouraging results on tissue-engineered materials or bone suggest that this methodology previously developed for structural applications could be further applied in the fields of biomedical engineering.

Resumen

La evaluación no destructiva es una tecnología emergente que permite aumentar la longevidad y fiabilidad de las estructuras de hoy en día, así como la caracterización de materiales avanzados y biomateriales en las ciencias médicas. Los ultrasonidos son en este momento una de las técnicas no destructivas de inspección más frecuentemente empleadas, ya que han demostrado que proporcionan resultados efectivos y fiables a un coste relativamente bajo, para estimar la calidad y el estado general de un material, así como para la caracterización de sus propiedades mecánicas. De hecho, la evaluación no destructiva ultrasónica es un método establecido para obtener parámetros físicos relevantes de cara a caracterizar patologías en medios isótropos y homogéneos. Por concepto de patología entendemos la presencia de defectos o cambios de consistencia en un material, que alteran las propiedades mecánicas lineales y no lineales del mismo. Sin embargo, las señales ultrasónicas obtenidas a partir de materiales estratificados (materiales compuestos, cultivos tisulares artificiales, materiales biológicos, etc.) requieren una atención particular a la hora de interpretar las señales (a saber múltiples ecos ultrasónicos solapados) debido a su complejidad estructural.

Para una evaluación competitiva de una patología y un control de calidad de los materiales estratificados, han sido desarrolladas técnicas de evaluación no destructiva ultrasónica cuantitativa, basándose en el uso de modelos teóricos de propagación de ondas ultrasónicas para extraer información adicional de las medidas experimentales. A pesar de la complejidad estructural de dichos materiales, se requieren modelos relativamente sencillos para una monitorización eficiente y en tiempo real de la salud estructural. Por consiguiente, la complejidad de las señales capturadas por los sensores nos ha llevado a comparar directamente las medidas experimentales con los resultados teóricos, con el propósito de extraer información cuantitativa de los defectos o de los cambios de consistencia. Un posible planteamiento para resolver este tipo de problema nos está proporcionado por el *procedimiento de estimación basado en modelos*. Sin embargo, los *procedimientos de estimación basados en modelos* convencionales desarrollados en el ámbito de la ingeniería mecánica pueden carecer de atractivo desde una perspectiva práctica (por ejemplo debido a las imperfecciones del sistema de adquisición, el exceso de recursos computacionales, o las incertidumbres del modelo, etc.). En respuesta a esos problemas, procedimientos alternativos han sido desarrollados en la comunidad de la tecnología de la información para realzar tanto la fiabilidad como el contenido cuantitativo acerca de las patologías de las señales ultrasónicas obtenidas a partir de sistemas de evaluación no destructiva convencionales. Por lo tanto, en esta tesis,

intentamos unificar los fundamentos de amabas áreas con el objeto de desarrollar métodos innovadores y eficientes para aplicaciones prácticas de evaluación no destructiva ultrasónica de medios estratificados, con el fin de enfrentarnos a la optimización del rendimiento de este tipo de procedimiento de estimación.

En particular, en esta investigación presentamos un procedimiento general que se fundamenta en un método avanzado de estimación basado en modelos para la evaluación no-destructiva ultrasónica de patologías, que incorpora y adapta técnicas clásicas de procesamiento y modelado de señales para extraer características relevantes de las señales ultrasónicas y realzar la interpretación de esas señales. Las principales contribuciones de este trabajo conciernen a los modelos desarrollados para dicho procedimiento de cara a resolver los problemas asociados con la propagación de ondas en materiales estratificados. En primer lugar, reconsideramos un planteamiento clásico conocido como el formalismo de la Matriz de Transferencia con la intención de revisar los fundamentos teóricos de nuestra investigación y obtener una formulación que nos permita extender ese método a problemas más complejos. Por otra parte, se ha demostrado que el *modelado de señal* es una herramienta útil para caracterizar materiales defectuosos bajo el concepto de evaluación no destructiva ultrasónica. Por lo tanto, introducimos un modelado de señal digital novedoso para la evolución no destructiva ultrasónica de materiales estratificados. Este modelo toma prestado conceptos de la teoría de filtros en celosía y los relaciona con la física involucrada en la interacción de las ondas con el material. Adicionalmente, demostramos que este modelo digital tiene numerosas ventajas frente a modelos puramente físicos o planteamientos de estimación espectral clásicos. Finalmente, proponemos una ampliación de esos dos modelos mencionados anteriormente, para introducir la no linealidad clásica en el comportamiento constitutivo de esos materiales.

En la siguiente parte del trabajo, se contempla el desarrollo de estrategias de optimización consistentes, así como la obtención de conjuntos de observaciones experimentales relevantes para lograr un método de estimación basado en un modelo de calidad. En particular, introducimos el contexto y la motivación de los materiales empleados, describimos su potencial y el reto que ofrecen desde una perspectiva estructural, y destacamos los requisitos de técnicas ultrasónicas eficientes para identificar los mecanismos de daño de dichos materiales. Adicionalmente, presentamos los especímenes testados y las configuraciones experimentales empleadas para analizarlos. Por último, proporcionamos la base teórica para definir los planteamientos sobre el problema inverso y la identificación de sistema empleados para caracterizar patologías de los especímenes.

Los métodos desarrollados han sido comparados y validados con medidas experimentales obtenidas a partir de medios estratificados formados por materiales tradicionales. Una vez validados, esos modelos han sido probados en aplicaciones de interés práctico, incluyendo:

- ▷ La detección e identificación de defectos generados por impacto y fatiga cíclica en placas de fibra de carbono. En ese caso, hemos llevado a cabo medidas en contacto y en inmersión.
- ▷ La monitorización de tejidos artificiales empleando un sistema ultrasónico embebido. Ese sistema innovador se valida en primer lugar con un proceso de solidificación de un gel y más adelante se usa para caracterizar el desarrollo de un tejido artificial basado en un constructo de fibrina agarosa.
- ▷ La evaluación de daños en huesos mediante técnicas de ultrasonidos no lineales. Para este fin, diseñamos un método de amplitud finita basado en la transmisión de ondas ultrasónicas no lineales.

Desde una perspectiva teórica, el modelado de señal digital propuesto abre nuevas perspectivas para el desarrollo de modelos para la evaluación no destructiva ultrasónica, ya que representa el material como un filtro digital con coeficientes sparse uniendo conceptos de la mecánica de sólidos y de la teoría de la señal. Por consiguiente, ese modelo preserva las ventajas tanto de modelos basados esencialmente en la física como de modelos paramétricos de señales (heurísticos). Desde una perspectiva práctica, ese modelo demuestra su habilidad para simular la propagación de ondas en medios estratificados. Adicionalmente, este modelo se puede insertar en un procedimiento de estimación basado en modelos de forma satisfactoria para monitorizar las propiedades mecánicas de materiales estratificados particularmente complejos.

La técnica de monitorización que presentamos ha permitido lograr por primera vez la reconstrucción de múltiples daños en placas de fibra de carbono a partir de una sola medida. A diferencia de otros estudios, las patologías no se identifican considerando el tiempo de vuelo o la atenuación ultrasónica de banda ancha, sino reconstruyendo la forma de onda completa. Además, los múltiples daños no solo aparecen a distintas posiciones del material, sino simultáneamente de forma distinta. Los otros resultados alentadores sobre cultivos tisulares artificiales y hueso sugieren que esa metodología previamente desarrollada para aplicaciones estructurales pueda aplicarse más a fondo en otros ámbitos de la ingeniería biomédica.

Acknowledgments

First of all, I would like to thank the two advisors responsible for the direction of my thesis, Prof. Dr. Guillermo Rus Carlborg of the Department of Structural Mechanics and Dr. Angel M. Gómez of the Department of Signal Theory, Networking and Communications. They have played an imperative role in the success of this work, joining and confronting their respective expertise in fields of apparently such distinct nature. Especially, I thank the first one for his constant dedication to the investigation and for teaching and passing me on this position, whereas I thank the second one for his patience, guidance and constructive suggestions over the course of these years. Also I thank Prof. Dr. Antonio M. Peinado Herreros, as the main investigator of the project that this dissertation is part off and as supervisor of my Master thesis, for his guidance and disposability over the course of these years. I also thank the Prof. Dr. Quentin Grimal and Pascal Laugier for supervising my research stay at the Laboratoire d'Imagerie Paramétrique, and sharing with me their expertise on bone quantitative ultrasound. Finally, I thankall my colleagues of the Nondestructive Evaluation Laboratory for making the everyday life at the lab enjoyable, and particularly for supporting me over the last few months.

I would like to thank the Consejería de Economía, Innovación y Ciencia de la Junta de Andalucia, Spain, for the FPI grant, being part of the project no. P08-TIC-03911, that allowed me to take part to the Master in Multimedia Systems, and especially to investigate within this interdisciplinary research area during three years. In addition, I acknowledge the Spanish Ministerio de Economía y Competitividad for project DPI2010-17065, and Junta de Andalucía for projects P11CTS-8089 and GGI3000IDIB, whose funding enables me to take part to numerous international congresses.

Abbreviations

AE	Acoustic emission
APM	Approximated Prony method
AR	Autoregressive
BEM	Boundary element method
BFGS	Broyden-Fletcher-Goldfarb-Shanno
BG	Bernoulli-Gaussian
BMD	Bone mineral density
BUA	Broadband ultrasonic attenuation
CAN	Contact acoustic nonlinearity
CFRP	Carbon fiber-reinforced polymers
DAET	Dynamic acousto-eslastic technique
DFT	Discrete Fourier transform
DFTF	Discrete-time Fourier transform
DMEM	Dulbecco's modified Eagle's medium
DXA	Dual X-ray absorptiometry
EM	Expectation maximization
EWVD	Enhanced Wigner-Ville distribution
FBG	fiber Bragg gratings
FBS	Fetal bovine serum
FD	Finite-difference
FDTD	Finite-difference time-domain
FEM	Finite element method
FIR	Finite impulse response
FFT	Fast Fourier transform
FP	Forward problem
FRP	Fiber-reinforced polymers
FSFS	Forward sequential feature selection
FT	Fourier transform
GA	Genetic Algorithm
GFRP	Glass fiber-reinforced polymers
GM	Global matrix
HOS	Higher-order statistics

ICA	Independent component analysis
IDFT	Inverse discrete Fourier transform
IFFT	Inverse fast Fourier transform
IP	Inverse problem
IR	Impulsive response
LDA	Linear discriminant analysis
LPC	Linear predictive coding
LS	Least squares
LTI	Linear time-invariant
MLE	Maximum likelihood estimation
MP	Matching pursuit
MPA	Maximum a posteriori
NDE	Nondestructive evaluation
NLS	Nonlinear least squares
NRUS	Nonlinear resonant ultrasound spectroscopy
NTM	Nonlinear transfer matrix
NWLS	Nonlinear weighted least squares
PBS	Phosphate buffered saline
PCA	Principal component analysis
PDF	Probability density function
PIP	Probabilistic inverse problem
PM	Prony method
PMMA	Poly(methyl methacrylate)
QNDE	Quantitative nondestructive evaluation
QUS	Quantitative ultrasound
RMS	Root mean square
SAGE	Space alternating generalized expectation
SAW	Surface acoustic waves
SD	Sparse deconvolution
SHM	Structure health monitoring
SM	Stiffness matrix
SNR	Signal-to-noise ratio
SSP	Split-spectrum processing
STFT	Short-time Fourier transform
SVD	Single value decomposition
TDOA	Time-difference of arrival
TM	Transfer matrix
TOA	Time-of-arrival
TOF	Time-of-flight
TOFM	Time-of-flight modulation

WT	Wavelet transform
WVD	Wigner-Ville distribution

List of Symbols

Symbol	Description
u_i	Cartesian components of the displacement vector
σ_{ij}	Cartesian components of the stress tensor
ε_{ij}	Cartesian components of the strain tensor
δ_{ij}	Kronecker symbol
n	Sample index
$x(n)$	Discrete-time input signal
$y(n)$	Discrete-time output signal
$e(n)$	Discrete-time error
$w_r(n)$	Rectangular window
$w_{han.}(n)$	Hanning window
$w_{ham.}(n)$	Hamming window
$w_{bar.}(n)$	Bartlett window
$w_{bla.}(n)$	Blackmann window
$X(\omega)$	Spectrum of the input signal
$Y(\omega)$	Spectrum of the output signal
$H(\omega)$	Frequency response
$H(\omega_k)$	Sampled version of the frequency response
$H(z)$	Discrete-time transfer function
$A(z)$	Polynomial expression in z
G	Filter gain
a_k	All-pole filter coefficients
b_k	All-zero filter coefficients
E	Error energy
R	Autocorrelation function
$c(n)$	Real cepstrum
$\hat{c}(n)$	Complex cepstrum
$\delta(n)$	Unitary impulse
$\mathfrak{F}$	Fourier transform
$\mathfrak{F}^{-1}$	Inverse Fourier transform
M	Number of material layers
$u(x,\Omega)$	Displacement (expressed in the frequency-domain)
$u^f(x,\Omega)$	Forward-propagating displacement component
$u^b(x,\Omega)$	Backward-propagating displacement component
$\boldsymbol{\mathcal{U}}_i(x,\Omega)$	State vector of a layer i
$\boldsymbol{\mathcal{D}}_{i,i+1}$	Discontinuity matrix of a layer i
$\boldsymbol{\mathcal{P}}_i(\Omega)$	Propagation matrix of a layer i
$\boldsymbol{\mathcal{T}}_i(\Omega)$	Transfer matrix of a layer i
$\boldsymbol{\mathcal{T}}(\Omega)$	Complete transfer matrix
$\mathcal{T}(\Omega)$	Elements of the complete transfer matrix
$\boldsymbol{T}^{(k)}$	Discrete version of the complete transfer matrix
$\mathcal{H}(\Omega)$	Frequency response at frequency Ω (complex scalar number)

Symbol	SI	Description
ρ	[kg/m^3]	Density
λ	[Pa]	Lamé's first constant
μ	[Pa]	Lamé's second constant
E	[Pa]	Young modulus
E^*	[Pa]	Dynamic modulus
$\bar{E}$	[Pa]	Storage modulus
$\tilde{E}$	[Pa]	Loss modulus
$\tan(\delta)$	[-]	Loss tangent
ν	[-]	Poisson ratio
c, c_p	[m/s]	Longitudinal wave velocity
Z	[Ω]	Material impedance
A, B	[m]	Displacement's amplitude
γ	[1/m]	Wave number
t	[s]	Time variable
x	[m]	Space variable
a	[m]	Thickness
Ω	[rd/s]	Continuous-time frequency
ω	[rd/sample]	Discrete-time frequency
F_s	[Hz]	Sampling frequency

Contents

List of Figures

Part I

INTRODUCTION

1

Context and Motivation

Nondestructive evaluation (NDE) is an emerging technology that enables to raise the remaining life and reliability of nowadays structures, as well as to characterize advanced materials and biomaterials in medical science. Ultrasound is currently one of the most frequently used NDE inspection techniques, since it has been proven to provide effective and reliable results at relatively low cost for the estimation of the quality and general condition of a material, and for the characterization of its mechanical properties. Ultrasound pulses are noninvasive and non-ionizing mechanical waves, whose propagation is governed by the theory of elasticity, and are therefore particularly sensitive to the mechanical properties, which are responsible for the final integrity and quality of the inspected material.

Important research areas related to ultrasonic NDE frequently involve the study of the wave interactions with multilayered structures. The interest of an accurate identification of multilayered materials properties is constantly growing, since they are encountered in a wide range of applications. In engineering applications, this concerns for instance the detection of poor cohesion and adhesion in joints, the measurement of elastic properties and thickness of layered materials, and the detection of damage in composites [1]. In material science developments, some layered materials are the products of synthetic chemistry and consist of a large class of compounds formed by metals, ceramics, and polymers [2]. In biomedical research, layered tissue mimicking fluids are developed and must have properties similar to amniotic fluid and typical soft tissue [3]. Also, the complex architecture of trabecular bone can be conveniently modeled as a simplified stratified medium of alternating solid and liquid layers [4, 5]. In the semiconductor industry, a large number of ob-

jects/components have multilayered structures, such as modern microelectronic packages, semiconductors, and thin/thick films [6].

In ultrasound-based inspection techniques, the received ultrasonic signal responses are evaluated to retrieve information about the inspected media. Thus, for competitive damage assessment and quality control of stratified materials, quantitative non-destructive evaluation (QNDE) techniques based on the use of theoretical models of the ultrasonic wave propagation have been developed to extract additional information from experimental measurements [7]. Despite the structural complexity of those materials (spatial heterogeneity of the mechanical properties, multiple damage mechanisms, dispersion, etc.), relative simple models are required for efficient and real-time monitoring of their structure health. Indeed, the complexity of the observations suggests to directly compare the experimental measurements with the theoretical results, with the purpose of extracting quantitative information from damage or consistency changes. A possible approach to solve this problem is provided by the model-based inverse problem (IP) framework, whose general outline was given by Tarantola [8]. The resolution of an IP identification approach is commonly defined in terms of the minimization of a cost functional consisting in the discrepancy between the experimental observations and the numerically predicted results [9]. Generally, the model parameters are found such that the l_2-norm of the residual (the difference between the observed signal and the predicted one) is minimized.

Generally, two key aspects of the model-based quantitative NDE are fundamentals: (1) An appropriate understanding and modeling of the interactions between ultrasonic waves and multilayered media is required; and (2) the model parameters extracted from the measurements should be sensitive enough to the pathologies (that is, damage or consistency changes) that manifest in the specimen under inspection, and minimally sensitive to the measurements noise and model uncertainties. Despite the potential strength of the model-based IP framework for NDE of multilayered materials, parts of its structure could not be attractive from the practical point of view: For a fast convergence of the minimization algorithm, this method requires precise and reliable observations. However, due to their structural complexity, multilayered materials require special treatment in ultrasonic signal interpretation. The random nature of the signal generation, the imperfections of the acquisition system, as well as the difficulties in understanding and analyzing multiple and overlapping ultrasonic echoes may have a drastic influence on the performance of the inversion scheme. Additionally, an accurate characterization of pathologies usually require the determination of several model parameters, at the cost of excessive computational resources. Thus, advanced features sensitive to the model parameters should be continuously extracted in order to improve the (real-time) monitoring of those materials.

In response to those problems, tremendous emphasis has been directed towards identifying procedures that enhance both the reliability and the quantitative informational content of signals obtained from conventional NDE systems [10]. Part of this emphasis has focused on the adaptation of advanced signal processing concepts to NDE problems, which

have already been successfully applied in other scientific fields such as electrical engineering, speech recognition or geophysics. Among others, those procedures have given raise to the development of heuristic inverse problems, based on empirical models (in contrast to phenomenological approaches relying on underlying physical processes). The absence of a direct link between the physical process and the empirical model allows one to investigate the feasibility of using a wide variety of models (e.g. the modeling of ultrasonic signals using autoregressive models [11]). Thus, the ability to reconstruct the ultrasonic signals can be evaluated in an analysis-by-synthesis scheme by estimating the model parameters of the system to identify (which relates the input-output signals) that minimize the modeling error.Most of the heuristic techniques devoted to material characterization aim at mapping the signal space (e.g. time-domain) into a smaller-dimensional feature space. Pattern recognition techniques can then be used for classifying or characterizing the damage by examining this feature space. Nonetheless, this consumes a huge amount of experimental data and requires an expensive training process. Moreover, the mapping process does usually not provide a satisfying understanding of the relations between the extracted features and the underlying mechanical properties that characterize the damage.

In this thesis, we intend to give solutions to those problems by developing efficient and novel methods for practical ultrasonic NDE applications on layered media. Concretely, we propose to combine the strength of both the phenomenological and empirical approaches, by inserting signal processing and modeling strategies with physical sense into a model-based inverse problem framework. Before proposing a concise literature review and introducing the theoretical basis to this dissertation, the following chapter exposes the objectives of the present thesis to provide an idea of the potential of its contributions.

In order to separate the theoretical background, contributions, methodology and the results, the thesis is divided into five parts:

Part I already introduced the context and motivation of this thesis in the present chapter. In **Chapter 2**, the objectives are carefully described in order to provide an idea of the potential of its contributions. A concise literature review is provided in **Chapter 3**, whereas **Chapter 4** introduces the theoretical basis to this dissertation.

Part II describes the main contributions of this dissertation. **Chapter 5** presents underlying concept of the model-based estimation procedure. In **Chapter 6**, we expose the theoretical development of the Transfer Matrix formalism for ultrasonic wave propagation in multilayered structures. Then, an alternative model for multilayered materials, which borrows concepts from lattice filter theory and bridge them with the physics involved in the wave-material interactions is presented in **Chapter 7**. Finally, in **Chapter 8**, we propose two models that extend the ones developed in Chapters 6 and 7, in order to cope with the

nonlinear constitutive behavior of multilayered structures.

Part III describes the materials and methods used over the course of this thesis, and includes among others the experimental configuration used to analyze the tested specimens and the theoretical background for the inverse problem and system identification approaches used for characterizing the pathologies of the introduced specimens (see **Chapter 9**).

Part IV presents the results obtained with the proposed models, and discusses several applications related to the identification of pathology in multilayered specimens. Five different applications are developed:

- **Chapter 10** evaluates our novel digital signal model: First, we propose a synthetic comparison with a standard technique, and then an experimental validation with measurements obtained from multilayered specimens consisting of traditional materials.
- **Chapter 11** investigates three different robust parametrization approaches for damage detection in CFRP plates, that are a classical spectral estimation approach, an heuristic sparse signal model and a physics-based digital signal model. In addition, we study a model-based estimation procedure for damage identification in CFRP plates. Two kind of damage mechanisms and different experimental approaches are investigated.
- **Chapter 12** described a probabilistic inverse problem for ultrasonic monitoring of tissue-engineered materials. First, our novel embedded ultrasonic system is validated on a gelation process, and then applied to show its potential for monitoring a fibrin-agarose based construct for artificial tissue development.
- **Chapter 13** investigates the potential of nonlinear ultrasound for bone damage assessment

Part V presents a discussion of the strength and limitations of the proposed contributions, and comment some aspects of the ongoing works currently under development at our laboratory.

2
Objectives

Anticipating and characterizing pathologies in advanced materials and bio-materials is a challenging problem. Ultrasonic non-destructive evaluation is a well-established method to obtain physically relevant parameters to identify alterations in isotropic homogeneous materials. However, due to their structural complexity, layered materials require special care in signal interpretation. Model-based inverse procedure and signal modeling strategies are thus proposed to improve the pathology identification. On this basis, the objectives of the present thesis are:

- ◇ To formulate a model-based estimation procedure to improve the identification of pathologies in layered systems. A side-objective is to obtain relevant experimental data by performing measurements using traditional and emerging ultrasonic techniques.
- ◇ To develop a digital signal model for ultrasonic waves that propagates normally through a stratified structure. A side objective is to review the formulation and implementation of the conventional Transfer Matrix method for that case, to provide a physics-based comparison.
- ◇ To extend those models for wave propagation through nonlinear layered media, by accounting for classical nonlinear constitutive behavior.

3

Literature review

The underlying methodology of a model-based inverse problem generally consists of three parts: An (1) experimental setup to monitor in real-time the interactions between the ultrasonic waves and the multilayered specimen under inspection, a (2) forward modeling that simulates the wave-material interactions, and finally an (3) inverse problem procedure based on optimization algorithms to reconstruct the structural variations due to pathologies which may occur during the monitored process. Since these three parts can benefit from advanced signal processing and modeling techniques, the emphasis throughout this review is on ultrasonic NDE oriented signal processing theory and methods.

The literature review is organized as follows: Section 3.1 briefly describes two of the most widely used ultrasonic testing methods, and discusses their limitations for inspecting multilayered structures. In Section 3.2, we present an overview of ultrasonic NDE signal processing techniques, focusing on detection enhancement problems, and defect characterization and classification. Section 3.3 outlines the model-based estimation framework, describing a wide range of modeling approaches for ultrasonic wave propagation in layered media. In addition, some optimization algorithms for system identification are presented. Finally, some fundaments of emerging nonlinear ultrasound techniques are introduced in Section 3.4, since they may have merit for characterizing layered media. The focus all over this review is mainly on two kinds of promising multilayered materials, those are carbon-fiber reinforced polymers (CFRP) and biomaterials (e.g. tissue-equivalent media and bone).

3.1 Experimental NDE

In modern ultrasonic NDE applications, a wide range of techniques has been developed for imaging defect location and sizing, including pulse-echo, through-transmission, guided waves, time-of-flight diffraction, scanning acoustic microscopy, laser ultrasonic imaging, or harmonic imaging. However, a review of the extensive literature on experimental ultrasound-based techniques is beyond the scope of this thesis. Here, we briefly comment on two of the most conventional ultrasonic testing modes that include pulse-echo and through-transmission techniques, and stress their pros and cons for evaluating multilayered materials.

For the pulse-echo mode, one transducer acts as transmitter-receiver, and this method thus requires that the waves travel twice through the sample thickness. When the ultrasonic waves encounter a damaged interface, the reflected energy in the form of pulse-echo amplitude is distinct from that in an undamaged situation. However, for multilayered materials, this method can hardly distinguish multiple damages. When the layer thickness is less than or comparable to the wavelength of the ultrasonic transducer, the reflected echoes from the front and back layer interfaces can overlap. Thus, confusion can be caused in case of either multiple defects or superimposed back-wall signals due to incompetent range resolution [12]. The usual approach to prevent overlaps is to increase the transducer frequency and/or decrease the pulse width. However, there are several situations where this approach is not an option, because high-frequency waves suffer from high attenuation during propagation, resulting in low penetration [13]. This method can also be combined with two-dimensional scanning, thus obtaining three-dimensional images of the specimen. In principle, this method should enable the determination of the depth of a defect, but due to the limited bandwidth of the instrumentation and the very strong echo from the front surface of the layered media, the signals reflected by intrinsic boundaries are masked by interferences. The information about the depth of the defect can then be extracted but only by using additional post-processing of the ultrasonic signals. As an alternative, through-transmission methods can be considered, since they usually only require one travel through the sample.

For the through-transmission mode, two transducers are used: The transmitter is placed on one side of the sample, whereas the receiver is placed on the reverse side of the sample. When the ultrasonic waves encounter defects on their path, the signal attenuates and thus reveals their presence. Typically, the ultrasound waves only travel once through the sample thickness, hence the wave attenuation is lower for the through-transmission mode than for the pulse-echo mode. Nonetheless, for through-transmission testing, the transducers installation (on the testing facility) undergoes several limitations. For instance, the need for accessing to both sides of the testing sample limits the application of through-transmission methods for on-site NDE inspections. Additionally, for local contact measurements, the variability of the transducers alignment with respect to the expected damage location can

alter the received signals, and thus their interpretation. On the other hand, immersion measurements requires two transducers to be mounted on the tank equipped with motion controller system for C-scans, but most available commercial C-scan immersion systems are designed to handle only one transducer [14]. One further disadvantage of this method is that it does not possess a resolution across the sample and it is impossible to determine between which layers the defects is located. As a consequence, important defect features can be missed or wrong located. In order to prevent those inconveniences, an alternative low-frequency through-transmission setup has been proposed (known as sub-wavelength technique), where a longitudinal waves are transmitted through layers, whose size is much smaller than the wavelength of the transmitter [15].

In principle, classical time-of-flight (TOF) methods could be adapted for ultrasonic NDE of layered media. However, for the purpose of identifying small thicknesses, the required frequency is very high, and the cost of these methods become prohibitive. For instance, in the case of composites, high-frequency waves begin to interact with micro-structural details (individual plies or fibers, resin-rich regions, etc.) which interfere with the damage characterization process. It is therefore essential to employ advanced signal enhancement techniques to extract useful diagnostic information from the measured ultrasonic NDE signals.

3.2 Overview of ultrasonic NDE oriented signal processing

Ultrasonic NDE of multilayered structures undergoes some specific problems. A first problem is the high attenuation due to scattering of ultrasonic waves and multiple reflections inside the samples caused by the different acoustic impedances of the layers or the possible presence of defects. The scattering by microstructure components of a material causes serious difficulties in the detection of discontinuities, as it reduces the signal-to-noise ratio (SNR). A second problem is penetration through multiple interfaces with high acoustic impedance changes. A third challenge is the axial resolution for detecting delamination and cracks at closely spaced interfaces, whose size is small in comparison to the wavelength of the emitted wave (sub-wavelength resolution). Indeed, when the layer thickness is less than or comparable to the wavelength of the transmitted wave, the multiple echoes can overlap and make the ultrasonic signal interpretation difficult. The different propagation modes, diffraction and dispersive attenuation make the interpretation of ultrasonic signals even more complex. In addition, ultrasonic echoes are often contaminated by noise generated from both the imperfections of the acquisition system and the propagation path through the inspected materials, which can hide the echoes caused by a possible defect [6]. The last commonly occurring problem is associated with the amount of data generated by an ultrasonic inspection of a specimen [16]. When a scan is performed, a time-domain waveform must be acquired at each spatial point. For even moderately sized specimens, the amount of data acquired is large, and the complete waveform can hardly be retained and displayed for each

measured point on the specimen. One common approach to resolve this problem is to reduce the waveform to a simple root mean square (rms)-value, which is generally displayed as a gray level on a two-dimensional plot. However, one obvious drawback to this method is the lack of detailed information about the flaw, since the location of (multiple) defects in a stack-up of layers cannot be isolated from these data.

The need for overcoming the aforementioned problems, accurately interpreting large volumes of inspection data, and minimizing errors due to human factors motivated the use of signal processing and classification techniques. Typically, such a NDE system that incorporates signal processing and classification techniques is divided in three steps: (1) The extraction of parameters from the ultrasonic signals, which should be sensitive enough to defects, and minimally sensitive to the noise of the measurement system, (2) an optimal representation of the features vector, by means of dimensionality reduction while retaining the discriminatory information, and (3) the definition of the algorithm of classification. The available bibliography is basically restricted to two topics, those are the enhancement of detection (noise reduction and echoes enhancement), and the defect characterization for signal classification. Since the eighties, those methods have been increasingly used to provide enhancement techniques for ultrasonic imaging, especially for elastography imaging (B-scans) or conventional C-scans. However, the processing of signals directly obtained from the ultrasonic transducers (A-scans) has been scarcely addressed. As the focus is on 1D ultrasonic signals, we make no attempt to review any of the 2D imaging techniques here. Concretely, we intent to give an overview on the signal processing methods that have been applied to ultrasonic signals, starting from relative simple time and frequency-domain approaches, while ending up with more complex approaches including redundant and sparse signal representations.

3.2.1 Enhancement of detection

Ultrasonic signals are often contaminated by noise and/or artifacts originated from both the measurement system (e.g. transducers and instrumentation) and the material under inspection. Consequently, noise places a fundamental limit on the detection of small defects and the measurement accuracy. To increase the probability of defect detection and to decrease the probability of false alarm, a number of signal processing techniques have been applied for noise reduction and enhancement of detected echoes.

In many applications, the noise is generally assumed to be an uncorrelated Gaussian random variable, with zero mean and a band-limited power spectral density function [17]. In areas where the measurements are repeatable, such as ultrasonic NDE, the SNR can be improved by signal averaging, since the specimen-dependent part of the signal remains the same for all measurements (and thus after averaging), whereas the disturbances can be reduced since they are randomly generated in each individual measurement.

Nevertheless, a small random time-shift may be present due to imperfections of the measurement system or unstable conditions in the propagation path, causing signal misalignment in the time-domain. Under these conditions, the process of signal averaging results in a signal shape distortion. Grennberg and Sandell [18] proposed a signal averaging method based on the Hilbert-transform correlation to obtain a higher SNR without signal distortion. Time delays of all the samples can also be estimated by the cross-correlation method, so that the signals can be aligned on the time axis for better averaging. Alternatively, one can design a filter in the frequency-domain, and by focusing on a frequency-band of interest, it is possible to suppress effects of the noise out this band over the time-domain signal.

However, for highly scattering materials, there is another type of noise called structural or grain noise, which is produced by the microstructures/grain boundaries of the inspected material. Each grain behaves like a scattering center, producing an echo that is isolated or superimposed with other echoes coming from other grains which can hide the echoes produced by a possible defect. Grain noise will exhibit a small-scale correlation and can be erroneously associated to defects. This noise is coherent with the emitted signal and cannot be eliminated by conventional techniques such as classical filtering (e.g. time-domain smoothing or frequency-domain filtering) or temporal averaging [19]. The major drawback of the time-domain processing is that it provides poor measurement accuracy, particularly when the echoes overlap. Therefore, it is often advantageous to process the signal in a transformed domain which allows highly flexible operations. In this case, a conventional approach for filtering out grain noise consists of observing the frequency spectrum of the ultrasonic signal, and particularly its power density spectrum. Indeed, one can assume that the echoes caused by the flaw differ in spectral content from those due to the background scattering noise. An optimal approach is to use a Wiener filter, which operates on the spectral differences between the two distinct signal contributions. Unfortunately, the Wiener filter requires a prior knowledge of the power spectral densities of both the noise and flaw echoes [20]. Autoregressive analysis has also been used as an alternative approximation to enhance ultrasonic signals. Wang *et al.* [11] used second and third-order autoregressive (AR) models to evaluate the spectral shift in grain signals by utilizing features such as resonating frequency, maximum energy frequency or AR-coefficients. On the other hand, Izquierdo *et al.* [19] presented a method that considers the time-varying spectral content of the received echoes, based on a time-varying autoregressive model of the structural noise.

Alternatively, deconvolution techniques may be useful to separate the signature of the material under investigation (i.e. the impulse response of the system) from the corrupted response of the measurement system (i.e. electronic system, ultrasonic transducers, and additive noise). The first proposals to solve the deconvolution problem in ultrasonic NDE used classical techniques, such as the Wiener filter, spectral extrapolation, estimation of the least squares [21], or homomorphic deconvolution by computation of the cepstrum [22]. Nonetheless, those conventional deconvolution techniques are sensitive to the additive

Gaussian noise and yield a minimum phase defect signature which contradicts the non-minimum phase property of ultrasonic signals. Thus, higher-order statistics (HOS)-based deconvolution methods have been developed to provide blind deconvolution techniques, avoiding any prior information on the signal noise or defect [23, 24].

However, in all these techniques, the signals are analyzed either in the time-domain or in the frequency-domain. It is noteworthy that an ultrasonic signal is usually a broad-band pulse modulated at the center frequency of the transducer, and is therefore time and frequency-limited. For this reason, the utilization of a time-frequency analysis, where the signal is decomposed both in the time and frequency-domain by means of the short-time Fourier transform (STFT), can be more appropriate. The added complexity of describing the originally 1D time-domain signal as a 2D representation results in a redundant signal representation, which can be advantageously used to improve the interpretation of the experimental data [25]. Time-frequency representation of ultrasonic signals is thus a useful tool for simultaneous characterization in time and frequency, in particular for detecting and characterizing dispersive effects and flaw echoes in high scattering materials [26].

Among the time-frequency analysis techniques, the Wigner-Ville distribution (WVD) has been used for the characterization of materials and localization of flaws. In particular, it has been applied to distinguish echoes from a crack from the noisy echoes generated by the scattered ultrasonic waves through the material grains [27]. However, due to the inability of reducing the cross-terms, useful information is always hidden, and it is therefore necessary to preprocess the signals before applying WVD. To get around it, Wu *et al.* [28] recently proposed an enhanced Wigner-Ville distribution (EWVD) for ultrasonic NDE of thin composite plates, based on the chirplet decomposition and signal elimination. Hence, useless echoes that affect the representation of flaws are conveniently eliminated from the WVD. In order to enhance the flaw visibility, a frequency diverse statistical filtering technique known as split-spectrum processing (SSP) was developed [29]. In this technique, the received ultrasonic wide-band signal is divided into a set of narrow-band signals using a bank of bandpass filters, in which nonlinear post-processing is applied to obtain a reconstructed signal less affected by noise [30]. Recently, SSP has been proposed for its ability to resolve echoes associated with delaminations in CFRP detected by ultrasonic methods [31, 32]. However, this technique is sensitive to the parameters of the filter bank, such as the center frequencies and bandwidth, and is consequently very difficult to employ in practical applications [6].

As an alternative to SSP, the Wavelet Transform (WT) has also been utilized to improve ultrasonic flaw detection in noisy environment. In contrast to SSP, the WT uses a constant relative bandwidth, resulting in a filter bank with a self-adjusting window structure that can display the temporal variation of the signal's spectral components with varying resolutions [25]. This property of the WT is extremely useful for detecting flaw echoes embedded in background noise, and the WT has thus widely been used for ultrasonic NDE of materials for pulse detection and noise suppression, both in its continuous [33, 34] and discrete form [35, 36]. Although this procedure may seem similar to thresholding the signal in the time

or frequency-domain, WT thresholding results in minimal averaging or smoothing of the signal in the time or frequency-domain, because each time-frequency contribution of the original signal is considered locally in the time-frequency domain. However, the operation can fail if the noise is correlated. Some efforts have been made to palliate this limitation of the wavelet thresholding. One is to utilize a 'level-dependent' soft threshold for a signal with stationary correlated noise [37]. Another is to use overcomplete and sparse signal representation techniques to cope with the ultrasonic flaw detection and noise suppression problem [38].

Indeed, redundant and sparse signal representations have drawn a lot of research attention over the past decade. Ultrasonic signals acquired from a multilayered structure generally consists of a limited number of echoes, since the layered structure contains a limited number of abrupt impedance changes. Consequently, the ultrasonic signal can be assumed to have a sparse representation [39]. A common approach is to use a linear time-invariant (LTI) model to describe the propagation of the ultrasonic wave inside a layered material, assuming that the echoes of the received signal are delayed and attenuated replica of the transmitted pulse corrupted by noise [40]. A widespread application of sparse signal representation that offers great advantages is sparse deconvolution (SD) [41, 42], which benefits to ultrasonic echo detection, defect sizing and noise suppression [6]. This technique is nowadays recognized as the state-of-the-art denoising technique.

The aforementioned techniques are usually employed as preprocessing steps (i.e. noise suppression or echoes enhancement) for damage classification or system identification procedures. In addition, most of these studies are restricted to backscattering approaches. Generally, these techniques are based on the assumption that the ultrasonic output signal results from the convolution of the input signal with the impulsive response (IR) of the specimen, plus an additive noise. They are then applied in an heuristic way, without an explicit model which bridges the extracted signal features to the mechanical and geometrical properties of the material, and thus a precise physical interpretation remains often unavailable. Although the sparse representation considerably improves this approach, as most of the parameters are forced to be zero, the lack of a physical interpretation is still present, since prior knowledge on the number of non-zero parameters is generally unavailable.

3.2.2 Defect characterization and signal classification

A number of signal processing methods have been proposed to classify defects detected by ultrasonic signals, such as pattern recognition techniques. Other related proposals dealt with the feasibility of using physical features from time and frequency representations of signals for flaw characterization, including maximum amplitude of the signal, pulse duration, waveform kurtosis, and rise and fall times [43]. A comparison of feature-based classifiers for ultrasonic structural health monitoring has recently been performed by Michaels *et al.* [44].

An essential element in NDE systems is the analysis of the captured signal, by means of a robust parameter extraction, in order to obtain relevant information from the tested specimen [45]. In some cases, the extracted signal parameters can be processed again to reduce the dimensionality of the feature vectors, in order to achieve the pursued information about the specimen [46, 47]. For a real-time system, the number of features used in the classification process needs to be reduced, since the computational burden of classification increases with those. Consequently, the fewest number of features which yield the highest correct classification of the materials should be selected [48].

Principal component analysis (PCA) has been widely used for extracting features from the defects in ultrasonic classification systems, since PCA gives an optimal linear transform for reducing the dimension of a data set providing uncorrelated components. In addition, noise may be reduced, as the data not contained in the first principal components may be mostly due to noise. Khelil *et al.* [49] extracted wavelets parameters from ultrasonic signals, and then obtained an optimized attribute vector applying PCA, which enabled them to discriminate between planar and volumetric defects. In another related proposal, Ramuhalli *et al.* [50] extended the PCA method to analyze 2D data for generating a reduced dimensional feature vector for classification of B-scan images. Alternatively, the classical linear discriminant analysis (LDA) has also been applied. LDA attempts to express a small amount of dependent variables as a linear combination of other features, in order to characterize or separate two or more classes of pathologies or defects. Signal parameters, such as wave velocity, dominant frequency, and signal attenuation were estimated, and then preprocessed by LDA obtaining a good fitting for archaeological period classification [51]. Another traditional approach is to take the wavelet transforms of the ultrasound signals, and then to use a subset of the coefficients as features for the classifier. To determine these optimal features, Meyer *et al.* [48] applied a forward sequential feature selection (FSFS) algorithm which retains the lowest number of features required to obtain the highest system performance. The single value decomposition (SVD) of the Hankel data matrix (obtained by assuming that the discrete output data from the system can be represented by a state space model) has also been employed to determine the position of defects in laminated materials [16].

Independent component analysis (ICA) is a relatively new method in which the goal is to find a linear representation of non-Gaussian data so that the components are statistically independent, or as independent as possible. Recently, ICA has been used for enhancement of ultrasonic flaw detection and noise suppression. For instance, ICA has been used for the diagnosis of the material consolidation status and for the determination of the thickness material profiles in restoration of historical buildings [52]. This recent contribution suggests that ICA may have a great potential to separate the multiple echoes in an ultrasonic signal obtained from a multilayered structure.

Once a set of optimum features has been selected, a suitable classifier is needed to classify the waveforms. A number of supervised and unsupervised classification algorithms such as K-means clustering algorithm, fuzzy C-means, distance-based recognition systems

[53], threshold-based decision [27, 54], Bayes' decision rule [48] and neural networks [55, 51] have been proposed for classifying signals. The success of all traditional classification algorithms depends heavily on the availability of an adequate and representative set of training examples, whose acquisition is often very expensive and time consuming. However, real defects in industry are very complicated, so that in practical ultrasonic NDE applications, accurately classifying defects remains a big challenge for current techniques. In addition, in those cases, the main objective is usually the minimization of type-I errors (that is, to avoid detecting damage that does not exist), and only a few proposals look for more specific information of the material [35, 30]. Finally, except the recent works by Hägglund *et al.* [56, 57] for classification of thin bonding layers within three-layered materials, proposals on the classification of complex damage mechanisms in multilayered specimens are inexistent.

3.3 Model-based estimation

Accurate estimation of the ultrasonic echo pattern is essential in determining the propagation path properties, i.e the layered structures that compose the specimen under inspection and the possible presence of defects (location, size, orientation, and microstructure). Many ultrasonic testing applications are based on the estimation of the time-of-arrival (TOA), time-of-flight (TOF), time-difference of arrival (TDOA), or the broadband ultrasonic attenuation (BUA) of ultrasonic echoes. However, the estimation of those characteristics undergoes severe limitations when dealing with complex media (e.g. layered material properties, frequency-dependent attenuation, dispersion effects, etc.). Thus, the extraction of this information requires models that explain the formation of echoes. This problem has been addressed in a number of ways, and gave raise to the so-called model-based estimation procedure which generally consists of two steps: (1) The formulation of a reliable model that idealizes the measurements of the ultrasonic wave-material interactions, and whose model parameters can be linked to the physical properties of the layers, and (2) the use of an optimization algorithm to estimate those model parameters. The model-based estimation procedure offers a convenient solution for (i) reconstructing unknown material properties, (ii) monitoring (i.e identify and quantify) a medium whose properties changes over time, (iii) restoration of the output signal in the presence of significant noise by deconvolution, and (iv) for resolving closely-spaced overlapping echoes providing valuable applications such as the thickness sizing of thin layers.

It is noteworthy that investigations on model-based estimation for ultrasonic NDE applications have given raise to slightly different designations and developments, in accordance with the scientific community of which the researchers stem. In the engineering community, wave propagation models are usually *physics-based models* that strongly rely on the rational principles of continuum mechanics. The optimization is then performed using an *inverse problem* procedure, and so the overall problem approach received the name of *model-based inverse problem*. In contrast, in the information technology community (e.g. signal theory, telecommunication, electrodynamics, etc.), those models are typically *signal-based parametric*

models inspired by concepts from lattice filter theory or circuit models. The *estimation of the model parameters* using optimization algorithms is ordinarily understood as solving a problem under a *system identification approach*. Both denominations will be employed over the course of this work, depending from which perspective the research is conducted.

3.3.1 Ultrasonic wave modeling

Over the last decades, considerable attention has been given to the modeling of wave interactions with multilayered materials, in a number of diverse disciplines such as geophysics, electromagnetics, optics, and acoustics. An exhaustive review of the literature on this subject is beyond the scope of this thesis, and the reader is referred to the classic monograph by Brekhovskikh [58] for a concise review of the mathematical framework and physical phenomena related to this topic. Typically, the resolution of a model-based estimation procedure requires numerous evaluation of the model (i.e. the forward problem) to update the material properties over the optimization process. This characteristics promotes the use of efficient and low complexity models (preferably semi-analytical), and as a matter of fact makes almost unviable numerical methods, such as finite-difference time-domain (FDTD), finite element (FEM) and boundary elements (BEM) methods, due to their prohibitive computational costs for accurate material characterization [59]. Here, for sake of simplicity, the review is restricted to the one-dimensional modeling of ultrasonic waves that propagate with normal incidence through layered media.

Physics-based models

A method that describes ultrasonic waves in multilayered media with an arbitrary number of layers is desirable. Thus, modeling tools have generally been developed from matrix formulations, which combine the principles of continuum mechanics within each layer with the transmission conditions at the layer interfaces, resulting in a matrix description of the system in terms of its external boundaries (incoming and outgoing wave displacements) [1]. In the latter half of last century, such matrix formulations have evolved and given raise to numerous works, based on two quite different approaches and many variants which are in accepted use (differing usually in their implemented form).

To solve the problem of wave propagation through planar multilayered structures, a very systematic Transfer Matrix (TM) method (i.e. also referred to as a *propagator matrix* method) has been developed and has received considerable attention for a wide range of applications from researchers involved in NDE (e.g. acoustics, optics and geophysics). The wave motion of a physical system is usually represented by a set of state equations describing the dynamic state of certain physical variables. In this method, the solution to these equations is a transfer matrix which maps the field variables from one layer to the next. The interface boundary conditions are automatically satisfied by multiplying the individual transfer matrices, and thus one just has to impose the appropriate boundary conditions to the remaining two surfaces [60]. The earliest development of the TM method for wave propagation in layered media was introduced by Thomson [61] , then extended by Haskell

[62] in the early fifties, and furthered afterwards by Gilbert and Backus [63]. During the following decades, this theoretical framework has given rise to numerous works almost entirely devoted to seismological applications. First attempts oriented to applications in the ultrasonic field arose in the late seventies [64, 65], and peaked in the early nineties, as indicates the meticulous review by Lowe [1]. Among others, these developments principally addressed the introduction of wave attenuation in the TM approach [66, 67], and its extension to anisotropic media [68, 69, 70], to cylindrically layered media [71, 72] and to multilayered anisotropic poro-elastic media [73]. Other related proposals adapted TM method to periodically stratified media composed of alternating elastic solid and ideal fluid layers [74] and to anisotropic periodically multilayered media [75]. Most of these works dedicated much effort to predict the transmitted waveforms, but it may also be useful to predict the transfer function of the material. This slightly different approach has lead to some alternative models for adhesively-bonded joints [76, 77] that are rather variants of the TM method than innovative approaches.

Although the TM approach is applicable in principle, its direct implementation has been found to suffer from numerical instabilities, particularly when considering layers of large thickness and high-frequency ultrasound. The cause of this problem is the poor conditioning of the transfer matrices when performing multiplications that combine both decaying and growing terms (i.e. small precision errors amplified by the exponential terms) [78]. Many modifications of the original transfer matrix have been proposed to palliate this precision problem. One common approach, known as the delta-operator technique, is to retain the concept of transfer matrices but to rearrange the equations to avoid that they become ill-conditioned [79, 67, 80, 81]. Such a technique preserves the advantage of a low complexity transfer matrix system but unfortunately fails to keep the conceptual simplicity of the Thomson-Haskell formulation. In addition, for propagation through anisotropic media, this technique requires the computation of large-order delta matrices and the derivation of many analytical expressions [82]. In an other related approach, Hosten [83] suggested to perform certain numerical test to limit those large *frequency-thickness* product values that ultimately cancel each other, in order to restore the stability of the system without loss of precision. More recently, Balasubramaniam [84] proposed an approximation algorithm that numerically truncates those higher values by imposing a maximum threshold for the exponential terms, thus limiting the error amplification and propagation. Although this approximation does not compromise the computational cost of the original TM approach, the truncation strongly depends upon the assigned threshold value, and is thus highly application-dependent.

As an alternative to the TM approach for a computationally stable solution, the Global Matrix (GM) method was introduced by Knopoff [85], and has been well documented [86, 87, 88]. In this method, a large single matrix represents the whole system, and is assembled by simultaneous matching of the boundary conditions at each layer interface. This technique is robust and can be implemented easily. However, this approach involves a

global banded matrix whose size increases with the number of layers, and thus unfortunately leads to considerable amount of memory storage and computation time when the system comprises many layers [1]. Among the recent contributions, it is worth to mention the stiffness matrix (SM) method which presents several advantages over the conventional TM method, and whose basis was already provided by Kausel and Roësset [89] in the early eighties. This method operates with total stresses and displacements via the stiffness matrix applied in a recursive algorithm, reduces the solution to a global banded linear system of equations, and is more convenient to incorporate imperfect interfaces. This approach has been successfully proven to resolve the numerical instability of the TM method [90, 91], and naturally provided the framework for developing recursive asymptotic method [92, 93]. A rigorous comparison of the numerical stability between the TM and the SM methods is given by Balasubramaniam *et al.* [94]. Although the SM method has been demonstrated to be computationally stable for large layer thickness, it becomes inaccurate and nearly singular when the layer thickness reduces toward zero. As a consequence, Tan [95] recently proposed an hybrid compliance-stiffness matrix method for stable analysis of elastic wave propagation in multilayered anisotropic media. As the SM method, this approach is able to eliminate the numerical instability of the TM method, and also preserves the convenience for incorporating imperfect interfaces. However, it has the advantage of remaining well-conditioned and accurate even for zero or small thicknesses.

Communication theory inspired models

Alternatively, wave propagation phenomena in layered systems have also been studied by considering only general principles about delay, continuity and energy conservation, and somehow leaving behind knowledge about physics and differential equations. This approach has given raise to a generic framework, that could be applicable to such diverse wave types as sound and water waves, light in thin films, normal incident elastic waves (both pressure and shear types), electromagnetic waves, transmission lines, and electrical ladder networks [96]. Within this framework, multilayered wave-interactions have been mostly described using concepts drawn from communication theory, since the resulting transmitted and reflected waves can be connected to equivalent circuit models and/or lattice filter theory. Here, we briefly review these two families of models.

Under certain assumptions, the characterization of layered materials can be well represented by means of equivalent models based on electric circuits [97]. An equivalent circuit may be understood as the modeling of a mechanical system based on the electric network theory, that is a one-dimensional model that describes the analogue electrical characteristics of an acoustic structure. The voltage and current in the equivalent system stand for stress and velocity of the material particles, respectively. The reason circuit analog models are good for wave propagation problems in stratified structures, is that they are exact for one-dimensional wave propagation (and thus serve as basis for validating numerical models) regardless of whether considering acoustic or electromagnetic waves, and provide a powerful

means of computing the response of the system, such as reflection and transmission coefficients [98, 99]. For instance, transmission lines have been used to represent the propagation of plane longitudinal waves in generally isotropic layered media [2]. In a similar proposal, Ghorayeb *et al.* [100] achieved a complete simulation of a dental ultrasound-system with its associated driver-receiver electronics, by incorporating the transducers, the focusing lens and the different tooth layers in a model based on transmission line theory. In the same vain, Challis *et al.* [101] proposed to simulate wave propagation in lossy materials with mechanical properties which vary gradually in the spatial dimension, by using electric circuit transmission line analogs to the viscoelastic mechanical system. Alternatively, Vogt and Ermert *et al.* [102] employed a linear ultrasonic two-port network model analog to conventional electrical networks to reconstruct layered media, which consist of discrete layers connected in series. The multiple reflections are considered by a stepwise estimation and secession of network elements. However, despite the conveniency of equivalent circuit models to reduce the computational cost for numerical evaluation, this approach becomes complicated under conditions less restrictive than those used here (e.g. attenuation, dispersion, nonlinearity) and requires a reasonable background in electronics.

The lattice filter theory has been routinely used in making acoustic tube models for the analysis and synthesis of speech, with the layer recursions being mathematically equivalent to the Levinson lattice recursions of linear prediction. It also found application in geophysical deconvolution, inverse scattering problems for oil exploration or the probing of tissue by ultrasound [103]. The Goupillaud specialization [104], i.e. elastic layers of equal-wave travel time, has been often used in geophysical applications to model wave propagation in inhomogeneous media. Despite the long history of mathematical developments for Goupillaud-type media, some recent proposals employed an innovative digital representation of the wave propagation in multilayered elastic media, by considering the bonded structure as an acoustic filter by means of the z-transform [105]. Among them, Velo *et al.* [106] developed a finite trigonometric series representation for the stress in a multilayered Goupillaud-type elastic strip, achieved by means of a z-transform method. As a result, they are able to identify optimal layered designs which provide the smallest stress amplitude. Gazonas *et al.* [107] derived the resonance frequency spectrum for an m-layered Goupillaud-type elastic medium, obtaining analytical stress solutions from a coupled first-order system of difference equations also using z-transform methods. Their results suggest that the natural frequency spectrum depends on the layer impedance ratios and is inversely proportional to the equal wave travel time for each layer. Nonetheless, the Goupillaud characteristics are unrealistic for many practical applications, since the layers of inhomogeneous materials does usually not have equal-wave travel time.

Signal-based parametric models

Over the past two decades, signal modeling and parameter estimation for detecting and estimating multiple interfering echoes has been a main subject of study in the field of ultrasonic imaging. To this end, parametric signal models have been developed, since they

offer several advantages over heuristic approaches (see Section 3.2) directly applied over experimental data: (1) High-resolution parameter estimates can be achieved, (2) the accuracy of the estimation can be evaluated, and (3) an analytical relationship between model parameters and physical parameters of the system can be established.

A common approach to address this problem is to approximate the output signal by a Bernoulli-Gaussian (BG) model [108, 109, 110], that is a parametric signal model, whose model parameters can be linked to the physical properties of reflectors and frequency characteristics of the propagation path, by assuming that the output signal is made of echoes that are time-shifted, amplitude-scaled, and noise-corrupted version of the input signal. Implicit to this method is the assumption that the desired system response is a spike train with unknown amplitudes and locations, where the number of spikes is considered to be unknown. In addition, there is no assumption or statistical knowledge imposed on the amplitude and locations of the spikes. Among the first proposed approaches, Demirli *et al.* [111] modeled ultrasonic backscattered echoes in terms of superimposed Gaussian echoes corrupted by noise. In this model, each Gaussian echo is a nonlinear function of a set of parameters that are sensitive to the echo shape, e.g. the echo bandwidth, time-of-arrival, center frequency, amplitude, and phase. These parameters have intuitive meanings for an ideal surface reflector in a homogeneous propagation path. The TOA is related to the location of the reflector, whereas the bandwidth factor determines the bandwidth of the echo or the time duration of the echo in the time-domain. On the other hand, the center frequency is governed by the transducer center frequency and the frequency characteristics of the propagation path. Finally, the specific amplitude and phase of the echo account for the impedance, size, and orientation of the reflector. Nonetheless, this model is not valid for any kind of signal waveform and one must have an accurate prior information of the input signal's appearance [112].

Dealing with thin layers or long input signal's time-support implies that the output signal consists of several reverberant and overlapping echoes. Hence, a parametrization of the layered structure instead of each echo is preferable, since the total number of parameters in the model can be kept small and is independent of the number of observable echoes. In that vein, Hägglund *et al.* [56] proposed a parametric modeling of the received ultrasound waveform, to be used for flaw detection in layered media. The model structure is chosen so that all dynamics of the waveform is captured by a small number of parameters. The material is modeled using a continuous AR-model with parameters connected to physical properties, related to the thicknesses of the material layers and the reflection coefficients given by the layer boundaries. The effects of dispersion and diffraction are assumed to be negligible and the different materials are considered to be lossless. In a later work, Hägglund *et al.* [113] improved their continuous AR-model with further parameters connected to physical properties, including the attenuation inside the layers. Alternatively, Hägglund *et al.* [114] used a physics-based parametric layer model to analyze the multilayered material, where the parameters of the model are associated with physical properties (e.g. the reflection coefficients,

the time-of-flight, and the attenuation) of each layer within the structure. It is noteworthy that this model is a slight variant of those described in the *physics-based models* section. The main advantage using this model is that the complexity of the model is connected to the number of layers rather than the number of observable echoes in the received ultrasonic waveform.

Finally, there are a number of uncertainties which cannot easily be described by a complete physics-based model, including certain material properties (e.g. the attenuation and dispersion) or subtle experimental setup characteristics (e.g. diffraction and misalignment effects). To cope with dynamics that the physical model is unable to handle, Martinsson *et al.* [115] proposed to use a combination of *hard* and *soft* modeling. As in [114], the *hard* (physical) model is applied to describe the multiple reflections and overlaps related to the specific measurement setup, while *soft* (empirical) models, in the form of FIR filters, are used to capture the unknown dispersion and attenuation effects from the layers, and to deal with unwanted diffraction and misalignment effects from the measurement setup. The main benefit of including soft models is that a complete representation of the waveform is possible, and the residual (i.e. mismatch between the modeled and observed waveform) only consists of measurement noise. On the other hand, the main drawback is that the number of parameters to estimate increases and the model has a loss in simplicity, so that the estimation algorithm requires higher computational resources and may suffer from numerical instability.

3.3.2 Inverse problem and estimation of the model parameters

In NDE of materials, the idea is that the ultrasonic data are related to the material properties through a known mathematical model. Generally, the mathematical model defines the forward problem in that it relates known material properties to the ultrasonic data. Thus, if experimentally measured ultrasonic data are available, computing the required material properties is just a matter of solving the inverse problem (IP), i.e. relating the known ultrasonic data to material properties using the inverse of the same model. However, although the forward approach might be relatively easy, the inverse scheme is often cumbersome, since IP's are usually highly nonlinear and hence, analytically intractable. Furthermore, the constraint of limited experimental data sets also increase the effort involved in the reconstruction. Consequently, numerical rather than closed-form solutions appear to be the practical answer for solving such nonlinear IP's. Therefore, formulating the identification IP in an optimization form is one of the most popular approach.

The optimization has been addressed in multiple ways, and a common approach is to formulate it as a nonlinear least-square problem. Generally, an ideal algorithm should cover several scopes, that are to (1) end up with a reasonably good approximation ('accuracy'), (2) achieve this with an affordable computational cost ('efficiency'), and (3) ensure the attainment of a (local) optimum ('convergence'). To this end, a broad spectrum of optimization

techniques have been developed, ranging from local to global methods. A partial classification of them is depicted in Figure 3.1. Here, we briefly review the advantages and inconvenients of those methods, and the reader is referred to the survey on the methods for local unconstrained optimization provided by Dennis and Schnabel [116] for completeness. The basic of those methods relies on the Newton's method, which is an iterative procedure that requires the computation of the gradient and the Hessian that arise when expressing the nonlinear function to optimize as a Taylor series expansion up to the second-order term. In the case that the gradient and the Hessian are not available, they can be calculated with finite-difference (FD) approximations. However, applying the Newton's method with an initial guess far from the optimum can deliver a quadratic model that does not properly represent the non-linear function or even lead to a non-positive definite Hessian matrix, therefore invalidating the convex quadratic model. Hence, to ensure the convergence starting from almost any initial guess, two families of strategies, termed globally convergent modifications of the Newton's method (e.g. line search and model trust region), have been devised. In identification IP's, the Hessian is however not easily available and its computation by FD's is expensive. Alternatively, the secant method is a class of algorithms that use cheaper ways of approximating the Hessian, usually by updating the approximate Hessian in the previous estimate. The best Hessian update is provided by the positive definite secant update or the Broyden-Fletcher-Goldfarb-Shanno (BFGS) method. Except the calculation of the Hessian by updating, the rest of the minimization algorithm remains as in the Newton's method, and so the aforementioned globally convergent modifications are also applicable to the secant method.

Local		Global
Optimization algorithms (Gauss-Newton, Quasi-Newton Secant, Levenberg-Marquardt, BFGS)	Simulated Annealing	Genetic and evolutionary algorithms
Linear and quadratic programming		Neural networks, Fuzzy inference
Kalman filter, projection filter		Random search

Figure 3.1: *A classification of optimization methods used to minimize the cost functional in an inverse problem approach*[1].

Newton's methods and the secant updates can be extended to the non-linear least square problem, taking advantage of its special structure. In that case, the non-linear residual function is expressed in terms of the Jacobian matrix. For instance, the Gauss-Newton method is based on approximating the Hessian by making use of the Jacobian, and is then solved by applying the Newton's method. This approximation increases the algorithm convergence, but has the disadvantage that it is not necessarily globally convergent, and that it is not well defined if the Jacobian does not have full column rank. Nonetheless, it can be shown that in the case that the Gauss-Newton's step is a descent direction, then the aforementioned

[1]Reproduced and adapted from Rus and Gallego [117].

globally convergent modifications can be applied, leading to the damped Gauss-Newton and Levenberg-Marquardt methods. The former is globally convergent although it may be very slow. In addition, this method is not well defined for non-full column rank Jacobian matrices. The latter is equivalent to the Gauss-Newton method modified by the model trust region approach, and improves the behavior of the algorithm for not full column rank Jacobian matrices. Since optimizations algorithms such as Gauss-Newton [118], Levenberg-Marquardt [119] or BFGS [120] are among the most popular in the literature to solve IP's, a brief summary of their characteristics is provided in Figure 3.2. Nonetheless, this corpus of methods are gradient-based techniques, and consequently have a high probability of entrapment at a local minimum for initial guesses that are not close to the global minimum. As an alternative, genetic algorithms (GA's) have hold a lot of promise in dealing with complex problems while requiring significantly few data, for searching such complex multimodal spaces for unique global optima. GA's are not gradient-based search techniques and no initial guesses are required. A deeper insight on GA's is given in Section 9.3.1.

	Gauss-Newton	Levenberg-Marquardt	BFGS
Convergence rate vs. probability of convergence	High convergence rate	Reasonable trade-off	High probability of convergence
Particularities	Good for local scope (near the solution)	Good for global scope (far from the solution)	Does not take advantage of the structure of the cost functional

Figure 3.2: *Characteristics summary of the optimization algorithms*[2].

There are relatively few works reported in the literature that deal with the estimation of material properties through judicious use of the experimentally obtained structural response and the response of the mathematical model of the structure. This is mainly due to the fact that most researchers focus their effort either in the experimental fields or in the modeling ones. For ultrasonic applications, we come across the same *duality* as for the models, depending whether the reported works stem from the engineering or information theory communities. In the engineering community, the *model-based IP* is usually solved for reconstructing altered mechanical properties of materials due to damage. Generally, the optimization algorithms are applied in a rather straightforward way, while the focus is on the physical interpretation of the reconstructed model parameters. In contrast, for researchers involved in the information theory, a thorough effort is made on the model parameters estimation and optimization algorithms during the *system identification approach*, at the cost of analyzing rather simple materials.

Model-based IP's

Since the nineties, a number of studies have been carried out to solve the inverse problem for thickness sizing of thin coatings and reconstructing the mechanical properties of damaged

[2]Reproduced and adapted from Rus and Gallego [117].

composites. In that vein, Kinra and Zhu [15] described a technique for ultrasonic NDE of a thin coating on a thick substrate. They developed an inverse algorithm, which utilizes the well-known Newton-Raphson method, to reconstruct the thickness and the phase velocity through a comparison of the theoretical and the measured transfer functions. Using this technique both the thickness and the wave velocity of the coating could be extracted from the same measurement without knowing either. In a similar proposal, Kinra *et al.* [121] presented an inverse algorithm, which utilizes either the Newton-Raphson or the Simplex method in conjunction with the incremental search method, to reconstruct simultaneously the thickness and phase velocity of the individual layers comprising three-layer specimens. The optimization was achieved by minimizing the difference between the theoretical and the experimental results in the frequency-domain in a mean squared sense. The most important conclusion of that preliminary work was that in addition to the magnitude spectrum, phase spectrum must be considered in the inverse problem. In another related proposal, Kinra and Iyer [122] used an inverse algorithm, which utilizes the well-known secant method [123] in conjunction with the method of least squares, to deduce any one of the four acoustical properties (thickness, wave velocity, density or attenuation) of a thin linear-viscoelastic plate (given the remaining three) through a comparison of between the experimentally obtained and theoretically predicted transfer function.

Alternatively, Balasubramaniam and Whitney [124] described an inverse technique for computing the material elastic constants from data acquired using an immersion through-transmission method for characterizing thick glass-epoxy composites. The group velocity was experimentally measured as a function of the energy propagation angle (group angle), from which the phase velocity was numerically computed as a function of the phase angle [125]. Then, the material constants were determined from phase velocity profiles using commercially available parameter identification software (SCIENTIST, MicroMath Scientific Software). In a similar approach, Balasubramaniam and Rao [126] employed an inverse technique based on genetic algorithms to reconstruct the material stiffness properties of unidirectional fiber-reinforced composites from obliquely incident ultrasonic bulk wave data.

As a drawback, it is worth to note that most of these works propose the simultaneous reconstruction of relatively few model parameters. In addition, some of the works dedicated to the resolution of IP's are purely theoretical, whereas they investigate the stability to noise by adding different distributions and amounts of synthetic random noise to noise-free data simulated by making use of the forward model. In light of these considerations, most of the actual IP solutions remain somehow far from practical applications, since real defects of multilayered media in industry are very complicated, i.e. damage may appear at several locations and simultaneously in different forms.

System identification approach

Independently of the previous works, a number of authors started to explore the merit of model-based system identification approaches for ultrasonic applications, by adapting classical methods originally developed for the analysis of speech or images. Investigations were

conducted in various applications such as transducer pulse-echo wavelet estimation, subsample time delay estimation, and thickness sizing of thin layers. From the information processing viewpoint, the system identification is especially challenging when dealing with overlapping echoes (i.e. the layer dimension is small in comparison with the wavelength of the input signal). In such a case, the discrimination and precise localization of the echoes is far from obvious. Another issue occurs when the noise level is high since echoes may be partly or completely drowned in noise due to the material attenuation. As described in Section 3.3.1, numerous authors modeled ultrasonic signals as the superposition of many Gaussian echoes corrupted by noise. The first approaches [127, 128] tended to decompose the observed data into their individual echoes and then to estimate the model parameters of each individual echo separably using the Expectation Maximization (EM) algorithm or the Space Alternating Generalized Expectation Maximization (SAGE) algorithm [129]. The translation of the complicated superimposed echoes estimation into isolated echo estimations provides computational versatility. In a similar proposal, Demirli and Saniie [111] addressed the estimation of those model parameters using the maximum likelihood estimation (MLE) principle, assuming that all of the parameters describing the shape of the echo are unknown but deterministic. When noise is considered as white Gaussian, the MLE problem simplifies to a least squares (LS) estimation problem. Nonetheless, the iterative LS optimization algorithms suffer from convergence problems and exponential growth in computation when the number of superimposed echoes increases. To overcome this problem, they proposed to use the EM-based algorithm. In a companion paper, Demirli and Saniie [130] showed that their method was able to perform deconvolution in the presence of significant noise, and could restore closely-spaced overlapping echoes beyond the resolution of the measuring system. Unfortunately, there is no guaranty that these iterative algorithms converge to the wanted optimum [40]. Furthermore, the EM algorithm converges very slowly [131], whereas the SAGE algorithm converges faster under certain conditions but becomes unstable for low SNR's [132].

Alternatively, Hägglund *et al.* [113] derived a MLE for estimating the parameters of the developed continuous AR-model to identify the properties of a thin three-layered structure. The noise on both the input and output ultrasonic signals is assumed to be white and Gaussian, implying that the MLE ends up in a Nonlinear Least Squares (NLS) problem. In addition, to achieve a faster iteration in the optimization process, analytical expressions for the gradient and the Hessian are derived. The iterative update of the models parameters to find the optimum is performed by using the Gauss-Newton linearization method. In a related proposal, Hägglund *et al.* [114] improved the MLE for estimating the model parameters by using the noise on both the input signals and the output signals to weight the modeling error, implying that the MLE ends up in a nonlinear weighted least squares (NWLS) problem [133]. According to Pintelon and Schoukens [134], the unknown model parameters are estimated from discrete Fourier-transformed data. In that case, the objective of the model parameters estimation is to find the parameters that minimize the square of the

error, weighted by the covariance matrix. In a similar approach, Martinsson *et al.* [115] also estimated the unknown model parameters from discrete Fourier transformed data using a NWLS fit. In contrast to his colleague, he proposed to use the Levenberg-Marquardt optimization method [135] to maximize the likelihood function, taking advantage of its ability to expand the search space and handle ill-conditioned Hessians.

Among the emerging studies on sparse representation for ultrasonic signals, a common approach is to model the sparse reflectivity sequence as a BG model and to use a maximum a posteriori (MAP) estimation for reconstruction [110]. The latter author proposed a genetic algorithm for optimizing that criterion, motivated by the fact that the latter is non-convex (i.e. has more than one local minimum). Unfortunately, this leads to nonlinear and computationally expensive solutions. As a consequence, truly optimal reconstructions are unfeasible, but many sub-optimal methods have been devised [136, 137]. A possible way for improving the optimization is to add a regularizing term to the usual squared error cost function that will penalize non-sparse solutions [138]. In this context, Soussen *et al.* [42] addressed the sparse deconvolution as an inverse problem where the detection and estimation of the spikes are performed jointly, by explicitly taking into account that the reflectivity sequence is sparse. This can be achieved using either l_1 or l_0-norm regularization [139, 140]. In both cases, the inversion problem results in a numerical optimization problem. For the l_1 case, the optimization is continuous and can be solved by recent efficient algorithms [141]. On the other hand, for the l_0 case, the optimization problem turns into a combinatorial problem whose goal is to find a sparse configuration with a limited number of spikes yielding the best fit to the data. The matching pursuit (MP) algorithm has been widely used in many signal processing areas, and offers a robust approach for solving the sparse deconvolution problem. MP is is a greedy algorithm for realizing sparse decomposition of a signal by splitting the signal into a linear expansion of waveforms selected from an overcomplete dictionary [142]. Due to their simple implementation and numerical efficiency, modified MP methods have recently seen the light in the NDE community [143, 144, 145]. In that vein, Guo *et al.* [39] proposed a method based on a MP algorithm to decompose an ultrasonic signal into elements of the Gabor dictionary to suppress noise and enhance flaws by using the sparse information to estimate the crack location and size. In an other related approach, Bossmann *et al.* [40] presented two sparse deconvolution methods for nondestructive testing. The first method is based on a (modified) MP algorithm [146], whereas the second uses the approximated Prony method (APM) [147]. Although greedy algorithms are relatively fast and have, therefore, been used extensively in practical applications, their performance is guaranteed only under very strict conditions. The reader is referred to the excellent review by Zhang and Harvey [6] for a deeper insight into the optimization algorithms for performing identification of (sparse) systems.

As a drawback, it is worth to mention the algorithms described in most of these works require an accurate initial guess for providing a precise parameter estimation. Some authors proposed to find the initial guess on the parameters from prior knowledge on the theoretical

values of the material, but this is often not possible in practical applications. In addition, most of those works deal with rather simple and conventional materials, which consist of single or few homogeneous isotropic layers in an undamaged state.

Despite of the satisfying properties of a model-based approach, several general issues which should be taken into account are summarized as follows: (1) if the observed data are nonlinear functions of parameters, the inverse problem (parameter estimation) is also nonlinear and does not have an explicit solution; (2) the noise embedded in the observed signals can difficult the estimation of the true parameters value. Hence, the degradation caused by noise needs to be eliminated or quantified as uncertainty bounds on the estimated parameters; and (3) the number of model parameters may a priori not be known, and therefore the model-order selection needs to be combined in the estimation problem [130].

This void in the mechanical characterization and interpretation of materials may be overcome by adopting a probabilistic model-based inverse problem strategy, coupled with a stochastic model-class selection formulation [148]. This approach allows one to obtain not only the optimal parameters in a model class, but also the uncertainty associated with the parameter estimates (due to measurements noise, heterogeneous material properties, approximated mathematical model, unknown number of model parameters, etc.).

3.4 Nonlinear acoustics

In linear acoustics, the presence of structural inhomogeneities lead to phase and/or amplitude variation of the received signal whereas its frequency remains the same than that of the emitted signal. The majority of well-known acoustic phenomena (i.e. time-of-flight (TOF) or broadband ultrasonic attenuation (BUA)) are associated with linear elastic material properties, and are described by a linear stress-strain relation (Hooke's law). In contrast, in nonlinear acoustics, when a sinusoidal ultrasonic wave at a given frequency is transmitted into a nonlinear medium, the fundamental wave distorts as it propagates, and therefore second and higher harmonics of the fundamental frequency are generated [149]. Those well-known acoustical manifestations of nonlinear behavior can be explained as follows: Due to the amplitude-dependent wave propagation velocity, the compression phase of a sinusoidal wave travels faster than the rarefaction phase, and thus the wave distorts after it has propagated for some distance through a nonlinear material being transformed into a saw-tooth wave. This steepening of the waveform in the time-domain causes an energy transfer from the fundamental frequency to higher harmonics. As a consequence, several higher harmonics can be observed as local maxima in the frequency-domain [150, 151].

Measurements of the amplitude of these harmonics thus provide a mean for extracting the coefficient of second and higher order terms in the nonlinear stress-strain relation, and deliver valuable information on the material degradation that uses to be far more sensitive than the linear acoustic properties. Measuring these amplitudes is commonly referred to as the finite-amplitude method, initially developed by Breazeale and Thompson [152]. The nonlinear coefficients are usually determined by measuring the second-harmonic generation

and sometimes higher harmonics for the longitudinal waves, and can be used to characterize acoustic nonlinear properties of gases, liquids, and solids. For this technique, the through-transmission mode in immersion is usually preferred. Instead of using two transducers, it is opportune to replace the receiver by a needle hydrophone (with a nearly linear frequency response), in order to conveniently measure the second and higher-harmonics. A finite-duration burst of (nearly) pure tone - typically around 20 cycles long - is launched towards the specimen, and the progress of some stationary peaks near the end of the tone-burst is followed and selected to compute the Fast Fourier Transform (FFT), and thus allows to obtain the second and higher-order harmonics amplitude.

In this dissertation, our goal is not to survey all papers published in this broad and rapidly growing area, but only to review some experimental and theoretical results that might be exploited in the present thesis. To this end, we provide some basis on the very restricted topic of classical nonlinear acoustics using the finite-amplitude method. First, we expose the underlying mechanisms of the elastic nonlinearity of materials. Then, some works that explore to the intrinsic nonlinearity of materials (that is the determination of the nonlinear elastic parameters) are reviewed, whereas a final subsection is devoted to studies that investigate the nonlinearity changes due to to material degradation.

3.4.1 Elastic nonlinearity of materials

The nonlinear elastic behavior of materials is an emergent and extremely rich topic, that has broad implications in material sciences, including rock physics and nondestructive evaluation [153]. There are actually two classes of material nonlinearities, which differentiate themselves both in intensity and origin of their nonlinear response [154]. The first class, called atomic nonlinear elasticity (also classical or Landau nonlinearity [155]), comprises most fluids, tissues and monocrystalline solids. In that case, the nonlinearity arises from the lattice anharmonicity of the interatomic/molecular potential, and is relatively weak because the intermolecular forces are extremely strong. The second class, called structural nonlinear elasticity (also mesoscopic/nanoscale or hysteretic/nonclassical nonlinearity [156]), involves heterogeneous and a wide range of consolidated materials (i.e. soils, cement, rocks, fluid-filled porous materials, bone, etc.). Those materials contain soft inclusions (e.g. cracks, pores, grain contacts, dislocations) embedded in a hard matrix (e.g. grains, crystals), producing a large nonlinear response. Manifestations of nonclassical nonlinearity include stress-strain hysteresis and discrete memory in quasi-static experiments, and specific dependencies of the harmonic amplitudes with respect to the drive amplitude, frequency-shift of the resonance curve, frequency mixing for multiple input signals, nonlinear attenuation and slow dynamic effects in dynamic wave experiments, which are remarkably different from those predicted by the classical theory.

Differences between nonclassical and classical nonlinear dynamic behavior include: (1) A downshift of the resonance frequency, proportional to the resonance amplitude in the nonclassical case versus a quadratic amplitude dependence in the classical case, (2) nonlinear attenuation versus amplitude independent attenuation, and (3) a quadratic amplitude

dependence of the third harmonic versus cubic in the classical case [157]. Another striking feature observed in the nonclassical nonlinear dynamic response of nonclassical materials is slow dynamics, i.e., the slow recovery of the linear material properties (wavespeed and attenuation) after a sample has been subjected to a force [158]. From the above manifestations, one can calculate a set of fundamental nonlinear parameters of the material and attempt to use them in order to infer the nature of the nonlinear response.

Classical acoustic nonlinearity is a direct measure of the material anharmonicity and it delivers unique information about the nonlinear behavior of the intermolecular lattice forces [159]. The nonlinear elastic properties of solids containing micro- and macro-defects (scaled from dislocations to volume inclusions) or structural changes may be manifested in specific types of acoustic nonlinearity, which can be used as a measure of the defectiveness of a material or the integrity of a product structure. Despite those different nonlinear mechanisms, a quantitative evaluation of elastic nonlinearity of any scale and type can be achieved by measurements of the classical nonlinear coefficients or some other parameters similar to them that are always proportional to the amplitudes of the higher harmonics generated [160]. The most frequently used experimental method for this purpose is the the finite-amplitude method.

3.4.2 Intrinsic material nonlinearity

First applications of nonlinear ultrasound using the finite-amplitude method were devoted to the experimental determination of the intrinsic nonlinear elastic properties of various fluids [161, 162], various solids, to investigate lattice structure [163] and dislocations in crystals [164, 165, 166], as well as various biological media at both the tissue and molecular level [167, 168, 169]. In addition, considerable theoretical progress in understanding nonlinear acoustic phenomena was also accomplished during that period. Indeed, the amplitude-dependent nonlinear effects can be described by the equations of state and continuity of the medium, resulting in nonlinear equations of motion. The nonlinear wave equation is usually obtained by including a nonlinear version of the Hooke's law (i.e. as a Taylor series expansion up to second or higher-order terms of the stress as function of the strain) in the equation of motion [170]. The solution to the nonlinear equation is then recovered by applying the perturbation theory [171]. As a result, second and higher-order harmonics are formed at some distance from a monochromatic source propagating in a nondissipative nonlinear medium, and their amplitude grow with the propagation distance (linearly for the second-order harmonic, quadratically for the third-oder one, and so on). It has been demonstrated that the n^{th} harmonic amplitude is proportional to the normalized Bessel function, and is known as the Fubini-Ghiron solution [161]. Also of interest is that purely longitudinal waves in elastic solids and nondissipative fluids are governed by an equation of motion of precisely the same form [172]. Nonetheless, this rather simple methodology assumes a lossless plane-wave propagation, so that neither diffraction nor attenuation and dispersion are taken into account for the determination of the nonlinear coefficients. In addition, most

of the studies are restricted to the determination of the second-order harmonics only. Nevertheless, some subsequent studies considered the influence of higher-order harmonics [173], incorporated the effects of attenuation, diffraction and dispersion [174, 175], or took into consideration the reflection and transmission coefficients for the fluid-solid interfaces (that is, when the measurements are performed in immersion) [176, 177].

Later, nonlinear acoustics has been used to investigate the elastic nonlinear effects in grained materials and rocks [178, 179] concerning their prospective applications in geology and seismology. In this context, Van den Abeele [180] presented a model that describes the interaction of frequency components in arbitrary pulsed elastic waves during one-dimensional propagation in an infinite medium with extreme nonlinear response. This model is based on the one-dimensional Green's function theory in combination with a perturbation method, and was initially developed for a general source function by McCall [181]. The solution is implemented numerically in an iterative procedure up to fourth-order nonlinear terms and allows one to include an arbitrary attenuation function. In a companion paper, they applied this theoretical model to laboratory data from dynamic wave experiments on a cylindrical rod of Berea sandstone [182]. As a result, abnormally efficient third-harmonic generation with respect to the existing Landau-theory and non-monotonic spectral distribution of the higher harmonics were observed, suggesting the need of including a further term into the nonlinear wave equation (i.e. because the constitutive relation not only depends on powers of the strain but also on the second derivative of the strain). The new phenomenological approach to describe these nonclassical phenomena is known as the Preisach-Mayergoyz space, developed in analogy with the treatment of magnetic hysteresis, and the reader is referred to the pioneer work of McCall and Guyer [183] for a detailed explanation. From then on, numerous works were dedicated to this exciting topic (see for instance references [184, 185, 186, 187], to name a few), whose review unfortunately remains beyond the scope of this dissertation.

Besides the various applications described above, another promising application of nonlinear acoustics is believed to be oriented to NDE purposes. An important reason for this prospect is that increasing nonlinear properties are always closely related to the amount and specific nature of defects in materials [188].

3.4.3 Wave-damage interactions

Most of these conventional ultrasonic NDE methods are very sensitive to gross defects, but much less sensitive to distributed micro-cracks, diffuse damage or material degradation. Furthermore, general degradation of strength is often found in apparently flawless materials [189]. It is well known that material failure is usually preceded by some kind of nonlinear mechanical behavior before significant plastic deformation or material damage occurs [190]. Therefore, the degree of material degradation can be evaluated by measuring the nonlinearity of the ultrasonic wave that propagates through the target material. Thus, one can expect that the magnitude of the second and higher-order harmonics will appear differently in normal and degraded material, when the same amplitude of wave and the same propagation

distance is used. For instance, the finite-amplitude technique has been proven to be useful for nondestructive detection of defects in ceramics [191], concrete structures [192, 193], composites [149], as well as fatigue cracks in metals, such as steels, titanium, and aluminum alloys [194, 195]. Such defects are due to internal stresses, micro-cracks, zero-volume disbonds, and usually precede the main cracking mechanisms and the subsequent failure of the material. The characteristics between such defects and common material heterogeneities (i.e. pores, grains, etc.) is that an internal interface separates the intact material and the inclusion. This contact interface can be either free (large pores, opened cracks), partially clamped ("clapping" mechanism between the states opened/closed cracks), or ideally bonded, and is thought to be mostly responsible for the high nonlinear behavior of degraded materials [196]. Therefore, a considerable number of authors have been involved in laboratory experiments to show that cracks and imperfect interfaces can behave in a nonlinear fashion [197, 198], and have thus opened new opportunities to detect partially closed cracks that may not be identified by conventional linear methods.

As a consequence, numerous theoretical studies have been dedicated to the modeling of those contact interfaces (known as contact acoustic nonlinearity (CAN)). First proposals considered boundary conditions that allow an interface to be either completely open or completely closed [199], but such a model can not provide a convincing description of the wave damage interactions involving a partially closed interface. For ideally bonded interfaces, a general approach to the boundary acoustic nonlinearity was first developed by Zhou and Shui [200], which showed that a weak nonlinear incident acoustic wave that interacts with an interface can generate strong reflected and transmitted harmonics. The theory was later extended to include the analysis of reflected and transmitted second-harmonics for an anisotropic interface [201]. In an other related proposal, Pecorari [202] presented a new set of boundary conditions to be enforced on an elastodynamic wave interacting with a nonlinear interface, focusing on the modeling of the nonlinear interaction of a bulk plane wave with a nominally flat interface formed by two rough surfaces in contact. The potential relevance of his model for evaluating partially closed interfaces was examined in a subsequent paper [203].

Despite the potential of such models for describing interfaces, the nonlinear mechanical behavior of layered media has been investigated using almost only homogenization approaches [204]. Since this approach does not directly consider the layer interfaces, it is limited in examining the global behavior of the material, neglecting the wave interactions that could be very important when identifying structural changes. Among the few works that take into account the propagation through nonlinear multilayers, it is worth to mention some proposals that investigate the possibility of modeling damaged interfaces in solids [205], the bond quality of adhesive layers [206], or layered liquid and tissue-equivalent media [207]. To our knowledge, the only model that straightforwardly formulated the one-dimensional nonlinear ultrasonic wave propagation through layered media is the proposal

by Yun *et al.* [208], which extends[3] the Transfer Matrix method described in Section 3.3.1. In addition, proposals on signal modeling for nonlinear ultrasonic systems or IP's dealing with the reconstruction of nonlinear coefficients are virtually nonexistent in the literature.

[3]This framework will be take up again in this dissertation for two reasons: (1) The original development has not been developed for NDE purposes, and has in the proposed form, a lack of applicability; and (2) the authors discovered that the original development war erroneous at some point.

4

Theoretical background

The aim of this chapter is to supply the theoretical basis on wave propagation phenomena and signal theory, that will be extensively used over the course of this thesis. Section 4.1 exposes the fundamental principles that give raise to the one-dimensional linear-elastic wave equation, and also provides an extension to cope with constitutive nonlinearity. Section 4.2 presents a number of signal processing techniques that will be used to improve the inverse problem strategy over the course of this dissertation.

4.1 Ultrasonic wave propagation

This section presents the basis to understand the wave propagation in solids. In first place, we briefly go over the equations that govern the three-dimensional linear wave propagation phenomena, to end up with the one-dimensional linear-elastic wave equation. Then, we extend this equation to solids with nonlinear constitutive behavior and thoroughly examine its solution.

4.1.1 Governing equations of the linear wave propagation

The formulation of the dynamic equilibrium equations is obtained by applying the linear momentum theorem for each direction of the three-dimensional orthonormal basis [209]. This formulation is given in index notation as,

$$\rho u_{i,tt} = \sigma_{ij,j} \tag{4.1}$$

where ρ denotes the density of the medium in which the waves are propagating. The components u_i and σ_{ij}, with $i, j = x, y, z$, are the cartesian components of the displacement vector, and those of the stress tensor, respectively. The relations between the stress and the strain tensor are established by the constitutive law as,

$$\sigma_{ij} = \lambda \varepsilon_{kk} \delta_{ij} + 2\mu \varepsilon_{ij} \tag{4.2}$$

where ε_{ij}, with $i, j = x, y, z$, are the cartesian components of the strain tensor, and $\varepsilon_{kk} = \varepsilon_{xx} + \varepsilon_{yy} + \varepsilon_{zz}$ is the dilatation (change in volume per unit volume). The Kronecker symbol δ_{ij} is defined as,

$$\delta_{ij} = \begin{cases} 1 & \text{for} \quad i = j \\ 0 & \text{for} \quad i \neq j \end{cases} \tag{4.3}$$

where λ and μ are the Lamé constants, which describe the behavior of linear-elastic, isotropic materials. The relations between the Lamé constants and the engineering moduli are derived as,

$$\lambda = \frac{E\nu}{(1+\nu)(1-2\nu)} \quad , \quad \mu = \frac{E}{2(1+\nu)} \tag{4.4}$$

where E and ν denote the Young modulus and the Poisson ratio, respectively. The kinematic relations establish a relation between the displacement field and the strain tensor as,

$$\varepsilon_{ij} = \frac{1}{2}(u_{i,j} + u_{j,i}) \tag{4.5}$$

It can be shown that substituting Equations (4.2) and (4.5) into Equation (4.1) leads to the generalized three-dimensional linear wave equation for the displacement $u(\boldsymbol{x}, t)$. Since the present work only deals with one-dimensional plane wave propagation in elastic media, those equations can be reduced to the one-dimensional case, yielding a generalized one-dimensional linear wave equation for the displacement $u(x, t)$ as,

$$\frac{\partial^2 u}{\partial t^2} = c_p^2 \frac{\partial^2 u}{\partial x^2} \tag{4.6}$$

where c_p denotes the longitudinal (P-wave) wave propagation velocity.

4.1.2 Foundations of the nonlinear wave propagation

To highlight the fundamental effects of nonlinear elastic materials, the classical approach of the nonlinear theory of elasticity is briefly presented here (details can be found in [155]). Assuming that the nonlinear contributions (e.g. geometric) of the wave propagation equation are negligible compared to constitutive nonlinearity, the only equation that differs from the linear theory is the constitutive law expressed in Equation 4.2. Thus, the one-dimensional relation between the stress and the strain is established with the nonlinear version of the Hooke's law as,

$$\sigma = E\varepsilon(1 + \beta\varepsilon + \delta\varepsilon^2 + \ldots) \tag{4.7}$$

where β and δ denote the nonlinear elastic coefficients of first- and second-order, respectively. The generalized one-dimensional nonlinear wave equation for the displacement $u(x,t)$ can thus be written as,

$$\frac{\partial^2 u}{\partial t^2} = c_p^2 \frac{\partial^2 u}{\partial x^2}\left(1 + 2\beta\frac{\partial u}{\partial x} + 3\delta\left(\frac{\partial u}{\partial x}\right)^2 + \ldots\right) \tag{4.8}$$

This expression means that the displacement depends on linear and nonlinear potencies of the linear deformation $\frac{\partial u}{\partial x}$. This deformation can be generated from the wave itself (wave of finite amplitude), as well as from an extern load applied to the concern solid. Alternatively, Equation 4.8 can be written as,

$$\frac{\partial^2 u}{\partial t^2} = \left(c_L^2 + c_{NL}^2\right)\frac{\partial^2 u}{\partial x^2} \tag{4.9}$$

where c_L and c_{NL} denote the longitudinal linear and nonlinear wave propagation velocity, respectively. They are defined as,

$$c_L = c_p = \sqrt{\frac{\lambda + 2\mu}{\rho}} \quad , \quad c_{NL} = c_p\sqrt{2\beta\frac{\partial u}{\partial x} + 3\delta\left(\frac{\partial u}{\partial x}\right)^2 + \ldots} \tag{4.10}$$

Note that by setting $\beta = \delta = 0$, we recover the linear wave equation.

Analytically calculated perturbation solutions

Let us now solve the nonlinear wave equation up to the second-order nonlinearity. Applying the *perturbation method* [171] enables us to write the wave displacement as,

$$u = u_0 + u_1 + u_2 + \ldots \tag{4.11}$$

where u_0 denotes the zero-order perturbation solution which corresponds to the fundamental solution of the linear wave equation. The first-and second-order perturbation solutions are denoted by u_1 and u_2, respectively. For convenience of the mathematical formulation, let us define the displacements' first- and second-derivatives with respect to the x coordinate as $u' = \frac{\partial u}{\partial x}$ and $u'' = \frac{\partial^2 u}{\partial x^2}$, respectively, and the second time-derivative as $\ddot{u} = \frac{\partial^2 u}{\partial t^2}$. Since the effect of the nonlinear terms β and δ is small, an approximate solution can be obtained by iteration. For this purpose, let us insert Equation (4.11) into Equation (4.9),

$$\begin{aligned}
\ddot{u}_0 + \ddot{u}_1 + \ddot{u}_2 + \ldots &= c_p^2\left(u_0'' + u_1'' + u_2'' + \ldots\right) \\
&+ 2c_p^2\beta\left(u_0'' + u_1'' + u_2'' + \ldots\right)\left(u_0' + u_1' + u_2' + \ldots\right) \\
&+ 3c_p^2\delta\left(u_0'' + u_1'' + u_2'' + \ldots\right)\left(u_0' + u_1' + u_2' + \ldots\right)^2
\end{aligned} \tag{4.12}$$

This equation delivers various sub-equations, obtained by rearranging the terms according to the perturbation order. Hence,

$$\begin{aligned}
&\text{Zero-order:} && \ddot{u}_0 - c_p^2 u_0'' &&= 0 \\
&\text{First-order:} && \ddot{u}_1 - c_p^2 u_1'' &&= 2c_p^2 \beta u_0'' u_0' \\
&\text{Second-order:} && \ddot{u}_2 - c_p^2 u_2'' &&= 2c_p^2 \beta \left(u_1'' u_0' + u_0'' u_1'\right) + 3c_p^2 \delta u_0'' \left(u_0'\right)^2 \\
&\ldots
\end{aligned} \tag{4.13}$$

Consequently, u_0 is the solution to the linear wave equation, that is Equation (4.8) for $\beta = \delta = 0$, whose general solution can be stated as,

$$u_0 = \sum_{n=1}^{\infty} \left(A_0^{(n)} \sin\left(n\left(\gamma x - \Omega t\right)\right) + B_0^{(n)} \cos\left(n\left(\gamma x - \Omega t\right)\right) \right) \qquad (n \in \mathbb{R}) \tag{4.14}$$

where $\gamma = \Omega / c_p$ and Ω are the wave number and continuous-time frequency, respectively. By considering a monochromatic wave that propagates in a semi-infinite nonlinear elastic medium, the zero-order perturbation solution (4.14) can be simplified as,

$$u_0 = A_0 \sin\left(\gamma x - \Omega t\right) \tag{4.15}$$

Let then u_1 be the first-order perturbation solution to Equation (4.8). Inserting the zero-order perturbation solution (4.15) within the first-order perturbation Equation (4.13b) leads to,

$$u_1'' - \frac{1}{c_p^2} \ddot{u}_1 = \beta \gamma^3 A_0^2 \sin\left(2\left(\gamma x - \Omega t\right)\right) \tag{4.16}$$

Equation (4.16) has the form of a classical partial differential equation with an inhomogeneous part. It is well-known from the mathematical analysis, that when the inhomogeneous part is linearly dependent to the general solution of the homogeneous part, the solution approach for the particular solution of u_1 must be multiplied by a sufficiently large power of x to become linearly independent. Thus, a particular solution may be obtained by the method of *variations of parameters* as,

$$u_1 = A(x) \sin\left(2\left(\gamma x - \Omega t\right)\right) + B(x) \cos\left(2\left(\gamma x - \Omega t\right)\right) \tag{4.17}$$

where $A(x)$ and $B(x)$ represent space-dependent amplitudes of the first-order perturbation solution. Inserting Equation (4.17) into Equation (4.16) leads to a pair of equations obtained by *matching like coefficients* of the sine and cosine terms,

$$\begin{aligned}
B''(x) + 4\gamma A'(x) &= 0 \\
A''(x) - 4\gamma B'(x) &= \beta \gamma^3 A_0^2
\end{aligned} \tag{4.18}$$

Let us write the space-dependent amplitudes as linear functions $A(x) = A_1 x + A_2$ and $B(x) = B_1 x + B_2$, and insert them in Equation (4.18):

$$\begin{aligned} 4\gamma A_1 &= 0 \quad &\Rightarrow \quad A_1 &= 0 \\ -4\gamma B_1 &= \beta\gamma^3 A_0^2 \quad &\Rightarrow \quad B_1 &= -\frac{1}{4}\beta\gamma^2 A_0^2 \end{aligned} \tag{4.19}$$

Therefore, the first-order perturbation solution can be stated as,

$$u_1 = A_2 \sin\left(2\left(\gamma x - \Omega t\right)\right) + \left(B_2 - \frac{1}{4}\beta\gamma^2 A_0^2 x\right)\cos\left(2\left(\gamma x - \Omega t\right)\right) \tag{4.20}$$

where A_2 and B_2 are constants corresponding to complementary solutions of Equation (4.13b). The constants can be determined by the boundary condition ($u_1(0,t) = 0$) and the Sommerfeld radiation-type condition, which requires that the solution represents a wave propagating in the positive x-direction (no reflection may occur since the layer is considered as semi-infinite). However, setting $A_2 = B_2 = 0$ simplifies the analysis without significantly affecting its accuracy. Indeed, Hamilton and Blackstock [171] demonstrated that any term of the wave displacement perturbation solution that remains independent of x may be ignored, regardless of wether it stems from the complementary or particular solution. Hence,

$$u_1 = -\frac{1}{4}\beta\gamma^2 A_0^2 x \cos\left(2\left(\gamma x - \Omega t\right)\right) \tag{4.21}$$

As can be observed, the first-order perturbation solution is generated by the fundamental waves, whose amplitude accumulates with the propagation distance x. In this case, the nonlinear effect is essentially due to frequency-mixing between two spectral components, i.e. the double-frequency component (second harmonics) is generated by a mixing of the fundamental waves with themselves [184]. The general solution up to first-order perturbation is therefore stated as,

$$u(x,t) = u_0(x,t) + u_1(x,t) = A_0 \sin\left(\gamma x - \Omega t\right) - \frac{1}{4}\beta\gamma^2 A_0^2 x \cos\left(2\left(\gamma x - \Omega t\right)\right) \tag{4.22}$$

and corresponds to the results obtained by Van den Abeele [180][1] and Pantea *et al.* [210][2]. In contrast, the first-order perturbation solution provided by Jhang and Kim [189] seems to be erroneous[3].

The second-order perturbation solution can be solved accordingly by inserting the zero and first-order perturbation solutions (4.15)-(4.21) within the second-order perturbation

[1]Note that he found that the nonlinear coefficient of first-order $\hat{\beta} = 8A_1/(\gamma^2 x A_0^2)$. However, be aware that the former makes use of a slightly different nonlinear wave equation where $\hat{\beta} = 2\beta$. It can be shown that both solutions are equivalent.

[2]Note that they made use of a slightly different nonlinear wave equation (negative nonlinear term) and zero-order solution (cosine instead of sine), which explain the slightly different result. It can be proven again that both solutions are equivalent.

[3]Even if they start from the same equation than us, their resulting solution factor $1/8$ instead of $1/4$ is wrong.

Equation (4.13c) as,

$$u_2'' - \frac{1}{c_p^2}\ddot{u}_2 = -2\beta\left(u_0''u_1' + u_1''u_0'\right) - 3\delta u_0''\left(u_0'\right)^2 \tag{4.23}$$

where,

$$\begin{aligned} u_0' &= \gamma A_0 \cos\left(\gamma x - \Omega t\right) \\ u_0'' &= -\gamma^2 A_0 \sin\left(\gamma x - \Omega t\right) \\ u_1' &= -\frac{1}{4}\beta\gamma^2 A_0^2 \cos\left(2\left(\gamma x - \Omega t\right)\right) + \frac{1}{2}\beta\gamma^3 A_0^2 x \sin\left(2\left(\gamma x - \Omega t\right)\right) \\ u_1'' &= \beta\gamma^3 A_0^2 \sin\left(2\left(\gamma x - \Omega t\right)\right) + \beta\gamma^4 A_0^2 x \cos\left(2\left(\gamma x - \Omega t\right)\right) \end{aligned} \tag{4.24}$$

Inserting Equations (4.24) in Equation (4.23), and making use of the trigonometric identities $\cos(3a) = \cos(a)(\cos^2(a) - 3\sin^2(a))$ and $\sin(3a) = \sin(a)(3\cos^2(a) - \sin^2(a))$ leads to,

$$\begin{aligned} u_2'' - \frac{1}{c_p^2}\ddot{u}_2 &= -\left(\frac{1}{2}\beta^2\gamma^5 x A_0^3 \cos\left(\gamma x - \Omega t\right) + \frac{3}{4}\left(\beta^2 - \delta\right)\gamma^4 A_0^3 \sin\left(\gamma x - \Omega t\right)\right. \\ &+ \left.\frac{3}{2}\beta^2\gamma^5 x A_0^3 \cos\left(3\left(\gamma x - \Omega t\right)\right) + \frac{1}{4}\left(5\beta^2 - 3\delta\right)\gamma^4 A_0^3 \sin\left(3\left(\gamma x - \Omega t\right)\right)\right) \end{aligned} \tag{4.25}$$

Following the aforementioned method of *variations of parameters*, a suitable approach for the particular solution of the second-order perturbation solution u_2 may be written as,

$$\begin{aligned} u_2 &= A(x)\sin\left(\gamma x - \Omega t\right) + B(x)\cos\left(\gamma x - \Omega t\right) \\ &+ C(x)\sin\left(3\left(\gamma x - \Omega t\right)\right) + D(x)\cos\left(3\left(\gamma x - \Omega t\right)\right) \end{aligned} \tag{4.26}$$

Inserting Equation (4.26) in Equation (4.25) leads to two pairs of uncoupled equations obtained by *matching like coefficients* of the sine and cosine terms,

$$\begin{aligned} B''(x) + 2\gamma A'(x) &= -\frac{1}{2}\beta^2\gamma^5 x A_0^3 \\ A''(x) - 2\gamma B'(x) &= -\frac{3}{4}\left(\beta^2 - \delta\right)\gamma^4 A_0^3 \\ D''(x) + 6\gamma C'(x) &= -\frac{3}{2}\beta^2\gamma^5 x A_0^3 \\ C''(x) - 6\gamma D'(x) &= -\frac{1}{4}\left(5\beta^2 - 3\delta\right)\gamma^4 A_0^3 \end{aligned} \tag{4.27}$$

Let us now write the space-dependent amplitudes as quadratic functions $K(x) = K_1x^2 + K_2x + K_3$, with $K = \{A, B, C, D\}$, and insert them in Equation (4.27):

$$\begin{aligned}
2B_1 + 2\gamma(2A_1x + A_2) &= -\frac{1}{2}\beta^2\gamma^5 x A_0^3 &\Rightarrow\quad A_1 &= -\frac{1}{8}\beta^2\gamma^4 A_0^3 \\
2A_1 - 2\gamma B_2 &= -\frac{3}{4}\left(\beta^2 - \delta\right)\gamma^4 A_0^3 &\Rightarrow\quad B_2 &= \frac{1}{4}\left(\beta^2 - \frac{3}{2}\delta\right)\gamma^3 A_0^3 \\
2D_1 + 6\gamma(2C_1x + C_2) &= -\frac{3}{2}\beta^2\gamma^5 x A_0^3 &\Rightarrow\quad C_1 &= -\frac{1}{8}\beta^2\gamma^4 A_0^3 \\
2C_1 - 6\gamma D_2 &= -\frac{1}{4}(5\beta^2 - 3\delta)\gamma^4 A_0^3 &\Rightarrow\quad D_2 &= \frac{1}{6}\left(\beta^2 - \frac{3}{4}\delta\right)\gamma^3 A_0^3
\end{aligned} \tag{4.28}$$

Therefore, the second-order perturbation solution can be stated as,

$$\begin{aligned}
u_2 &= \left(A_3 - \frac{1}{8}\beta^2\gamma^4 x^2 A_0^3\right)\sin(\gamma x - \Omega t) + \left(B_3 + \frac{1}{4}\left(\beta^2 - \frac{3}{2}\delta\right)\gamma^3 x A_0^3\right)\cos(\gamma x - \Omega t) \\
&+ \left(C_3 - \frac{1}{8}\beta^2\gamma^4 x^2 A_0^3\right)\sin(3(\gamma x - \Omega t)) + \left(D_3 + \frac{1}{6}\left(\beta^2 - \frac{3}{4}\delta\right)\gamma^3 x A_0^3\right)\cos(3(\gamma x - \Omega t))
\end{aligned} \tag{4.29}$$

where the constants K_3 corresponding to complementary solutions can be set to zero as done for the first-order perturbation solution (see Equations (4.20)-(4.21)). Hence,

$$\begin{aligned}
u_2 &= -\frac{1}{8}\beta^2\gamma^4 x^2 A_0^3\left(\sin(\gamma x - \Omega t) + \sin(3(\gamma x - \Omega t))\right) \\
&+ \frac{1}{4}\gamma^3 x A_0^3\left(\left(\beta^2 - \frac{3}{2}\delta\right)\cos(\gamma x - \Omega t) + \left(\frac{2}{3}\beta^2 - \frac{1}{2}\delta\right)\cos(3(\gamma x - \Omega t))\right)
\end{aligned} \tag{4.30}$$

As can be observed, the second-order perturbation solution is composed of two parts, which are both generated by interactions of the zero-order with the first-order perturbation solution. In this case, the nonlinear effect is essentially frequency mixing between three spectral components: The triple-frequency component (third harmonics) is generated by a *positive* mixing of the fundamental waves with the second harmonics (Ω+2Ω), while the resulting single-frequency component (first harmonics) is generated by a *negative* mixing of the fundamental waves with the second harmonics (2Ω-Ω).

The general solution up to second-order perturbation is easily obtained by combining Equation (4.30) with Equation (4.22) as,

$$\begin{aligned}
u(x,t) &= u_0(x,t) + u_1(x,t) + u_2(x,t) \\
&= A_0\sin(\gamma x - \Omega t) - \frac{1}{4}\beta\gamma^2 A_0^2 x\cos(2(\gamma x - \Omega t)) \\
&- \frac{1}{8}\beta^2\gamma^4 x^2 A_0^3\left(\sin(\gamma x - \Omega t) + \sin(3(\gamma x - \Omega t))\right) \\
&+ \frac{1}{4}\beta^2\gamma^3 x A_0^3\left(\cos(\gamma x - \Omega t) + \frac{2}{3}\cos(3(\gamma x - \Omega t))\right) \\
&- \frac{3}{8}\delta\gamma^3 x A_0^3\left(\cos(\gamma x - \Omega t) + \frac{1}{3}\cos(3(\gamma x - \Omega t))\right)
\end{aligned} \tag{4.31}$$

and corresponds to the results by Melngailis *et al.* [163][4] and Van den Abeele [180][5]. It is noteworthy that higher-order perturbation solutions could be found accordingly. The elementary relationships for the β, δ-model up to second-order perturbation solutions can be summarized as follows, looking at the individual spectral components and their dependence on distance x, frequency Ω, and amplitude A_0 of the fundamental waves [184]:

$$u_1(x,t) \propto \beta \left(\frac{\Omega}{c_p}\right)^2 A_0^2 x \quad , \quad u_2(x,t) \propto \begin{cases} \beta^2 \left(\frac{\Omega}{c_p}\right)^4 A_0^3 x^2 & \text{, if } \beta^2 \left(\frac{\Omega}{c_p}\right) x \gg |\delta| \\ \delta \left(\frac{\Omega}{c_p}\right)^3 A_0^3 x & \text{, if } \beta^2 \left(\frac{\Omega}{c_p}\right) x \ll |\delta| \end{cases} \tag{4.32}$$

Manifestations of nonlinear constitutive behavior

Let us finally consider a simple example to highlight the well-known acoustical manifestations of nonlinear constitutive behavior, i.e. the steepening of the waveform in the time-domain and the observation of higher harmonics as local maxima in the frequency-domain. To this end, we developed the model in Equation (4.31) up to 10 harmonics. For clarity, we refer to the first-order (one nonlinear parameter) Taylor series expansion as the β-model, and to the extended second-order expansion as the β, δ model. The input is a monochromatic continuous pressure wave at frequency $F = 5$ MHz and four drive displacement amplitudes (A_0, $2A_0$, $3A_0$, and $4A_0$, where $A_0 = 5$ nm). The propagation distance is $x = 20$ cm, and the linear wave velocity in the model is fixed to $c_p = 1500$ m/s (attenuation is neglected). Strain values of the wave responses can be obtained from those classical nonlinear models. The values of the nonlinear parameters are indicated in the figures below. Figure 4.1 depicts the linear case, where as expected the frequency of the output remains the same than that of the input. In addition, there is no amplitude-dependent propagation, so that the ratio between the amplitudes remains equivalent.

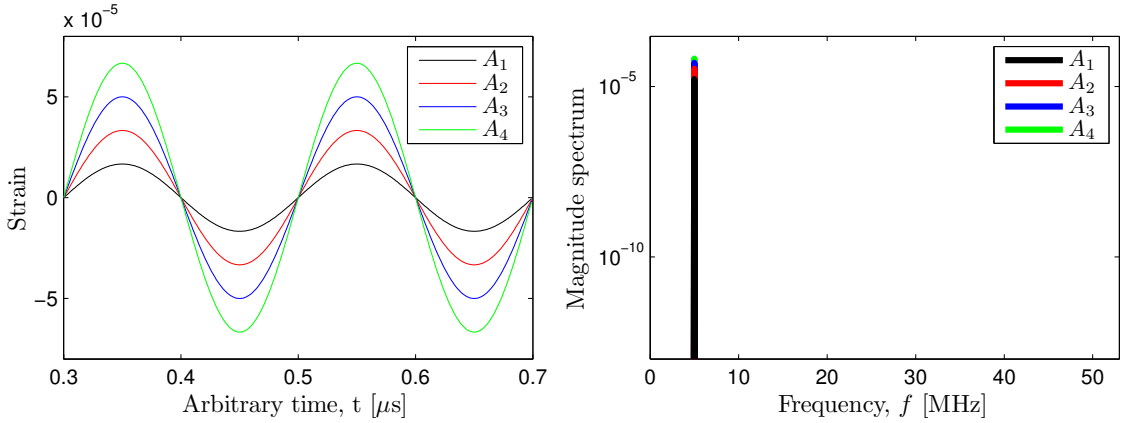

Figure 4.1: *Linear model ($\beta = \delta = 0$).*

[4]Note that in his proposed form, $a = 2\beta$ and $\delta = 0$.

[5]He found that the amplitude of the third harmonics (when neglecting δ) was $A_2 = \bar{\beta}^2 A_0^3 \gamma^4 x/32$ (with $\bar{\beta} = 2\beta$).

Figure 4.2 shows the β-model. As can be observed, an increase of the drive amplitude leads to increased asymmetry in the waveforms (i.e. saw-tooth form), which corresponds to a larger distribution of energy into higher-order harmonics. The harmonic energy contained in the spectral components tends to fall off rapidly and nearly exponentially as a function of the frequency [184].

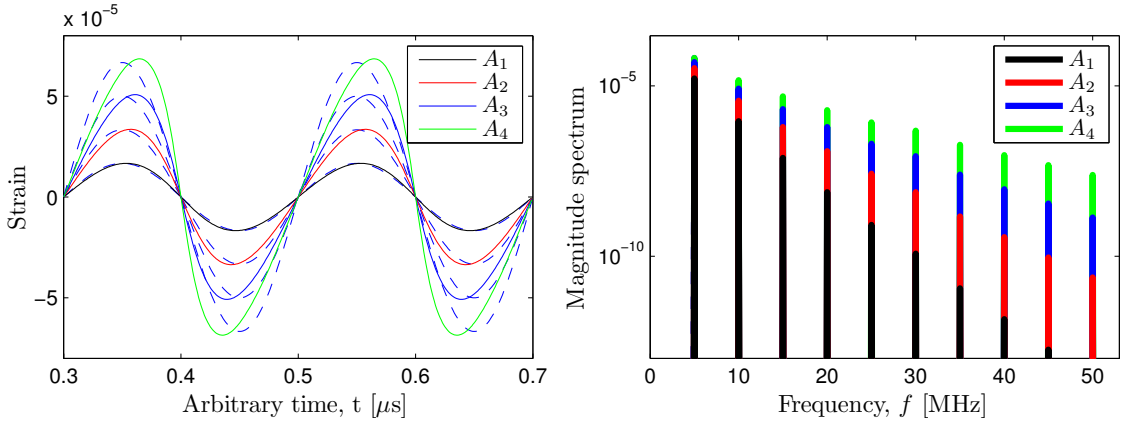

Figure 4.2: *Nonlinear β-model: $\beta = 5$ ($\delta = 0$).*

On the other hand, Figure 4.3 illustrates the β, δ-model with β set equal to zero and a positive δ-value. The distortion from a sinusoidal waveform increases with increasing drive amplitude, and the spectral components are characterized by the presence of odd harmonics, as predicted by Equation (4.31).

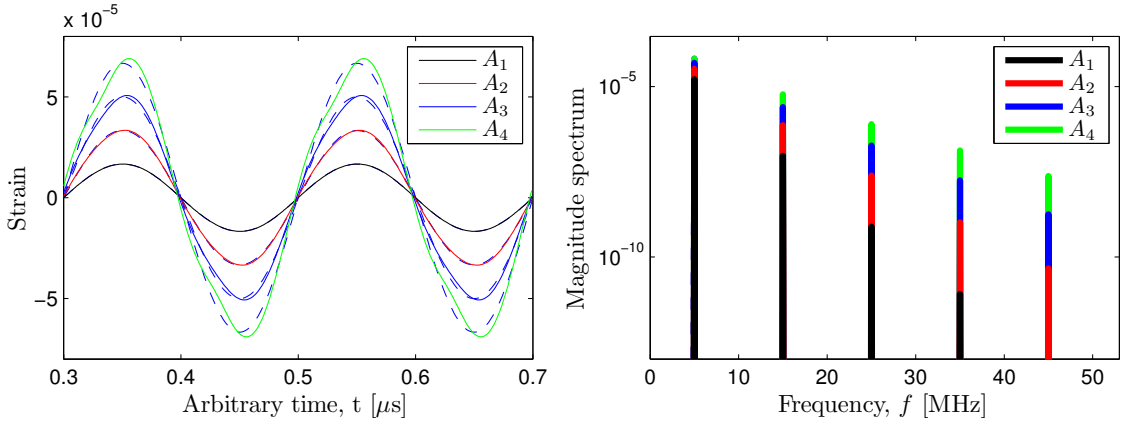

Figure 4.3: *Nonlinear β, δ-model: $\beta = 5$, $\delta = 20000$.*

Note also that the magnitude spectrum is identical for positive or negative δ-values, as depicted in Figure 4.4 for the largest input energy $4A_0$. Time-domain differences could however be observed in the phase-spectrum.

Finally, Figure 4.5 depicts the combination of first- and second-order nonlinearity (β, δ-model), for a positive δ-value which is much larger than β^2, since values for $|\delta|$ of one or two orders of magnitude larger than β^2 is typically required to visually alter the distorted waveform [184]. As can be observed, in that case the spectral components are made of both

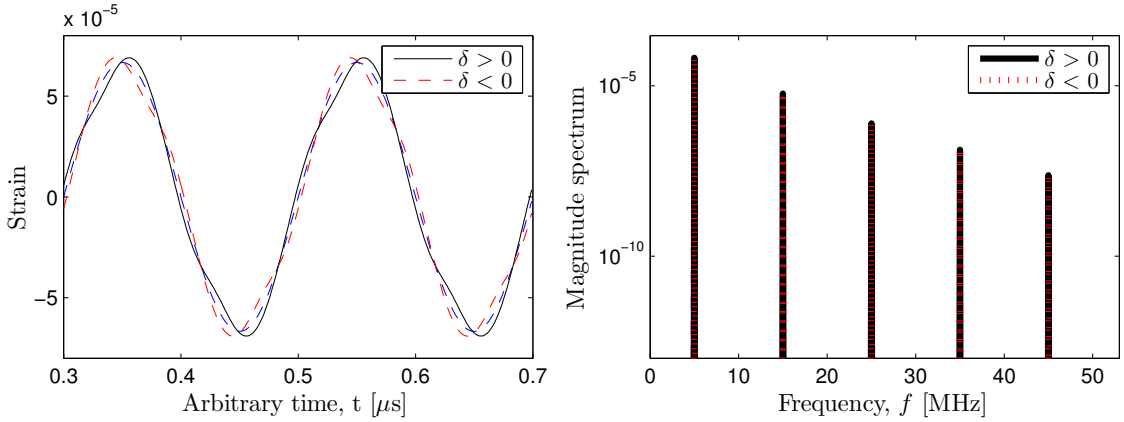

Figure 4.4: *Nonlinear β, δ-model: $\beta = 0$, $\delta = \pm 20000$ (for $4A_0$).*

even and odd harmonics, and for sufficient input energy, the spectrum shows a predilection for odd harmonics (e.g. for $4A_0$).

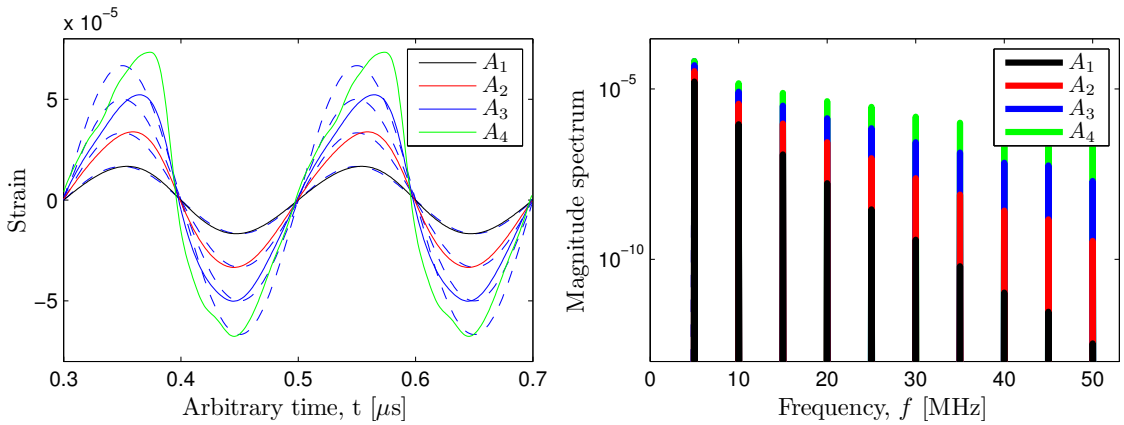

Figure 4.5: *Nonlinear β, δ-model: $\beta = 5$, $\delta = 20000$.*

In addition, Figure 4.6 shows the combination of first- and second-order nonlinearity (β, δ-model for a drive amplitude $4A_0$), for positive and negative δ-values which are much larger than β^2. As can be observed, the distortions of the waveforms significantly change, depending upon the sign and the value of the second-order nonlinear parameter δ. As in the previous case, and for sufficient larger values of δ, the spectrum shows a predilection for odd harmonics (e.g. for δ_2).

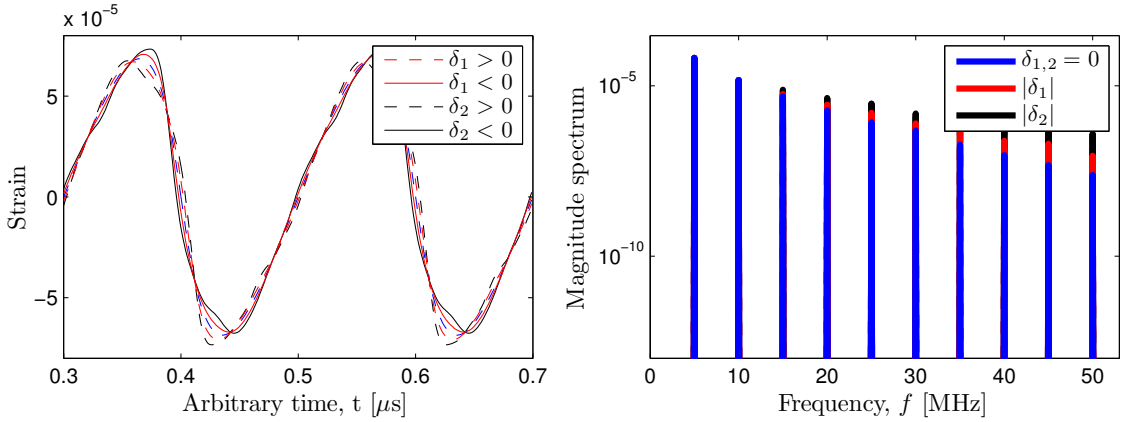

Figure 4.6: *Nonlinear β, δ-model: $\beta = 5$, $\delta_1 = \pm 10000$, $\delta_2 = \pm 20000$ (for $4A_0$).*

4.2 Signal processing and feature extraction

The optimization of the inverse problem strategy proposed in this dissertation makes an extensive use of signal theory principles, including analysis and parametrization techniques. Thus, this section describes the basis to understand those principles, with the aim of providing a suitable representation of ultrasonic signals, appropriate for pathology identification.

The signal processing techniques described here can be classified in three categories. In first place, we describe some techniques that can be used to preprocess ultrasonic signals, by means of noise reduction and echoes enhancement. Then, different parametrization approaches can be applied to the preprocessed signals (e.g. nonparametric and parametric signal models), and the obtained spectral parameters are usually transformed (e.g. homomorphic transformations), to provide a more uncorrelated and dimensionally reduced representation. It results from the applied analysis that an ultrasonic signal can be represented by a feature vector containing the analysis parameters. Finally, in some cases, this feature vector can be post-processed, by means of a further reduction of its dimensionality.

4.2.1 Preprocessing

This section describes some techniques that can be used to preprocess ultrasonic signals. Ultrasonic signals are generally contaminated by noise originated from both the measurement system and the material under inspection. First, the SNR can be improved by signal averaging, since the specimen-dependent part of the signal remains the same for all measurements (and thus after averaging), whereas the disturbances can be reduced since they are randomly generated in each individual measurement. Figure 4.7 depicts the effect of signal averaging on two ultrasonic signals, which results from the measurement of undamaged (high SNR) and damaged (low SNR) area of a layered material. The signals corresponding to an undamaged and damaged area are labeled as $y_{i,0}(n)$ and $y_{i,d}(n)$ ($i = 1, \ldots, N_r$), respectively, where N_r denotes the number of measurements repetition. The resulting average

are respectively denoted by $y_0(n)$ and $y_d(n)$. The improvement of the SNR is commonly quantified in dB by applying the simple formula $10\log_{10}(N_r)$.

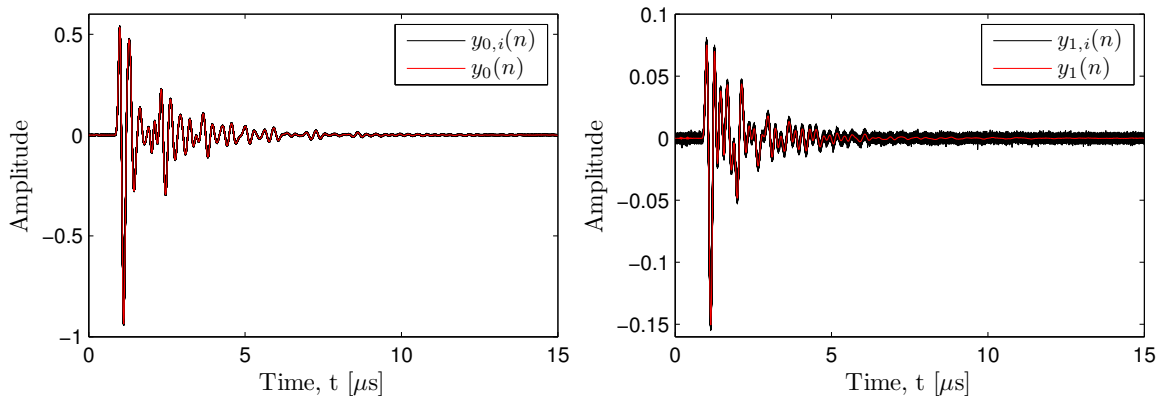

Figure 4.7: *Process of temporal signal averaging on ultrasonic signals obtained from a layered media: High SNR (left) versus low SNR (right).*

In order to further reduce part of the noise and focus on the frequency band of interest, the signals can be decimated at a sampling frequency $\bar{F}_s = F_s/N_d$, where F_s and N_d denote the original sampling frequency and the decimation rate, respectively. Figure 4.8 depicts the effect of decimation on the time-domain waveform $y_0(n)$ and magnitude spectrum $|Y_0(\omega)|$ of the averaged ultrasonic signal.

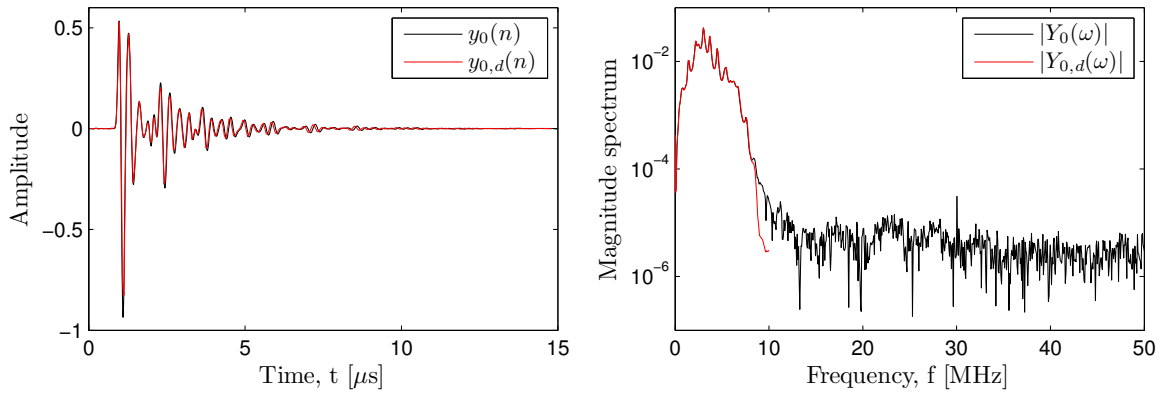

Figure 4.8: *Process of decimation on the time-domain waveform and magnitude spectrum of an ultrasonic signal measured from an undamaged area.*

Secondly, for very low SNR (i.e. low signal amplitude or high damage environment), the signals generally suffer from misalignment effects with respect to the abscissa. On can easily overcome this artifact by applying a baseline correction, that is subtracting the signal's mean to the signal:

$$y_{corr}(n) \quad = \quad y(n) - \bar{y}(n) \quad = \quad y(n) - \frac{1}{N}\sum_{n=0}^{N-1} y(n) \tag{4.33}$$

Thirdly, by considering that a NDE system must be insensitive to changes in signals amplitude or energy, ultrasonic signals can be normalized. Typically, the normalization is

performed by making use of the *root mean square* (rms) of the signal, so that the signal energy amounts to one. Alternatively, a signal can be normalized with respect to its amplitude, so that its absolute peak value amounts to one. Those operations can be expressed as,

$$y_{ener.}(n) = \frac{y(n)}{y_{rms}(n)} = \frac{y(n)}{\sqrt{\frac{1}{N}\sum_{n=0}^{N-1}(y(n))^2}} \quad , \quad y_{peak}(n) = \frac{y(n)}{\max(|y(n)|)} \tag{4.34}$$

where N denotes the number of samples of the signal. Note that $y_{ener.}(n)$ is less sensitive to noise than $y_{peak}(n)$, as the signal's variability is divided by the square root of the number of samples.

Finally, the selection of an appropriate analysis window is considered. The multiplication of a signal by a window in the time-domain corresponds to a convolution in the frequency-domain, which results in two main effects: Spectrum estimation errors (*rippling*) increase, and resolution loss between neighboring frequencies (*leakage*). The degree of *rippling* depends on the relative amplitude between the main lobe and the side lobes, while the resolution is mainly influenced by the main lobe bandwidth [211]. Thus, the choice of the applied window depends on its discriminative characteristics regarding: (1) the spectral modulations (*ripples*) amplitude according to the window type, and (2) the window size, inversely related to the *ripples* amplitude. There are many windows that the literature referrers to, among them the ones of Hanning, Hamming, Blackman, Bartlett, etc. [212]. The default window is the rectangular (Dirichlet) one and is defined as,

$$w_r(n) = \begin{cases} 1 & 0 \leq n \leq L \\ 0 & \text{otherwise} \end{cases} \tag{4.35}$$

where L denotes the window length. For a given length L, this window has the narrowest main lobe, but the highest side lobes of all commonly used windows. Consequently, other window types were designed as a trade-off between main lobe bandwidth and side lobes relative amplitude. Among them, *raised cosine* based windows have been developed. For instance, the Hanning window is obtained as,

$$w_{han.}(n) = \begin{cases} \frac{1}{2}\left(1 - \cos\left(2\pi\frac{n}{L}\right)\right) & 0 \leq n \leq L \\ 0 & \text{otherwise} \end{cases} \tag{4.36}$$

On the other hand, the Hamming window is defined as,

$$w_{ham.}(n) = \begin{cases} 0.54 - 0.46\,\cos\left(2\pi\frac{n}{L}\right) & 0 \leq n \leq L \\ 0 & \text{otherwise} \end{cases} \tag{4.37}$$

Alternatively, a Bartlett (triangular) window can be used,

$$w_{bar.}(n) = \begin{cases} \dfrac{2n}{L} & 0 \leq n \leq L/2 \\ 2\left(1 - \dfrac{n}{L}\right) & L/2 \leq n \leq L \\ 0 & \text{otherwise} \end{cases} \tag{4.38}$$

Finally, the Blackmann window is defined as,

$$w_{bla.}(n) = \begin{cases} 0.42 - 0.5\cos\left(2\pi\dfrac{n}{L}\right) + 0.08\cos\left(4\pi\dfrac{n}{L}\right) & 0 \leq n \leq L \\ 0 & \text{otherwise} \end{cases} \tag{4.39}$$

The *bell-shaped* curves of those windows are depicted in the left plot of Figure 4.9. Additionally, the right plot shows the DFT of both the rectangular and Hamming windows, in order to illustrate the aforementioned trade-off between main lobe bandwidth and side lobes relative amplitude.

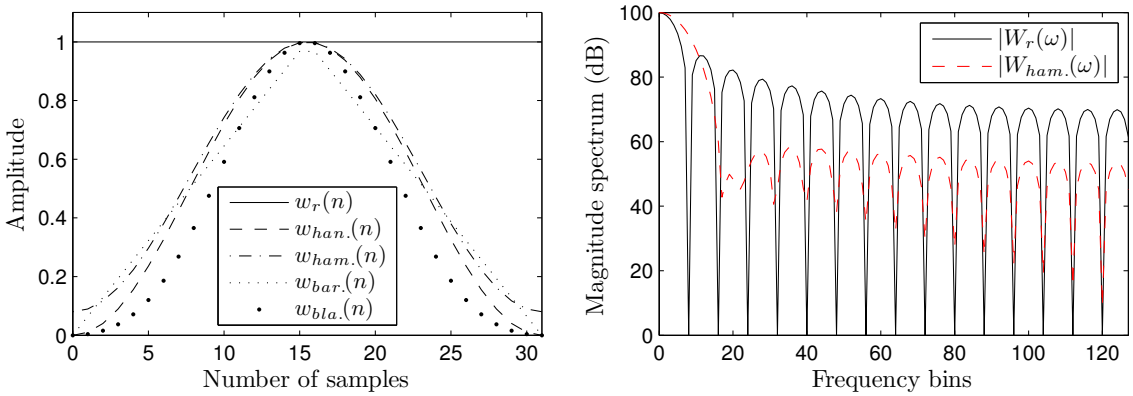

Figure 4.9: Preprocessing analysis windows.

The characteristics of those windows, such as the main lobe bandwidth, side lobe relative amplitude and side lobes decreasing slope, are summarized in Table 4.1.

Window shape	Approximate main lobe bandwidth	Relative peak side lobe amplitude [dB]	Side lobes fall-off [dB/oct.]
Rectangular	L/8	-13	-6
Hanning	L/4	-31	-18
Hamming	L/4	-41	-6
Bartlett	L/4	-25	-12
Blackmann	L/2	-57	-18

Table 4.1: *Windows characteristics after Oppenheim and Schafer* [211].

It is worth to point out that signal windowing is generally used while dealing with signals of infinite length. Hence, by increasing the window size, it is possible to avoid the

inconveniences due to the aforementioned trade-off between resolution and precision. In contrast, ultrasonic signals are finite by nature, i.e. they start and end up with samples whose amplitude approximately amounts to zero. Thus, in that case, the window is foremost used to weight the signal samples over the time. This can be appreciated in Figure 4.10, where a Hamming window $w_{ham.}(n)$ has been applied over an ultrasonic signal $y_0(n)$. As can be observed, while in the original signal (left) predominates the first wave packet (wave front), the windowed signal (right) exhibits accentuated echoes amplitude, representative of the successive reflections of the transmitted signal between the specimen/transducers interface.

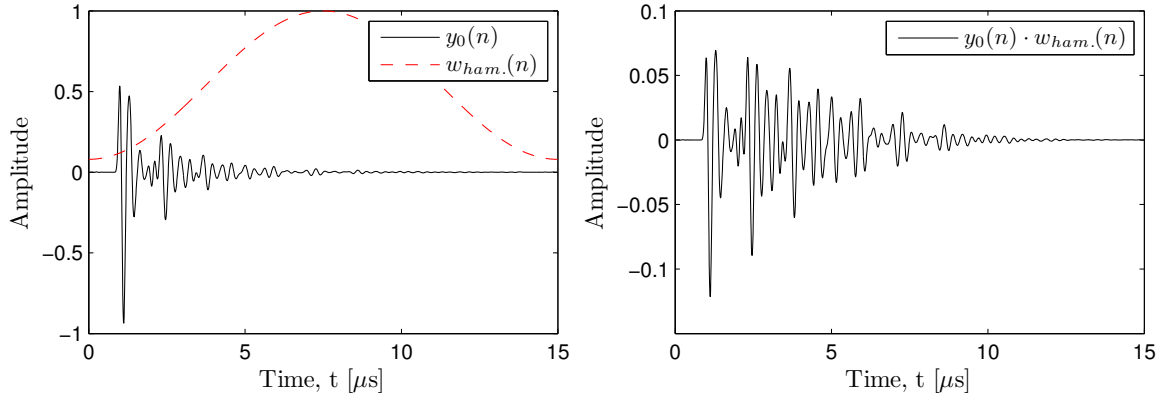

Figure 4.10: *Echoes enhancement of an ultrasonic signal by temporal signal windowing.*

The influence of the signal windowing will be further discussed in next sections, while dealing with other domains of signal representation.

4.2.2 Spectral estimation

The proposed feature extraction procedure relies on processing methods that are based on two different approaches, respectively known as nonparametric techniques and parametric signal modeling. While nonparametric techniques directly estimate the spectral features from the signal itself, the fundamental idea of parametric signal modeling is based on the vision of the ultrasonic signal as a discrete-time random process. Random processes can be modeled by filtering white noise with a linear shift-invariant filter that has a rational system function. In such a case, the ultrasonic signal is viewed as a filter output, where the spectrum estimate is given by its frequency response. In particular, autoregressive (AR) processes are considered. AR models have been found to provide a sufficiently accurate representation for many types of signals in many different applications [213], where as in NDE systems, the pursued information is hidden in a random-nature signal. If an AR model is assumed, a linear predictive coding (LPC) spectrum estimate can be obtained.

Nonparametric techniques

When considering nonparametric techniques, the spectral analysis can be achieved by determining the magnitude spectrum of the signal, easily obtained by applying the DFT. Figure 4.11 depicts the magnitude spectrum of an ultrasonic signal, before and after applying an

analysis window. As can be observed, applying an analysis window over the time-domain signal has significant implications on the magnitude spectrum. On the one hand, the signal envelope, which corresponds to the redundant character of the signal, remains almost unchanged. On the other hand, the fine spectrum presents an accentuated *peakiness* due to the enhanced echoes.

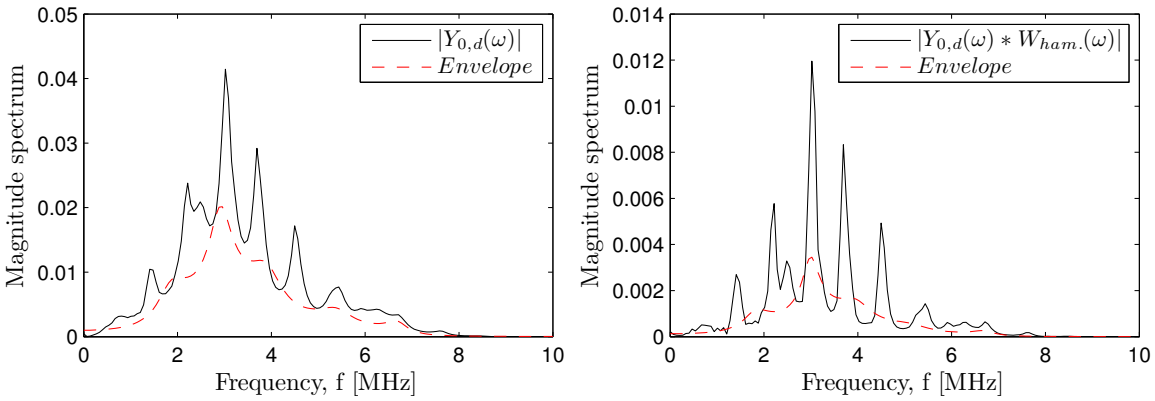

Figure 4.11: *Magnitude spectrum of an ultrasonic signal, before (left) and after (right) applying an analysis window.*

Parametric signal modeling

Let us consider an AR process, and thus the ultrasonic signal $y(n)$ is the response of an all-pole filtering to an excitation $x(n)$ [214]. The transfer function $H(z)$ of an all-pole filter is defined as,

$$H(z) = \frac{G}{A(z)} \tag{4.40}$$

where G denotes the filter gain, which depends upon the signal nature. On the other hand, $A(z)$ is a polynomial expression in z^{-1} of the form,

$$A(z) = 1 + \sum_{k=1}^{p} a_k z^{-k} \tag{4.41}$$

where the a_k and p denote the filter coefficients and the model-order, respectively. The difference equation corresponding to Equation (4.40) can be written as,

$$y(n) = Gx(n) - \sum_{k=1}^{p} a_k y(n-k) \tag{4.42}$$

In addition, for a given a signal $y(n)$, a linear prediction of that signal can be defined as,

$$\tilde{y}(n) = -\sum_{k=1}^{p} a_k \cdot y(n-k) \tag{4.43}$$

When predicted samples are compared to the original ones, the prediction error can be computed as,

$$e(n) \quad = \quad y(n) - \tilde{y}(n) \quad = \quad y(n) + \sum_{k=1}^{p} a_k y(n-k) \tag{4.44}$$

From where Equation (4.42) is recovered, when considering $e(n) = Gx(n)$. The LPC coefficients a_k can be calculated as the ones that minimizes the predictive error energy, that is,

$$\frac{\partial E}{\partial a_k} \quad \doteq \quad 0 \quad \text{, with} \quad E \quad = \quad \sum_{n=1}^{p} \left(e(n)\right)^2 \tag{4.45}$$

leading to the following classical linear equations system,

$$\sum_{k=1}^{p} a_k \sum_{n} y(n-k)y(n-i) \quad = \quad \sum_{n} y(n)y(n-i) \qquad (1 \leq i \leq p) \tag{4.46}$$

This system can be solved by the *autocorrelation method*, where the autocorrelation function is defined as,

$$R(i-k) \quad = \quad \sum_{n} y(n-k)y(n-i) \tag{4.47}$$

resulting in,

$$\sum_{k=1}^{p} a_k R(i-k) \quad = \quad R(i) \qquad (1 \leq i \leq p) \tag{4.48}$$

Note that the autocorrelation matrix that multiplies the vector of coefficients a_k is an Hermian Toeplitz matrix. This Toeplitz structure allows to solve this equations system efficiently by applying the Levinson-Durbin recursion [213]. The corresponding LPC spectrum can be obtained by substituting $z = e^{j\omega}$ into Equation (4.40). Hence,

$$H(\omega) \quad = \quad H(z)|_{z=e^{j\omega}} \quad = \quad \sum_{k=0}^{p} a_k e^{j\omega k} \qquad (G = 1) \tag{4.49}$$

Figure 4.12 depicts the LPC spectrum of an ultrasonic signal for a model-order equal to 18.

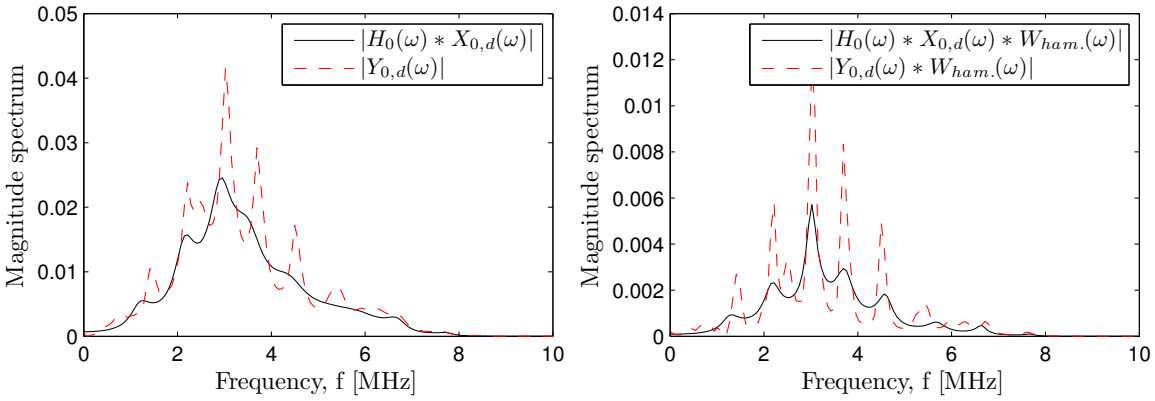

Figure 4.12: *Modeled LPC spectrum of an ultrasonic signal, before (left) and after (right) applying an analysis window.*

As can be observed, a relatively low model-order leads to a smoothing of the magnitude spectrum and resonance peaks estimation. Again, the application of an analysis window enables us to preserve parts of the fine spectrum information, even at such a low model-order. However, there are some uncertainties regarding this modeling: Determining the order p of the LPC analysis for ultrasonics is an open issue, which does not have an intrinsic meaning as in other applications. As a consequence, the performance of this modeling will depend on whether or not an AR model is consistent with the way in which the data is generated.

4.2.3 Homomorphic transformations

Systems that satisfy the generalized principle of superposition are called *homomorphic* since they can be represented by algebraically linear mapping between output and input signal spaces [215]. Among the homomorphic transformations, the *cepstrum*[6] is a conventional technique which consists of converting a convolution into a sum [216]. Concretely, the *cepstrum* $\hat{c}(n)$ of a discrete signal $y(n)$ is defined as the IDFT of the logarithmic spectrum,

$$\hat{c}(n) \;=\; \mathfrak{F}^{-1}\left[\log\left(Y(\omega)\right)\right] \;=\; \frac{1}{2\pi}\int_{-\pi}^{\pi}\log\left(Y(\omega)\right)d\omega \tag{4.50}$$

where $Y(\omega)$ denotes the spectrum of that signal $y(n)$. Generally, the spectrum $Y(\omega)$ is a complex and even function obtained by applying the DFT. Thus, $\hat{c}(n)$ is usually called *complex cepstrum* even if it represents a real signal (given that $log(Y(\omega))$ is also an even function), since the term *complex* refers to the use of the complex logarithm, not to the signal itself. Alternatively, a *real cepstrum* can be obtained by considering the magnitude spectrum $|Y(\omega)|$,

$$c(n) \;=\; \frac{1}{2\pi}\int_{-\pi}^{\pi}\log\left(|Y(\omega)|\right)d\omega \tag{4.51}$$

By decomposing the spectrum $Y(\omega)$ into its respective magnitude $|Y(\omega)|$ and phase $\angle Y(\omega)$, an expression that relates the *complex* and *real cepstra* can be found as,

$$\hat{c}(n) \;=\; c(n) + j\,\mathfrak{F}^{-1}[\angle Y(\omega)] \tag{4.52}$$

As can be observed, the *real cepstrum* is the IDFT of the real part of $Y(\omega)$, and is thus equal to the conjugate-symmetric part of $\hat{c}(n)$, denoted by $\hat{c}^*(n)$. Hence, there is a further expression that relates both the *complex* and the *real cepstra*,

$$\hat{c}(n) + \hat{c}^*(n) \;=\; 2\,c(n) \;\Leftrightarrow\; c(n) \;=\; \frac{\hat{c}(n) + \hat{c}^*(n)}{2} \tag{4.53}$$

[6]The term *cepstrum* has been defined as an anagram of the word spectrum. Playing further on the anagram theme, a filter that operates on a *cepstrum* might be called a *lifter*, and so the *quefrency*, *repiod* and *saphe* respectively stand for the frequency, period, and phase in the cepstral-domain.

In addition, in practice, the *real cepstrum* can be easily obtained by applying the FFT as,

$$c(n) \quad = \quad IFFT\left[\log\left(|FFT(y(n))|\right)\right] \tag{4.54}$$

where IFFT denotes the inverse fast Fourier transform In such a case, the *real cepstrum* is usually called *cepstrum FFT*. The *cepstrum FFT* of an ultrasonic signal is depicted in Figure 4.13.

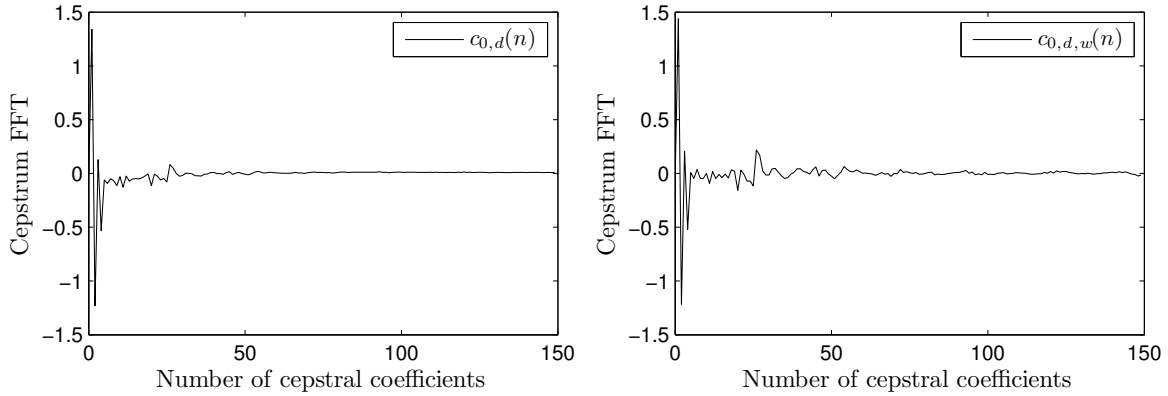

Figure 4.13: *Cesptrum FFT of an ultrasonic signal, before (left) and after (right) applying an analysis window.*

As can be observed, the low-order *cepstral* coefficients are nearly similar for the cases with/without an analysis window. In contrast, there is a significant increase in amplitude for higher-order *cepstral* coefficients around 25, 50, and 75 for the case where an analysis window has been applied. It is noteworthy that these *quefrencies* corresponds to time-equivalent sample delays between wave echoes, i.e. the time that needs the wave front to cross two, four and six times the specimen. Thus, due to the harmonic nature of the ultrasonic signals, the wave echoes appear as equidistant peaks at higher *quefrencies*, rightly separated by a value that corresponds to the fundamental period of the analyzed signal echoes. Consequently, the *cepstral* representation enables us to decompose the spectrum in its two main characteristics, that are the spectral envelope (i.e. lower *quefrencies*) and the fine spectrum (i.e. higher *quefrencies*).

In an algebraic sense, the associated *complex cepstrum* could be obtained accordingly. However, computing the *complex cepstrum* is usually cumbersome due to the unwrapping of the digital phase [217]. Indeed, the existence of the *complex cepstrum* is only ensured under the restriction that the complex logarithm could be represented by a convergent power series of the form,

$$\hat{C}(z) \quad = \quad \log\left[Y(z)\right] \quad = \quad \sum_{x=-\infty}^{\infty} \hat{c}(n) z^{-n}, \quad |z| = 1 \tag{4.55}$$

In such a case, $\log\left[Y(z)\right]$ must have the properties of the z-transform for a stable signal [218].

4.2.4 *Parameter conversion*

By applying a *cepstral* analysis, a more uncorrelated and dimensionally reduced (lower computational cost) signal representation can be obtained. Depending on the used spectral representation, different types of *cepstra* can be obtained. The most direct way is to use the *cesptrum FFT* (i.e. IFFT of the logarithmic magnitude spectrum), as described in the previous section. In the case of the LPC modeling, the *cepstrum* is a signal corresponding to the logarithmic LPC spectrum,

$$\hat{H}(\omega) \quad = \quad \log\left(H(z)|_{z=e^{j\omega}}\right) \quad = \quad \sum_{n=-\infty}^{\infty} c(n)e^{j\omega n} \tag{4.56}$$

Additionally, the corresponding *complex cepstrum* can be expressed as,

$$\hat{c}(n) \quad = \quad \log(G)\delta(n) + \hat{a}(n) \tag{4.57}$$

where $\delta(n)$ represents a unitary impulse, and $\hat{a}(n)$ denotes the *complex cepstrum* of the sequence a_k. Alternatively, Equation (4.57) can also be calculated in a recursive way as,

$$\hat{c}(n) \quad = \quad \begin{cases} 0 & (n < 0) \\ \log(G) & (n = 0) \\ -a_1 & (n = 1) \\ -a_n - \sum_{k=1}^{n-1} \frac{k}{n}\hat{c}(k)a_{n-k} & (n > 1) \end{cases} \tag{4.58}$$

Commonly, this formulation is known as *cepstrum LPC*. Its corresponding *real cesptrum* can be obtained by making use of Equation (4.53) as,

$$c(n) \quad = \quad \begin{cases} \dfrac{\hat{c}(-n)}{2} & (n < 0) \\ \log(G) & (n = 0) \\ \dfrac{\hat{c}(n)}{2} & (n > 0) \end{cases} \tag{4.59}$$

4.2.5 *Dimensionality reduction and deconvolution property*

It can be useful to reduce the number of *cepstral* coefficients, by applying a window to rule out lower and/or higher *quefrencies*. This process is called *liftering* and is defined as,

$$\tilde{c}(n) \quad = \quad c(n)l(n) \qquad\qquad (n = 0, \ldots, N-1) \tag{4.60}$$

The default window is the rectangular one, obtained as

$$l_r(n) = \begin{cases} 1 & 1 \leq n \leq L \\ 0 & \text{otherwise} \end{cases} \tag{4.61}$$

An analogy with the well-known filters (e.g. low-pass, high-pass and band-pass) used in the frequency-domain can be established, and thus several littering windows can be directly derived from the rectangular one in the cepstral-domain. Let us consider for instance a *short-pass liftering*, which corresponds to a smoothing of the spectrum, preserving its spectral envelope while removing the fine spectrum information. This lifter has been usually applied to seismic signals or dereverberation problems, to cancel multiple equidistant echoes [219]. Figure 4.14 depicts such a lifter applied on the *cepstrum FFT* obtained from an ultrasonic signal, along with the resulting smoothing of the spectrum.

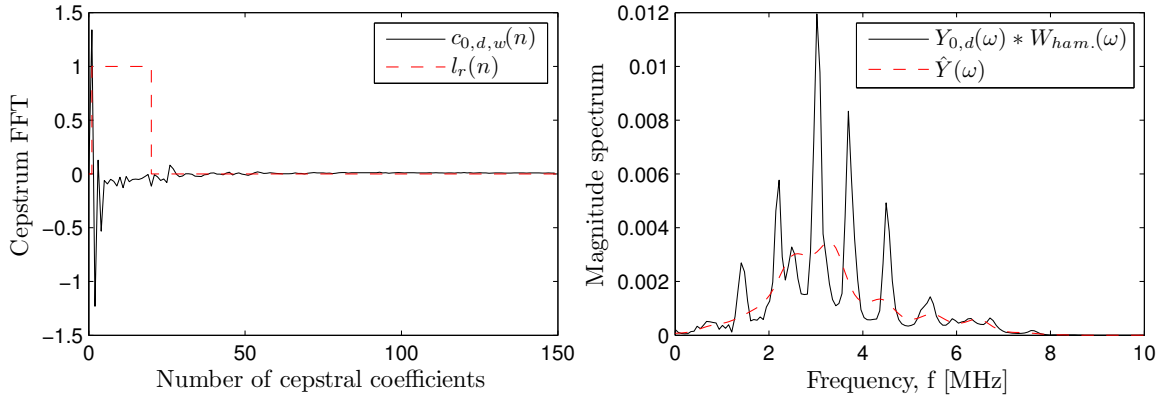

Figure 4.14: *Influence of a rectangular short-pass liftering, whose longitude amounts to* 20*, on the magnitude spectrum of the ultrasonic signal.*

Although it has been less studied, it is interesting to point out that *liftering* the *complex cepstrum* allows to observe the effects of removing quefrencies on the time-domain waveform. Figure 4.15 shows such effect for an ultrasonic signal.

On the other hand, applying windows different from the rectangular one allows to weight the *cepstral* coefficients depending on their discriminative performance for pathology detection. Tokhura [220] introduced a window formed by the inverse of the standard deviation of the *cepstral* coefficients $\sigma_c(n)$ (*statistical weighting*), which can be related to the slope of the considered *cepstrum*,

$$l_{sw}(n) = \begin{cases} \dfrac{1}{\sigma_c(n)} & 1 \leq n \leq L \\ 0 & \text{otherwise} \end{cases} \tag{4.62}$$

Other window shapes are proposed by Junqua and Wakita [221]. Among others, a *general exponential lifter* can be used for cases where the *cepstral* distance is too sensitive to the spectral

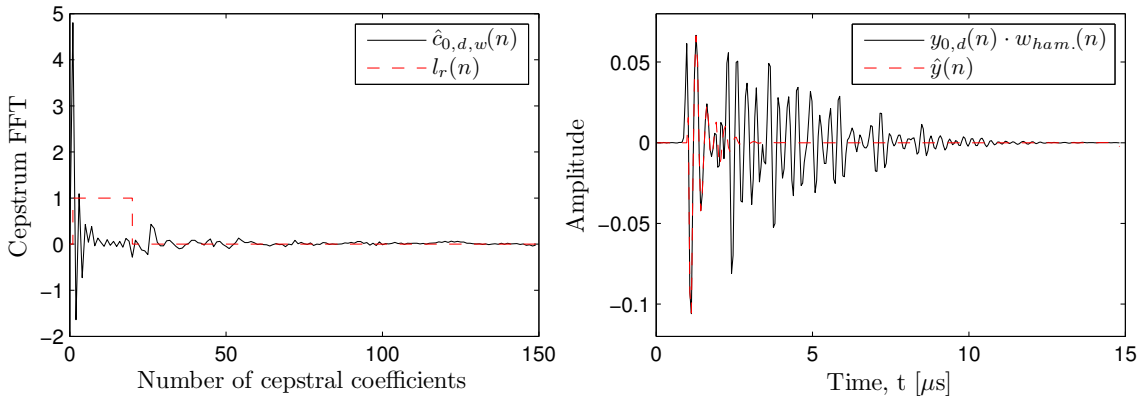

Figure 4.15: *Influence of a rectangular short-pass liftering ($L = 20$) on the time-domain waveform of an ultrasonic signal.*

peaks and not sensitive enough to the spectral slope,

$$l_{gel}(n) = \begin{cases} n^s & 1 \leq n \leq L \quad (s \geq 0) \\ 0 & \text{otherwise} \end{cases} \tag{4.63}$$

Alternatively, the *bandpass liftering*, based on a "sine-on-a-pedestal-shaped-function", has also been used in linear predictive analysis,

$$l_{bp}(n) = \begin{cases} 1 + 10.5 \sin\left(\frac{\pi n}{L}\right) & 1 \leq n \leq L \\ 0 & \text{otherwise} \end{cases} \tag{4.64}$$

Juang *et al.* [222] reviewed the sources of the LPC spectrum variation for speech signals, and pointed out the following statements, which can be extrapolated to NDE systems:

(a) The variation of the low-order *cepstral* coefficients is mainly due to the variation of the recording and transmission of the speech signal, as well as to the speaker characteristics, etc. Similarly, in a NDE system, the low-order *cepstral* coefficients can be related to the variations of the used transducers that produce the excitation signal transmitted through the specimen.

(b) The variation of high-order *cepstral* coefficients is inherent to the analysis process. Thus, in a NDE system, the high-order *cepstral* coefficients appear to be related to the material properties.

Consequently, the *liftering* window should reduce the undesirable variations due to coefficients of lower and higher orders. *Statistical weighting* allows to avoid the variation-type (a), but can strengthen the variation-type (b) in case of large window longitude. In order to

remove both variation types, a *raised sine* window has been defined as,

$$l_{rs}(n) = \begin{cases} 1 + \frac{1}{2} L \sin\left(\frac{\pi n}{L}\right) & 1 \leq n \leq L \\ 0 & \text{otherwise} \end{cases} \tag{4.65}$$

A further advantage of working in the cepstral-domain is its inherent deconvolutional capability. Indeed, by using a logarithmic domain, a response signal $y(n)$ resulting from the filtering $h(n)$ of an excitation signal $x(n)$ is equivalent to the sum of the corresponding *cepstra* $c_x(n)$ and $c_h(n)$, respectively. Consequently, the *cepstrum* provides an efficient and flexible analysis tool for measuring the likelihood between spectra. Typically, the waveforms recorded from measurements on undamaged and damaged area of a layered material differentiate themselves mainly in the wave echoes, whereas the wave front remains almost unchanged. Thus, the deconvolution property of the *cepstrum*, along with the excitation signal invariance, enables us to enhance the filter damage information when comparing the *cepstra* of undamaged $c_{y,0}(n)$ and damaged signals $c_{y,1}(n)$, by ruling out the excitation information:

$$\begin{aligned} \Delta c_{(0,1)}(n) &= \left(c_{y,1}(n) - c_{y,0}(n)\right) \\ &= \left(c_{x,1}(n) + c_{h,1}(n)\right) - \left(c_{x,0}(n) + c_{h,0}(n)\right) \\ &= \left(c_{h,1}(n) - c_{h,0}(n)\right) \end{aligned} \tag{4.66}$$

Let us introduce a rectangular *liftering scan*, with a given width and displacement, which can be applied over the *cepstrum* subtraction defined in Equation (4.66). By determining the variations within that window, it is possible to generate a graph of the *cepstral* difference evolution. As a consequence, this process enables us to detect the *cepstral* coefficients which contain some potential damage information, as depicted in Figure 4.16.

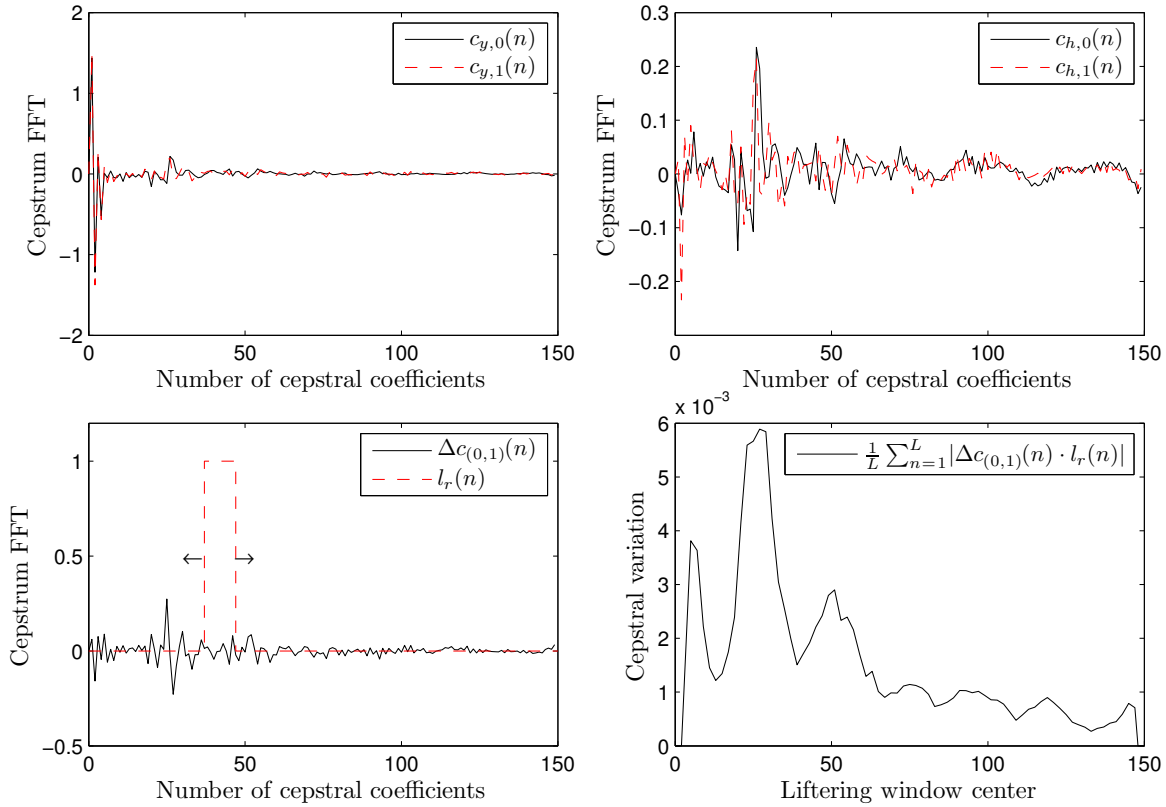

Figure 4.16: *Deconvolution property: (a) Cepstra of undamaged and damaged ultrasonic signals; (b) Cepstra of undamaged and damaged filters (obtained by ruling out the excitation signal); (c) Rectangular liftering scan (width* $= 10$*, displacement* $= 2$*) applied on the cepstral distance; and (d) Evolution of the cepstral variation.*

As can be observed, the *cesptral* distance (i.e. damage information) shows high values at low-order *cepstral* coefficients, and at high-order *cepstral* coeffecients with a common *repiod* that approximately amount to 25, which corresponds to the period of the wave echoes in the time-domain.

Part II

CONTRIBUTIONS

5

Model-based estimation procedure

The first objective of this dissertation is aimed at providing solutions to several problems that arise in *the model-based estimation procedure* for ultrasonic NDE of layered materials, by making use of digital signal processing and modeling techniques. To this end, this chapter presents a first contribution, which can be understood as a conceptual one. Indeed, on the light of the considerations done over the course of the literature review, we came across a *duality* when looking at the proposals for identifying layered structures, depending whether they stem from the engineering or information theory communities (see Figure 5.1). Therefore, we intent to unify the grounds implied in both area, facing toward the optimization of the performance of such procedure.

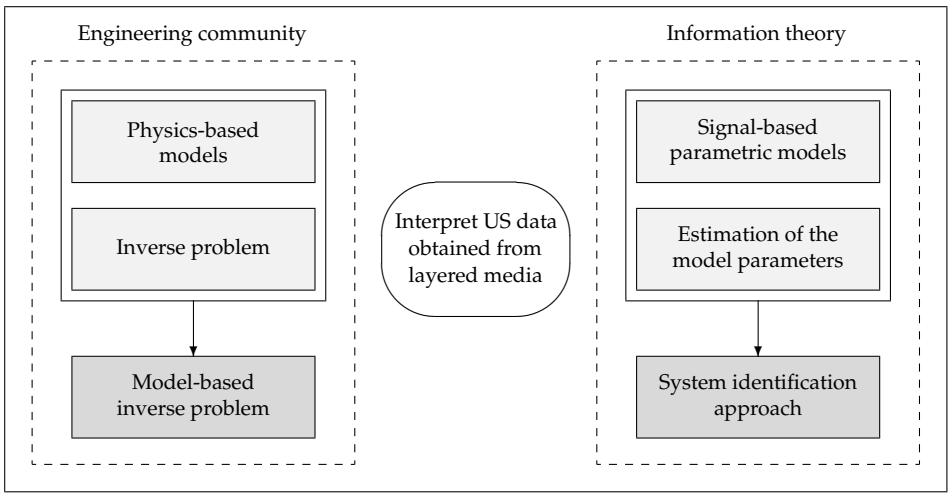

Figure 5.1: *Overview of the duality involved in the model-based estimation procedure.*

Generally, two key aspects of a *model-based estimation procedure* are fundamentals: (1) An appropriate understanding and modeling of the interactions between ultrasonic waves and multilayered media is required; and (2) the model parameters extracted from the measurements should be sensitive enough to the pathologies (that is, damage or consistency changes) that manifest in the specimen under inspection, and minimally sensitive to the measurements noise and model uncertainties. It is noteworthy that point (1) relies on the physics involved in the problem (i.e. its resolution is proper to engineers), whereas point (2) depends upon the signal features (i.e. their extraction is specific to researchers concerned with signal theory).

From an engineering perspective, a conventional *model-based inverse problem* is traditionally solved by minimizing the discrepancy between the experimental observations and the observations predicted by a *physics-based model* by comparing the waveforms in the time-domain, as depicted in Figure 5.2. Despite the potential strength of *model-based inverse problem*, parts of its structure could not be attractive from a practical point of view for inspecting multilayered media: For a fast convergence of the minimization algorithm, this method requires precise and reliable observations. However, due to their structural complexity, multilayered materials require special treatment in ultrasonic signal interpretation. The random nature of the signal generation, the imperfections of the acquisition system, as well as the difficulties in understanding and analyzing multiple and overlapping ultrasonic echoes may have a drastic influence on the performance of the inversion scheme. Additionally, an accurate characterization of pathologies usually require the determination of several model parameters, at the cost of excessive computational resources.

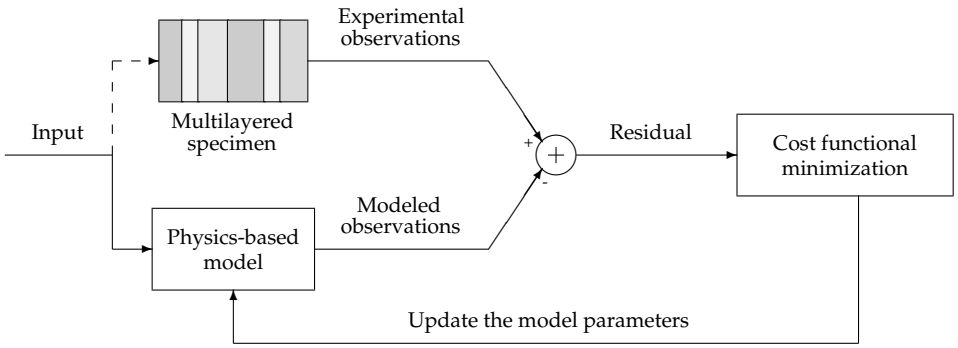

Figure 5.2: *Traditional model-based inverse problem framework.*

From a signal theory perspective, tremendous emphasis has been directed towards *system identification approaches* that enhance both the reliability and the quantitative informational content of signals obtained from conventional NDE systems [10]. Part of this emphasis has focused on the adaptation of advanced signal processing concepts to NDE problems, which had already been successfully applied in other scientific fields such as electrical engineering, speech recognition or geophysics. Among others, those procedures have given raise to the development of inverse problems based on *signal-based parametric models* (trained

over empirical data, in contrast to phenomenological approaches relying on deterministic physical laws[1]). Thus, the ability to reconstruct the ultrasonic signals can be evaluated by estimating the model parameters of the system to identify (which relates the input-output signals) that minimize the modeling error, as depicted in Figure 5.3.

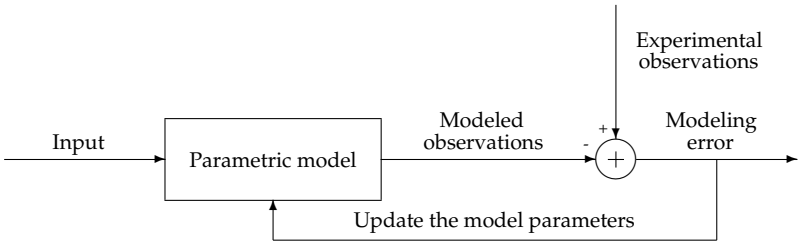

Figure 5.3: *System identification approach.*

From Figure 5.2, one could conclude the difficulty of directly extracting pathology-sensitive features from the ultrasonic signals captured by the transducers. In contrast, Figure 5.3 definitely lacks physical interpretation. In response to those problems, we propose an novel evaluation method based on an analysis-by-synthesis scheme [223, 45], which can be represented by means of the conceptual diagram depicted in Figure 5.4.

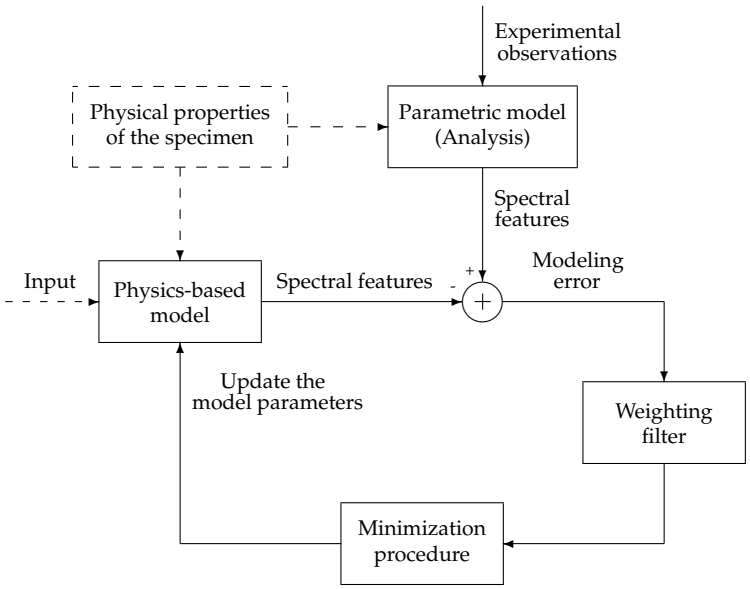

Figure 5.4: *Analysis-by-synthesis scheme.*

[1]From an engineering viewpoint, one usually develops models on the basis of the partial differential equations that describe the physical phenomena of interest (e.g. in our case, the wave equation), in an attempt of reproducing the experimental observation (i.e. the wave response). Alternatively, researchers involved in signal theory use to propose models, whose physical basis is empirical and directly inspired by the appearance of the experimental observation (e.g. in our case, the number, delay and amplitude of echoes contained in the wave response). In particular, the latter approach has a greater flexibility when it comes time to choose the model type and order (e.g. the modeling of ultrasonic signals using low-order autoregressive models [11]), which enables to adjust better the observations. However, it suffers from the absence of a direct link between the signal model parameters and the physical properties of the process.

As a can be observed, the model generates spectral features from the model pathology-sensitive parameters. The analysis-by-synthesis scheme enables us to perform a consistent optimization of the model parameters, in order to minimize the spectral distortion between the experimental observations and the modeled ones. Optionally, one could add a weighting filter that prioritize some spectral components over others. It is noteworthy that this analysis-by-synthesis scheme shows some similarities to those used in today's speech encoders. Consequently, the underlying signal processing and modeling techniques of the analysis-by-synthesis scheme offer several advantages: (1) The noise reduction of the captured signals, (2) a robust parametrization of the signals, to extract pathology-sensitive model parameters, (3) the definition of a distance between the observed and modeled features with a mechanical sense, and (4) an efficient model parameters estimation to identify the pathology.

The remaining chapters of the contributions focus on the different models developed over the course of this dissertation, and their use in the model-based estimation procedure. Despite the valuable efforts required for the development of consistent optimization strategies and the obtaining of relevant experimental observations, those steps of the model-based estimation procedure are moved to Part III, since they are not novel *per se*.

6

Transfer Matrix formalism

In this chapter, we revisit the Transfer Matrix (TM) formalism. The aim of the reconsideration of this classical method is threefold: To (1) review the theoretical grounding for our dissertation, (2) discuss some aspects regarding its implementation, and (3) obtain a formulation that offers us the possibility of extending the TM method to nonlinear media in a natural way. For these purposes, we first expose the theoretical development for a monochromatic linear-elastic wave, and then provide some answers to deal with practical issues such as material damping or discrete-time input signals.

6.1 Theoretical basis

The problem of a normally incident plane longitudinal ultrasonic wave that propagates through a multilayered elastic material is considered. A through-transmission configuration is adopted, representative of the successive reflections that suffer the transmitted signal between layers and specimen/transducers interfaces.

A general harmonic solution to the one-dimensional linear plane wave Equation (4.6) can be stated in the frequency-domain as,

$$u(x,\Omega) \;=\; u^f(x,\Omega) + u^b(x,\Omega) \;=\; Ae^{-j\frac{\Omega}{c}x} + Be^{j\frac{\Omega}{c}x} \tag{6.1}$$

where $u^f(x,\Omega)$ and $u^b(x,\Omega)$ stand for the forward- and backward-propagating parts of the linear displacement $u(x,\Omega)$, respectively. The constants A and B are the wave amplitudes of the forward- and backward-propagating parts, respectively. The ratio between the

continuous-time frequency Ω and the longitudinal wave velocity c is usually referred as the wave number $\gamma = \Omega/c$ [1]. The former is defined as,

$$c = \sqrt{\frac{E(1-\nu)}{\rho(1+\nu)(1-2\nu)}} \tag{6.2}$$

where E, ν and ρ denote the Young modulus, the Poisson ratio and the density of the medium in which the wave propagates, respectively.

The wave interactions within multilayered materials can be approximated by a semi-analytical model based on the TM formalism, which is here derived according to Cretu and Nita [224]. This formalism describes the wave propagation phenomena in finite elastic media, and is here strictly derived for the case of successive homogeneous layers. Let us consider sharp discontinuities between M homogeneous linear-elastic media with the same cross-sections, as depicted in Figure 6.1.

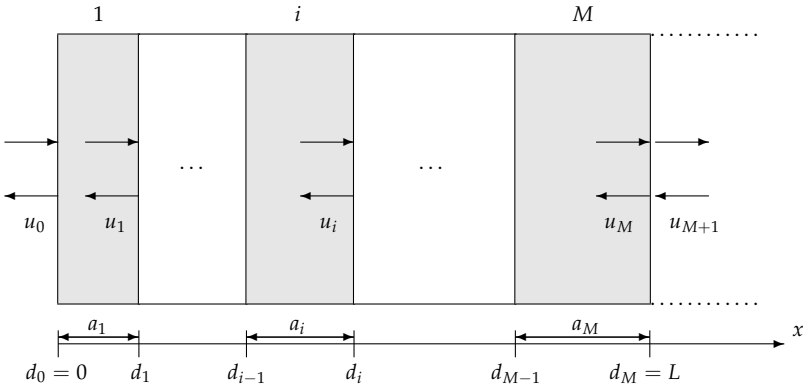

Figure 6.1: *Multilayered structure.*

Hence, the general harmonic solution stated in Equation (6.1) can be particularized for each layer i ($i = 1, \ldots, M$) as,

$$u_i(x, \Omega) = A_i e^{-j\frac{\Omega}{c_i}x} + B_i e^{j\frac{\Omega}{c_i}x} \tag{6.3}$$

In the case of a perfectly bounded interface, the transmission conditions imply the continuity of displacement $u_i(x, \Omega)$ and stress $\sigma_i(x, \Omega)$ across the interface. Making use of these conditions at an arbitrary interface $x = d_i$ ($i = 1, \ldots, M$),

$$\begin{aligned} u_i(d_i, \Omega) &= u_{i+1}(d_i, \Omega) \\ \sigma_i(d_i, \Omega) &= \sigma_{i+1}(d_i, \Omega) \end{aligned} \tag{6.4}$$

a hard transition from layer i to layer $i+1$ can be characterized by the discontinuity matrix $\boldsymbol{\mathcal{D}}_{i,i+1}$,

$$\boldsymbol{\mathcal{U}}_{i+1}(d_i, \Omega) = \boldsymbol{\mathcal{D}}_{i,i+1}\boldsymbol{\mathcal{U}}_i(d_i, \Omega) \qquad (i = 1, \ldots, M) \tag{6.5}$$

[1] Note that in the engineering community, the wave number is commonly denoted by k. Here, we reserve this symbol for the representation of the discrete frequencies, as done by researchers involved in signal theory.

where $\boldsymbol{\mathcal{U}}_j(x,\Omega) = \left[u_j^f(x,\Omega)\; u_j^b(x,\Omega)\right]^T$ and,

$$\boldsymbol{\mathcal{D}}_{i,i+1} = \frac{1}{2}\begin{pmatrix} 1+\dfrac{Z_i}{Z_{i+1}} & 1-\dfrac{Z_i}{Z_{i+1}} \\ 1-\dfrac{Z_i}{Z_{i+1}} & 1+\dfrac{Z_i}{Z_{i+1}} \end{pmatrix} \tag{6.6}$$

The discontinuity matrix depends only on the acoustic impedances $Z_j = \rho_j c_j$ of the two layers being in contact (see Appendix A.1). On the other hand, considering an harmonic wave propagating in the same homogeneous layer i from position $x = d_{i-1}$ to position $x = d_i$, its transformed displacement at the respective locations can be expressed by the propagation matrix $\boldsymbol{\mathcal{P}}_i(\Omega)$,

$$\boldsymbol{\mathcal{U}}_i(d_i,\Omega) = \boldsymbol{\mathcal{P}}_i(\Omega)\boldsymbol{\mathcal{U}}_i(d_{i-1},\Omega) \qquad (i = 1,\ldots,M) \tag{6.7}$$

with

$$\boldsymbol{\mathcal{P}}_i(\Omega) = \begin{pmatrix} e^{-j\frac{\Omega}{c_i}a_i} & 0 \\ 0 & e^{j\frac{\Omega}{c_i}a_i} \end{pmatrix} \tag{6.8}$$

where $a_i = d_i - d_{i-1}$ is the thickness of layer i (see Appendix A.2). Thus, the relation between the input and output state vectors for a layer i can be expressed by $\boldsymbol{\mathcal{U}}_{i+1}(d_i,\Omega) = \boldsymbol{\mathcal{T}}_i(\Omega)\boldsymbol{\mathcal{U}}_i(d_{i-1},\Omega)$, where a transfer matrix $\boldsymbol{\mathcal{T}}_i(\Omega) = \boldsymbol{\mathcal{D}}_{i,i+1}\boldsymbol{\mathcal{P}}_i(\Omega)$ for a single layer is obtained by combining discontinuity and propagation matrices ($i = 1,\ldots,M$),

$$\boldsymbol{\mathcal{T}}_i(\Omega) = \frac{1}{2}\begin{pmatrix} \left(1+\dfrac{Z_i}{Z_{i+1}}\right)e^{-j\frac{\Omega}{c_i}a_i} & \left(1-\dfrac{Z_i}{Z_{i+1}}\right)e^{j\frac{\Omega}{c_i}a_i} \\ \left(1-\dfrac{Z_i}{Z_{i+1}}\right)e^{-j\frac{\Omega}{c_i}a_i} & \left(1+\dfrac{Z_i}{Z_{i+1}}\right)e^{j\frac{\Omega}{c_i}a_i} \end{pmatrix} \tag{6.9}$$

so that the complete transfer matrix, describing the reflection and transmission processes of a multilayered structure, is easily obtained as the product of matrices from successive layers $\boldsymbol{\mathcal{T}}(\Omega) = \prod_{i=0}^{M-1}\boldsymbol{\mathcal{T}}_{M-i}(\Omega)$, leading to a relation between the input and the output state vectors as,

$$\boldsymbol{\mathcal{U}}_{M+1}(L,\Omega) = \boldsymbol{\mathcal{T}}(\Omega)\boldsymbol{\mathcal{U}}_1(0,\Omega) \tag{6.10}$$

where $x = 0$ and $x = L$ correspond to the boundaries of the system.

To solve the resulting system for a through-transmission configuration (the incident wave arises from the left, travels several times through the specimen, and is detected at the right-hand side), the boundary conditions must be specified[2]. First, the incident wave is

[2]Note that the theoretical development done so far may also be valid for other purpose involving the echogenic principle, such as conventional ultrasonic pulse-echo techniques or back-scattering approaches.

modeled by a forward prescribed displacement $u_0^f(0,\Omega)$, whose associated boundary condition involves the continuity of displacement at the left boundary $x = 0$,

$$u_0^f(0,\Omega) \;=\; u_1^f(0,\Omega) + u_1^b(0,\Omega) \tag{6.11}$$

where $u_0^f(0,\Omega)$ is the Fourier transform of the incident monochromatic wave. On the other hand, the wave response is obtained by modeling the receiver as a semi-infinite layer, whose boundary condition is expressed by the radiation energy condition [209] as,

$$u_{M+1}^b(L,\Omega) \;=\; 0 \tag{6.12}$$

Inserting Equations (6.11) and (6.12) into Equation (6.10) leads to,

$$\begin{bmatrix} u_{M+1}^f(L,\Omega) \\ 0 \end{bmatrix} \;=\; \begin{pmatrix} \mathcal{T}_{11}(\Omega) & \mathcal{T}_{12}(\Omega) \\ \mathcal{T}_{21}(\Omega) & \mathcal{T}_{22}(\Omega) \end{pmatrix} \begin{bmatrix} u_1^f(0,\Omega) \\ u_0^f(0,\Omega) - u_1^f(0,\Omega) \end{bmatrix} \tag{6.13}$$

where the $\mathcal{T}_{ij}(\Omega)$ denote the elements of the transfer matrix $\boldsymbol{\mathcal{T}}(\Omega)$. The wave displacement at the receiver position L, in terms of that at the transmitter position 0, is found by solving the former linear equation system,

$$u_{M+1}^f(L,\Omega) \;=\; \frac{\det\left(\boldsymbol{\mathcal{T}}(\Omega)\right)}{\mathcal{T}_{22}(\Omega) - \mathcal{T}_{21}(\Omega)} u_0^f(0,\Omega) \;=\; \mathcal{H}(\Omega) u_0^f(0,\Omega) \tag{6.14}$$

where $\mathcal{H}(\Omega)$ is a complex scalar number, which depends on the frequency of the incident wave.

Finally, it is worth to note that Equation (6.14) is a theoretical result valid for any single continuous-time frequency Ω and any number of layers M. In addition, the derivation of the complete transfer matrix is straightforward and only relies on the principles of the continuum mechanics. Nonetheless, in practice, the input signal is usually a bandpass ultrasonic signal at a relatively low center frequency[3] containing a wide range of frequencies around it, and is commonly represented as a digital time-domain signal. This issue is discussed in the Section 6.3.

6.2 TM formalism extension to absorbing layers

Typically, no substantial changes are required for the TM formalism when dealing with absorbing layers. Indeed, material damping may be introduced in a number of ways. Here, the

[3]That is, a frequency whose wavelength is compatible with the specimen thickness. Therefore, this configuration does not lead to so-called "large-problems" [78], where transfer matrices become ill-conditioned when implementing the TM method. This assumption is reasonable, since it matches the configuration of the subwavelength technique used in the experimental section of this thesis (see Section 9.2).

damping is defined in terms of the dynamic modulus E^* as in [225], and can be expressed for each layer i as,

$$E_i^* = \bar{E}_i + j\tilde{E}_i = \bar{E}_i(1 + j\tan(\delta_i)) \tag{6.15}$$

where $\bar{E}_i$, $\tilde{E}_i$ and $\tan(\delta_i)$ are the storage modulus, the loss modulus and the (dimensionless) loss tangent, respectively. Thus, the complex wave velocity c_i^* can be defined as,

$$c_i^* = \bar{c}_i\sqrt{1 + j\tan(\delta_i)} \tag{6.16}$$

where $\bar{c}_i$ denote the real part of the complex wave velocity. Supposing that the loss is small, a first-order expansion of the square root containing the loss tangent leads to,

$$c_i^* \approx \bar{c}_i\left(1 + j\frac{\tan(\delta_i)}{2}\right) \tag{6.17}$$

Thus, any trivial harmonic solution to the viscoelastic wave equation could be written as,

$$e^{-j\frac{\Omega}{c_i^*}x} = e^{-j\frac{\Omega}{\bar{c}_i}(1-j\frac{\tan(\delta_i)}{2})x} = e^{-j\frac{\Omega}{\bar{c}_i}x}e^{-\frac{\Omega\tan(\delta_i)}{2\bar{c}_i}x} \tag{6.18}$$

As can be observed, the first exponential is complex and represents the harmonic propagation, whereas the second exponential is real and is responsible for the exponential decay of the wave with propagation distance x, known as attenuation. For a small loss, the attenuation may be defined as $\alpha_i = -\Omega\tan(\delta_i)/(2\bar{c}_i)$. Hence,

$$e^{-j\frac{\Omega}{c_i^*}x} = e^{-j\frac{\Omega}{\bar{c}_i}x}e^{\alpha_i x} \tag{6.19}$$

Thus, Equation (6.9) can be easily extended to the case of absorbing layers by substituting the wave velocity c_i by a complex one c_i^*.

6.3 Numerical implementation of the TM formalism

Let us consider that the incident wave $u_0(0, nT)$ at the transmitter position $x = 0$ is represented as a discrete-time signal with N samples ($n = 0, \ldots, N-1$). By applying the Discrete Fourier Transform (DFT), an approximated discrete frequency representation with components $u_0(0, \omega_k)$ ($k = 0, \ldots, N-1$) can be obtained. The TM formalism can then be applied to each frequency bin, in order to obtain the receiver side components $u_{M+1}(L, \omega_k)$. Finally, by applying the inverse Discrete Fourier Transform (IDFT), the wave response $u_{M+1}(L, nT)$ at the receiver position $x = L$ is recovered. The general scheme of this numerical procedure for M layers is depicted in Figure 6.2.

Under this approach, we are employing a discrete-time or normalized frequency $\omega = \Omega/F_s$ ($\omega \in [0, 2\pi]$), where F_s is the sampling frequency. The DFT frequencies ω_k cover the whole frequency range,

$$\omega_k = 2\pi\frac{k}{N} \qquad (k = 0, \ldots, N-1) \tag{6.20}$$

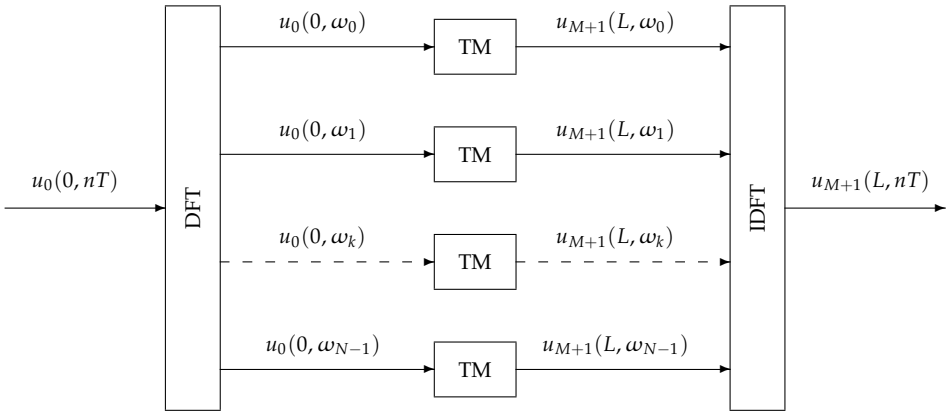

Figure 6.2: *General scheme of the TM formalism numerical procedure.*

According to this scheme, the transfer matrix for a single layer (see Equation (6.9)) can be discretized as well as,

$$\boldsymbol{T}_i^{(k)} \quad = \quad \boldsymbol{\mathcal{T}}_i(\Omega)|_{\Omega=\omega_k F_s} \tag{6.21}$$

leading to the following discrete solution,

$$u_{M+1}^f(L, \omega_k) \quad = \quad \frac{\det\left(\boldsymbol{T}^{(k)}\right)}{T_{22}^{(k)} - T_{21}^{(k)}} u_0^f(0, \omega_k) \quad = \quad H(\omega_k) u_0^f(0, \omega_k) \tag{6.22}$$

where $u_0^f(0, \omega_k)$ is the k^{th}-frequency component of the incident wave obtained by applying the DFT, namely $u_0^f(0, \omega_k) = \sum_{k=0}^{N-1} u_0(0, nT) e^{-jn\omega_k}$, and $\boldsymbol{T}^{(k)}$ denotes the complete transfer matrix corresponding to that frequency, whose elements are labeled as $T_{ij}^{(k)}$. It is worth to point out that each $\boldsymbol{T}_i^{(k)}$ ($i = 0, \ldots, M-1$, $k = 0, \ldots, N-1$) is a 2×2 matrix of complex numbers, allowing a numerical solution for Equation (6.22). Considering the frequency response $H(\omega)$ of the multilayered material for a through-transmission configuration, the proposed formalism implicitly provides a sampled version of it, namely $H(\omega_k) = \mathcal{H}(\Omega)|_{\Omega=\omega_k F_s}$ ($k = 0, \ldots, N-1$). Hence, this formalism does not enable to obtain an analytic representation of the complete frequency response of the material, and in practice its accuracy strongly depends on the number of signal samples N.

7

Signal modeling approach

In this chapter, we propose an alternative model for multilayered materials, which borrows concepts from lattice filter theory and bridge them with the physics involved in the wave-material interactions. In first place, the through-transmission configuration is considered as a discrete-time linear system. Thus, the multilayered material under investigation can be represented by a transfer function, which relates the discrete input and output signals [114]. Then, the ties between the signal model parameters and the physical properties of the layers are carefully inspected. Finally, we show that this model can be represented as a digital filter, and discuss strengths and limitations.

7.1 The two-port model

Multilayered wave-interactions can be described using conventional networks, which consist of discrete layers connected in series [102]. Thus, each layer unit i can be modeled by the two-port network depicted in Figure 7.1. In this figure, the frequency response $H_i(\omega)$ (ω is the normalized frequency defined in the previous chapter) and gains $\{G_{t_i}, G_{r_i}, \hat{G}_{t_i}, \hat{G}_{r_i}\}$ characterize the intra-layer i propagation and the impedance ratios between layers i and $i+1$, respectively. It is worth to mention that the negative signs at the nodes stand for the π-phase shifts ($e^{j\pi}$) that suffer the back-propagating components at the layer discontinuities.

According to Figure 7.1, outputs $Y_i^f(\omega)$ and $Y_i^b(\omega)$ are obtained from inputs $X_i^f(\omega)$ and $X_i^b(\omega)$ as,

$$\begin{aligned} Y_i^f(\omega) &= X_i^f(\omega)H_i(\omega)G_{t_i} - X_i^b(\omega)\hat{G}_{r_i} \\ Y_i^b(\omega) &= X_i^b(\omega)\hat{G}_{t_i}H_i(\omega) - X_i^f(\omega)H_i(\omega)G_{r_i}H_i(\omega) \end{aligned} \tag{7.1}$$

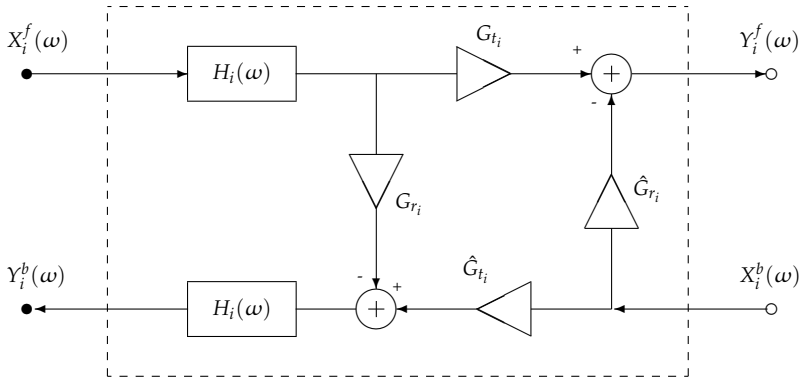

Figure 7.1: *Two-port network for a layer unit i.*

Working through these analytical expressions allows us to write the system in matrix form, with $\boldsymbol{U}_i(\omega) = \left[X_i^f(\omega)\ Y_i^b(\omega)\right]^T$ and $\boldsymbol{U}_{i+1}(\omega) = \left[X_{i+1}^f(\omega)\ Y_{i+1}^b(\omega)\right]^T$,

$$\boldsymbol{U}_{i+1}(\omega) = \begin{pmatrix} \left(G_{t_i} - \dfrac{G_{r_i}\hat{G}_{r_i}}{\hat{G}_{t_i}}\right) H_i(\omega) & -\dfrac{\hat{G}_{r_i}}{\hat{G}_{t_i}}\dfrac{1}{H_i(\omega)} \\ \dfrac{G_{r_i}}{\hat{G}_{t_i}} H_i(\omega) & \dfrac{1}{\hat{G}_{t_i}}\dfrac{1}{H_i(\omega)} \end{pmatrix} \boldsymbol{U}_i(\omega) \tag{7.2}$$

where the output vector of layer i corresponds to the input vector of layer $i+1$, i.e. $\boldsymbol{U}_{i+1}(\omega) = \left[Y_i^f(\omega)\ X_i^b(\omega)\right]^T$. The two-port network of layer i may be written as $\boldsymbol{U}_{i+1}(\omega) = \boldsymbol{T}_i(\omega)\boldsymbol{U}_i(\omega)$, and thus the total frequency response of the material is obtained as $\boldsymbol{T}(\omega) = \prod_{i=0}^{M-1} \boldsymbol{T}_{M-i}(\omega)$. Consequently, the relation between the input and output state vectors of the complete multilayered system $\boldsymbol{U}_{M+1}(\omega) = \boldsymbol{T}(\omega)\boldsymbol{U}_1(\omega)$ can be written as,

$$\begin{bmatrix} X_{M+1}^f(\omega) \\ Y_{M+1}^b(\omega) \end{bmatrix} = \begin{pmatrix} T_{11}(\omega) & T_{12}(\omega) \\ T_{21}(\omega) & T_{22}(\omega) \end{pmatrix} \begin{bmatrix} X_1^f(\omega) \\ Y_1^b(\omega) \end{bmatrix} \tag{7.3}$$

where the $T_{ij}(\omega)$ are the matrix elements of the total frequency response $\boldsymbol{T}(\omega)$. The boundary conditions for a through-transmission configuration (Equations (6.11)-(6.12)) can be represented as well in terms of signal theory concepts, as depicted in Figure 7.2.

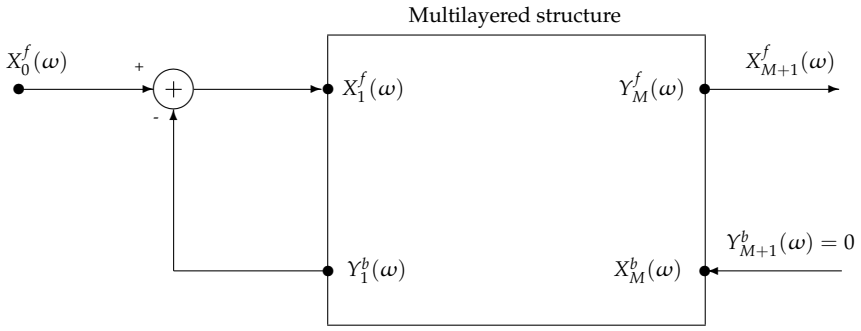

Figure 7.2: *Multilayered structure and boundary conditions in terms of signal modeling principles.*

From this figure, the boundary conditions are set in the two-port connections as,

$$\begin{array}{rcl} X_1^f(\omega) & = & X_0^f(\omega) - Y_1^b(\omega) \\ Y_{M+1}^b(\omega) & = & 0 \end{array} \tag{7.4}$$

Inserting Equation (7.4) into Equation (7.3) allows to find the output of the system as,

$$X_{M+1}^f(\omega) \;=\; \frac{\det\left(\boldsymbol{T}(\omega)\right)}{T_{22}(\omega) - T_{21}(\omega)} X_0^f(\omega) \;=\; H(\omega) X_0^f(\omega) \tag{7.5}$$

It is worth to point out the similarity of this equation with Equation (6.14) and Equation (6.22). This point will be further discussed in the next section.

7.2 Bridging the signal modeling and the physics

Let us now demonstrate that the TM formalism (see Chapter 6) may be regarded as a particular case of the innovative scheme proposed in the above section. For this purpose, the ties between the signal model parameters (gains and frequency responses) and the mechanical features (impedance ratios and material damping) are carefully inspected.

In the particular case of an incident wave propagating normally through an interface separating two media, the gains $\{G_{t_i}, G_{r_i}, \hat{G}_{t_i}, \hat{G}_{r_i}\}$ depicted in Figure 7.1 are related to the reflection and transmission coefficients associated to the reflected and transmitted wave parts generated by the incident wave. For an incident wave amplitude that amounts to unity, a simple relationship can be established between G_{r_i} and G_{t_i} [226],

$$G_{r_i} + G_{t_i} \;=\; 1 \tag{7.6}$$

When the incident wave travels from medium $i+1$ to medium i, the same relationship can be found for $\hat{G}_{r_i}$ and $\hat{G}_{t_i}$. It is noteworthy that G_{t_i} (resp. $\hat{G}_{t_i}$) may be greater than unity, and that G_{r_i} (resp. $\hat{G}_{r_i}$) may be negative. Indeed, energy is not determined by the wave amplitude alone, but depends upon the medium in which the wave propagates. The energy conservation principle [226] yields,

$$\langle P_{in} \rangle \;=\; \langle P_r \rangle + \langle P_t \rangle \tag{7.7}$$

where $\langle P_{in} \rangle$, $\langle P_t \rangle$ and $\langle P_r \rangle$ are the average power per unit area of the incident, transmitted and reflected wave components, respectively. The former equation can be explicitly written as,

$$\frac{1}{2}\rho_i c_i \omega^2 \;=\; \frac{1}{2}\rho_i c_i \omega^2 G_{r_i}^2 + \frac{1}{2}\rho_{i+1} c_{i+1} \omega^2 G_{t_i}^2 \tag{7.8}$$

From Equations (7.7)-(7.8), we can obtain the following relationships between gains and acoustic impedances,

$$G_{r_i} \;=\; \frac{Z_{i+1} - Z_i}{Z_i + Z_{i+1}} \quad , \quad G_{t_i} \;=\; \frac{2Z_i}{Z_i + Z_{i+1}} \tag{7.9}$$

Similar relationships can be obtained when the incident wave arises from the opposite side,

$$\hat{G}_{r_i} = \frac{Z_i - Z_{i+1}}{Z_i + Z_{i+1}} \quad , \quad \hat{G}_{t_i} = \frac{2Z_{i+1}}{Z_i + Z_{i+1}} \tag{7.10}$$

By inserting Equations (7.9)-(7.10) into the equation system (7.2), the following expression is obtained,

$$\boldsymbol{u}_{i+1}(\omega) = \frac{1}{2} \begin{pmatrix} \left(1 + \frac{Z_i}{Z_{i+1}}\right) H_i(\omega) & \left(1 - \frac{Z_i}{Z_{i+1}}\right) \frac{1}{H_i(\omega)} \\ \left(1 - \frac{Z_i}{Z_{i+1}}\right) H_i(\omega) & \left(1 + \frac{Z_i}{Z_{i+1}}\right) \frac{1}{H_i(\omega)} \end{pmatrix} \boldsymbol{u}_i(\omega) \tag{7.11}$$

which shows a high similarity with Equation (6.9). Let us now assume that the intra-layer frequency response $H_i(\omega)$ of Figure 7.1 has the form,

$$H_i(\omega) = e^{-j\omega m_i} \tag{7.12}$$

where $m_i = \frac{F_s a_i}{c_i}$, that is, the filter response $H_i(\omega)$ consists of an unitary gain and a linear phase with a constant group delay m_i. The latter corresponds to a delay equivalent to the time needed by the wave to cross the thickness of a layer i. By sampling this frequency response, we obtain:

$$H_i(\omega)|_{\omega=\omega_k} = H_i(\omega_k) = e^{-j\omega_k \frac{F_s a_i}{c_i}} \tag{7.13}$$

As can be observed, by inserting Equation (7.13) into the Equation (7.11), Equation (6.21) (i.e. the discrete version of Equation (6.9)) is recovered. Moreover, when dealing with absorbing layers, the definition of the frequency response $H_i(\omega)$ can be extended to,

$$H_i(\omega) = G_{\alpha_i} e^{-j\omega m_i} \tag{7.14}$$

where G_{α_i} denotes the attenuation associated to a layer i. By defining this attenuation as a constant gain $G_{\alpha_i} = e^{\alpha_i a_i}$, we recover a discretized version of the expression obtained in Equation (6.19),

$$H_i(\omega_k) = e^{\alpha_i a_i} e^{-j\omega_k \frac{F_s a_i}{c_i}} = e^{-j\frac{\Omega}{c_i^*} a_i}|_{\Omega=\omega_k F_s} \tag{7.15}$$

Thus, as can be seen, the TM formalism is indeed a particular case of our proposed signal modeling framework, which could be extended by defining the intra-layer response $H_i(\omega)$ in other different or more complex ways.

7.3 Solving the signal modeling approach

The theoretical result presented in Equation (7.5) is unfortunately not straightforwardly implementable, since the derivation of the total frequency response $\boldsymbol{T}(\omega) = \prod_{i=0}^{M-1} \boldsymbol{T}_{M-i}(\omega)$

is, in general, cumbersome. However, in the particular case of the layer frequency response definition made in Equation (7.14), equation system (7.2) can be rewritten as,

$$\boldsymbol{U}_{i+1}(\omega) \;=\; \begin{pmatrix} G_i^{(A)} e^{-j\omega m_i} & G_i^{(B)} e^{j\omega m_i} \\ G_i^{(C)} e^{-j\omega m_i} & G_i^{(D)} e^{j\omega m_i} \end{pmatrix} \boldsymbol{U}_i(\omega) \;=\; \boldsymbol{T}_i(\omega)\boldsymbol{U}_i(\omega) \tag{7.16}$$

where the $G_i^{(j)}$ (with $j = \{A, B, C, D\}$) stand for the resulting gains computed from the layer discontinuities $\{G_{t_i}, G_{r_i}, \hat{G}_{t_i}, \hat{G}_{r_i}\}$ and the absorption ones G_{α_i}. It can be proven that a product of matrices with the previous form can be expressed as a sum of matrices with a similar form (composed of gain-exponential elements). Hence, by making use of the distributive property (see Appendix B.1), the complete matrix product $\boldsymbol{T}(\omega) = \prod_{i=0}^{M-1} \boldsymbol{T}_{M-i}(\omega)$ can be translated into a sum of matrices as,

$$\begin{aligned} \boldsymbol{U}_{M+1}(\omega) \;&=\; \prod_{i=0}^{M-1} \begin{pmatrix} G_{M-i}^{(A)} e^{-j\omega m_{M-i}} & G_{M-i}^{(B)} e^{j\omega m_{M-i}} \\ G_{M-i}^{(C)} e^{-j\omega m_{M-i}} & G_{M-i}^{(D)} e^{j\omega m_{M-i}} \end{pmatrix} \boldsymbol{U}_1(\omega) \\ &=\; \sum_{k=1}^{2^{M-1}} \begin{pmatrix} \bar{G}_k^{(A)} e^{-j\omega \bar{m}_k} & \bar{G}_k^{(B)} e^{j\omega \bar{m}_k} \\ \bar{G}_k^{(C)} e^{-j\omega \bar{m}_k} & \bar{G}_k^{(D)} e^{j\omega \bar{m}_k} \end{pmatrix} \boldsymbol{U}_1(\omega) \end{aligned} \tag{7.17}$$

where the group delays $\bar{m}_k$ are obtained as a linear combination of the group delays m_{M-i}, and the gains labeled with an overscore result from multiplicative combinations of the original gains. It must be noted that subindex k does not correspond to any layer number but to the leaves of the resulting distributive decomposition tree. Unlike the TM formalism, the presented signal-based framework enables to compute analytically the complete frequency response $H(\omega)$ of the material for a through-transmission configuration. Note that the latter does not depend upon the number of signal samples N. However, this approach suffers of a strong lake of efficiency (even worse than the TM formalism) as the complexity burden increases exponentially along the number of layers M.

To avoid this, we take advantage of the mathematical formulation previously developed to define a novel digital signal model for wave propagation problems. To this end, for each layer i, we introduce a discrete-time transfer function $H_i^D(z) = G_{\alpha_i} z^{-m_i}$ in the z-domain, whose frequency response approximates that proposed in Equation (7.14),

$$H_i(\omega) \;\approx\; H_i^D(z)|_{z=e^{j\omega}} \;=\; G_{\alpha_i} e^{-j\omega m_i} \tag{7.18}$$

where it is must be noted that the delays $m_i \in \mathbb{N}$ are now integer thickness-equivalent sample delays that approximate the delays $m_i = \frac{F_s a_i}{c_i}$ by rounding their values or adjusting the sampling frequency. The transfer function $H_i^D(z)$ stands for a single-coefficient finite impulse response (FIR) filter, with a constant gain G_{α_i} and delay m_i. Substituting Equations (7.9)-(7.10) and $H_i^D(z)$ in the layer matrix of Equation (7.2) yields a z-transformed layer

matrix $\boldsymbol{T}_i^D(z)$ which can be rewritten in terms of z-domain polynomial expressions as,

$$\boldsymbol{U}_{i+1}(z) = \frac{G_{\alpha_i} z^{-m_i}}{1+G_{r_i}} \begin{pmatrix} 1 & G_{r_i} G_{\alpha_i}^{-2} z^{2m_i} \\ G_{r_i} & G_{\alpha_i}^{-2} z^{2m_i} \end{pmatrix} \boldsymbol{U}_i(z) = \boldsymbol{T}_i^D(z) \boldsymbol{U}_i(z) \tag{7.19}$$

It can be proven (see Appendix B.2) that the product of M-layers, $\boldsymbol{T}^D(z) = \prod_{i=0}^{M-1} \boldsymbol{T}_{M-i}^D(z)$, has the following general form,

$$\boldsymbol{T}^D(z) = \left(\prod_{i=1}^{M} \frac{G_{\alpha_i} z^{-m_i}}{1+G_{r_i}} \right) \begin{pmatrix} P_M(G_\alpha, z) & \left(\prod_{i=1}^{M} G_{\alpha_i}^{-2} z^{2m_i} \right) Q_M(G_\alpha^{-1}, z^{-1}) \\ Q_M(G_\alpha, z) & \left(\prod_{i=1}^{M} G_{\alpha_i}^{-2} z^{2m_i} \right) P_M(G_\alpha^{-1}, z^{-1}) \end{pmatrix} \tag{7.20}$$

where the functions $P_M(G_\alpha, z)$ and $Q_M(G_\alpha, z)$ stand for polynomials which are built up following a recursive scheme,

$$\begin{aligned} P_M(G_\alpha, z) &= P_{M-1}(G_\alpha, z) + G_{r_M} G_{\alpha_M}^{-2} z^{2m_M} Q_{M-1}(G_\alpha, z) \\ Q_M(G_\alpha, z) &= G_{r_M} P_{M-1}(G_\alpha, z) + G_{\alpha_M}^{-2} z^{2m_M} Q_{M-1}(G_\alpha, z) \end{aligned} \tag{7.21}$$

with $P_1(G_\alpha, z) = 1$ and $Q_1(G_\alpha, z) = G_{r_1}$. These polynomials incorporate all the multiple transmissions/reflections and attenuation effects of the multilayered structure.

Once the boundary conditions are considered (Equation (7.4)), a discrete-time transfer function of the multilayered structure can be written as,

$$X_{M+1}^f(z) = \left(\prod_{i=1}^{M} \frac{1}{1+G_{r_i}} \right) \left(\frac{P_M(G_\alpha, z) P_M(G_\alpha^{-1}, z^{-1}) - Q_M(G_\alpha, z) Q_M(G_\alpha^{-1}, z^{-1})}{\left(\prod_{i=1}^{M} G_{\alpha_i}^{-1} z^{m_i} \right) P_M(G_\alpha^{-1}, z^{-1}) - \left(\prod_{i=1}^{M} G_{\alpha_i} z^{-m_i} \right) Q_M(G_\alpha, z)} \right) X_0^f(z) \tag{7.22}$$

It must be considered that the polynomials $P_M(G_\alpha, z)$ and $Q_M(G_\alpha, z)$ are not independent, existing a surprising relationship between them (see Appendix B.3), which can be written down as,

$$P_M(G_\alpha, z) P_M(G_\alpha^{-1}, z^{-1}) - Q_M(G_\alpha, z) Q_M(G_\alpha^{-1}, z^{-1}) = \prod_{i=1}^{M} (1 - G_{r_i}^2) \tag{7.23}$$

which leads us to an iterative approach. Inserting Equation (7.23) into Equation (7.22) enables the following simplified filter,

$$X_{M+1}^f(z) = \frac{\prod_{i=1}^{M} G_{t_i} G_{\alpha_i} z^{-m_i}}{P_M(G_\alpha^{-1}, z^{-1}) - \left(\prod_{i=1}^{M} G_{\alpha_i}^2 z^{-2m_i} \right) Q_M(G_\alpha, z)} X_0^f(z) = \frac{N(z)}{D(z)} X_0^f(z) \tag{7.24}$$

This result allows any multilayered material to be modeled as a linear time-invariant (LTI) digital filter (with rational z-transform). The filter coefficients are linked to the physical properties of the material and are obtained from them analytically. In addition, it can be shown that the proposed recursive framework remains valid for any arbitrary discrete-time transfer function $H_i^D(z)$, and could thus be employed in the case of more complex layers' mechanical behavior.

7.4 Discussion

It can be proven that the formalism which delivers the transfer function of Equation (7.20), along with Equation (7.21), extends the recursive formalism proposed by Claerbout [96] for Goupillaud-type structures (i.e. structures which consist of equal wave travel time layers) which, in our proposed form, is now valid for absorbing layers of unequal wave travel time. On the other hand, the iterative expression delivered by Equation (7.24) also extends the energy considerations done by Claerbout [96] to absorbing non-Goupillaud-type structures. Additionally, our approach is straightforward and computationally more efficient than the one proposed by Treitel [226], who suggested that the effect of a multilayered material with arbitrary time delays could be obtained from Goupillaud-type media by lumping several successive layers together by setting the reflection coefficients to zero and the transmission coefficients to unity, at the number of interfaces existing between the constituent iso-time-delay layers.

A bare inspection of Equation (7.24) reveals that the lowest polynomial coefficient of the denominator $D(z)$ is provided by $P_1(G_\alpha^{-1}, z^{-1}) = 1$, ensuring that the filter is causal and realizable. On the other hand, the highest coefficient is 2Λ, with $\Lambda = \sum_{i=1}^{M} m_i$, due to the term $\prod_{i=1}^{M} z^{-2m_i}$ in the denominator. As can be observed, Λ corresponds to a sample delay equivalent to the time needed by the incident wave to cross the total thickness of the multilayered structure. In addition, the numerator $\prod_{i=1}^{M} G_{t_i} G_{\alpha_i} z^{-m_i}$ can be replaced by $b_0 z^{-\Lambda}$, i.e. a gain corresponding to the multiplication of the transmission G_{t_i} and attenuation coefficients G_{α_i} across all layers plus a total thickness sample delay. Finally, Equation (7.24) implies that most of the coefficients a_k are zeros (since $\Lambda \gg M$). Thus, as can be observed, Goupillaud-type structures are a particular case of our formalism, for which the gains $G_{\alpha_i} = 1$ and the unitary sample delays $m_i = 1\ \forall i$, thus leading to the trivial case $\Lambda = M$ (that is, a standard linear prediction form). Hence, the discrete-time transfer function $H^D(z)$ can be alternatively written as a classical delayed all-pole filter with sparse coefficients,

$$H^D(z) = \frac{b_0}{1 + \sum_{k=1}^{2\Lambda} a_k z^{-k}} z^{-\Lambda} \qquad \text{where} \quad ||a_k||_0 \ll 2\Lambda \tag{7.25}$$

where the sparsity is represented as a measure of the cardinality, that would be se so-called l_0-norm. The proposed sparse digital signal model offers several advantages in comparison with previously used physical or signal models. First, this generic model is valid for

an arbitrary number of absorbing layers of unequal-wave travel time, independent of the digital input signal characteristics (e.g. its central frequency and number of samples), and not restricted to any particular boundary conditions. In second place, the model parameters are obtained from a rigorous analysis of the physics involved in the wave-material interactions, and thus the sparsity arises naturally and does not rely on heuristic approaches, as in [6, 40]. Thirdly, this model can be represented as a sparse digital filter, which has thus obvious practical implications. Figure 7.3 summarizes the computational process used to take layered material properties and convert them to a functional digital filter.

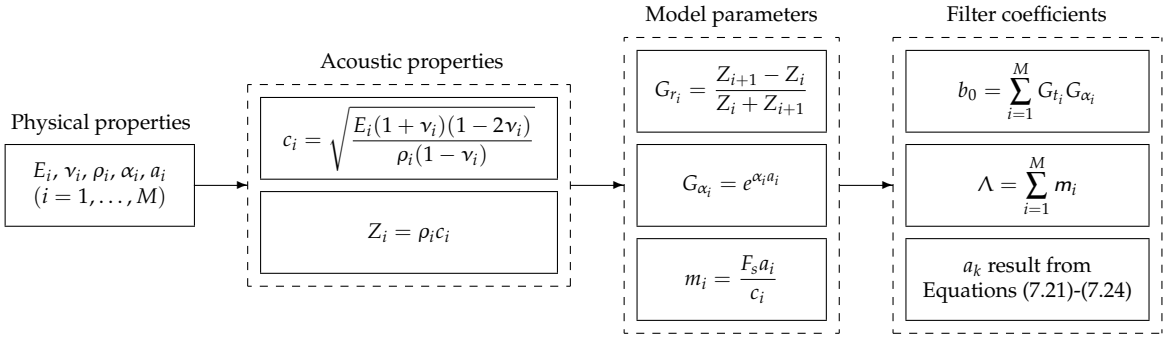

Figure 7.3: Computational process to take layered material properties and convert them to a functional digital filter.

It is worth to point out that the proposed recursive formalism to obtain $H^D(z)$ is straightforward and efficient, and also that the frequency response of the structure can easily be obtained by evaluating z in the unitary circle. As a drawback, it should be mentioned that, formally, digital filters require integer delays m_i. Nevertheless, there are well-known ways of overcoming this issue, as increasing the sampling frequency (i.e. using digital interpolation), or by applying fractional delay filter formalisms [227]. Additionally, since the whole formalism is expressed in terms of polynomials in z, one can easily obtain the difference equation, which allows, given a discrete-time input signal $x(n)$, to directly obtain the output signal $y(n)$ by filtering. The sparse structure of the filter, whose maximum number of coefficients is 2Λ but most of them are zeros, is particularly suitable for this task. The latter evidences the simplicity of this proposal, when comparing it to the numerical procedure implied in the TM formalism described in Figure 6.2. Furthermore, in our case, the resulting inverse filter $H^{D^{-1}}(z)$ is a FIR filter, which is inherently stable and can be computed straightforwardly. Thus, ultrasonic output signals obtained from specimens could easily be whitened by inverse filtering. While the inverse filtered response from the undamaged specimen should be similar to the original input signal applied, the opposite is expected for damaged specimens, due to the corresponding model mismatch, resulting in an effective damage detection procedure with a relatively low cost.

8

Nonlinear extensions

In this chapter, we propose two models that extend the ones developed in Chapters 6 and 7, in order to cope with the nonlinear constitutive behavior of multilayered structures. In a first approach, we take advantage of the simple matrix formulation provided by the TM formalism to derive an extended transfer matrix that accounts for constitutive nonlinearity. In a second proposal, we extend the two-port network used during the signal modeling approach to include an additional frequency response for layers with nonlinear constitutive behavior, and thus obtain zero-order and first-order contributions to a discrete-time transfer function for nonlinear multilayered materials.

8.1 Nonlinear extension of the Transfer Matrix formalism

In this section, the TM formalism is extended to the calculation of nonlinear ultrasonic waves up to the first-order nonlinearity (see Chapter 4). To this end, the problem of a linear longitudinal ultrasonic wave that propagates through a nonlinear multilayered elastic material is considered. Instead of directly solving the nonlinear problem, this formalism enables us to decompose the nonlinear problem into two linear subsets which can be solved separately. Concretely, those subsets provide both the zero-order and first-order contributions to the nonlinear wave displacement. In addition, one can prove that the zero-order contribution is equivalent to the solution delivered by the TM formalism (and thus that the latter is a special case of the nonlinear problem).

8.1.1 *Theoretical development*

A general harmonic solution to the one-dimensional nonlinear plane wave Equation (4.8) up to first-order nonlinearity ($\delta = 0$) can be stated in the frequency-domain as in [178][1],

$$\begin{aligned} u(x,\Omega) &= u^{(0),f}(x,\Omega) + u^{(1),f}(x,\Omega) + u^{(0),b}(x,\Omega) + u^{(1),b}(x,\Omega) \\ &= Ae^{-j\frac{\Omega}{c}x} + \frac{1}{2}\beta\left(\frac{\Omega}{c}\right)^2 xA^2e^{-2j\frac{\Omega}{c}x} + Be^{j\frac{\Omega}{c}x} + \frac{1}{2}\beta\left(\frac{\Omega}{c}\right)^2 xB^2e^{2j\frac{\Omega}{c}x} \end{aligned} \tag{8.1}$$

where $u^{(h),f}(x,\Omega)$ and $u^{(h),b}(x,\Omega)$ stand for the forward- and backward-propagating parts of the nonlinear displacement $u(x,\Omega)$, respectively. Note that those parts now consist of both the zero-order (Ω) and first-order (2Ω) perturbation solutions, denoted by the upper index $h \in \{0,1\}$, respectively[2]. Consequently, the fundamental waves (zero-order contribution to the nonlinear displacement) are now labeled with an upper index $h = 0$, whereas the second harmonics (first-order contribution to the nonlinear displacement) are labeled with an upper index $h = 1$.

The wave interactions within nonlinear multilayered materials can be approximated by a semi-analytical model based on an extension of the TM formalism [208], which from now on will be called the Nonlinear Transfer Matrix (NTM) formalism. The latter describes the wave propagation phenomena in finite nonlinear-elastic media, and is here strictly derived for the case of successive homogeneous layers. Note that only the nonlinear effects of second harmonics from fundamental waves in the media are considered (and thus, higher-order harmonics and/or the intrinsic nonlinearity of the interfaces are neglected). To this end, let us consider sharp discontinuities between M homogeneous nonlinear-elastic media with the same cross-sections, as depicted in Figure 8.1.

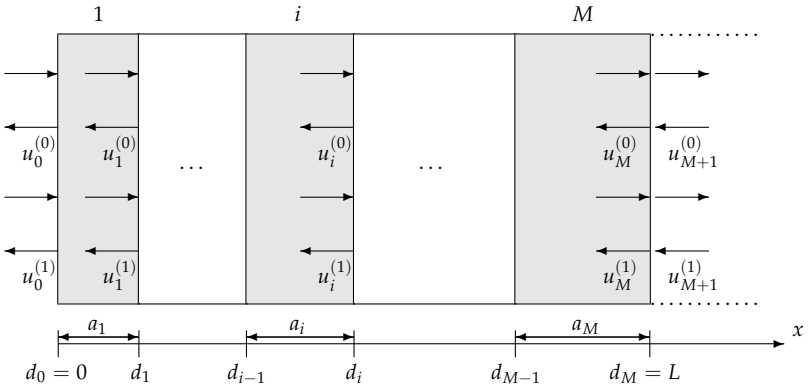

Figure 8.1: *Wave components in a nonlinear multilayered structure.*

[1] In that proposed form, the solution was developed for a nonlinear semi-infinite medium. We adapt it here to a bounded medium, in order to account for forward- and backward propagating components.

[2] Note that for the linear case, we disregarded the upper index (0) to lighten the notation. Now that we consider both fundamental and second harmonics, the upper index (0) is assigned to all variables related to the linear case.

Hence, the general harmonic solution stated in Equation (8.1) can be particularized for each layer i ($i = 1, \ldots, M$) as,

$$\begin{aligned} u_i(x,\Omega) &= A_i e^{-j\frac{\Omega}{c_i}x} + \left(\bar{A}_i + \frac{1}{2}\beta_i \left(\frac{\Omega}{c_i}\right)^2 x A_i^2\right) e^{-2j\frac{\Omega}{c_i}x} \\ &+ B_i e^{j\frac{\Omega}{c_i}x} + \left(\bar{B}_i + \frac{1}{2}\beta_i \left(\frac{\Omega}{c_i}\right)^2 x B_i^2\right) e^{2j\frac{\Omega}{c_i}x} \end{aligned} \tag{8.2}$$

Note that this solution is slightly different to that defined in Equation (8.1). As can be observed, the first-order perturbation solution is now formed of two parts: One, denoted by the quadratic amplitudes of A and B, is generated by the fundamental waves, whose amplitude accumulates with the propagation distance x. The other, denoted by the amplitudes $\bar{A}$ and $\bar{B}$, keeps constant amplitude during the propagation. The latter are introduced in the equation not to represent the intrinsic nonlinearity of the actual layer i, but instead, to be responsible for propagating the nonlinear components from previous layers to next layers[3].

In the case of a perfectly bounded interface, the transmission conditions imply the continuity of displacement $u^{(h)}(x,\Omega)$ and stress $\sigma^{(h)}(x,\Omega)$ across the interface between layers i and $i+1$, for both the zero-order and first-order contributions. Applying those conditions at an arbitrary interface $x = d_i$ ($i = 1, \ldots, M$) leads to,

$$\begin{aligned} u_i^{(h)}(d_i,\Omega) &= u_{i+1}^{(h)}(d_i,\Omega) \\ \sigma_i^{(h)}(d_i,\Omega) &= \sigma_{i+1}^{(h)}(d_i,\Omega) \end{aligned} \qquad (\forall h \in \{0,1\}) \tag{8.3}$$

Note that the zero-order perturbation solution was governed by the equations of the TM formalism. Here, we focus on the first-order perturbation solution to determine the contribution of the second harmonics to the nonlinear displacement. For this purpose, a hard transition from layer i to layer $i+1$ can be described by the first-order discontinuity matrix $\boldsymbol{\mathcal{D}}_{i,i+1}^{(1)}(\Omega)$,

$$\boldsymbol{\mathcal{U}}_{i+1}^{(1)}(d_i,\Omega) = \boldsymbol{\mathcal{D}}_{i,i+1}^{(1)}(\Omega)\boldsymbol{\mathcal{U}}_i^{(1)}(d_i,\Omega) \qquad (i = 1, \ldots, M) \tag{8.4}$$

where the displacement vector for nonlinear acoustic waves must now be extended to,

$$\boldsymbol{\mathcal{U}}_j^{(1)}(x,\Omega) = \left[\left(u_j^{(0),f}(x,\Omega)\right)^2 \;\; \left(u_j^{(0),b}(x,\Omega)\right)^2 \;\; \left(u_j^{(0),f}(x,\Omega)\cdot u_j^{(0),b}(x,\Omega)\right) \;\; \left(u_j^{(1),f}(x,\Omega)\right) \;\; \left(u_j^{(1),b}(x,\Omega)\right)\right]^T \tag{8.5}$$

[3]Let us consider for instance a nonlinear multilayered media which consist of alternating linear and nonlinear layers to underline this concept. If one would omit those parts, the nonlinear components would get stuck into the nonlinear layers and could not be detected at the material boundaries, since they would never propagate through the linear layers.

and the first-order discontinuity matrix $\boldsymbol{\mathcal{D}}_{i,i+1}^{(1)}(\Omega)$ can be expressed as,

$$\boldsymbol{\mathcal{D}}_{i,i+1}^{(1)}(\Omega) = \begin{pmatrix} \mathcal{D}_{i,11}^2 & \mathcal{D}_{i,12}^2 & 2\mathcal{D}_{i,11}\mathcal{D}_{i,12} & 0 & 0 \\ \mathcal{D}_{i,12}^2 & \mathcal{D}_{i,11}^2 & 2\mathcal{D}_{i,11}\mathcal{D}_{i,12} & 0 & 0 \\ \mathcal{D}_{i,11}\mathcal{D}_{i,12} & \mathcal{D}_{i,11}\mathcal{D}_{i,12} & \mathcal{D}_{i,11}^2 + \mathcal{D}_{i,12}^2 & 0 & 0 \\ \mathcal{D}_{i,41}(\Omega) & \mathcal{D}_{i,41}(\Omega) & -\mathcal{D}_{i,43}(\Omega) & \mathcal{D}_{i,11} & \mathcal{D}_{i,12} \\ -\mathcal{D}_{i,41}(\Omega) & -\mathcal{D}_{i,41}(\Omega) & \mathcal{D}_{i,43}(\Omega) & \mathcal{D}_{i,12} & \mathcal{D}_{i,11} \end{pmatrix} \tag{8.6}$$

where the $\mathcal{D}_{i,jk}$ and $\mathcal{D}_{i,jk}(\Omega)$ denote linear and nonlinear frequency-dependent elements of the first-order discontinuity matrix $\boldsymbol{\mathcal{D}}_{i,i+1}^{(1)}(\Omega)$ for a layer i, respectively. As demonstrated in Appendix C.1, linear elements $\mathcal{D}_{i,11}$ and $\mathcal{D}_{i,12}$ correspond to,

$$\mathcal{D}_{i,11} = \frac{1}{2}\left(1 + \frac{Z_i}{Z_{i+1}}\right) \quad , \quad \mathcal{D}_{i,12} = \frac{1}{2}\left(1 - \frac{Z_i}{Z_{i+1}}\right) \tag{8.7}$$

whereas nonlinear frequency-dependent elements $\mathcal{D}_{i,41}(\Omega)$ and $\mathcal{D}_{i,43}(\Omega)$ can be written down as,

$$\begin{aligned} \mathcal{D}_{i,41}(\Omega) &= -\frac{j}{4}\left(\beta_i \frac{\Omega}{c_i}\frac{Z_i}{Z_{i+1}} + \frac{1}{2}\beta_{i+1}\frac{\Omega}{c_{i+1}}\left(1 - 3\left(\frac{Z_i}{Z_{i+1}}\right)^2\right)\right) \\ \mathcal{D}_{i,43}(\Omega) &= -j\left(\beta_i \frac{\Omega}{c_i}\frac{Z_i}{Z_{i+1}} - \frac{1}{4}\beta_{i+1}\frac{\Omega}{c_{i+1}}\left(1 + 3\left(\frac{Z_i}{Z_{i+1}}\right)^2\right)\right) \end{aligned} \tag{8.8}$$

As can be observed, this matrix does not only depend on the acoustic impedances Z_j of the two layers being in contact (in contrast to the linear case), but also on the continuous-time frequency Ω and the first-order nonlinear elastic properties β_j of those layers. On the other hand, considering a harmonic wave propagating in the same nonlinear homogeneous layer i from position $x = d_{i-1}$ to position $x = d_i$, its transformed displacement at the respective locations can be expressed by the first-order propagation matrix $\boldsymbol{\mathcal{P}}_i^{(1)}(\Omega)$,

$$\boldsymbol{\mathcal{U}}_i^{(1)}(d_i, \Omega) = \boldsymbol{\mathcal{P}}_i^{(1)}(\Omega)\boldsymbol{\mathcal{U}}_i^{(1)}(d_{i-1}, \Omega) \qquad (i = 1, \ldots, M) \tag{8.9}$$

with

$$\boldsymbol{\mathcal{P}}_i^{(1)}(\Omega) = \begin{pmatrix} e^{-2j\frac{\Omega}{c_i}a_i} & 0 & 0 & 0 & 0 \\ 0 & e^{2j\frac{\Omega}{c_i}a_i} & 0 & 0 & 0 \\ 0 & 0 & 1 & 0 & 0 \\ \eta_i(\Omega)e^{-2j\frac{\Omega}{c_i}a_i} & 0 & 0 & e^{-2j\frac{\Omega}{c_i}a_i} & 0 \\ 0 & \eta_i(\Omega)e^{2j\frac{\Omega}{c_i}a_i} & 0 & 0 & e^{2j\frac{\Omega}{c_i}a_i} \end{pmatrix} \tag{8.10}$$

where $\eta_i(\Omega) = \frac{1}{2}\beta_i \left(\Omega/c_i\right)^2 a_i$ (see Appendix C.2)[4]. Thus, the relation between the input and output state vectors for a nonlinear layer i can be expressed by $\boldsymbol{\mathcal{U}}_{i+1}^{(1)}(d_i,\Omega) = \boldsymbol{\mathcal{T}}_i^{(1)}(\Omega)\boldsymbol{\mathcal{U}}_i^{(1)}(d_{i-1},\Omega)$, where a first-order transfer matrix $\boldsymbol{\mathcal{T}}_i^{(1)}(\Omega) = \boldsymbol{\mathcal{D}}_{i,i+1}^{(1)}(\Omega)\boldsymbol{\mathcal{P}}_i^{(1)}(\Omega)$ for a single layer is obtained by combining first-order discontinuity and propagation matrices ($i = 1,\ldots,M$),

$$\boldsymbol{\mathcal{T}}_i^{(1)}(\Omega) = \begin{pmatrix} \mathcal{D}_{i,11}^2 e^{-2j\frac{\Omega}{c_i}a_i} & \mathcal{D}_{i,12}^2 e^{2j\frac{\Omega}{c_i}a_i} & 2\mathcal{D}_{i,11}\mathcal{D}_{i,12} & 0 & 0 \\ \mathcal{D}_{i,12}^2 e^{-2j\frac{\Omega}{c_i}a_i} & \mathcal{D}_{i,11}^2 e^{2j\frac{\Omega}{c_i}a_i} & 2\mathcal{D}_{i,11}\mathcal{D}_{12} & 0 & 0 \\ \mathcal{D}_{i,11}\mathcal{D}_{i,12} e^{-2j\frac{\Omega}{c_i}a_i} & \mathcal{D}_{i,11}\mathcal{D}_{i,12} e^{2j\frac{\Omega}{c_i}a_i} & \mathcal{D}_{i,11}^2 + \mathcal{D}_{i,12}^2 & 0 & 0 \\ \left(\mathcal{D}_{i,41}(\Omega) + \eta_i(\Omega)\mathcal{D}_{i,11}\right) e^{-2j\frac{\Omega}{c_i}a_i} & \left(\mathcal{D}_{i,41}(\Omega) + \eta_i(\Omega)\mathcal{D}_{i,12}\right) e^{2j\frac{\Omega}{c_i}a_i} & -\mathcal{D}_{i,43}(\Omega) & \mathcal{D}_{i,11} e^{-2j\frac{\Omega}{c_i}a_i} & \mathcal{D}_{i,12} e^{2j\frac{\Omega}{c_i}a_i} \\ \left(-\mathcal{D}_{i,41}(\Omega) + \eta_i(\Omega)\mathcal{D}_{i,12}\right) e^{-2j\frac{\Omega}{c_i}a_i} & \left(-\mathcal{D}_{i,41}(\Omega) + \eta_i(\Omega)\mathcal{D}_{i,11}\right) e^{2j\frac{\Omega}{c_i}a_i} & \mathcal{D}_{i,43}(\Omega) & \mathcal{D}_{i,12} e^{-2j\frac{\Omega}{c_i}a_i} & \mathcal{D}_{i,11} e^{2j\frac{\Omega}{c_i}a_i} \end{pmatrix} \tag{8.11}$$

so that the complete first-order transfer matrix, describing the reflection and transmission processes of a nonlinear multilayered structure, is easily obtained as the product of matrices from successive layers $\boldsymbol{\mathcal{T}}^{(1)}(\Omega) = \prod_{i=0}^{M-1} \boldsymbol{\mathcal{T}}_{M-i}^{(1)}(\Omega)$, leading to a relation between the input and the output state vectors as,

$$\boldsymbol{\mathcal{U}}_{M+1}^{(1)}(L,\Omega) = \boldsymbol{\mathcal{T}}^{(1)}(\Omega)\boldsymbol{\mathcal{U}}_1^{(1)}(0,\Omega) \tag{8.12}$$

where $x = 0$ and $x = L$ correspond to the transmitter and receiver positions, respectively.

As in the linear case, the resulting system for a through-transmission configuration can be solved by specifying the boundary conditions. First, the incident wave is modeled by a purely linear forward prescribed displacement, whose associated boundary condition involves the continuity of displacement at the left boundary $x = 0$,

$$\begin{aligned} u_0^{(0),f}(0,\Omega) &= u_1^{(0),f}(0,\Omega) + u_1^{(0),b}(0,\Omega) \\ 0 &= u_1^{(1),f}(0,\Omega) + u_1^{(1),b}(0,\Omega) \end{aligned} \tag{8.13}$$

where $u_0^{(0),f}(0,\Omega)$ is the Fourier transform of the incident monochromatic wave. On the other hand, the first-order contribution to the nonlinear wave response is obtained by modeling the receiver as a semi-infinite layer, whose boundary condition is expressed by the radiation energy condition [209] as,

$$\begin{aligned} u_{M+1}^{(0),b}(L,\Omega) &= 0 \\ u_{M+1}^{(1),b}(L,\Omega) &= 0 \end{aligned} \tag{8.14}$$

[4]Note that the result provided by Yun *et al.* [208] in Equations (24)-(25) seems to be erroneous. It is indeed intuitively obvious that the nonlinear properties β_i will not explicitly appear in the lower-right terms of the first-order propagation matrix.

Inserting Equations (8.13) and (8.14) into Equation (8.12) leads to,

$$\begin{bmatrix} \left(u_{M+1}^{(0),f}(L,\Omega)\right)^2 \\ 0 \\ 0 \\ u_{M+1}^{(1),f}(L,\Omega) \\ 0 \end{bmatrix} = \boldsymbol{\mathcal{T}}^{(1)}(\Omega) \begin{bmatrix} \left(u_1^{(0),f}(0,\Omega)\right)^2 \\ \left(u_0^{(0),f}(0,\Omega) - u_1^{(0),f}(0,\Omega)\right)^2 \\ u_1^{(0),f}(0,\Omega) \cdot \left(u_0^{(0),f}(0,\Omega) - u_1^{(0),f}(0,\Omega)\right) \\ u_1^{(1),f}(0,\Omega) \\ -u_1^{(1),f}(0,\Omega) \end{bmatrix} \tag{8.15}$$

with,

$$\boldsymbol{\mathcal{T}}^{(1)}(\Omega) = \begin{pmatrix} \mathcal{T}_{11}^{(1)}(\Omega) & \mathcal{T}_{12}^{(1)}(\Omega) & \mathcal{T}_{13}^{(1)}(\Omega) & 0 & 0 \\ \mathcal{T}_{21}^{(1)}(\Omega) & \mathcal{T}_{22}^{(1)}(\Omega) & \mathcal{T}_{23}^{(1)}(\Omega) & 0 & 0 \\ \mathcal{T}_{31}^{(1)}(\Omega) & \mathcal{T}_{32}^{(1)}(\Omega) & \mathcal{T}_{33}^{(1)}(\Omega) & 0 & 0 \\ \mathcal{T}_{41}^{(1)}(\Omega) & \mathcal{T}_{42}^{(1)}(\Omega) & \mathcal{T}_{43}^{(1)}(\Omega) & \mathcal{T}_{44}^{(1)}(\Omega) & \mathcal{T}_{45}^{(1)}(\Omega) \\ \mathcal{T}_{51}^{(1)}(\Omega) & \mathcal{T}_{52}^{(1)}(\Omega) & \mathcal{T}_{53}^{(1)}(\Omega) & \mathcal{T}_{54}^{(1)}(\Omega) & \mathcal{T}_{55}^{(1)}(\Omega) \end{pmatrix} \tag{8.16}$$

where the $\mathcal{T}_{ij}^{(1)}(\Omega)$ denote the elements of the first-order transfer matrix $\boldsymbol{\mathcal{T}}^{(1)}(\Omega)$. A careful inspection of this matrix enables us to relate its 19 non-zero elements to only 5 independent elements, namely $\mathcal{T}_{11}^{(1)}(\Omega)$, $\mathcal{T}_{12}^{(1)}(\Omega)$, $\mathcal{T}_{41}^{(1)}(\Omega)$, $\mathcal{T}_{42}^{(1)}(\Omega)$, and $\mathcal{T}_{43}^{(1)}(\Omega)$. A thorough derivation of those identities is provided in Appendix C.3. As a result, the first-order transfer matrix $\boldsymbol{\mathcal{T}}^{(1)}(\Omega)$ can be rewritten as,

$$\boldsymbol{\mathcal{T}}^{(1)}(\Omega) = \begin{pmatrix} \mathcal{T}_{11}^{(1)}(\Omega) & \mathcal{T}_{12}^{(1)}(\Omega) & 2\sqrt{\mathcal{T}_{11}^{(1)}(\Omega)\mathcal{T}_{12}^{(1)}(\Omega)} & 0 & 0 \\ \mathcal{T}_{12}^{(1)}(-\Omega) & \mathcal{T}_{11}^{(1)}(-\Omega) & 2\sqrt{\mathcal{T}_{11}^{(1)}(-\Omega)\mathcal{T}_{12}^{(1)}(-\Omega)} & 0 & 0 \\ \sqrt{\mathcal{T}_{11}^{(1)}(\Omega)\mathcal{T}_{12}^{(1)}(-\Omega)} & \sqrt{\mathcal{T}_{11}^{(1)}(-\Omega)\mathcal{T}_{12}^{(1)}(\Omega)} & \sqrt{\mathcal{T}_{11}^{(1)}(\Omega)\mathcal{T}_{11}^{(1)}(-\Omega)} + \sqrt{\mathcal{T}_{12}^{(1)}(\Omega)\mathcal{T}_{12}^{(1)}(-\Omega)} & 0 & 0 \\ \mathcal{T}_{41}^{(1)}(\Omega) & \mathcal{T}_{42}^{(1)}(\Omega) & \mathcal{T}_{43}^{(1)}(\Omega) & \sqrt{\mathcal{T}_{11}^{(1)}(2\Omega)} & \sqrt{\mathcal{T}_{12}^{(1)}(2\Omega)} \\ \mathcal{T}_{42}^{(1)}(-\Omega) & \mathcal{T}_{41}^{(1)}(-\Omega) & \mathcal{T}_{43}^{(1)}(-\Omega) & \sqrt{\mathcal{T}_{12}^{(1)}(-2\Omega)} & \sqrt{\mathcal{T}_{11}^{(1)}(-2\Omega)} \end{pmatrix} \tag{8.17}$$

Hence, the first-order contribution to the nonlinear wave displacement at the receiver position L, in terms of that at the transmitter position, is found by solving Equation (8.15) as,

$$\begin{aligned} u_{M+1}^{(1),f}(L,\Omega) = & \left(\frac{\mathcal{T}_{11}^{(1)}(-\Omega)\left(\mathcal{T}_{41}^{(1)}(\Omega)\left(\sqrt{\mathcal{T}_{11}^{(1)}(-2\Omega)} - \sqrt{\mathcal{T}_{12}^{(1)}(-2\Omega)}\right) + \mathcal{T}_{42}^{(1)}(-\Omega)\left(\sqrt{\mathcal{T}_{11}^{(1)}(2\Omega)} - \sqrt{\mathcal{T}_{12}^{(1)}(2\Omega)}\right)\right)}{\left(\sqrt{\mathcal{T}_{11}^{(1)}(-\Omega)} - \sqrt{\mathcal{T}_{12}^{(1)}(-\Omega)}\right)^2 \left(\sqrt{\mathcal{T}_{11}^{(1)}(-2\Omega)} - \sqrt{\mathcal{T}_{12}^{(1)}(-2\Omega)}\right)} \right. \\ & + \frac{\mathcal{T}_{12}^{(1)}(-\Omega)\left(\mathcal{T}_{42}^{(1)}(\Omega)\left(\sqrt{\mathcal{T}_{11}^{(1)}(-2\Omega)} - \sqrt{\mathcal{T}_{12}^{(1)}(-2\Omega)}\right) + \mathcal{T}_{41}^{(1)}(-\Omega)\left(\sqrt{\mathcal{T}_{11}^{(1)}(2\Omega)} - \sqrt{\mathcal{T}_{12}^{(1)}(2\Omega)}\right)\right)}{\left(\sqrt{\mathcal{T}_{11}^{(1)}(-\Omega)} - \sqrt{\mathcal{T}_{12}^{(1)}(-\Omega)}\right)^2 \left(\sqrt{\mathcal{T}_{11}^{(1)}(-2\Omega)} - \sqrt{\mathcal{T}_{12}^{(1)}(-2\Omega)}\right)} \\ & \left. - \frac{\sqrt{\mathcal{T}_{11}^{(1)}(-\Omega)\mathcal{T}_{12}^{(1)}(-\Omega)}\left(\mathcal{T}_{43}^{(1)}(\Omega)\left(\sqrt{\mathcal{T}_{11}^{(1)}(-2\Omega)} - \sqrt{\mathcal{T}_{12}^{(1)}(-2\Omega)}\right) + \mathcal{T}_{43}^{(1)}(-\Omega)\left(\sqrt{\mathcal{T}_{11}^{(1)}(2\Omega)} - \sqrt{\mathcal{T}_{12}^{(1)}(2\Omega)}\right)\right)}{\left(\sqrt{\mathcal{T}_{11}^{(1)}(-\Omega)} - \sqrt{\mathcal{T}_{12}^{(1)}(-\Omega)}\right)^2 \left(\sqrt{\mathcal{T}_{11}^{(1)}(-2\Omega)} - \sqrt{\mathcal{T}_{12}^{(1)}(-2\Omega)}\right)} \right) \left(u_0^{(0),f}(0,\Omega)\right)^2 \\ = & \mathcal{H}^{(1)}(\Omega)\left(u_0^{(0),f}(0,\Omega)\right)^2 \end{aligned} \tag{8.18}$$

where, in the end, $\mathcal{H}^{(1)}(\Omega)$ is simply a complex scalar number, which depends both on the frequency and twice the frequency of the incident wave. As expected, this first-order contribution depends upon the square of the linear displacement at the transmitter position. Finally, the nonlinear wave displacement can be obtained as the sum of the zero-order contribution plus the first-order contribution,

$$\begin{aligned} u^{f}_{M+1}(L,\Omega) &= u^{(0),f}_{M+1}(L,\Omega) + u^{(1),f}_{M+1}(L,\Omega) \\ &= \mathcal{H}^{(0)}(\Omega) u^{(0),f}_{0}(0,\Omega) + \mathcal{H}^{(1)}(\Omega) \left(u^{(0),f}_{0}(0,\Omega) \right)^2 \end{aligned} \tag{8.19}$$

where $\mathcal{H}^{(0)}(\Omega)$ is the complex scalar number obtained in Equation (6.14) using the TM formalism. Although the NTM formalism relies on physical principles described by a nonlinear partial differential equation, one of its strength is that it provides a solution by solving only linear equations. As can observed, the nonlinear problem has been solved by calculating the first-order contribution to the nonlinear wave displacement and adding it to the zero-order contribution found with the TM formalism (see Equation (8.19)). In addition, it is noteworthy that this formalism could be extended in the same fashion to account for the contributions of third and higher-order harmonics, and/or to second-order nonlinearity ($\delta \neq 0$). However, in those cases, the dimension of the complete higher-order transfer matrix would significantly increase due to the frequency-mixing effects involved in the higher-order harmonics generation (e.g. when fundamental (Ω) and second-order harmonics (2Ω) mixed up, they generate both fundamental $(2\Omega - \Omega)$ and third-order $(\Omega + 2\Omega)$ harmonics).

As for the linear case, the NTM formalism could also be extended to account for material attenuation. Since the mathematics involved in this task is nearly identical to that of the linear case, we do not report it here. Again, this theoretical result is valid for any single continuous-time frequency Ω and any number of layers M. Practical issues are discussed in next section.

8.1.2 Numerical implementation of the NTM formalism

Equation (8.19) suggests that one has to solve both the TM and NTM formalisms to obtain the nonlinear wave displacement. However, one could intuitively expect that the linear TM formalism is a special case of NTM one, and that the first-order transfer matrix $\boldsymbol{\mathcal{T}}^{(1)}(\Omega)$ somehow encompasses the zero-order one $\boldsymbol{\mathcal{T}}^{(0)}(\Omega)$. Indeed, by setting the nonlinear parameters to zero ($\beta_i = 0$, $\forall i$), we can obtain a simplified version of the first-order transfer matrix $\boldsymbol{\mathcal{T}}^{(1)}(\Omega)$ as,

$$\boldsymbol{\mathcal{T}}^{(1)}_{\beta\to 0}(\Omega) = \begin{pmatrix} \mathcal{T}^{(1)}_{11}(\Omega) & \mathcal{T}^{(1)}_{12}(\Omega) & 2\sqrt{\mathcal{T}^{(1)}_{11}(\Omega)\mathcal{T}^{(1)}_{12}(\Omega)} \\ \mathcal{T}^{(1)}_{12}(-\Omega) & \mathcal{T}^{(1)}_{11}(-\Omega) & 2\sqrt{\mathcal{T}^{(1)}_{11}(-\Omega)\mathcal{T}^{(1)}_{12}(-\Omega)} \\ \sqrt{\mathcal{T}^{(1)}_{11}(\Omega)\mathcal{T}^{(1)}_{12}(-\Omega)} & \sqrt{\mathcal{T}^{(1)}_{11}(-\Omega)\mathcal{T}^{(1)}_{12}(\Omega)} & \sqrt{\mathcal{T}^{(1)}_{11}(\Omega)\mathcal{T}^{(1)}_{11}(-\Omega)} + \sqrt{\mathcal{T}^{(1)}_{12}(\Omega)\mathcal{T}^{(1)}_{12}(-\Omega)} \end{pmatrix} \tag{8.20}$$

Solving the two first rows of the simplified underlying system leads to,

$$\left(u_{M+1}^{(0),f}(L,\Omega)\right)^2 = \left(\frac{\det\left(\sqrt{\boldsymbol{\mathcal{T}}_{2\times2}^{(1)}(\Omega)}\right)}{\sqrt{\mathcal{T}_{11}^{(1)}(-\Omega)}-\sqrt{\mathcal{T}_{12}^{(1)}(-\Omega)}}\right)^2 \left(u_0^{(0),f}(0,\Omega)\right)^2 = \left(\mathcal{H}^{(0)}(\Omega)\right)^2 \left(u_0^{(0),f}(0,\Omega)\right)^2 \tag{8.21}$$

where $\boldsymbol{\mathcal{T}}_{2\times2}^{(1)}(\Omega)$ denotes the 2×2 sub-matrix encompassed by $\boldsymbol{\mathcal{T}}_{\beta\to0}^{(1)}(\Omega)$ or $\boldsymbol{\mathcal{T}}^{(1)}(\Omega)$. As can be observed, this equation delivers the square of the zero-order contribution to the nonlinear wave displacement at the receiver position L, in terms of that at the transmitter position. In other words, this equation represents a quadratic form of the solution obtained with the TM formalism in Equation (6.14), when considering the following identities (details can be found in Appendix C.4):

$$\sqrt{\mathcal{T}_{11}^{(1)}(\Omega)} = \mathcal{T}_{11}^{(0)}(\Omega) = \mathcal{T}_{22}^{(0)}(-\Omega) \quad , \quad \sqrt{\mathcal{T}_{12}^{(1)}(\Omega)} = \mathcal{T}_{12}^{(0)}(\Omega) = \mathcal{T}_{21}^{(0)}(-\Omega) \tag{8.22}$$

Consequently, one could obtain both the zero-order and first-order contributions to the nonlinear wave displacement from Equation (8.15). Therefore, in practice, the solution to the NTM formalism expressed in Equation (8.19) can be solved straightforwardly without implementing previously the TM formalism. In addition, the latter can be simultaneously recovered by setting the nonlinear parameters to zero. Despite the fact that the TM formalism is a special case of the NTM one is somehow trivial, it is nevertheless interesting to mention how the first-order transfer matrix encompass the zero-order one,

$$\boldsymbol{\mathcal{T}}^{(1)}(\Omega) = \begin{pmatrix} \left\{\boldsymbol{\mathcal{T}}^{(0)}(\Omega)\right\}^2 & \mathbf{0} \\ \boldsymbol{\mathcal{T}}_{NL}^{(1)}(\Omega) & \boldsymbol{\mathcal{T}}^{(0)}(2\Omega) \end{pmatrix} \tag{8.23}$$

where $\left\{\boldsymbol{\mathcal{T}}^{(0)}(\Omega)\right\}^2$ and $\boldsymbol{\mathcal{T}}_{NL}^{(1)}(\Omega)$ denote the quadratic form of the zero-order transfer matrix $\boldsymbol{\mathcal{T}}^{(0)}(\Omega)$ and the sub-matrix of $\boldsymbol{\mathcal{T}}^{(1)}(\Omega)$ that explicitly contains the nonlinear terms, respectively. Although this representation has no practical implication (since we showed that it is not necessary to first solve the linear problem), it may have conceptual implication at the time of understanding how transfer matrices of higher-orders will grow up. Hence, it is to expect that a second-order transfer matrix will contain (1) a cubic form of the zero-order transfer matrix, (2) a mixed matrix made of a quadratic form of the zero-order transfer matrix combined with the nonlinear terms of first-order β, (3) a zero-order transfer matrix evaluated at thrice the frequency, and finally (4) a matrix that explicitly contains the nonlinear terms of second-order β^2 (and eventually δ if one considers nonlinearity of second-order).

As discussed in Section 6.3, in practice, the input signal is usually a purely linear band-pass ultrasonic signal at a relatively low center frequency containing a wide range of frequencies around it, and is commonly represented as a digital time-domain signal. Thus, the incident wave $u_0^{(0)}(0, nT)$ at the transmitter position $x = 0$ can be represented as a discrete-time signal with N samples ($n = 0, \ldots, N-1$). By applying the DFT, a discrete frequency representation with components $u_0^{(0)}(0, \omega_k)$ ($k = 0, \ldots, N-1$) can be obtained. The NTM formalism can then be applied to each frequency bin, in order to obtain the zero-order and first-order contributions for the receiver side components, denoted by $u_{M+1}^{(0)}(L, \omega_k)$ and $u_{M+1}^{(1)}(L, \omega_k)$, respectively. Finally, by applying the IDFT to both contributions, one can recover the zero-order $u_{M+1}^{(0)}(L, nT)$ and first-order contributions $u_{M+1}^{(1)}(L, nT)$ to the nonlinear wave response $u_{M+1}(L, nT)$ at the receiver position $x = L$. The general scheme of this numerical procedure for M layers is depicted in Figure 8.2.

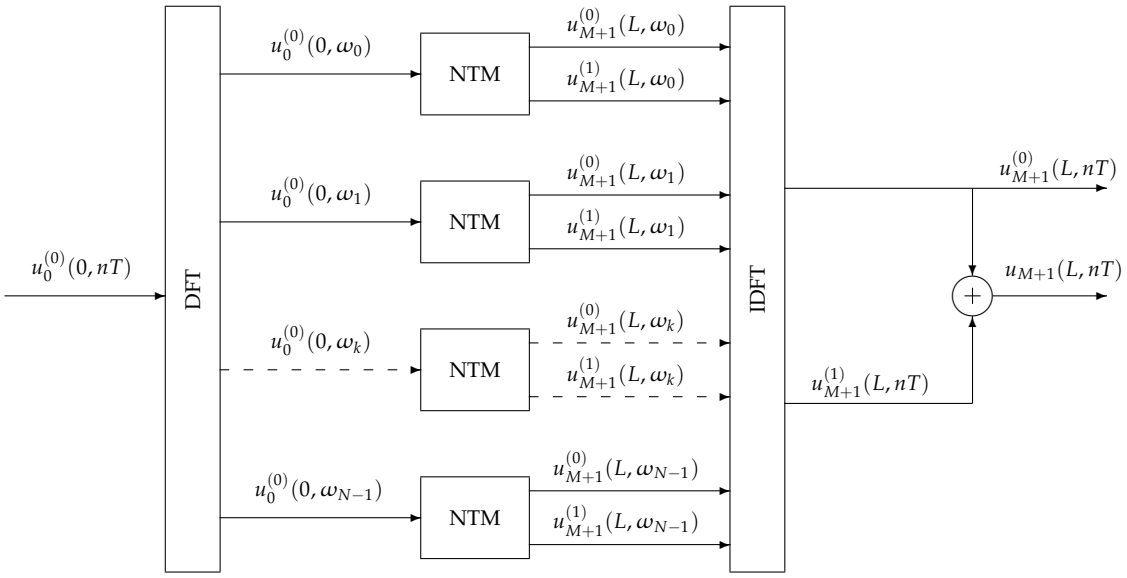

Figure 8.2: *General scheme of the NTM formalism numerical procedure.*

Under this approach, some considerations must be made regarding the Shannon-Nyquist theorem while dealing with nonlinear systems, since a sampling frequency of $F_s/2$ is no more valid. As can be observed in the proposed framework, second harmonics appear at the frequency 2Ω and thus require the consideration of a sampling frequency of at least $F_s = 4F_{max}$ (that is, the input signal must now be a band-limited signal oversampled with a sampling rate of 2) [5].

According to this scheme, the first-order transfer matrix for a single layer (see Equation (8.11)) can be discretized as well as,

$$\boldsymbol{T}_i^{(1)}(\omega_k) \quad = \quad \boldsymbol{\mathcal{T}}_i^{(1)}(\Omega)|_{\Omega=\omega_k F_s} \tag{8.24}$$

[5] In practice, the sampling frequency is usually selected as $F_s \gg 4F_{max}$, so that, even in the nonlinear regime, the proposed framework will not fail.

leading to the following discrete solution,

$$u^{f}_{M+1}(L,\omega_k) \;=\; \mathcal{H}^{(0)}(\omega_k)u_0^{(0),f}(0,\omega_k) + \mathcal{H}^{(1)}(\omega_k)\left[u_0^{(0),f}(0,\omega_k)\right]^2 \tag{8.25}$$

where $\mathcal{H}^{(0)}(\omega_k)$ and $\mathcal{H}^{(1)}(\omega_k)$ implicitly contain the zero-order and first-order contributions to the complete first-order transfer matrix $\boldsymbol{T}_i^{(1)}(\omega_k)$ corresponding to the k^{th}-frequency component. It is worth to point out that each $\boldsymbol{T}_i^{(1)}(\omega_k)$ ($i = 0,\ldots,M-1$, $k = 0,\ldots,N-1$) is a 5×5 matrix of complex numbers, allowing a numerical solution for Equation (8.25). The computational cost of that solution is significantly higher than for the linear case, due to the larger dimension of $\boldsymbol{T}_i^{(1)}(\omega_k)$ and particularly due to the k^{th}-frequency component dependency of the first-order discontinuity matrix $\boldsymbol{D}_{i,i+1}^{(1)}(\omega_k)$. Even though, the NTM formalism allows to handle nonlinear problems in a relatively straightforward and efficient way, especially since only five elements ($\mathcal{T}_{11}^{(1)}(\omega_k)$, $\mathcal{T}_{12}^{(1)}(\omega_k)$, $\mathcal{T}_{41}^{(1)}(\omega_k)$, $\mathcal{T}_{42}^{(1)}(\omega_k)$, and $\mathcal{T}_{43}^{(1)}(\omega_k)$) of the 5×5 complete first-order transfer matrix are really needed to be computed.

8.2 Nonlinear signal modeling approach

In this section, we propose to extend the signal modeling approach described in Chapter 7 to account for constitutive nonlinearity. To this end, the problem of a linear longitudinal ultrasonic wave that propagates through a nonlinear multilayered elastic material is considered. Representing a nonlinear system in terms of signal modeling concepts is generally cumbersome as most of them have been developed for linear systems. Thus, instead of directly solving the nonlinear problem, we propose to compute the first-order contribution to the nonlinear wave displacement separately. Doing so, the through-transmission configuration for the isolated first-order component can be considered as well as a discrete-time linear system. Consequently, the nonlinear multilayered material under investigation can be represented by a pair of transfer functions, which relate the discrete input and output signals, and account for both the zero-order and first-order contributions to the nonlinear wave displacement. As for the NTM formalism, be aware that, under this approach, the input signal must now be a band-limited signal up to $F_s/4$ instead of $F_s/2$ (that is, the input signal must be oversampled with a sampling rate of 2).

8.2.1 Theoretical foundations

Let us consider the four-port network depicted in Figure 8.3. In this figure, the frequency responses $H_i^{(0)}(\omega)$ and $H_i^{(1)}(\omega)$ stand for the intra-layer i propagation of fundamental waves and second harmonics, respectively[6]. Note that $\omega \in [0, 2\pi]$ is the normalized frequency defined in the previous section. The gains $\{G_{t_i}, G_{r_i}, \hat{G}_{t_i}, \hat{G}_{r_i}\}$ characterize the impedance ratios between layers i and $i+1$, according to those defined for the linear case. Additionally, we introduce a further frequency response $H_i^{NL}(\omega)$, which characterizes the contribution of the

[6] As done above for the NTM formalism, the upper index (0) is now assigned to all variables related to the linear signal model, due to the presence of both fundamental waves and second harmonics. For sake of clarity, let us rename those frequency responses as the zero-order and first-order frequency responses.

linear wave component to the second harmonics when accumulating over the propagation path of a layer i. From now on, this frequency response will be called the nonlinear frequency response of a layer i. The negative signs at the nodes stand for the π-phase shifts ($e^{j\pi}$) that suffer the back-propagating components at the layer discontinuities. Be aware that the symbol $*$ denotes a convolution of time-domain signals, which is equivalent to a spectral multiplication. Also note that $X_i^{f,0}(\omega)$ and $X_i^{b,0}(\omega)$ are always $F_s/4$ band-limited signals, that is, $X_i^{j,0}(\omega) = 0$ for $\pi/2 < |\omega| < 3\pi/2, \forall j = f, b$.

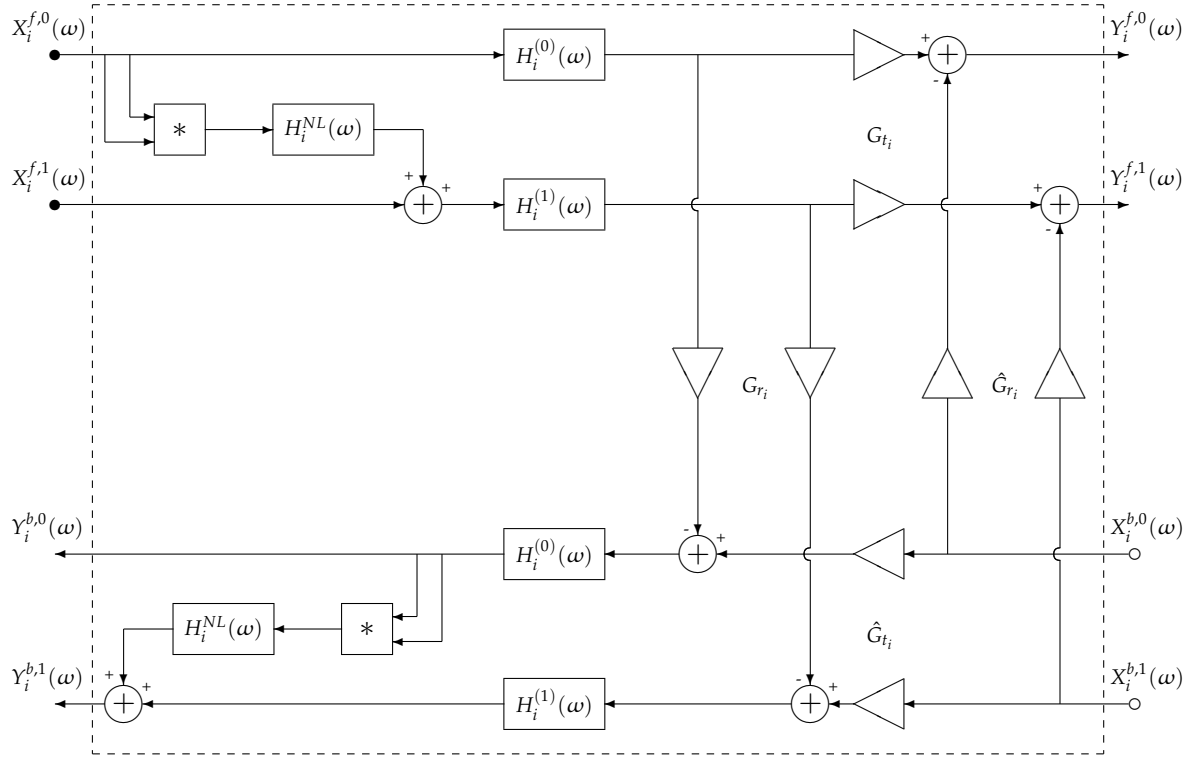

Figure 8.3: *Four-port network for a nonlinear layer unit i.*

According to Figure 8.3, outputs $Y_i^{f,0}(\omega)$, $Y_i^{b,0}(\omega)$, $Y_i^{f,1}(\omega)$, and $Y_i^{b,1}(\omega)$ are obtained from inputs $X_i^{f,0}(\omega)$, $X_i^{b,0}(\omega)$, $X_i^{f,1}(\omega)$, and $X_i^{b,1}(\omega)$ as,

$$\begin{aligned}
Y_i^{f,0}(\omega) &= X_i^{f,0}(\omega)H_i^{(0)}(\omega)G_{t_i} - X_i^{b,0}(\omega)\hat{G}_{r_i} \\
Y_i^{b,0}(\omega) &= X_i^{b,0}(\omega)\hat{G}_{t_i}H_i^{(0)}(\omega) - X_i^{f,0}(\omega)H_i^{(0)}(\omega)G_{r_i}H_i^{(0)}(\omega) \\
Y_i^{f,1}(\omega) &= \left[X_i^{f,1}(\omega) + H_i^{NL}(\omega)\left(X_i^{f,0}(\omega)\right)^2\right]H_i^{(1)}(\omega)G_{t_i} - X_i^{b,1}(\omega)\hat{G}_{r_i} \\
Y_i^{b,1}(\omega) &= X_i^{b,1}(\omega)H_i^{(1)}(\omega)\hat{G}_{t_i} - \left[X_i^{f,1}(\omega) + H_i^{NL}(\omega)\left(X_i^{f,0}(\omega)\right)^2\right]H_i^{(1)}(\omega)G_{r_i}H_i^{(1)}(\omega) \\
&- \left(Y_i^{b,0}(\omega)\right)^2 H_i^{NL}(\omega)
\end{aligned} \tag{8.26}$$

Working through these analytical expressions allows us to write the system in matrix form, with $\boldsymbol{u}_i^{(1)}(\omega) = \left[\left(X_i^{f,0}(\omega)\right)^2 \;\; \left(Y_i^{b,0}(\omega)\right)^2 \;\; X_i^{f,0}(\omega)\cdot Y_i^{b,0}(\omega) \;\; X_i^{f,1}(\omega) \;\; Y_i^{b,1}(\omega)\right]^T$ and

$$\boldsymbol{U}_{i+1}^{(1)}(\omega) = \left[\left(X_{i+1}^{f,0}(\omega) \right)^2 \quad \left(Y_{i+1}^{b,0}(\omega) \right)^2 \quad X_{i+1}^{f,0}(\omega) \cdot Y_{i+1}^{b,0}(\omega) \quad X_{i+1}^{f,1}(\omega) \quad Y_{i+1}^{b,1}(\omega) \right]^T,$$

$$\boldsymbol{U}_{i+1}^{(1)}(\omega) = \begin{pmatrix} \left[\left(G_{t_i} - \frac{G_{r_i}\hat{G}_{r_i}}{\hat{G}_{t_i}} \right) H_i^{(0)}(\omega) \right]^2 & \left[-\frac{\hat{G}_{r_i}}{\hat{G}_{t_i}} \frac{1}{H_i^{(0)}(\omega)} \right]^2 & -2\left(G_{t_i} - \frac{G_{r_i}\hat{G}_{r_i}}{\hat{G}_{t_i}} \right) \frac{\hat{G}_{r_i}}{\hat{G}_{t_i}} & 0 & 0 \\ \left[\frac{G_{r_i}}{\hat{G}_{t_i}} H_i^{(0)}(\omega) \right]^2 & \left[\frac{1}{\hat{G}_{t_i}} \frac{1}{H_i^{(0)}(\omega)} \right]^2 & 2\frac{G_{r_i}}{\hat{G}_{t_i}^2} & 0 & 0 \\ \left(G_{t_i} - \frac{G_{r_i}\hat{G}_{r_i}}{\hat{G}_{t_i}} \right) \frac{G_{r_i}}{\hat{G}_{t_i}} \left(H_i^{(0)}(\omega) \right)^2 & -\frac{\hat{G}_{r_i}}{\hat{G}_{t_i}^2} \frac{1}{\left(H_i^{(0)}(\omega) \right)^2} & \frac{1}{\hat{G}_{t_i}} \left(G_{t_i} - 2\frac{G_{r_i}\hat{G}_{r_i}}{\hat{G}_{t_i}} \right) & 0 & 0 \\ H_i^{NL}(\omega) \left(G_{t_i} - \frac{G_{r_i}\hat{G}_{r_i}}{\hat{G}_{t_i}} \right) H_i^{(1)}(\omega) & -H_i^{NL}(\omega) \frac{\hat{G}_{r_i}}{\hat{G}_{t_i}} \frac{1}{H_i^{(1)}(\omega)} & 0 & \left(G_{t_i} - \frac{G_{r_i}\hat{G}_{r_i}}{\hat{G}_{t_i}} \right) H_i^{(1)}(\omega) & -\frac{\hat{G}_{r_i}}{\hat{G}_{t_i}} \frac{1}{H_i^{(1)}(\omega)} \\ H_i^{NL}(\omega) \frac{G_{r_i}}{\hat{G}_{t_i}} H_i^{(1)}(\omega) & H_i^{NL}(\omega) \frac{1}{\hat{G}_{t_i}} \frac{1}{H_i^{(1)}(\omega)} & 0 & \frac{G_{r_i}}{\hat{G}_{t_i}} H_i^{(1)}(\omega) & \frac{1}{\hat{G}_{t_i}} \frac{1}{H_i^{(1)}(\omega)} \end{pmatrix} \boldsymbol{U}_i^{(1)}(\omega) \tag{8.27}$$

where the output vector of layer i corresponds to the input vector of layer $i+1$, i.e. $\boldsymbol{U}_{i+1}^{(1)}(\omega) = \left[\left(Y_i^{f,0}(\omega) \right)^2 \quad \left(X_i^{b,0}(\omega) \right)^2 \quad Y_i^{f,0}(\omega) \cdot X_i^{b,0}(\omega) \quad Y_i^{f,1}(\omega) \quad X_i^{b,1}(\omega) \right]^T$. The four-port network of layer i may be written as $\boldsymbol{U}_{i+1}^{(1)}(\omega) = \boldsymbol{T}_i^{(1)}(\omega)\boldsymbol{U}_i^{(1)}(\omega)$, and thus the total frequency response of the nonlinear material is obtained as $\boldsymbol{T}^{(1)}(\omega) = \prod_{i=0}^{M-1} \boldsymbol{T}_{M-i}^{(1)}(\omega)$. Consequently, the relation between the input and output state vectors of the complete nonlinear multilayered system $\boldsymbol{U}_{M+1}^{(1)}(\omega) = \boldsymbol{T}^{(1)}(\omega)\boldsymbol{U}_1^{(1)}(\omega)$ can be written as,

$$\begin{bmatrix} \left(X_{M+1}^{f,0}(\omega) \right)^2 \\ \left(Y_{M+1}^{b,0}(\omega) \right)^2 \\ X_{M+1}^{f,0}(\omega) \cdot Y_{M+1}^{b,0}(\omega) \\ X_{M+1}^{f,1}(\omega) \\ Y_{M+1}^{b,0}(\omega) \end{bmatrix} = \begin{pmatrix} T_{11}^{(1)}(\omega) & T_{12}^{(1)}(\omega) & T_{13}^{(1)}(\omega) & 0 & 0 \\ T_{21}^{(1)}(\omega) & T_{22}^{(1)}(\omega) & T_{23}^{(1)}(\omega) & 0 & 0 \\ T_{31}^{(1)}(\omega) & T_{32}^{(1)}(\omega) & T_{33}^{(1)}(\omega) & 0 & 0 \\ T_{41}^{(1)}(\omega) & T_{42}^{(1)}(\omega) & T_{43}^{(1)}(\omega) & T_{44}^{(1)}(\omega) & T_{45}^{(1)}(\omega) \\ T_{51}^{(1)}(\omega) & T_{52}^{(1)}(\omega) & T_{53}^{(1)}(\omega) & T_{54}^{(1)}(\omega) & T_{55}^{(1)}(\omega) \end{pmatrix} \begin{bmatrix} \left(X_1^{f,0}(\omega) \right)^2 \\ \left(Y_1^{b,0}(\omega) \right)^2 \\ X_1^{f,0}(\omega) \cdot Y_1^{b,0}(\omega) \\ X_1^{f,1}(\omega) \\ Y_1^{b,0}(\omega) \end{bmatrix} \tag{8.28}$$

where the $T_{ij}^{(1)}(\omega)$ are the matrix elements of the total frequency response of first-order $\boldsymbol{T}^{(1)}(\omega)$. The boundary conditions for that through-transmission configuration (Equations (8.13)-(8.14)) can be represented as well in terms of signal theory concepts, as depicted in Figure 8.4.

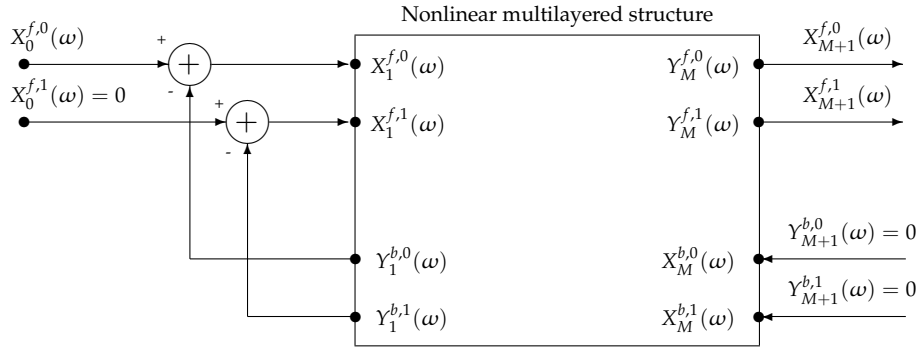

Figure 8.4: *Nonlinear multilayered structure and boundary conditions in terms of signal modeling principles.*

From this figure, the boundary conditions are set in the four-port connections as,

$$\begin{array}{rcl} X_1^{f,0}(\omega) & = & X_0^{f,0}(\omega) - Y_1^{b,0}(\omega) \\ X_1^{f,1}(\omega) & = & -Y_1^{b,1}(\omega) \\ Y_{M+1}^{b,0}(\omega) & = & 0 \\ Y_{M+1}^{b,1}(\omega) & = & 0 \end{array} \tag{8.29}$$

Inserting Equations (8.29) into Equation (8.28) leads to,

$$\begin{bmatrix} \left(X_{M+1}^{f,0}(\omega)\right)^2 \\ 0 \\ 0 \\ X_{M+1}^{f,1}(\omega) \\ 0 \end{bmatrix} = \boldsymbol{T}^{(1)}(\omega) \begin{bmatrix} \left(X_1^{f,0}(\omega)\right)^2 \\ \left(X_0^{f,0}(\omega) - X_1^{f,0}(\omega)\right)^2 \\ X_1^{f,0}(\omega) \cdot \left(X_0^{f,0}(\omega) - X_1^{f,0}(\omega)\right) \\ X_1^{f,1}(\omega) \\ -X_1^{f,1}(\omega) \end{bmatrix} \tag{8.30}$$

It is worth to point out the similarity of this equation with Equation (8.15). This point will be further discussed in the next section.

8.2.2 Bridging the nonlinear signal modeling and the physics

In section 7.2, we already examined the ties between the signal model parameters (gains and frequency responses) and the mechanical features (impedance ratios and material damping). Here, we can also link the nonlinear signal model parameters (nonlinear and first-order frequency responses) to the nonlinear mechanical features (constitutive nonlinearity of the material). For this purpose, let us first replace the gains and zero-order frequency responses from Equations (7.9), (7.10), and (7.14) into Equation (8.27). Hence,

$$\boldsymbol{T}_i^{(1)}(\omega) = \begin{pmatrix} D_{i,11}^2 G_{\alpha_i}^2 e^{-2j\omega m_i} & D_{i,12}^2 G_{\alpha_i}^{-2} e^{2j\omega m_i} & 2D_{i,11}D_{i,12} & 0 & 0 \\ D_{i,12}^2 G_{\alpha_i}^2 e^{-2j\omega m_i} & D_{i,11}^2 G_{\alpha_i}^{-2} e^{2j\omega m_i} & 2D_{i,11}D_{i,12} & 0 & 0 \\ D_{i,11}D_{i,12} G_{\alpha_i}^2 e^{-2j\omega m_i} & D_{i,11}D_{i,12} G_{\alpha_i}^{-2} e^{2j\omega m_i} & D_{i,11}^2 + D_{i,12}^2 & 0 & 0 \\ D_{i,11} H_i^{NL}(\omega) H_i^{(1)}(\omega) & D_{i,12} H_i^{NL}(\omega) \dfrac{1}{H_i^{(1)}(\omega)} & 0 & D_{i,11} H_i^{(1)}(\omega) & D_{i,12} \dfrac{1}{H_i^{(1)}(\omega)} \\ D_{i,12} H_i^{NL}(\omega) H_i^{(1)}(\omega) & D_{i,11} H_i^{NL}(\omega) \dfrac{1}{H_i^{(1)}(\omega)} & 0 & D_{i,12} H_i^{(1)}(\omega) & D_{i,11} \dfrac{1}{H_i^{(1)}(\omega)} \end{pmatrix} \tag{8.31}$$

with

$$D_{i,11} = \frac{1}{2}\left(1 + \frac{Z_i}{Z_{i+1}}\right) \quad , \quad D_{i,12} = \frac{1}{2}\left(1 - \frac{Z_i}{Z_{i+1}}\right) \tag{8.32}$$

Again, this matrix shows a high similarity with that of Equation (8.11). Let us now assume that the first-order frequency response $H_i^{(1)}(\omega)$ of Figure 8.3 has the form,

$$H_i^{(1)}(\omega) = \left(H_i^{(0)}(\omega)\right)^2 = G_{\alpha_i}^2 e^{-2j\omega m_i} = G_{\alpha_i} H_i^{(0)}(2\omega) \tag{8.33}$$

From this equation, it results that the output of a signal passing through $H_i^{(1)}(\omega)$ is equivalent to that of a signal passing twice through $H_i^{(0)}(\omega)$. In other words, the second harmonics attenuate and suffer a delay that is twice that of the fundamental waves. Alternatively, we can view $H_i^{(1)}(\omega)$ as a spectral expansion of $H_i^{(0)}(\omega)$ (in the same way as in a digital sampling frequency interpolation) by a factor of 2, which once again supports the fact that $X_i^{j,0}(\omega)$ must be band-limited to $F_s/4$, $\forall j = f, b$. By sampling this frequency response, we obtain:

$$H_i^{(1)}(\omega) \;=\; e^{2\alpha_i a_i} e^{-2j\omega \frac{F_s a_i}{c_i}} \;=\; e^{-2j\frac{\Omega}{c_i^*} a_i}\Big|_{\Omega=\omega F_s} \tag{8.34}$$

On the other hand, let us consider that a sampled version of the nonlinear frequency response $H_i^{NL}(\omega)$ of Figure 8.3 may have the form,

$$H_i^{NL}(\omega) \;=\; \frac{1}{2}\beta_i \left(\frac{F_s \omega}{c_i}\right)^2 a_i \;=\; \eta_i(\Omega)\big|_{\Omega=\omega F_s} \tag{8.35}$$

that is, the nonlinear filter response $H_i^{NL}(\omega)$ has a quadratic response, which accounts for the nonlinear accumulation over a distance a_i corresponding to the thickness of a layer i, and corresponds to a discrete-time version of the nonlinear term in Equation (8.10). As expected, this response cannot be represented by means of a LTI filter. Nevertheless, one could intent to approximate it by using such a filter for the frequency region of interest. Inserting Equations (8.34)-(8.35) into Equation (8.31) leads to,

$$\boldsymbol{T}_i^{(1)}(\omega) \;=\; \begin{pmatrix} D_{i,11}^2 e^{-2j\omega\frac{F_s a_i}{c_i^*}} & D_{i,12}^2 e^{2j\omega\frac{F_s a_i}{c_i^*}} & 2D_{i,11}D_{i,12} & 0 & 0 \\ D_{i,12}^2 e^{-2j\omega\frac{F_s a_i}{c_i^*}} & D_{i,11}^2 e^{2j\omega\frac{F_s a_i}{c_i^*}} & 2D_{i,11}D_{12} & 0 & 0 \\ D_{i,11}D_{i,12} e^{-2j\omega\frac{F_s a_i}{c_i^*}} & D_{i,11}D_{i,12} e^{2j\omega\frac{F_s a_i}{c_i^*}} & D_{i,11}^2 + D_{i,12}^2 & 0 & 0 \\ \eta_i(\omega F_s) D_{i,11} e^{-2j\omega\frac{F_s a_i}{c_i^*}} & \eta_i(\omega F_s) D_{i,12} e^{2j\omega\frac{F_s a_i}{c_i^*}} & 0 & D_{i,11} e^{-2j\omega\frac{F_s a_i}{c_i^*}} & D_{i,12} e^{2j\omega\frac{F_s a_i}{c_i^*}} \\ \eta_i(\omega F_s) D_{i,12} e^{-2j\omega\frac{F_s a_i}{c_i^*}} & \eta_i(\omega F_s) D_{i,11} e^{2j\omega\frac{F_s a_i}{c_i^*}} & 0 & D_{i,12} e^{-2j\omega\frac{F_s a_i}{c_i^*}} & D_{i,11} e^{2j\omega\frac{F_s a_i}{c_i^*}} \end{pmatrix} \tag{8.36}$$

and, as can be observed, Equation (8.24) (i.e. a discrete version of Equation (8.11)) is approximately recovered. However, a few elements of the discrete transfer matrix of first-order $\boldsymbol{T}_i^{(1)}(\omega_k)$ for a nonlinear layer i, namely $\mathcal{D}_{i,41}(\omega_k)$ and $\mathcal{D}_{i,43}(\omega_k)$, do not explicitly arise in the nonlinear signal modeling approach. This issue, along with the solution to Equation (8.30), are discussed in next section.

8.2.3 Discussion

Let us first explain why some elements present in the NTM formalism are difficult to integrate in the nonlinear signal model. A careful inspection of Equations (C.1)-(C.4) shows that the nonlinear frequency-dependent elements $\mathcal{D}_{i,41}(\Omega)$ and $\mathcal{D}_{i,43}(\Omega)$ of the first-order discontinuity matrix naturally arise from the transmission conditions at a nonlinear interface, and more concretely from the formulation of the stress continuity. Indeed, the latter

depends upon the derivative of the displacement for the first-order perturbation solution and the square of the derivative for the zero-order solution. Both of them contribute to elements involving the square of the linear displacement, and thus to $\mathcal{D}_{i,41}(\Omega)$. In addition, the square of the derivative for the zero-order solution contributes to elements involving cross-terms, and thus to $\mathcal{D}_{i,43}(\Omega)$. Unfortunately, such concepts as derivatives of propagating distance-dependent amplitudes are hardly expressible in terms of a network-like model[7].

Nevertheless, we could argue that those nonlinear terms arising from the first-order discontinuity matrix might be negligible in comparison to the ones arising from the first-order propagation matrix (which are both phenomenologically and from a signal perspective well-defined), and could thus further solve the nonlinear contribution to this system. To this end, making use of the physical interpretations done in the previous section enables us to rewrite the total frequency response of first-order $\boldsymbol{T}^{(1)}(\omega)$ as,

$$\boldsymbol{T}^{(1)}(\omega) = \begin{pmatrix} T_{11}^{(1)}(\omega) & T_{12}^{(1)}(\omega) & 2\sqrt{T_{11}^{(1)}(\omega)T_{12}^{(1)}(\omega)} & 0 & 0 \\ T_{12}^{(1)}(-\omega) & T_{11}^{(1)}(-\omega) & 2\sqrt{T_{11}^{(1)}(-\omega)T_{11}^{(1)}(-\omega)} & 0 & 0 \\ \sqrt{T_{11}^{(1)}(\omega)T_{12}^{(1)}(-\omega)} & \sqrt{T_{11}^{(1)}(-\omega)T_{12}^{(1)}(\omega)} & \sqrt{T_{11}^{(1)}(\omega)T_{11}^{(1)}(-\omega)} + \sqrt{T_{12}^{(1)}(\omega)T_{12}^{(1)}(-\omega)} & 0 & 0 \\ T_{41}^{(1)}(\omega) & T_{42}^{(1)}(\omega) & T_{43}^{(1)}(\omega) & \sqrt{T_{11}^{(1)}(2\omega)} & \sqrt{T_{12}^{(1)}(2\omega)} \\ T_{42}^{(1)}(-\omega) & T_{41}^{(1)}(-\omega) & T_{43}^{(1)}(-\omega) & \sqrt{T_{12}^{(1)}(-2\omega)} & \sqrt{T_{11}^{(1)}(-2\omega)} \end{pmatrix} \tag{8.37}$$

Again, this matrix shows a high similarity with that of Equation (8.17). Details on the relations between the elements of that matrix can be found in Appendix D. Thus, the first-order contribution to the nonlinear system can be found by solving Equation (8.30) as,

$$\begin{aligned} X_{M+1}^{(1),f}(\omega) &= \left(\frac{T_{11}^{(1)}(-\omega)\left(T_{41}^{(1)}(\omega)\left(\sqrt{T_{11}^{(1)}(-2\omega)} - \sqrt{T_{12}^{(1)}(-2\omega)}\right) + T_{42}^{(1)}(-\omega)\left(\sqrt{T_{11}^{(1)}(2\omega)} - \sqrt{T_{12}^{(1)}(2\omega)}\right)\right)}{\left(\sqrt{T_{11}^{(1)}(-\omega)} - \sqrt{T_{12}^{(1)}(-\omega)}\right)^2 \left(\sqrt{T_{11}^{(1)}(-2\omega)} - \sqrt{T_{12}^{(1)}(-2\omega)}\right)} \right. \\ &+ \frac{T_{12}^{(1)}(-\omega)\left(T_{42}^{(1)}(\omega)\left(\sqrt{T_{11}^{(1)}(-2\omega)} - \sqrt{T_{12}^{(1)}(-2\omega)}\right) + T_{41}^{(1)}(-\omega)\left(\sqrt{T_{11}^{(1)}(2\omega)} - \sqrt{T_{12}^{(1)}(2\omega)}\right)\right)}{\left(\sqrt{T_{11}^{(1)}(-\omega)} - \sqrt{T_{12}^{(1)}(-\omega)}\right)^2 \left(\sqrt{T_{11}^{(1)}(-2\omega)} - \sqrt{T_{12}^{(1)}(-2\omega)}\right)} \\ &- \left. \frac{\sqrt{T_{11}^{(1)}(-\omega)T_{12}^{(1)}(-\omega)}\left(T_{43}^{(1)}(\omega)\left(\sqrt{T_{11}^{(1)}(-2\omega)} - \sqrt{T_{12}^{(1)}(-2\omega)}\right) + T_{43}^{(1)}(-\omega)\left(\sqrt{T_{11}^{(1)}(2\omega)} - \sqrt{T_{12}^{(1)}(2\omega)}\right)\right)}{\left(\sqrt{T_{11}^{(1)}(-\omega)} - \sqrt{T_{12}^{(1)}(-\omega)}\right)^2 \left(\sqrt{T_{11}^{(1)}(-2\omega)} - \sqrt{T_{12}^{(1)}(-2\omega)}\right)} \right) \left(X_0^{(0),f}(\omega)\right)^2 \\ &= H^{(1)}(\omega)\left(X_0^{(0),f}(\omega)\right)^2 \end{aligned} \tag{8.38}$$

As for the zero-order contribution, the obtained theoretical result is unfortunately not straightforwardly implementable, since the derivation of the total frequency response of first-order $\boldsymbol{T}^{(1)}(\omega) = \prod_{i=0}^{M-1} \boldsymbol{T}_{M-i}^{(1)}(\omega)$ is cumbersome.

To get around it, we could, on the one hand, apply the formulation proposed in Equation (7.17). However, it is far from obvious that a product of matrices with the form of the

[7]Let us consider for instance a simple function $f(x) = A(x)e^{-jx}$ to highlight this fact. By deriving this function with respect to x, on could obtain $f'(x) = -jA(x)e^{-jx} + A'(x)e^{-jx} = -jf(x) + A'(x)e^{-jx}$. In analogy to our case, we see that the derivative can be expressed by means of the function itself multiplied by some constant plus an additional term. The first term can easily be represented in a circuit model, whereas the second one is relatively complex to predict, foremost depending on the form that takes $A(x)$.

frequency response of first-order $\boldsymbol{T}_i^{(1)}(\omega)$ could be expressed as a sum of matrices that retains the same form, especially due to the asymmetry of the exponential elements, which prohibits the use of the distributive property (in any case, such an approach would suffer of a drastic lake of efficiency, worse than the NTM formalism). On the other hand, we can take advantage of the digital signal model proposed in Section 7.3 to address the solution to the first-order contribution. Indeed, part of the elements of the total frequency response of first-order $\boldsymbol{T}^{(1)}(\omega)$ can be expressed in terms of the z-domain polynomial expressions $P_M(G_\alpha, z)$ and $Q_M(G_\alpha, z)$ obtained in Equation (7.21). Nonetheless, we encounter a further problem in our intent to express the nonlinear frequency response $H_i^{NL}(\omega)$ as a discrete-time transfer function in the z-domain. Thus, we provide here a possible *procedure to follow*, rather than a straightforward and rigorous solution. This solution is subjected to find a discrete-time transfer function $H_i^{NL}(z)$ in the z-domain, whose frequency response approximates sufficiently well that proposed in Equation (8.35) for the frequency range of interest. Indeed, a frequency response with a quadratic response could be approximated (e.g by a Taylor series expansion), but it is not clear how to determine the type and order of the approximation. Substituting Equations (7.9)-(7.10), $H_i^{(0),D}(z)$, $H_i^{(1),D}(z)$ and $H_i^{NL}(z)$ in the first-order layer matrix of Equation (8.27) yields a z-transformed layer matrix of first-order $\boldsymbol{T}_i^{(1)}(z)$ which can be rewritten in terms of z-domain polynomial expressions as,

$$\boldsymbol{T}_i^{(1)}(z) = \left(\frac{G_{\alpha_i} z^{-m_i}}{1+G_{r_i}}\right)^2 \begin{pmatrix} 1 & G_{r_i}^2 G_{\alpha_i}^{-4} z^{4m_i} & 2G_{r_i} G_{\alpha_i}^{-2} z^{2m_i} & 0 & 0 \\ G_{r_i}^2 & G_{\alpha_i}^{-4} z^{4m_i} & 2G_{r_i} G_{\alpha_i}^{-2} z^{2m_i} & 0 & 0 \\ G_{r_i} & G_{r_i} G_{\alpha_i}^{-4} z^{4m_i} & \left(1+G_{r_i}^2\right) G_{\alpha_i}^{-2} z^{2m_i} & 0 & 0 \\ (1+G_{r_i})\, H_i^{NL}(z) & G_{r_i}(1+G_{r_i})\, H_i^{NL}(z) G_{\alpha_i}^{-4} z^{4m_i} & 0 & 1+G_{r_i} & G_{r_i}(1+G_{r_i})\, G_{\alpha_i}^{-4} z^{4m_i} \\ G_{r_i}(1+G_{r_i})\, H_i^{NL}(z) & (1+G_{r_i})\, H_i^{NL}(z) G_{\alpha_i}^{-4} z^{4m_i} & 0 & G_{r_i}(1+G_{r_i}) & (1+G_{r_i})\, G_{\alpha_i}^{-4} z^{4m_i} \end{pmatrix} \tag{8.39}$$

It can be proven that the product of M-layers, $\boldsymbol{T}^{(1)}(z) = \prod_{i=0}^{M-1} \boldsymbol{T}_{M-i}^{(1)}(z)$, has the following general form,

$$\boldsymbol{T}^{(1)}(z) = \left(\prod_{i=1}^{M} \frac{G_{\alpha_i} z^{-m_i}}{1+G_{r_i}}\right)^2 \begin{pmatrix} P_M^2(G_\alpha, z) & \left(\prod_{i=1}^{M} G_{\alpha_i}^{-4} z^{4m_i}\right) Q_M^2(G_\alpha^{-1}, z^{-1}) & 2\left(\prod_{i=1}^{M} G_{\alpha_i}^{-2} z^{2m_i}\right) P_M(G_\alpha, z) Q_M(G_\alpha^{-1}, z^{-1}) & 0 & 0 \\ Q_M^2(G_\alpha, z) & \left(\prod_{i=1}^{M} G_{\alpha_i}^{-4} z^{4m_i}\right) P_M^2(G_\alpha^{-1}, z^{-1}) & 2\left(\prod_{i=1}^{M} G_{\alpha_i}^{-2} z^{2m_i}\right) P_M(G_\alpha^{-1}, z^{-1}) Q_M(G_\alpha, z) & 0 & 0 \\ P_M(G_\alpha, z) Q_M(G_\alpha, z) & \left(\prod_{i=1}^{M} G_{\alpha_i}^{-4} z^{4m_i}\right) P_M(G_\alpha^{-1}, z^{-1}) Q_M(G_\alpha^{-1}, z^{-1}) & \left(\prod_{i=1}^{M} G_{\alpha_i}^{-2} z^{2m_i}\right) \left(P_M(G_\alpha, z) P_M(G_\alpha^{-1}, z^{-1}) + Q_M(G_\alpha, z) Q_M(G_\alpha^{-1}, z^{-1})\right) & 0 & 0 \\ R_M(G_\alpha, z) & \left(\prod_{i=1}^{M} G_{\alpha_i}^{-4} z^{4m_i}\right) S_M(G_\alpha^{-1}, z^{-1}) & 2\left(\prod_{i=1}^{M} G_{\alpha_i}^{-2} z^{2m_i}\right) V_M(G_\alpha, z) & \left(\prod_{i=1}^{M} (1+G_{r_i})\right) P_M(G_\alpha^2, z^2) & \left(\prod_{i=1}^{M} (1+G_{r_i}) G_{\alpha_i}^{-4} z^{4m_i}\right) Q_M(G_\alpha^{-2}, z^{-2}) \\ S_M(G_\alpha, z) & \left(\prod_{i=1}^{M} G_{\alpha_i}^{-4} z^{4m_i}\right) R_M(G_\alpha^{-1}, z^{-1}) & 2\left(\prod_{i=1}^{M} G_{\alpha_i}^{-2} z^{2m_i}\right) V_M(G_\alpha^{-1}, z^{-1}) & \left(\prod_{i=1}^{M} (1+G_{r_i})\right) Q_M(G_\alpha^2, z^2) & \left(\prod_{i=1}^{M} (1+G_{r_i}) G_{\alpha_i}^{-4} z^{4m_i}\right) P_M(G_\alpha^{-2}, z^{-2}) \end{pmatrix} \tag{8.40}$$

where the functions $R_M(G_\alpha, z)$, $S_M(G_\alpha, z)$ and $V_M(G_\alpha, z)$ stand for polynomials which are built up following a recursive scheme,

$$\begin{aligned}
R_M(G_\alpha, z) &= (1+G_{r_M})H_M^{NL}(z)\left(P_{M-1}^2(G_\alpha, z) + G_{r_M}G_{\alpha_M}^{-4}z^{4m_M}Q_{M-1}^2(G_\alpha, z)\right) \\
&+ (1+G_{r_M})\left(R_{M-1}(G_\alpha, z) + G_{r_M}G_{\alpha_M}^{-4}z^{4m_M}S_{M-1}(G_\alpha, z)\right) \\
S_M(G_\alpha, z) &= (1+G_{r_M})H_M^{NL}(z)\left(G_{r_M}P_{M-1}^2(G_\alpha, z) + G_{\alpha_M}^{-4}z^{4m_M}Q_{M-1}^2(G_\alpha, z)\right) \\
&+ (1+G_{r_M})\left(G_{r_M}R_{M-1}(G_\alpha, z) + G_{\alpha_M}^{-4}z^{4m_M}S_{M-1}(G_\alpha, z)\right) \\
V_M(G_\alpha, z) &= 2(1+G_{r_M})H_M^{NL}(z)\left(G_{\alpha_M}^2 z^{-2m_M}P_{M-1}(G_\alpha, z)Q_{M-1}(G_\alpha^{-1}, z^{-1})\right. \\
&+ \left. G_{r_M}G_{\alpha_M}^{-2}z^{2m_M}P_{M-1}(G_\alpha^{-1}, z^{-1})Q_{M-1}(G_\alpha, z)\right)
\end{aligned} \tag{8.41}$$

with $R_1(G_\alpha, z) = (1+G_{r_1})H_1^{NL}(z)$, $S_1(G_\alpha, z) = G_{r_1}(1+G_{r_1})H_1^{NL}(z)$ and $V_1(G_\alpha, z) = 0$. Note that these polynomials incorporate all the nonlinear effects of the multilayered structure. Once the boundary conditions are considered (Equation (8.29)), the first-order contribution to the nonlinear displacement leads to,

$$\begin{aligned}
X_{M+1}^{f_r(1)}(z) &= \frac{1}{D^{(1)}(z)}\left(\prod_{i=1}^{M}\frac{G_{\alpha_i}^2 z^{-2m_i}}{1+G_{r_i}}\right)\left(\left(\left(\prod_{i=1}^{M}G_{\alpha_i}^{-4}z^{4m_i}\right)P_M(G_\alpha^{-2}, z^{-2}) - Q_M(G_\alpha^2, z^2)\right)\right. \\
&\cdot \left(R_M(G_\alpha, z)P_M^2(G_\alpha^{-1}, z^{-1}) + S_M(G_\alpha^{-1}, z^{-1})Q_M^2(G_\alpha, z) - 2V_M(G_\alpha, z)P_M(G_\alpha, z)Q_M(G_\alpha^{-1}, z^{-1})\right) \\
&+ \left(P_M(G_\alpha^2, z^2) - \left(\prod_{i=1}^{M}G_{\alpha_i}^{-4}z^{4m_i}\right)Q_M(G_\alpha^{-2}, z^{-2})\right) \\
&\cdot \left.\left(S_M(G_\alpha, z)P_M^2(G_\alpha^{-1}, z^{-1}) + R_M(G_\alpha^{-1}, z^{-1})Q_M^2(G_\alpha, z) - 2V_M(G_\alpha^{-1}, z^{-1})P_M(G_\alpha, z)Q_M(G_\alpha^{-1}, z^{-1})\right)\right)\left(X_0^{f_r(0)}(z)\right)^2
\end{aligned} \tag{8.42}$$

where the denominator of first-order $D^{(1)}(z)$ can be written as,

$$D^{(1)}(z) = \left(P_M(G_\alpha^{-1}, z^{-1}) - \left(\prod_{i=1}^{M}G_{\alpha_i}^2 z^{-2m_i}\right)Q_M(G_\alpha, z)\right)^2\left(P_M(G_\alpha^{-2}, z^{-2}) - \left(\prod_{i=1}^{M}G_{\alpha_i}^2 z^{-2m_i}\right)Q_M(G_\alpha^2, z^2)\right) \tag{8.43}$$

Note that the form that takes Equation (8.42) complicates drastically a possible simplification. Nonetheless, the underlying structure of the polynomial expressions suggests that the discrete-time transfer function of first-order $H^{(1)}(z)$ could be alternatively written as,

$$H^{(1)}(z) = \frac{\prod_{i=1}^{M}G_{t_i}H_i^{NL}(z)G_{\alpha_i}^2 z^{-2m_i}\Delta_M(G_\alpha, z)}{\left(P_M(G_\alpha^{-1}, z^{-1}) - \left(\prod_{i=1}^{M}G_{\alpha_i}^2 z^{-2m_i}\right)Q_M(G_\alpha, z)\right)^2\left(P_M(G_\alpha^{-2}, z^{-2}) - \left(\prod_{i=1}^{M}G_{\alpha_i}^2 z^{-2m_i}\right)Q_M(G_\alpha^2, z^2)\right)} \tag{8.44}$$

where $\Delta_M(G_\alpha, z)$ is a polynomial which accounts for the complex interactions between $P_M(G_\alpha, z)$, $Q_M(G_\alpha, z)$, $R_M(G_\alpha, z)$, $S_M(G_\alpha, z)$, and $V_M(G_\alpha, z)$. In that case, $H^{(1)}(z)$ seems to be a delayed pole-zero filter with sparse coefficients. As intuitively expected, the numerator now consists of a delay and attenuation that are twice that of the linear case, and the first-order denominator incorporates a quadratic form of the zero-order one. Finally, it is worth to point out that the nonlinear terms ($H_i^{NL}(z)$ and $\Delta_M(G_\alpha, z)$) only arise in the numerator.

If one could compute such a filter, the nonlinear wave displacement could be written as the sum of the zero-order and first-order contributions,

$$X_{M+1}^{f,(1)}(z) \quad = \quad H^{(0)}(z)X_0^{f,(0)}(z) + H^{(1)}(z)\left(X_0^{f,(0)}(z)\right)^2 \tag{8.45}$$

In addition, such a filter would preserve all the advantages of the zero-order one discussed in Section 7.4. As for the NTM formalism, be aware that the zero-order contribution $H^{(0)}(z)$ could be directly obtained by solving the two first rows of the underlying system to Equation (8.40), without solving previously the linear digital signal model described in Equation (7.25).

Although the nonlinear signal model, in its proposed form, lacks of practical applicability, future research in that vein should be conducted, especially on the feasibility of expressing the nonlinear frequency response as a discrete-time transfer function, along with the possibility of representing some missing physical components into the network diagram. Finding a discrete-time transfer function $H^{NL}(z)$ that approximates the nonlinear frequency response $H^{NL}(\omega)$ for the frequency range of interest in a suitable way is particularly challenging, since the resulting filter of first-order $H^{(1)}(z)$ might have a huge number of coefficients.

Part III

METHODOLOGY

9 Materials and methods

This chapter describes the materials and methods used over the course of this work. In Section 9.1, we introduce the context and motivation of the employed materials, describing their potential and the challenge that they offer from a structural viewpoint, and focusing on the requirement of efficient ultrasonic NDE techniques to identify their damage mechanisms. Section 9.2 presents the specimens tested and the experimental configuration used to analyze them. Finally, Section 9.3 provides the theoretical background for the inverse problem and system identification approaches used for characterizing the pathologies of the introduced specimens.

9.1 Context and motivation

The aim of this section is twofold: First, we describe the potential of the chosen *multilayered*[1] materials, focusing on the challenge that they offer from both a structural and socio-economical point of view. Secondly, we emphasize the structural complexity of those materials, and thus the need of reliable ultrasonic NDE techniques to (i) characterize their mechanical properties, and (ii) monitor their structural health for damage assessment or quality control purposes.

9.1.1 Carbon fiber-reinforced polymers

Fiber-reinforced polymers (FRP), such as carbon and and glass fiber-reinforced polymers (CFRP and GFRP) and the promising self-reinforced polymers (e.g. isotactic polypropylene),

[1]Note that the chosen materials are not necessarily layered by nature. Under layered materials, we understand that the presence of the material in the experimental environment (e.g. water, embedded system) will produce bounded interfaces, so that the overall system could be considered as layered.

are high performance and competitive advanced materials with a growing applicability due to their extreme strength-to-weight and rigidity-to-weight efficiency ratios. Continued improvements in the development of cost-effective manufacturing methods and development of low-cost fibers and resin materials have increased the use of composites for aerospace and automotive products. More recently, those materials originally developed for aeronautical purposes, have presented themselves as a feasible alternative to design civil engineer structures (e.g. buildings and bridges) [228, 229, 230], for which lightweight, high strength, and construction time exigences are converted into critical design aspects (see Figure 9.1). Nonetheless, the ever expanding structural applications of composites expose them to various environmental and loading conditions, causing higher probability of induced (micro-) damage in the material. Depending upon the material and laminate stacking sequence, the induced damage generally consists of a complex and interacting global ensemble of discrete damage modes, which may finally lead to failure [231].

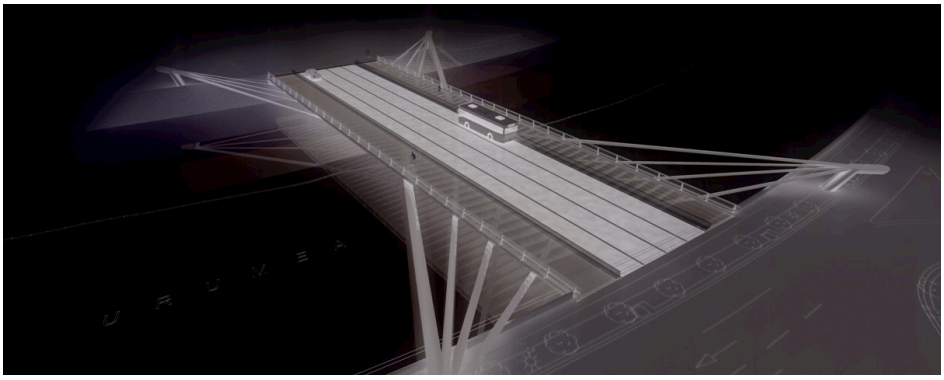

Figure 9.1: *Example of a novel infrastructural application involving an all-composite bridge made of carbon and glass fiber-reinforced polymers.*[2]

Hence, despite their outstanding characteristics, the application of FRP has been limited by the problem of damage tolerance [232]. Indeed, one of the major drawbacks associated with composite materials is their vulnerability to impact damage (e.g. hail, bird strike, tool drop, or runway stones during taxiing), which usually occurs in the phase of manufacturing, service or maintenance. Composite laminates do not allow significant energy dissipation by plastic deformation, and this leads to weaker through-the-thickness than in-plane mechanical properties for the structure [233]. As a consequence, during an impact the fibers absorb part of the energy and distribute some of the load through the laminate thickness, leading to a quite complex three-dimensional damage pattern consisting of delamination, sub-surface matrix cracking, fiber-matrix debonding and fiber fracture [234]. During the structure's life cycle, the occurrence of two kinds of impact loading has to be regarded: Low and high-velocity impacts. The latter are easy to detect, since high-speed impactors interact with the material for a short time period, and thus lead to evident external and visible damage. In

[2]Courtesy from colleagues of the Nondestructive Evaluation Laboratory, which were awarded with the Silver Medal at the 1^{st} Structural Engineering Design International Contest for their *all-composite* bridge proposal (2008).

contrast, the former can cause significant internal degradation that remains invisible from the front surface, with inner damage spreading over a wider area than that starting from the contact point of the impactor. Generally[3], three phases of impact damages can be roughly identified: Initially, matrix cracks are generated by shear or tensile stresses mainly in the intermediate or back-wall layers. Then, delaminations grow from the crack tips between layers of different orientation (the higher the orientation mismatch, the larger the delaminations). They typically appear in regular patterns producing altogether a three-dimensional spiral staircase. Finally, as the impact energy is further increased, fiber breakage appear initially on the surface of the sample and may propagate into intermediate layers, leading in some cases to total perforation of the laminate [235] (see Figure 9.2). All these complex failure mechanisms can in turn induce severe degradation to the residual macro-scale mechanical properties of the material, while remaining invisible from the surface [236].

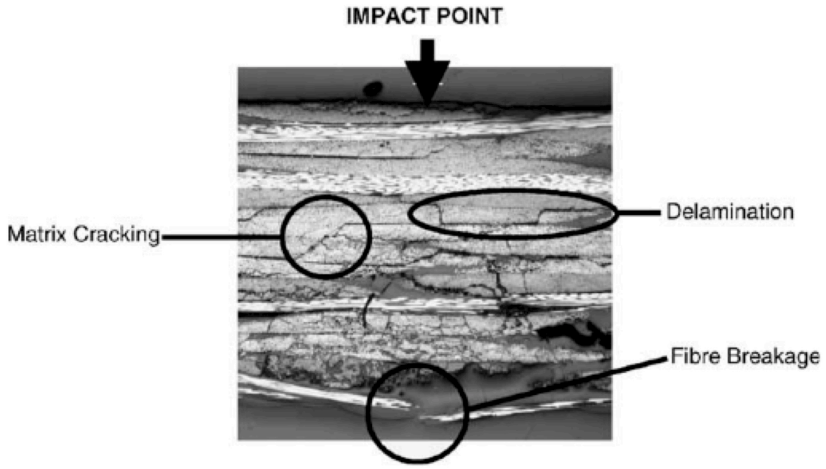

Figure 9.2: *Impact damage mechanisms (identified in micrographs*[4]).

Due to their excellent properties for light-weight structures, FRP's are employed in many types of industry (e.g. aircraft, wind turbine, rotor-machinery, automobile) which, however, implies cyclic loading in operation. Cyclic mechanical loading usually induces many matrix cracks, fibre-matrix debonding, delamination, and fibre fracture, accompanied by stiffness degradation of the composite before ultimate failure [238]. Investigations on CFRP under fatigue loads have shown an occurrence of several consecutive damage mechanisms, and strong correlations have been found between stiffness reduction and development of defects, thus allowing grouping of different damage mechanisms into three characteristic phases during fatigue life. Under dynamic tension, phase I is characterized by the appearance of matrix cracks and fibre-matrix interfacial cracking forms parallel to the fibre orientation mainly in the off-axis layers which encounter the highest stress non-parallel to the reinforcement direction. These intralaminar cracks through the whole thickness of the

[3]That is, for cross-ply and quasi-isotropic laminates, since this family of stacking sequence is the most used in the industry (the damage propagation pattern could be slightly different for angle-ply and asymmetric laminates.)

[4]Reproduced from Mitrevski *et al.* [237].

layers reduce the stiffness of the affected plies. After saturation of these transverse cracks, phase II is marked by the formation of longitudinal cracks in the vicinity of the areas where transverse cracks predominate. As a consequence, delimitation formation can be observed at the intersections of transverse and longitudinal cracks. Phase III initiates the final damage mode, longitudinal splitting, where entire parts of the 0°-plies are detached from the remaining laminate due to longitudinal cracks and delamination growth. In addition, both transverse and longitudinal cracks lead to fibre fracture due to stress concentrations at the crack tips or induced shear stress due to kinking at crack bridging zones, leading to a steep decline in stiffness until final failure [239, 240]. Compressive fatigue loading involves a slightly different damage formation (e.g. initial stiffness loss is smaller) which cannot be classified in these three phases. Due to the combination of damage mechanisms induced by tension and compression, reversed loads result in faster material degradation and earlier ultimate failure at comparable stresses [241].

Alternatively, industrial concern has tended to focus on the problem of *fatigue after impact damage* (also known as post-impact fatigue damage), which has led to the development of the 'no-growth' concept [242]. As a consequence, the fatigue behavior of composites after impact damage has been investigated extensively. However, the effect of damage growth mechanisms on post-impact fatigue response is not fully understood and an effective damage-tolerance methodology of post-impact composites has not been established yet [243]. Experimental investigations have given raise to the following observations: Impact damage leads to shorter life, especially in the compressive loading regime where buckling in the vicinity of delaminations occurs [244]. Under compressive fatigue loading, impact damage leads to growth of the delaminations opposite to the impact site in loading direction and transverse to it as well as to buckling of strips around the damage zone [245]. Larger accumulated damage in the impact zone leads to a stronger decrease of lifetime and rapid delamination growth is usually an indication of imminent failure [246]. Many damage and life prediction models based on the observation of crack densities and stiffness degradation have been developed. However, industrial applications usually preclude simple (destructive) determination of these parameters in operation. Therefore, early and proactive detection of the embedded damages are important from both the mechanical performance and the safety perspectives. Thus, to guarantee a reliable level of performance, NDE techniques have been developed to measure the material stiffness properties and discriminate between the different failure mechanisms.

Over the past decades, several inspection techniques for monitoring mechanically induced damage in composites have been proposed, such as cracks counting, structural health monitoring (SHM) via embedded piezo-actuators, acoustic emission (AE), liquid penetrants, X-ray radiography, thermography, and fiber-optic and fiber Bragg gratings (FBG's). Nonetheless, most of these techniques undergo several restrictions. The application of crack counting is limited to transparent and unpainted materials [247]. SHM uses variations in

electric sensitivity, and thus requires conductive materials [239]. On the other hand, AE involves the detection of energy released by the material under stress during cracking events. This method is very efficient for monitoring structures under in-service conditions, but does not provide a precise identification of the size, shape and location of flaws, especially in anisotropic materials such as composites. In addition, environmental noise can easily mask the measurements [248]. Liquid penetrants are used to infiltrate flaws and damaged components, but can usually only resolve damage connected to the surface. Alternatively, X-ray radiography can be adopted for the through-thickness detection of defects. However, the resulting image is usually difficult to interpret, particularly in the presence of numerous superimposed damage planes that hinder the locating of different delaminated and cracked layers. Thermographic inspection is based on the analysis of thermal patterns induced either by heating the specimen or by applying a mechanical oscillatory load. This technique is sensitive to delaminations, but is not able to provide information on the through-thickness location of the flaw [235].

Ultrasound is currently one of the most frequently used and accepted NDE techniques that are proven to provide effective and reliable results at relatively low cost [14]. The usually adopted normal incidence technique [249, 250] is most sensitive to flaws that lie parallel to the surface (delaminations). In contrast, matrix cracks, lying perpendicularly to the surface, and fiber fracture paths are difficult to detect because they do not offer a wide enough reflecting surface. By orienting the transducer at an angle to the tested surface, in order to acquire the energy backscattered from damage, transverse cracks running parallel to the fiber direction can be detected [251, 252]. Thus, for a complete non-destructive evaluation of the induced damage, more that one measurement technique is usually required. As a drawback, it is worth to mention that standard ultrasound techniques usually imply the use of an immersion bath and often double-sided access which hampers *in-situ* applications. However, recent improvements could tend to overcome this limitation. For instance, Chen *et al.* [245] proposed an emerging ultrasonic imaging technology based on acoustography, which resulted in a new measurement system that could be used for *in-situ* imaging of impact damage in composite specimens during long-term fatigue tests. In another related proposal, Matikas [149] proposed the use of advanced nondestructive evaluation techniques such as ultrasonic microscopy (i.e the propagation of surface acoustic waves (SAW)) and nonlinear acoustics to characterize the damage and monitor in real-time aging structural components used in aerospace applications. More recently, Rheinfurth *et al.* [239] experimentally explored the applicability of air-coupled Lamb waves to monitoring mechanically induced fatigue damage in composites. This non-contact technique enabled them to perform measurements without unclamping of the specimens out of the servo-hydraulic testing machine used for cyclic loading. These encouraging results motivated us to further explore classical and emerging ultrasound laboratory techniques to monitor the mechanical properties of damaged composites, in order to enhance our understanding of this complex material and to think up possible improvements for in-service conditions assessment.

9.1.2 Tissue-equivalent materials

Tissue engineering is a continuously growing field that aims at developing biological substitutes that restore, maintain, or improve tissue function [253]. Tissue engineering is therefore of crucial importance to study aspects of cell physiology and pathology, and is also geared toward the realization of implantable tissues. The majority of tissue-engineered materials are grown by culturing cells from a patient or donor, then seeding them onto an appropriate scaffold, and finally stimulating them to form specific tissues that mimic the complex 3D structures and biological functions of natural tissues [254]. This approach has successfully been applied to deliver tissue-engineered materials for treating cartilage, skin, cornea, and bone defects. Currently, most of the research focuses almost exclusively on the biological aspects of tissue culture at the detriment of manufacturing and product realization issues. Thus, there is still a lack of commercial and clinical viability for many tissue-engineered materials, mainly due to poor process control and monitoring in tissue production [255].

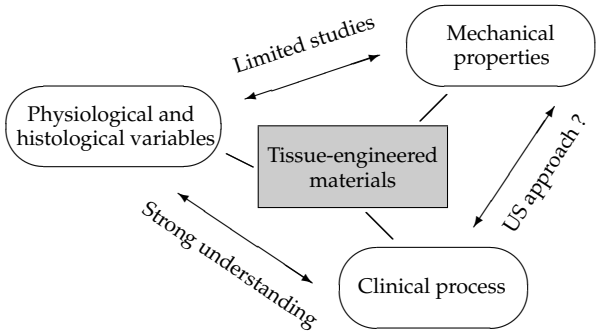

Figure 9.3: *Overview of the ties between engineering and biology at the time of studying tissue culture.*

Typically, the process of tissue engineering involves several stages including cell culture, scaffold production, bioreactor system, and final product preservation, whereas the main monitoring requirement is to assess the culture's progress during production, and to relate it to such factors as cells number and structure. Current available analysis methods for evaluating tissue formation are histology and direct mechanical measurements. Although these methods provide valuable information for cell phenotype and proliferation, as well as mechanical characterization such as compressive moduli of scaffolds, they are not suitable for continuous monitoring of the sample *in vivo* as they destroy cells and scaffolds (i.e. extracellular matrix). In addition, these methods require large sample numbers for statistical analysis, since the different samples are prepared and measured at varying times, and the tissue growth usually undergoes high deviation between specimens [256]. Thus, tissue engineers need a real-time system that could non-invasively monitor tissue growth and consequent scaffold degradation in the same specimen over time. Nevertheless, only a few attempts to develop such methods have been reported.

Among the process monitoring techniques that have been applied to move tissue engineering forward, it is worth to mention well-established nonlinear optical techniques, such as the multi-photon excitation microscopy or second harmonic imaging. The former ones have been used for noninvasive *in vivo* characterization and imaging of sub-cellular properties [257, 258]. However, the potential of these techniques greatly depends on practical factors, such as the engineering of high-quality probes (in terms of reproducibility) and strategies to incorporate the monitoring tools in the cell-culture environment. Alternatively, other imaging methods, such as magnetic resonance imaging and computed tomography, provide scaffold structural information, but are limited to deliver only morphological information, and the imaging reconstruction procedures are quite extensive [259].

In tissue engineering, biodegradable polymer scaffolds are used to deliver cells and regenerate tissue as well as provide temporary mechanical support. In principle, the degradation rate of the scaffold should match the rate of tissue formation, hence the degradation behavior of a scaffold has a critical impact on the long-term performance of a tissue-engineered construct *in vivo*. Among them, hydrogels (e.g. agarose, fibrin, collagen) have been extensively used as scaffold materials because of their viscoelastic characteristics, biocompatibility, the simplicity of their fabrication and their high water content, providing a highly hydrated environment to the embedded cells, which is permeable for oxygen, nutrients and cellular wastes [260, 261]. However, a major limitation of hydrogel-based scaffolds is that their mechanical properties are usually significantly weaker than those of natural tissues [262].

A novel spherical indentation method for characterizing the viscoelastic properties of hydrogel-based constructs under cell culture conditions has been proposed [263]. A sensitive long working distance microscope was used for measuring the time-dependent deformation of thin circular hydrogel membranes under a constant load. Then, the elastic modulus as a function of time could be determined by making use of a theory of viscoelasticity for large deformation. It is noteworthy that this kind of measurements can be performed for specimens that are fully immersed in solution and at elevated temperatures with no risk of damaging the instrumentation. However, the method is only applicable to relatively thin and large membranes and has to evoke specially designed sample holders to minimize any clamping stress applied on the hydrogel membranes. Hence, Yang *et al.* [264] developed an alternative indentation system, ideally sample holder-free, combined with a high-resolution imaging technique (optical coherence tomography) for *in situ* characterization of thick specimens in a nondestructive fashion and under sterile conditions.

Alternatively, ultrasound may have potential to provide real-time assessment of the macroscopic construct properties, since the intrinsic ultrasonic properties are directly related to the structure and composition of the tissue under investigation. The use of ultrasound for monitoring properties of tissue-engineered products has received only little attention until recently. Among this few works, Hattori *et al.* [265] developed a new evaluation system for articular cartilage, which revealed that ultrasound analysis is able to quantitatively evaluate

cartilage degeneration and cartilage repair. In a similar work, their ultrasonic evaluation system was capable of judging the success or failure of cartilage regeneration procedures, and therefore suggested that ultrasound is a valuable tool for diagnosis of cartilage regeneration [266]. In another related work, Rice *et al.* [267] performed high-frequency ultrasound measurements in pulse-echo mode to determine the propagation and backscatter properties of cartilage specimens. Then, they compare the ultrasonic properties (velocity and attenuation) obtained at different time steps during the process evolution with mechanical tests and biochemical properties of the matrix. More recently, Kreitz *et al.* [268] demonstrated the potential of ultrasound for quantitative *in vitro* evaluation of tissue development in fibrin-based tissue-engineered structures. These encouraging results motivated us to further develop ultrasound-based system under culturing environment to monitor the alteration of the mechanical properties of the constructs over time, in order to enhance our understanding of the bioprocess of tissue-engineered products.

9.1.3 Bone damage assessment

Osteoporosis has been recognized as a *silent epidemic* in our aging Western societies, which affects approximately 40% of women and 20% of men over the age of 50 years. In addition, the aging of the population in most countries will increase the overall burden of osteoporosis tremendously. By 2050, the worldwide incidence of hip fracture is projected to increase by 240% in women and 310% in men, and the related costs in Europe are expected to increase to €76.7 billion based on the foreseen changes in the demography[5]. However, osteoporosis still focuses less public attention compared to other diseases that are less frequent, and thus urgent scientific developments in early diagnostics are of paramount importance to manage this future health challenge successfully.

The consequences of osteoporosis on life quality and on the health care expenses are certainly not negligible. This skeletal disease results from a period of asymptotic bone loss and hence reduced bone strength (see Figure 9.4), whose subsequent degradation leads to a severe increase in fracture risk. Therefore, understanding the underlying determinants for bone strength and developing technologies for optimal prediction of fracture risk is of the utmost importance. Nowadays, the standard approach for the diagnosis of osteoporosis and fracture risk prediction is to use ionizing dual X-ray absorptiometry (DXA) in order to assess bone mineral density (BMD). Growing evidence indicates (1) that low BMD, however, is not the sole factor accounting for the fracture risk [269], and (2) that BMD alone cannot explain therapeutic benefits of anti-resorptive agents in treating osteoporosis [270]. Indeed, BMD explains about 70-75% of the variability in strength, while the remaining variability could be due to cumulative and synergistic effects of other factors such as bone microstructure, architecture, measurement artefacts and the state of remodeling. Although osteoporosis results from a complex incompletely understood set of physiological and biochemical processes, the clinical manifestation (fracture or deformation) is purely mechanical [271].

[5]National Osteoporosis Foundation, http://www.iofbonehealth.org.

This has triggered studies for alternative diagnostic modalities showing capacity to reach a complete quantitative assessment of bone quality beyond BMD. The term 'bone quality' summarizes the aspects of bone that contribute to fracture risk but are not encompassed by BMD measurements. It comprises a number of variables such as bone microstructure, bone matrix constituents (organic and mineral phases), tissue material properties or prevalence of micro-cracks [272].

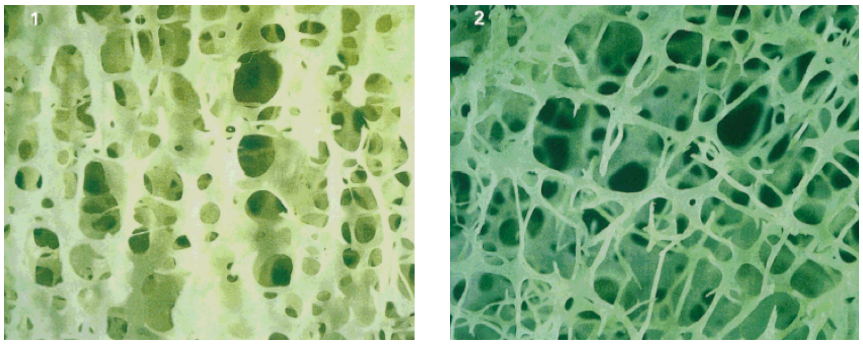

Figure 9.4: *Photomicrographs of trabecular bone obtained from a normal (left) and osteoporotic subject (right). The loss of bone mass in the osteoporotic bone is apparent with associated changes in trabecular architecture.*[6]

Among others, quantitative ultrasound (QUS) techniques have been developed in the past two decades to overcome limitations of DXA. The significant growth of the QUS research field has been based on the affordability of this non-ionizing technology and the potential of ultrasound waves to probe bone quality features. In addition, QUS offers other advantages in comparison with DXA: (1) it requires an equipment that is more portable and less expensive, and (2) its non-ionizing nature makes it attractive for studies on children or people who have concerns with small radiation doses [274]. Most of the QUS methods described in the literature for bone damage assessment are based on broadband ultrasound attenuation (BUA), speed of sound and broadband ultrasound backscattering. These acoustic properties are used in the assessment of bone density and other properties such as bone stiffness and strength. Hence, the mechanical nature of QUS enables to detect not only bone density but also bone elasticity and bone morphology, and thus provides an indication of not only the quantity of bone, but also the quality of bone. However, these techniques are almost insensitive to progressive induced damage.

Several studies have evidenced the significant consequences of micro-damage on bone mechanical properties [275, 276], suggesting the importance of micro-damage assessment. It is hypothesized that micro-damage in bone is induced by daily cyclic loading, which can lead to an imbalance in the bone remodeling process, and thus to an accumulation of micro-cracks. Whether the increase in crack density is a cause or a consequence of the decrease in the bone toughness properties with age is still not resolved. Some recent experimental observations tangentially suggest that nonlinear and/or hysteretic mechanical properties may be a key signature to quantify bone changes and could unveil deeper dimensions of its micro

[6] Reproduced from Borah *et al.* [273].

and macrostructure. Those observations have given raise to a number of studies directed towards the relationship between cracks density and level of nonlinearity. Nonlinear acoustic methods developed for nondestructive testing of traditional materials have been proven to have potential in detection of micro-cracks [277], and have been conveniently adapted to bone damage assessment purposes. Among the first works undertaken on bone nonlinearity, Hoff *et al.* [278] aimed at diagnosing osteoporosis using nonlinear acoustics to detect microscopic cracks in human bone. To this end, they constructed a system to measure second harmonic generation in human heel bone. Nonetheless, this study has not yet been able to verify a difference between normal and osteoporotic bone. After those initial measurements oriented at indicating a correlation between bone mass density and second harmonic generation, Engan *et al.* [279] proposed improved experiments with volunteers covering a range of T-score values obtained by DXA. However, this study neither provided results that could discriminate osteoporotic from healthy bone.

Alternatively, the nonlinear resonant ultrasound spectroscopy (NRUS) technique has been conveniently applied to assess damage in cortical bone [280, 281]. Their results demonstrated that nonlinear ultrasound could be used to assess progressively induced damage. This technique has recently been optimized by developing an accurate data processing protocol used to overcome the effects of environmental condition changes that take place during an experiment, and that may mask the intrinsic nonlinearity [282]. In another related work, Renaud *et al.* [283] proposed a method to measure acoustic nonlinearity in trabecular bone using the time-of-flight modulation (TOFM) method. Ultrasonic short bursts times-of-flight (TOF) are modulated as a result of nonlinear interactions with a low-frequency wave in the medium. The TOF variations are directly related to elastic modulus variations, and enable them to derive both the classical and hysteretic nonlinear parameters from these measurements. In the same vein, Moreschi *et al.* [284] developed a dynamic acousto-elastic technique (DAET) based on two acoustic waves coupling to measure viscoelastic and dissipative nonlinearities in trabecular bone, with the aim of validating the technique sensitivity to monitor micro- damage in human calcaneus. In another related study, the feasibility of assessing bone status by measuring the nonlinear parameter B/A in bovine trabecular bone has been evaluated by using a finite-amplitude through-transmission method [285]. Recently, the concept of probing nonlinear elasticity at an interface prosthesis/bone has been proposed as a promising method to monitor the osseointegration/sealing of a prosthesis. To this purpose, Rivière *et al.* [286] compared two approaches named the scaling subtraction method and the cross-correlation method, and showed that a nonlinear parameter derived from the cross-correlation method can be as sensitive as a clinical device based on linear elasticity measurement. Later, Rivière *et al.* [287] applied the time reversed elastic nonlinearity diagnostic to two mock models, and the obtained results suggested that nonlinear elasticity can provide new information regarding the interface, complementary to the linear wave velocity and attenuation.

These encouraging results motivated us to make further use of nonlinear ultrasound techniques, in particular the finite-amplitude through-transmission method, since it may have the potential of being transferred to *in vivo* measurements, in contrast to the other techniques (e.g. NRUS) which are restricted to *in vitro* applications in their actual forms.

9.2 Experimental work description

This section exposes several aspects of the experimental work carried out over the course of this dissertation, focusing on the samples preparation description and the experimental configuration used to evaluate those samples. The proposed methodology is organized in four parts: Firstly, Section 9.2.1 describes a conventional through-transmission technique for measuring the properties of traditional materials with known acoustic properties. This experiment serves us as a calibration for our system and provides us fundamental experimental data for validating our models. Secondly, Section 9.2.2 presents some conventional through-transmission measurement techniques applied for damage assessment in carbon fiber-reinforced polymers. Both the impact and post-impact fatigue damage mechanisms are investigated. In Section 9.2.3, we then introduce a novel embedded system for ultrasonic monitoring of tissue-engineered products. This system is calibrated on a tissue-equivalent material, and then applied for monitoring the generation of an artificial tissue culture. In Section 9.2.4, we finally investigate the feasibility of measuring the acoustic nonlinearity of cortical bone using a finite-amplitude through-transmission method, based on the second harmonic generation technique.

9.2.1 System calibration

In this section, we analyze several traditional materials (i.e. metals and plastics) with the aim of evaluating the performance of the theoretical models described in Part II. The materials were chosen so that they cover a relatively wide range of mechanical (e.g. wave velocity, density, etc.) and geometrical (e.g. thickness) properties. The properties reported in the literature for those materials are summarized in Table 9.1.

Material	Wave velocity c_p $[m/s]$	Density ρ $[kg/m^3]$	Attenuation α $[Np/m]$	Thickness a $[mm]$
Aluminium	[6320-6420][7,8]	2700[7]	3 @ 5 MHz / 20 @ 10 MHz[9]	3.79 / 9.90
Brass	[4369-4700][7,10]	[8480-8600][7,10]	-	2.90
PMMA	[2673-2750][11]	[1180-1200][11]	[50-72] @ [4-7] MHz[11]	2.61 / 9.98

Table 9.1: *Mechanical and geometrical properties of traditional materials.*

[7] http://www.ondacorp.com/images/Solids.pdf
[8] http://www.olympus-ims.com/en/ndt-tutorials/thickness-gage/appendices-velocities/
[9] http://www.astm.org/BOOKSTORE/DS68/pg41.pdf
[10] http://www.ndtsystems.com/Reference/Velocity_Table/velocity_table.html
[11] Reported by Carlson *et al.* [288]. The attenuation has a nearly linear behavior for the given frequency range.

For this experiment, we assemble the aforementioned single layers together to obtain a set of multilayered materials (ranging from 2 to 4 layers). This operation has been carefully carried out in immersion with degassed water as coupling medium to avoid voids or bubbles getting stuck between the layers. To evaluate the reproducibility of the experiment, each layered configuration has also been tested in its reverse side (assuming that we are working in the linear regime), and the layered specimens were completely dismounted and assembled again between each experiment. The resulting combinations are summarized in Table 9.2. Note that the one-layer specimens consisting of the same material involved layers of different thicknesses, which are denoted with increasing indexes from the thinest to the largest layer[12].

Type of multilayer	Specimen	Materials
Single layer	$S_{1,1}$	Aluminium^a
	$S_{1,2}$	Aluminium^b
	$S_{1,3}$	Brass
	$S_{1,4}$	PMMA^a
	$S_{1,5}$	PMMA^b
Two layers	$S_{2,1}$	Aluminium^b - PMMA^a
	$S_{2,2}$	PMMA^a - Aluminium^b
	$S_{2,3}$	Aluminium^b - PMMA^b
	$S_{2,4}$	PMMA^b - Aluminium^b
Three layers	$S_{3,1}$	PMMA^a - Aluminium^b - PMMA^b
	$S_{3,2}$	PMMA^b - Aluminium^b - PMMA^a
Four layers	$S_{4,1}$	Aluminium^a - PMMA^a - Aluminium^b - PMMA^b
	$S_{4,2}$	PMMA^b - Aluminium^b - PMMA^a - Aluminium^a
	$S_{4,3}$	Brass - PMMA^a - Aluminium^b - PMMA^b
	$S_{4,4}$	PMMA^b - Aluminium^b - PMMA^a - Brass

Table 9.2: *Overview of the obtained one-layer and multilayered specimens.*

In this first experiment, the specimens were excited by a low-frequency ultrasonic sine-burst at two different frequencies (5.5 and 6 MHz), consisting of one cycle of 8 Vpp amplitude. This excitation signal was generated by an arbitrary wave generator (Agilent 33220). The water path between the unfocused transducers was fixed to 124 mm, that is a large enough distance so that the echoes from the transducers-material interactions does not interfer with echoes from the layers of the material. The specimens were approximately located in the middle of the distance between the transducers, and scanned over a two-dimensional plane parallel to the transducer areas (C-scan mode). The scan was carried out in an immersion tank with degassed water at room temperature equipped with three-dimensional

[12]Those layers were not necessarily cut off from the same sample, and thus may have slightly different mechanical properties.

motion controllers. The response signals were registered during 20 μs. The response signals were sampled with a high resolution A/D converter after 40 dB pre-amplification stage, applying a sampling frequency of $F_s = 100$ MHz, providing $N = 2000$ samples, which were uniformly quantized with 12 bits. Figure 9.5 depicts the experimental setup used to register the ultrasonic signals.

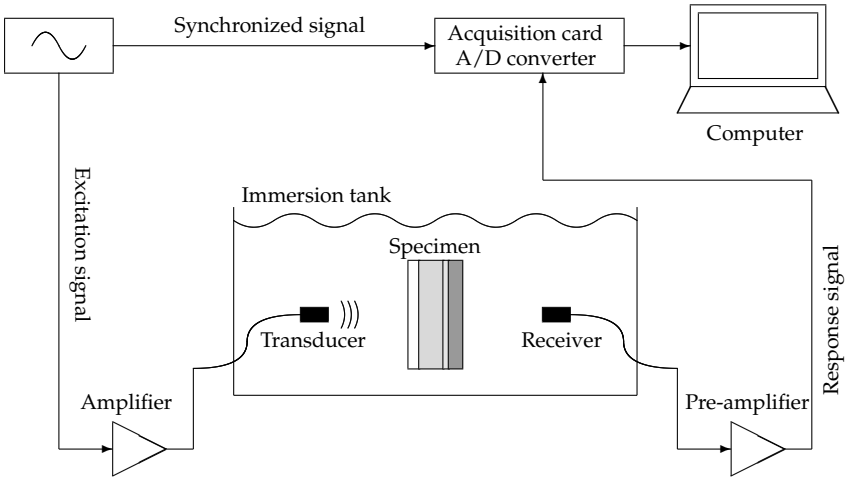

Figure 9.5: *Experimental configuration for the system calibration (immersion measurements).*

The measurement procedure was repeated for each frequency over an area of 2×2 mm^2 with a step of 1 mm close to the center of the specimens, providing 2×9 measurements for each specimen. Each of these measurements corresponds to the resulting average of 500 captures of the signal, providing an effective reduction of noise for the detected response signal, increasing the signal-to-noise ratio around 27 dB. Only compressional waves were generated by the transducers and no mode conversion waves were measured in the present case, although the methodology could be extended to other measurements configuration[13]. Figure 9.6 illustrates the experimental configuration for a layered specimen.

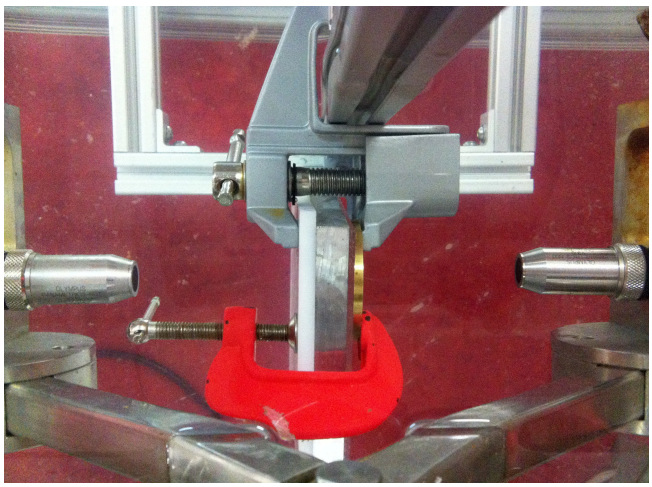

Figure 9.6: *Experimental configuration for measuring a layered specimen.*

[13]Be aware that this will be the case for all the considered experiments.

9.2.2 *Linear ultrasonic through-transmission measurements*

In this section, several CFRP plates with distinct structural complexity and exposed to different damaging mechanisms have been evaluated. To obtain the ultrasonic measurements, linear normal incidence techniques were adopted, either in contact or in immersion. To this end, a through-transmission sub-wavelength technique has been proposed, where longitudinal waves are transmitted through layers, whose size is much smaller than the wavelength of the transmitter.

Impact damage assessment

Typically, the properties of laminates are provided by the manufacturer. In our case, several mechanical and geometrical properties of the analyzed specimen (labeled as specimen (A)) were unknown after manufacture, and were therefore characterized at our laboratory. The fiber properties can be extracted by burning off the resin of a specimen's sample in an oven at 500°C during approximately sixteen hours. In first place, we introduced images of the burned samples in an AutoCAD software to count the number of layers of each sample, to measure the thickness of each layer by digital media, and to determine the orientation of the fibers with respect to the longitudinal axis of the specimen. Secondly, we weighted the fibers of each layer, and this enabled us to calculate their density and elastic constants. Finally, the elastic constants of the polymer matrix can be deduced from those of the fibers by making use of well-known mixing rules. From those measurements, it results that Specimen (A) is a symmetric CFRP plate consisting of five layers, whose mechanical and geometrical properties are summarized in Table 9.3.

Specimen	Layer (n°)	Y. Modulus $E\ [GPa]$	P. Ratio $\nu\ [-]$	Density $\rho\ [kg/m^3]$	Attenuation $\alpha \cdot 10^6\ [m^{-1}]$	Thickness $a\ [mm]$
(A)	I, V	12.0427	0.2937	1874.7	2.3059	0.255
	II, IV	8.9068	0.3148	1456.4	2.3059	0.185
	III	7.0132	0.3308	1140.1	2.3059	0.770

Table 9.3: *Mechanical and geometrical properties of the layers $I - V$ that compose the multilayered specimen (A).*

Damages were generated by applying several free-fall impact energies (0.388, 0.674, 1.313, 2.280, and 5.385 Joules), varying the mass and height of each impactor to obtain five relevant damage locations (labeled from 0 to 5, where 0 indicates no-damage). The impact damage generation procedure is depicted in Figure 9.7.

In this first experiment, the specimens were excited by a low-frequency ultrasonic sine-burst at a central frequency of 5 MHz, consisting of one cycle of 0.2 μs and 5 Vpp amplitude. This excitation signal was generated by an arbitrary wave generator (Agilent 33220). The response signals were registered during 10 μs, that is, up to the time for which there were no more reflections from the specimen/transducers interfaces. The response signals were sampled with a high resolution A/D converter after 40 dB pre-amplification stage, applying a

Figure 9.7: *Impact damage generation procedure: (1) CFRP plates; (2) drop weight tower; and (3) impacted area of the specimen.*

sampling frequency of $F_s = 200$ MHz, providing $N = 2000$ samples, which were uniformly quantized with 12 bits.

Initially, the response signal was measured at the undamaged location for calibration. Then, the measurement procedure was repeated ten times on each location, to generate a relevant data set that account for the uncertainties due to the variability of the transducers alignment with respect to the impact location. Each of these measurements corresponds to the resulting average of 300 captures of the signal, providing an effective reduction of noise for the detected response signal, increasing the signal-to-noise ratio around 25 dB. Due to the high impedance of the interface air/solid, the transducers were adhered to the specimen with a coupling gel, to favor the transmission of the ultrasonic waves. Figure 9.8 depicts the experimental setup used to register the ultrasonic signals. Figure 9.8 depicts the experimental setup used to register the ultrasonic signals.

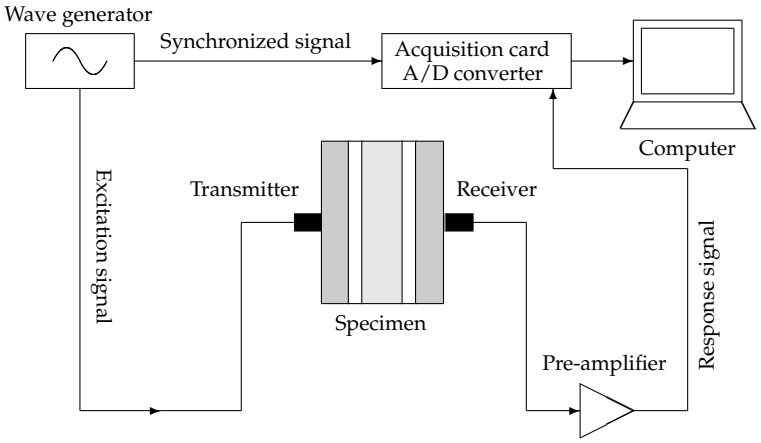

Figure 9.8: *Experimental configuration of the excitation-propagation-measurement system (contact measurements).*

'Fatigue after impact damage' assessment

In this case, the properties of laminates were completely provided by the manufacturer. The specimen (labeled as specimen (B)) was manufactured from a Cycom 977-2-35-12k HTS prepreg with a stacking sequence which corresponds to a $[0/90]_{4s}$ lay-up[14]. During lay-

[14]Courtesy from the Institute of Polymers and Composites, TU Hamburg-Harburg, Germany

up, the laminates were compacted every four layers in the stacking sequence by applying vacuum for 15 minutes. Curing was realized in an autoclave at 177°C for three hours with a pressure of 7 bar. From the manufactured plates, the specimen (B) with the dimensions $250 \times 35 \times 2$ mm^3 was machined. The mechanical and geometrical properties are given in Table 9.4.

Layer	Y. Modulus $E\ [GPa]$	P. Ratio $\nu\ [-]$	Density $\rho\ [kg/m^3]$	Attenuation $\alpha \cdot 10^6\ [m^{-1}]$	Thickness $a\ [mm]$
$0° - orientation$	11.1616	0.3007	1589.5	1.7673	0.1215
$90° - orientation$	11.1616	0.3007	1589.5	1.7673	0.1215

Table 9.4: *Mechanical and geometrical properties of the layers that compose the multilayered specimen (B).*

In first place, impact damage was introduced with a drop weight tower. A photo sensor activating a clamp ensured anti-rebound after the first impact, and the contact force was measured with a strain gauge full bridge included in the semi-spherical striker. The impact damaged specimen was subjected with 3.8 Joule impact energy. Then, fatigue testing was conducted with a servo-hydraulic Instron/Schenk 100 kN fatigue testing machine with hydraulic clamps at a stress ratio of $R = -1$. The clamping pressure was set according to loading forces. The fatigue damage was generated by applying fatigue load in tension-compression (up to 100000 cycles). The specimens and the *fatigue after impact damage* generation procedure are depicted in Figure 9.9.

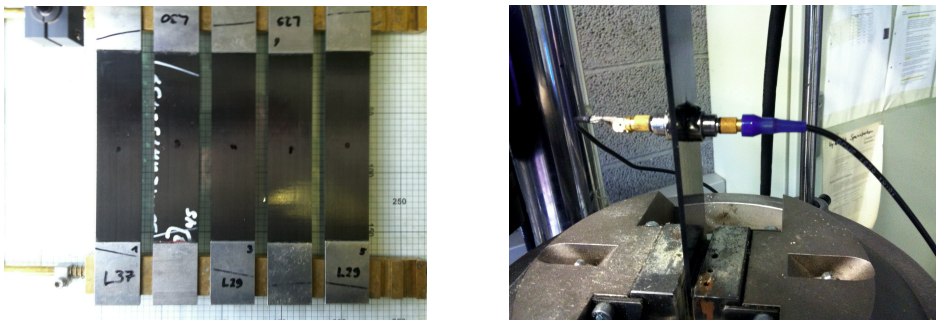

Figure 9.9: *'Fatigue after impact damage' generation procedue: (1) CFRP plates with marked impacted area; and (2) CFRP plate mounted on the servo-hydraulic fatigue testing machine.*

In this second experiment, the specimen was excited by a low-frequency ultrasonic sine-burst at a central frequency of 5 MHz, consisting of one cycle of 0.2 μs and 5 Vpp amplitude. This excitation signal was generated by an arbitrary wave generator (Agilent 33220). The specimen was located at the focal distance ($d_f = 30$ mm) of the focused transducers, and scanned over a two-dimensional plane parallel to the transducer areas (C-scan mode) in an immersion tank with degassed water at room temperature equipped with three-dimensional motion controllers. The response signals were registered during 10 μs, that is, up to the

time for which there were no more reflections from the specimen/transducers interfaces. The response signals were sampled with a high resolution A/D converter after 40 dB pre-amplification stage, applying a sampling frequency of $F_s = 200$ MHz, providing $N = 2000$ samples, which were uniformly quantized with 12 bits.

Initially, the response signal was measured at an undamaged location (far from the impacted area) for calibration. Then, the measurement procedure was repeated over an area of 40×20 mm^2 with a step of 1 mm around the impacted area, providing a data set of 860 measurements (plus one taken in water only after removing the specimen). Each of these measurements corresponds to the resulting average of 500 captures of the signal, providing an effective reduction of noise for the detected response signal, increasing the signal-to-noise ratio around 27 dB. Figure 9.10 depicts the experimental setup used to register the ultrasonic signals.

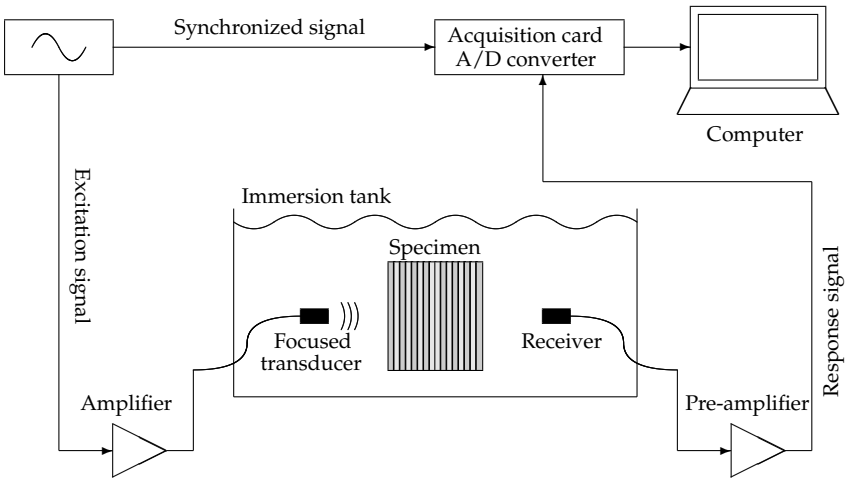

Figure 9.10: *Experimental configuration of the excitation-propagation-measurement system (immersion measurements).*

9.2.3 Embedded systems for ultrasonic monitoring of biomaterials

In this section, an ultrasound-monitoring Petri dish has been designed to monitor in real-time the evolution of relevant mechanical properties during engineered tissue formation processes. This system has several advantages: (i) the entire sample holding equipment can be autoclaved and measurements can be taken under sterile conditions; and (ii) the system is capable of working under cell culture conditions (37°C, 5% CO_2) and testing of the tissue-engineered material can be done while submerged in culture media. It is noteworthy that these environmental properties are of extreme importance when measuring mechanical properties of tissue culture, since changes in environment can significantly affect those properties [289].

The Petri dish with a specifically designed high-frequency ultrasonic transmitter and receiver in angle position was manufactured for real-time measurement of mechanical properties of thin layers of tissue culture, whose thickness is of the order of 100 μm. The bottom part of the Petri dish that holds the tissue culture is circular and made of a biocompatible

material, in order to mimic a conventional culture flask. A thin cover is carefully deposed above the tissue culture to ensure that the thickness of the tissue layer remains constant at the measurement location. In addition, this cover is made of a material with a much higher impedance than that of the tissue layer to provide a high reflection coefficient (i.e. a nearly perfect reflector). This cover is narrow enough (few millimeters) to guarantee that it won't hamper the culture medium (e.g. nutrients) to reach the tissue layer. The monitored Petri dish is connected to the electronic setup detailed in Figure 9.11.

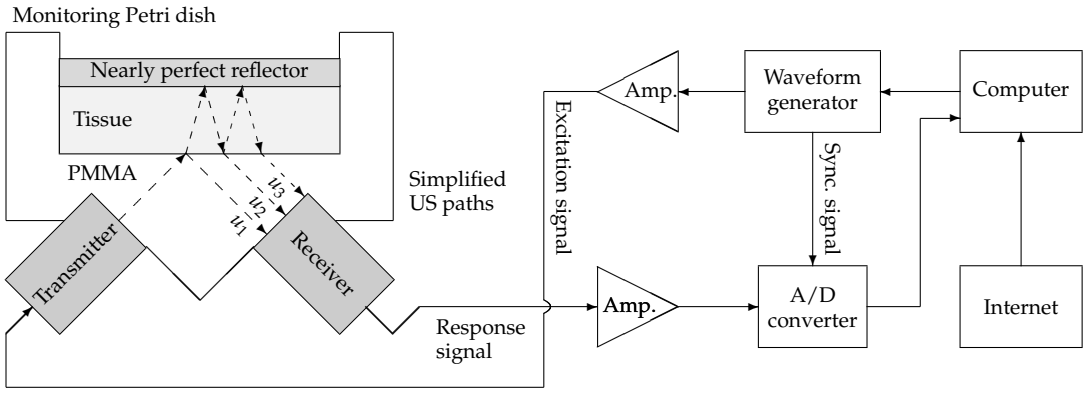

Figure 9.11: *Schematic experimental and electronic setup for the ultrasonic embedded system.*

The transmitting and receiving transducers are designed to be in angle position (45°) in order to avoid reverberation echoes inside the petri dish plate parts. The transmitted signal is generated as a one-cycle burst composed by a 20 MHz sine of amplitude that amounts to 5 Vpp with a repetition rate of 1000 pulses/second, using an arbitrary wave generator (Agilent 33220). The recorded signals are digitized with a high resolution A/D converter after 40 dB preamplification, during a period of 5 μs and a sampling rate of 400 MHz. Each measurement corresponds to the average of 300 captures of the signal, providing an effective reduction of noise according to the signal-to-noise ratio (25 dB). Only compressional waves are generated by the transducers and no mode conversion waves are measured in the present case, although the methodology could be extended to shear or other waves. The recorded signals are mainly composed of three different waveforms (simplified paths of Figure 9.11), namely (1) the wave front that propagates only through the Petri dish layer (labeled as u_1), (2) a wave that crosses both the Petri dish layer and the specimen (labeled as u_2), and (3) a wave echo produced by the former wave after crossing twice the specimen (labeled as u_3).

Any new diagnostic technique for monitoring tissue culture needs an evaluation stage in terms of its potential, limitations and sensitivity prior to employ it for biological process. In this context, tissue-equivalent materials play an important role in evaluating novel diagnostic methods for monitoring tissue-engineered products [290]. In our case, a tissue-equivalent phantom is important for quality control of the developed ultrasound diagnostic system. In addition, synthetic materials used in tissue-equivalent phantoms must be manufactured in a controlled way to be acoustically equivalent to human tissues [291]. One of the most used

materials, due to its manageability and capacity to mimic speed of sound in soft tissue, is a mixture based on a polysaccharide gel (agar), distilled water, glycerol and graphite. The glycerol concentration determines the speed of sound in the medium, whereas the graphite concentration determines the attenuation [292].

In first place, the sensitivity and reproducibility of the system has been verified by monitoring a gelation process. The materials and the concentration for the gel culture (labeled as specimen (C)) were chosen according to Ortega *et al.* [292]: 92.5% of water, 5% of glycerol and 2.5% of agar. In order to obtain an homogeneous solution, water has been first heated and then the remaining components have been added. The final mixture was carefully deposed on the dish, resulting in a gel layer of about 300 μm thickness, and a diameter of 2 cm. The gelation process has been monitored during half an hour at 5 s intervals, resulting in a database of 350 measurements. At the initial time of the process, the wave velocity in the gel layer is unknown. Nonetheless, it is well-known that its value amounts approximately to 1500 [m/s], and thus the resulting wavelength (75 μm) is compatible with the gel layer thickness. The material properties of the Petri dish material (PMMA, polymetylmetacrilate) and the gel culture are summarized in Table 9.5.

Material	Modulus [GPa]	Poisson ν	Density ρ [kg/m^3]	Velocity c_p [m/s]
PMMA	$E = 2.96$	0.43	1180	2672
Gel (initial)	unknown	0.5	1000	unknown

Table 9.5: *Mechanical and geometrical properties of the layers that compose the multilayered embedded specimen (C).*

In second place, this diagnostic technique has been applied for monitoring the generation of artificial human oral mucosa[15]. The isolation and culture of human gingival fibroblasts has been achieved according to Ximenes Oliveira [293]: First, oral mucosa samples were obtained from patients submitted to different procedures of minor oral surgery. Secondly, the samples were washed with phosphate buffered saline (PBS) to eliminate adhered materials. Thirdly, an enzymatic method was carried out to digest the extracellular matrix of the oral mucosa chorion and to separate the stromal fibroblasts, by using the type I collagenase sterile solution of Clostridum hystoliticum at 2% in Dulbecco's modified Eagle's medium (DMEM), during 10-12 hours at 37°C. To obtain primary cell cultures, the enzymatic solution with stromal cells was then centrifuged at 1000 rpm, during 10 minutes, and the achieved cell pellet was cultured in culture flasks of 25 cm^2 surface area, using DMEM as culture medium, complemented with 10% fetal bovine serum (FBS) and 1% antibiotic. Finally, the cells were incubated at 37°C with 5% carbon dioxide, and the culture medium was changed every three days. On the other hand, a fibrin-agarose stromal substitute has been elaborated: First, the fibrin was obtained from frozen plasma of human blood donors.

[15]Courtesy from the Tissular Engineering Group, Department of Histology, University of Granada

To produce a fibrin-agarose gel, 15.2 ml of human plasma were then added to 150000 cultured fibroblasts resuspended in 1.5 ml of DMEM with 10% FBS. To prevent degradation of the scaffold by fibrinolysis, the mixture was supplemented with 300 μl of tranexamic acid. Finally, 2ml of 1% CaCl2 were added to the solution to precipitate fibrin polymerization. At the same time, type VII agarose was melted and solved in PBS, and added to the fibrin mixture at a final concentration of 2%.

In this experiment, the cells-seeded construct (labeled as specimen (D)) was carefully deposed on the dish, resulting in a tissue layer of about 100 μm thickness, and a diameter of 1 cm. Before the construct starts hardening, the cover was meticulously deposed above it, then the culture media was added, and the embedded system was finally placed in chamber under cell culture conditions (37°C, 5% CO_2). The biological process has been monitored during seven days at 2 min intervals, resulting in a database of 5016 measurements. As for the gel, the wave velocity in the tissue layer is unknown at the initial time of the process. Figure 9.12 provides an overview of the embedded ultrasonic system and samples preparation.

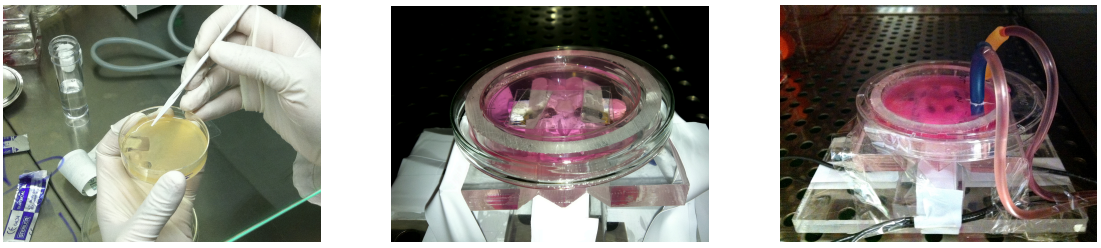

Figure 9.12: *Embedded ultrasonic system: (1) Elaboration of the fibrin-agarose stromal substitute; (2) monitoring Petri dish with ultrasonic transducers in angle position; and (3) tissue culture submerged in culture media under physiological conditions.*

9.2.4 Nonlinear ultrasonic measurements

In vivo bone strength assessment has long been focused on trabecular bone, considered to be more rapidly lost than cortical bone. This approach has neglected the role of decay of cortical bone in pathogenesis of bone fragility. Indeed, in the femoral neck, the cortical shell contributes to 40-90% of the bending rigidity, and cortical porosity is a crucial factor for determining bone fragility [294, 295]. As a consequence, the relative contributions of cortical versus trabecular bone to bone strength have been revisited recently [296], and the results suggest that fracture risk assessment should include accurate evaluation of cortical bone.

In this study, we present a through-transmission finite-amplitude nonlinear ultrasound technique to quantify the inherent nonlinearity of bone, which may have the potential of being transferred to *in vivo* measurements. A cortical bone sample has been taken from a bovine diaphysis (femur)[16]. A transverse cross-section, 4 mm in thickness, has been cut in a plane perpendicular to the long bone axis using a diamond saw. The fresh section was fixed on a sample holder, shock frozen in liquid nitrogen, and then prepared to obtain

[16]Courtesy from the Laboratoire d'Imagerie Paramétrique, UMPC-CNRS, Paris.

parallel, flat and smooth bone surfaces using an ultra milling machine. After soft tissue removal, the specimen was kept frozen at -20°C as a method of storage, allowing repeatable use of the sample (i.e it was demonstrated that freezing and storage do not significantly alter the elastic properties of cadaver bone specimens). A side-objective of this experiment is to evaluate the relation between an increase of nonlinearity and an increase of (micro-) cracks. To this end, damage has been induced to the specimen by applying the percussive drilling technique [297], which consists in generating periodic impact forces to enhance dynamic crack creation and propagation in the material (see Figure 9.13).

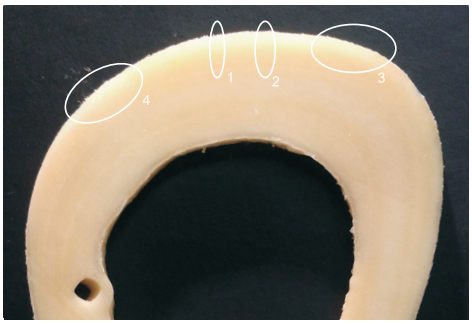

Figure 9.13: *Cross-section of the cortical bone sample (4 millimeters thick, out of plane of the figure): Areas 1 and 2 indicate damage zone induced by traditional drilling (with drill diameters of 2 and 4 millimeters, respectively), whereas areas 3 and 4 indicate damage zone induced by percussive drilling (with a drill diameter of 6 millimeters).*

To evaluate the sensitivity of the proposed methodology, the experiments have also been conducted on traditional and other advanced materials. The presence of non-linear distortions from the electronic equipment represents the major practical difficulty of this technique when analyzing the response signals, since it may mask the intrinsic nonlinear response of the material under investigation. Hence, the experiment has been first carried out on water and serves us as a calibration of the instrumentation, now that several references in the literature provide tabulated values for the nonlinear parameter of first-order for water. Secondly, a PMMA beam, with dimensions $130 \times 30 \times 20$ mm^3, with increasing drilled hole density along its length (see Figure 9.14) has been analyzed, providingan efficient way to evaluate the relation between increasing drilled hole density and increasing nonlinearity. The holes were generated at high drill feed rate, with the aim of generating hairline cracks around the perimeter of the drilled holes [298, 299]. Finally, the CFRP plate described in Section 9.2.2 has been evaluated, and provides us a mean for validation of the proposed methodology, by contrasting the results with those obtained with other NDE techniques (e.g. micrographs and X-ray imaging).

In this experiment, the specimens were excited by 25 low-frequency ultrasonic sine-bursts at a central frequency of $f_c = 667$ kHz at five different energies corresponding to $2^{(j-1)} \cdot 200$ mV, with $j = 1, \ldots, 5$. In order to obtain the attenuation of the second harmonics, the specimens were excited as well at twice the central frequency (that is, 50 sine-bursts

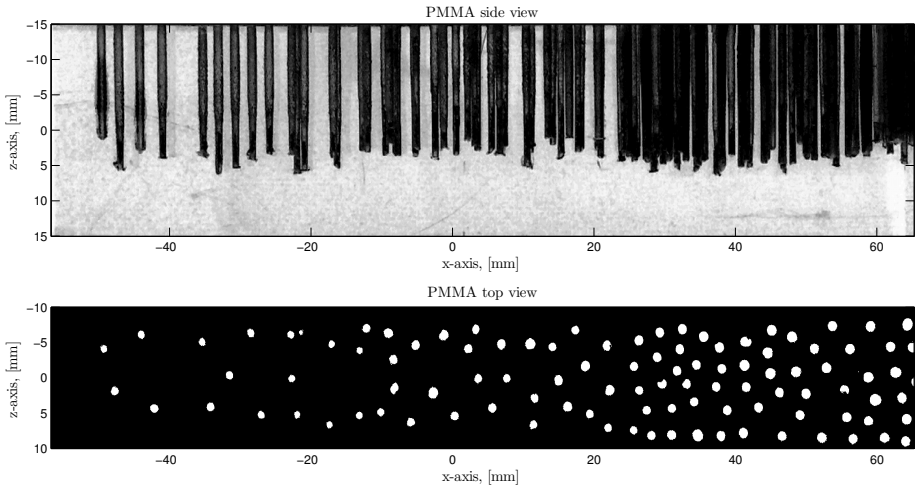

Figure 9.14: *Side and top views of the PMMA beam with increasing drilled hole density along its length (with a drill diameter of 1 millimeter).*

at 1.33 MHz). Those excitation signals were generated by an arbitrary wave generator (Agilent 33220), using a focused transducer. The specimens were located at the focal distance ($d_f = 30$ mm), and scanned over a two-dimensional plane parallel to the transducer areas in an immersion tank with degassed water at room temperature equipped with three-dimensional motion controllers. The response signals were registered during 15 μs at two different time intervals using a needle hydrophone with a linear response up to 20 MHz. The first interval is chosen to capture the time of arrival (TOA) of the waves, whereas the second one windows a stationary 10-cycle burst response (respectively 20 cycles at twice the central frequency). The response signals were sampled with a high resolution A/D converter after 40 dB pre-amplification stage, applying a sampling frequency of $F_s = 133$ MHz, providing $N = 2000$ samples on each time interval, which were uniformly quantized with 12 bits. Each of the measurements corresponds to the resulting average of 500 captures of the signal, providing an effective reduction of noise for the detected response signal, increasing the signal-to-noise ratio around 27 dB. Figure 9.15 depicts the experimental setup used to record the ultrasonic signals.

9.3 Inverse problem and system identification

An inverse problem (IP) can be defined in opposition to the forward problem (FP). A FP consists of finding the response of a system given a known model. In contrast, an IP consists of retrieving unknown information of the model given the response of a system. Recently, some authors have applied IP's to identify damages or characterize material properties, defining a corpus of knowledge for reconstructing an unknown part of a system model. The theoretical background on the inverse problem (IP) theory described here is provided by Tarantola *et al.* [8].

The model-based IP grounds today's most powerful reconstruction method for finding an optimal solution. It generally consists of four steps:

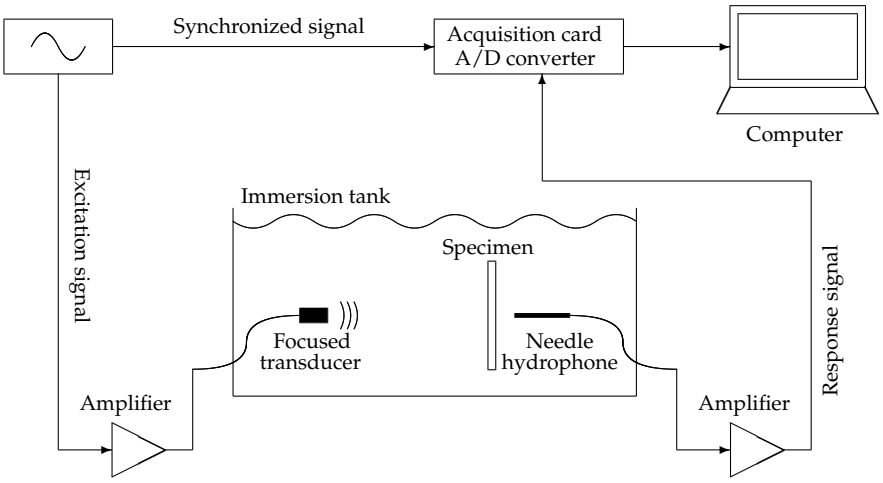

Figure 9.15: *Experimental configuration of the nonlinear excitation-propagation-measurement system.*

- Obtaining a set of experimental measurements given a specific experimental design, which interrogates the system by propagating some physical magnitude that interacts with the unknown part of the system and manifests on an accessible part of it.
- Solving computationally a mathematical model that is generated by assuming some physical assumptions. The unknown part of the model to be reconstructed depend on some defined parameters. This model simulates the measurements given a set of parameter values.
- Defining a Cost Function (CF) by means of some metrics. The CF represents the discrepancy between experimental and simulated measurements.
- Finding the values of the parameters that minimize the CF.

9.3.1 Deterministic approach

The fundamental idea of the IP consists of the use of an iterative strategy based on the minimization of the discrepancy between the experimental and numerically predicted response signals, denoted by $\boldsymbol{y}$ and $\boldsymbol{y}(\boldsymbol{\theta})$ respectively, where $\boldsymbol{\theta}$ denotes a finite set of parameters used to describe the damage state of the system. The discrepancy is represented by a residual feature vector $\boldsymbol{r}(\boldsymbol{\theta})$ defined as,

$$\boldsymbol{r}(\boldsymbol{\theta}) \quad = \quad \boldsymbol{y} - \boldsymbol{y}(\boldsymbol{\theta}) \tag{9.1}$$

Since two vectors cannot be compared directly, a scalar number called cost functional $f(\boldsymbol{\theta})$ is derived from them. Typically, the IP approach consists of three steps, that are the parametrization (how to choose the parameters $\boldsymbol{\theta}$), the cost functional definition (how to define $f(\boldsymbol{\theta})$), and the optimization (how to choose the algorithm to minimize $f(\boldsymbol{\theta})$).

Parametrization

The issue of the parametrization is cumbersome when dealing with a large set of model parameters $\boldsymbol{\theta}$, describing the properties of the material for the present problem. Thus, many IP's are ill-posed: Solutions may not exist, they could be unstable and non-converging, or there may exist multiple solutions. From the conceptual point of view, parametrization can be understood as a powerful regularization tool for IP's, since it provides prior information in the form of hypothesis on the possible form of the sought solutions. Therefore, the choice of parameters has crucial implications in the convergence, the sensitivity and uniqueness of the results.

Cost functional

There are many ways to design a cost functional. The necessary conditions are (a) that a full coincidence of prediction and measurement (zero discrepancy) should coincide with the absolute minimum of the cost functional, and (b) that of uniqueness of this minimum. This quadratic or least squares type definition is meaningful in a probabilistic sense, as well as in an algebraic sense, as a measure of a distance between bad and good results. The cost functional $f(\boldsymbol{\theta})$ is chosen after a residual vector $\boldsymbol{r}(\boldsymbol{\theta})$ as,

$$f(\boldsymbol{\theta}) \quad = \quad \frac{1}{2}\sum_{n=1}^{N} r(n,\boldsymbol{\theta})^2 \tag{9.2}$$

in the case of a L_2-norm definition, or as,

$$f(\boldsymbol{\theta}) \quad = \quad \sum_{n=1}^{N} |r(n,\boldsymbol{\theta})| \tag{9.3}$$

in the case of a L_1-norm definition, being less sensitive to outliers. In contrast to gradient-based algorithms, for which the cost functional is defined as $f(\boldsymbol{\theta})$, the latter is usually defined in an alternative way as $f^L(\boldsymbol{\theta})$ when the minimization is carried out by global search algorithms,

$$f^L(\boldsymbol{\theta}) \quad = \quad \log\left(f(\boldsymbol{\theta}) + \varepsilon\right) \tag{9.4}$$

where ε is a small non-dimensional value (here adopted as $\varepsilon = 10^{-16}$) that ensures the existence of $f^L(\boldsymbol{\theta})$ when $f(\boldsymbol{\theta})$ tends to zero, and speeds up the convergence of the selected optimization algorithm [300, 301].

Optimization

According to Lee and Wooh [302], the model parameters $\boldsymbol{\theta}$ that characterize the damage are found by a search algorithm that minimizes the cost functional by means of a least-square estimation of the residual energy,

$$\hat{\boldsymbol{\theta}} \quad = \quad \arg\min_{\boldsymbol{\theta}} f^L(\boldsymbol{\theta}) \tag{9.5}$$

The cost functional minimization can be performed by two alternative families of methods. The former consists of conventional gradient-based methods, such as the Gauss-Newton algorithms, the Broyden-Fletcher-Goldfarb-Shanno (BFGS) algorithm, or simulated annealing, just to name some of the most popular ones. The other family involves random search algorithms, for instance genetic algorithms (GA) [303] or particle sworm algorithms. In this study, BFGS algorithm is used as a local search algorithm based on Hessian update [120], and assisted by finite differentiation and line search, for calibrating the model at the initial time of the monitoring process. GA are then applied to minimize Equation (9.5), motivated by the fact that the cost functional $f^L(\boldsymbol{\theta})$ is non-convex, implying that the cost functional may have more than one local minimum. This algorithm performs a stochastic search through the space of possible solutions and yields a higher probability of finding the global optimum compared to standard iterative gradient-based optimization algorithms [304]. As a further drawback, it is noteworthy that the convergence of gradient-based algorithms strongly relies on the initial guess that needs to be provided. A deeper insight on GA is provided in next section.

Genetic algorithms

The GA is an heuristic optimization technique based on the rules of natural selection and genetics, which simulates the mechanism of survival competitions. First, a population of individuals (called chromosomes) is randomly generated. The population comprises a group of chromosomes that represent possible solutions $\boldsymbol{\theta}_i$ ($i = 1, \ldots, N_p$) in a (multidimensional) problem domain. Each solution $\boldsymbol{\theta}_i$ is evaluated by computing its cost functional $f^L(\boldsymbol{\theta}_i)$, for which one forward problem is solved independently. A new (child) population is formed by stochastically modifying the survivors, applying genetic operators such as tournament, crossover, and mutation to inject genetic diversity in the population (i.e to ensure that the solution does not fall in local minima). Then, the child chromosomes with higher fitness replace some of their parent chromosomes. The process runs until a stopping criterion (for instance a number of generations N_g) is reached. The choice of N_g , as well as the probabilities of the genetic operators, are set so, that the convergence to a global optimum is guaranteed, while establishing a trade-off between the system identification error and the computational cost. The termination criterion can of course be modified, for instance by creating some convergence criterion and then ending the iterations when this criterion is met. In this work, we simply applied the algorithm to a group of *representative* signals and examined the evolution of the currently best solution for these. After a certain number of iterations, we could no longer see any further improvement of the solutions and N_g was fixed to this number when applying the algorithm to the remaining signals [110]. The flowchart of the system identification approach by applying genetic algorithms is depicted in Figure 9.16.

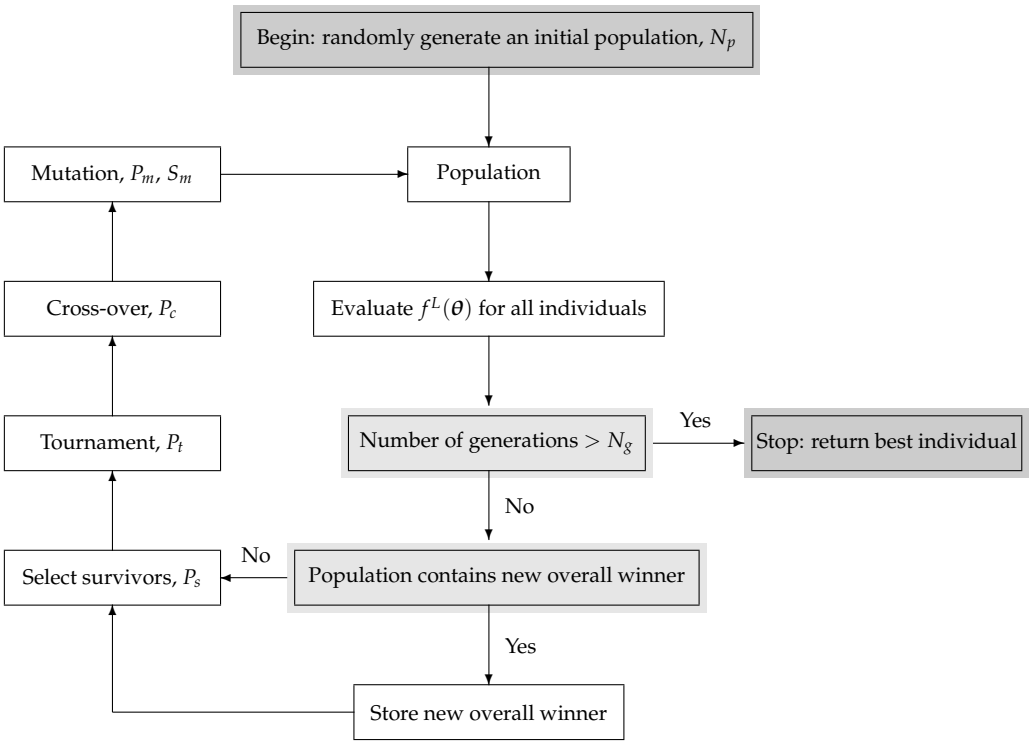

Figure 9.16: *Flowchart of the system identification approach by applying genetic algorithms. User-dependent variables: N_p: Number of individuals in population; N_g: Number of generations; P_s: Fraction of surviving individuals; P_t: Probability of tournament; P_c: Probability of crossover; P_m: Probability of mutation; and S_m: Scale of mutation.*

9.3.2 Probabilistic inverse problem

Reconstructing the values of the model parameters (moduli, attenuation parameters, etc.) has a limited meaning if one considers the existence of intrinsic noise in the measurements, heterogeneity of properties within the specimen, and even the fact that the model used to idealize its behavior is just an approximation of reality. To provide a suitable answer, probabilistic instead of deterministic values should be provided, which carry information about the degree of uncertainty and the nature of their scattering. This can be solved by treating the input and known data as uncertain and therefore probabilistic, and consequently obtaining the solution model in terms of a set of probability density functions (PDF) over each model parameter as a combination of the degree of certainty of them provided by the measurements on one hand, and the model on the other hand.

Following the probabilistic formulation of the model reconstruction inverse problem established by Tarantola *et al.* [8], the solution is not a single-valued set of model parameters $\mathcal{M}$. On the contrary, the solution is provided by PDF $p(\mathcal{M})$ of the values of the model parameters $\mathcal{M}$ within the manifold $\mathfrak{M}$ of possible values. The probability density p is assigned the meaning of plausibility of the model values $\mathcal{M}$ to be true. The theory of evidential probability concerns the impact of evidence on physical probability. It is motivated by two basic ideas [305]: Probability assessments should be based upon relative frequencies, to the extent that we know them, and the assignment of probability to specific individual events should

be determined by everything that is known about that individual. In particular, the probability of a hypothesis H is given the sense of degree of support (or plausibility or belief) of H given empirical evidence. Here, this formulation is generalized to the case where several model classes $\mathcal{C}$ are candidates to idealize the real input-output system. Including this variable into the inverse problem formulation will allow to derive the model-class selection formulation as a particular case of inverse problem.

Since an absolute probability cannot be computed, statistical inference theory is used to incorporate to the prior information about the measured observations $\mathcal{O}$, the model parameters $\mathcal{M}$ and the model class $\mathcal{C}$, the information of idealized relationship between them $\mathcal{O} = \mathcal{O}(\mathcal{M})$ computed by a model pertaining to a model class $\mathcal{C}$. The former are defined by the probability densities to prior data, labeled as $p^0(\mathcal{O})$, $p^0(\mathcal{M})$ and $p^0(\mathcal{C})$ respectively, whereas the additional information provided by the model class $\mathcal{C}$ about the relationship between observations and model is given by the PDF $p^m(\mathcal{O}, \mathcal{M}|\mathcal{C})$. The posterior probability $p(\mathcal{O}, \mathcal{M}, \mathcal{C})$ of the hypothetical model $\mathcal{M}$ is obtained jointly with the observations $\mathcal{O}$ and class $\mathcal{C}$ as,

$$p(\mathcal{O}, \mathcal{M}, \mathcal{C}) \quad = \quad k_1 \frac{p^0(\mathcal{O}, \mathcal{M}, \mathcal{C}) p^m(\mathcal{O}, \mathcal{M}, \mathcal{C})}{\mu(\mathcal{O}, \mathcal{M}, \mathcal{C})} \tag{9.6}$$

where $\mu(\mathcal{O}, \mathcal{M}, \mathcal{C})$ is the noninformative density function and k_1 is a normalization constant. Some assumptions will be made at this point:

1. Assuming that $\mathcal{O}$, $\mathcal{M}$ and $\mathcal{C}$ are independent *a priori* allows to split the joint prior information $p^0(\mathcal{O}, \mathcal{M}, \mathcal{C}) = p^0(\mathcal{O}) p^0(\mathcal{M}) p^0(\mathcal{C})$ and the uniform distribution $\mu(\mathcal{O}, \mathcal{M}, \mathcal{C}) = \mu(\mathcal{O}) \mu(\mathcal{M}) \mu(\mathcal{C})$.
2. The probabilistic model can be represented by a computation of $\mathcal{O}$ depending on $\mathcal{M}$, which yields $p^m(\mathcal{O}, \mathcal{M}, \mathcal{C}) = p^m(\mathcal{O}|\mathcal{M}, \mathcal{C}) p^m(\mathcal{M}, \mathcal{C}) p^m(\mathcal{C})$.
3. The model is not assumed to provide conditional information between model and class, i.e. $p^m(\mathcal{M}, \mathcal{C}) = \mu(\mathcal{M})$ and $p^m(\mathcal{C}) = \mu(\mathcal{C})$ are noninformative. This simplifies the expression to,

$$p(\mathcal{O}, \mathcal{M}, \mathcal{C}) \quad = \quad k_1 \frac{p^0(\mathcal{O}) p^0(\mathcal{M}) p^0(\mathcal{C}) p^m(\mathcal{O}|\mathcal{M}, \mathcal{C})}{\mu(\mathcal{O})} \tag{9.7}$$

   The posterior probability of the model $\mathcal{M}$ is then obtained from the joint probability $p(\mathcal{O}, \mathcal{M}, \mathcal{C})$ by extracting the marginal probability $p(\mathcal{M})\big|_{\mathcal{C}=\mathcal{C}_i}$ for all possible observations $\mathcal{O} \in \mathfrak{O} \Rightarrow p^0(\mathcal{C} = \mathcal{C}_i) = 1$, given that the model class $\mathcal{C}_i \in \mathfrak{C}$ is assumed to be true,

$$p(\mathcal{M})\big|_{\mathcal{C}=\mathcal{C}_i} \quad = \quad \int_{\mathcal{C}=\mathcal{C}_i} \int_{\mathfrak{O}} p(\mathcal{O}, \mathcal{M}, \mathcal{C}) d\mathcal{O} d\mathcal{C} \quad = \quad k_2 \int_{\mathfrak{O}} \frac{p^0(\mathcal{O}) p^0(\mathcal{M}) p^m(\mathcal{O}|\mathcal{M}, \mathcal{C})}{\mu(\mathcal{O})} d\mathcal{O} \tag{9.8}$$

   where k_2 is a normalization constant that replaces the dropped distributions.
4. We assume to have no prior information about the model $p^0(\mathcal{M})$, which is therefore represented by the noninformative distribution $p^0(\mathcal{M}) = \mu(\mathcal{M})$, which can in turn be

dropped in the case that Jeffreys parameters [306] are adopted,

$$p(\mathcal{M})\big|_{\mathcal{C}=\mathcal{C}_i} = k_3 \int_{\mathfrak{O}} p^0(\mathcal{O}) p^m(\mathcal{O}|\mathcal{M},\mathcal{C}) d\mathcal{O} \tag{9.9}$$

where k_3 is a normalization constant that replaces the dropped uniform distributions, and is needed for $p(\mathcal{M})\big|_{\mathcal{C}=\mathcal{C}_i}$ to fulfill the theorem of total probability, that is:

$$\int_{\mathfrak{M}} p(\mathcal{M})\big|_{\mathcal{C}=\mathcal{C}_i} d\mathcal{M} = 1 \tag{9.10}$$

5. The observations are assumed to follow a Gaussian distribution $\mathcal{O} \sim \mathcal{N}(E[\mathcal{O}^{\text{exp}}], C^{\text{exp}})$ whose mean is that of the experimental observations $\mathcal{O}^{\text{exp}}$, and whose covariance matrix C^{exp} stands for the measurement noise.
6. The observations are assumed to be a Gaussian process $\mathcal{O} \sim \mathcal{N}(\mathcal{O}(\mathcal{M}), C^{\text{num}})$ centered at the numerically computed ones $E[\mathcal{O}^{\text{num}}] = \mathcal{O}(\mathcal{M})$ with covariance matrix C^{num}.

The probabilistic observations $\mathcal{O}$ are in our case a vector of functions of time $\mathcal{O} = o_i(t)$ at every measuring time $t \in [0, T]$ and repetition $i \in [1...N_i]$, and the assumptions made above are valid for every instant t and sensor i. Considering that the compound probability of the information from all sensors and time instants is the product of that of each one individually, and that this product is equivalent to a summation within the exponentiation (since an integration along the continuous time can be seen as a summation over every infinitesimal dt), the Gaussian distribution allows an explicit expression of the probability densities,

$$J(\mathcal{M}) = \frac{1}{2} \sum_{i,j=1}^{N_i} \int_{t=0}^{t=T} \left(o_i(t,\mathcal{M}) - o_i^{\text{exp}}(t)\right) \left(c_{ij}^{\text{exp}} + c_{ij}^{\text{num}}\right)^{-1} \left(o_j(t,\mathcal{M}) - o_j^{\text{exp}}(t)\right) dt \tag{9.11}$$

where the term $J(\mathcal{M})$ corresponds to a misfit function between model and observations,

$$p(\mathcal{M})\big|_{\mathcal{C}=\mathcal{C}_i} = k_4 e^{-J(\mathcal{M})} \tag{9.12}$$

where the constant k_4 is derived from the theorem of total probability applied over all possible models $\mathfrak{M}$, which is integrated by Quasi Montecarlo using a Sobol sequence with 2^{18} points. The best-fitting model is found by minimizing $J(\mathcal{M})$ instead of maximizing $p(\mathcal{M})$ since,

$$\hat{\mathcal{M}} = \underset{\mathcal{M}}{\text{argmax}} \left\{ p(\mathcal{M})\big|_{\mathcal{C}=\mathcal{C}_i} = k_4 e^{-J(\mathcal{M})} \right\} = \underset{\mathcal{M}}{\text{argmin}} \left\{ J(\mathcal{M}) \right\} \tag{9.13}$$

The probabilistic nature of the reconstruction is partly motivated by the fact that the model itself may not necessarily reproduce the experimental setup, but is just an approximation. If several models are candidates based on different hypothesis about the system, the former probabilistic formulation of the inverse problem will be shown to be able to provide information to rank them. The bottom idea is the following: if the model-class (based on

the candidate hypothesis) is considered as an uncertain discrete variable, its probability can eventually be extracted as a marginal probability from Equation (9.7). The probability of each model-class will therefore have the sense of degree of certainty of being true in the sense that the probabilistic conjunction of certainty provided by the experimental measurements and model are coherent.

Let model class $\mathcal{C} \in \mathfrak{C}$ denotes an idealized mathematical model hypothesized to simulate the experimental system, whereas model $\mathcal{M}$ denotes the set of model parameters that the model-class depends on. Different model classes can be formulated and hypothesized to idealize the experimental system, and each of them can be used to solve the probabilistic inverse problem, yielding different values of model parameters. To select among the infinitely many possible model classes that can be defined, a probabilistic criteria can be defined based on their compatibility between prior information about observations $\mathcal{O}$, model parameters $\mathcal{M}$ and model class $\mathcal{C}$, and probabilistic model information [148].

The goal is to find the probability $p(\mathcal{C})$, understood as a measure of plausibility of a model class $\mathcal{C}$ [307]. It can be derived as the marginal probability of the posterior probability $p(\mathcal{O}, \mathcal{M}, \mathcal{C})$ defined in Equation (9.7),

$$p(\mathcal{C}) \;=\; \int_{\mathfrak{O}} \int_{\mathfrak{M}} p(\mathcal{O}, \mathcal{M}, \mathcal{C}) d\mathcal{M} d\mathcal{O} \;=\; k_1 p^0(\mathcal{C}) \int_{\mathfrak{O}} \int_{\mathfrak{M}} \frac{p^0(\mathcal{O}) p^0(\mathcal{M}) p^m(\mathcal{O}|\mathcal{M}, \mathcal{C})}{\mu(\mathcal{O})} d\mathcal{M} d\mathcal{O} \tag{9.14}$$

Once $p(\mathcal{C})$ is computed for every class, its value allows to rank the models according to how compatible they are with the observations. This also allows us to find a correct trade-off between model simplicity (i.e. low number of model parameters) and fitting to observations (i.e. reasonably low system identification error).

In the case that the model parameters m are Jeffrey's constants, they can be replaced by unitary logarithmic parameters $\overline{m}$,

$$m_m \;=\; m_m^0 e^{\overline{m} \ln\left(m_m^1 / m_m^0\right)} \tag{9.15}$$

which maps the dimensional parameters m_m from the preferential range $m_m \in [m_m^0, m_m^1]$ to a non-dimensional Jeffrey's parameter range $\overline{m} \in [0, 1]$. This furthermore stabilizes the search algorithms and, in this case, the noninformative distribution $\mu(\mathcal{M})$ can just be replaced by a constant.

Part IV

RESULTS

10

Evaluation of the digital signal model

In this chapter, we evaluate the performance of the digital signal model for describing multilayered specimens. In Section 10.1, we propose a synthetic comparison between the TM formalism and our novel model. Section 10.2 presents an experimental validation where the signals predicted by our model are contrasted against signals obtained experimentally.

10.1 Synthetic comparison between the TM formalism and the digital signal model

In this section, a numerical study is carried out to compare our novel digital signal model with the TM formalism. For the sake of verisimilitude, the numerical characteristics (e.g. material, frequency, etc.) of that experiment are chosen according to the experimental framework described in Section 9.2.2. That is, we model ultrasonic signals that mimic the measurements used to characterize a CFRP composite plate obtained using a through-transmission configuration with a low-frequency ultrasonic signal containing a wide range of frequencies. Considering the transmitter as a damped mechanical system with a single degree-of-freedom, the Fourier transform of the input signal $X(F)$, with $F = \Omega/2\pi$, is often assumed to be Gaussian [308] with the center frequency F_c of the transducer as mean and half bandwidth B as standard deviation. Hence,

$$X(F) = \frac{1}{\sqrt{2\pi}B} e^{-\frac{(F-F_c)^2}{2B^2}} \tag{10.1}$$

where the frequencies F, F_c and B are expressed in Hertz. The characteristics of the transmitted wave are set to $F_c = 5$ MHz and $B = 2.5$ MHz, respectively. A high resolution is chosen for signal sampling with a frequency $F_s = 200$ MHz, while a signal period of 10 μs is considered in order to ensure the capture of several wave echoes, providing $N = 2000$ samples. The resulting discrete-time input signal $x(n)$ and its magnitude spectrum $|X(\omega)|$ are shown in Figure 10.7.

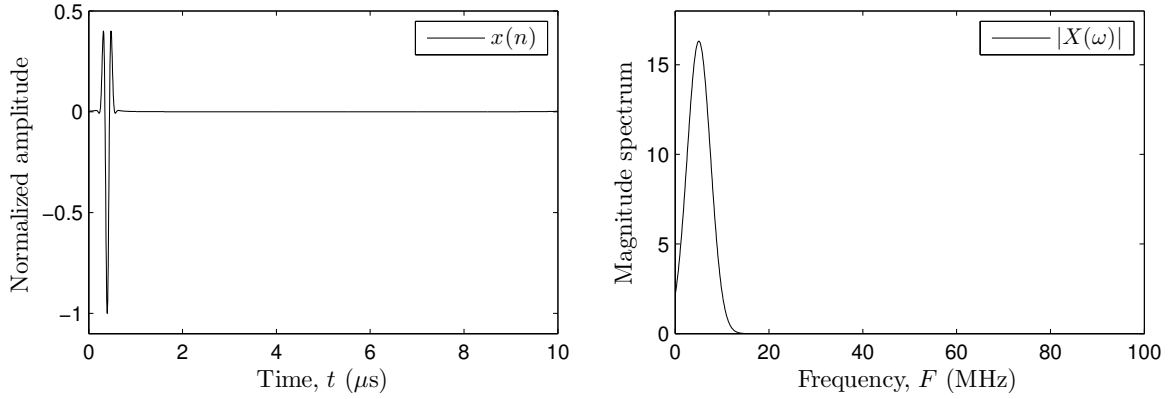

Figure 10.1: *Discrete-time input signal $x(n)$ (left) and its magnitude spectrum $|X(\omega)|$ (right). Note that the abscissas have been scaled with sampling frequency $F_s = 200$ MHz.*

The specimen considered is a layered CFRP symmetric plate which consists of five layers. Since a major damage mode in composites is delamination, an interface layer of much smaller thickness than both plies and wavelength of the central frequency is assumed between every two consecutive layers in the material. Thus, the resulting multilayered specimen consists of $M = 9$ layers, whose mechanical and geometrical properties are summarized in Table 10.1. These properties are chosen according to the experimental values provided in Table 9.3.

Layer (n°)	Young Modulus E $[GPa]$	Poisson Ratio ν $[-]$	Density ρ $[kg/m^3]$	Attenuation $\alpha \cdot 10^6$ $[m^{-1}]$	Thickness a $[mm]$
I, V	12.0427	0.2937	1874.7	2.3059	0.255
II, IV	8.9068	0.3148	1456.4	2.3059	0.185
III	7.0132	0.3308	1140.1	2.3059	0.770
$\mathcal{I}$	5.1321	0.3500	1002.0	2.3059	0.010

Table 10.1: *Mechanical and geometrical properties of the layers $I - V$ and interfaces $\mathcal{I}$ that compose the multilayered specimen used for the experimental comparison.*

From these properties, a discrete-time transfer function $H^D(z)$ can be obtained through Equation (7.25). Figure 10.2 depicts the numerator $N(z)$ and denominator $D(z)$ coefficients of this function for the considered specimen. As can be observed, and in accordance with the discussion in Section 7.4, the numerator consists of a single coefficient $b_0 = 0.86$ at a sample-equivalent delay equal to the total thickness of the plate $\Lambda = 114$, while the denominator is mostly composed of zeros (as predicted from Equations (7.24)-(7.25)).

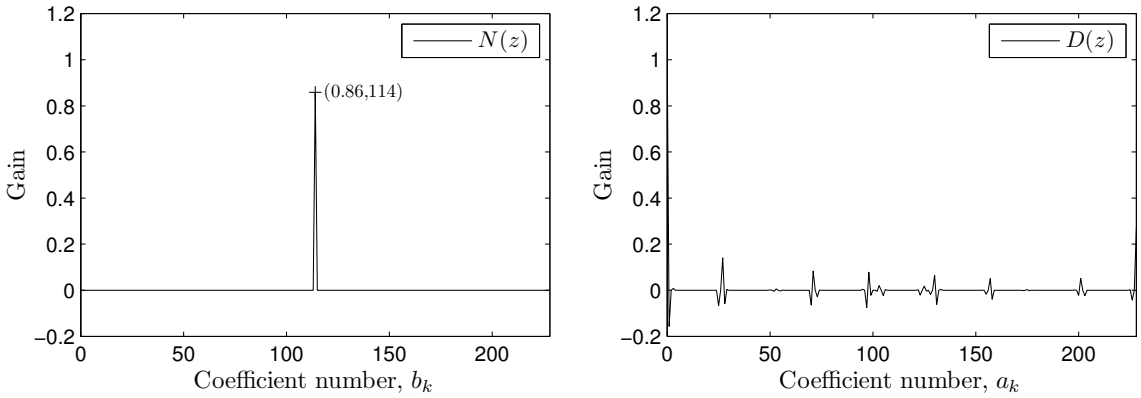

Figure 10.2: Representation of the numerator $N(z)$ (left) and denominator $D(z)$ (right) coefficients from the discrete-time transfer function $H^D(z)$ for an undamaged specimen.

Similarly, a transfer function can also be obtained for a damaged specimen. We briefly recall that, in CFRP plates, three phases of impact damages can be roughly identified, namely (1) matrix cracks in intermediate or back-wall layers, (2) delaminations between layers of different orientation, and (3) fiber breakage [235]. To illustrate the influence of impact damages on the filter coefficients, we impose matrix cracks (stiffness reduction of 5 %) to the back-wall layer (V) and a delamination between layers IV and V, modeled as a stiffness reduction (75 %) of the interface layer $\mathcal{I}$ in-between.

Figure 10.3 shows the transfer function coefficients for this synthetically damaged specimen. The shift ($\Lambda = 115$) and gain loss of the coefficient $b_0 = 0.64$ indicate a wave velocity and amplitude reductions, which are strongly correlated with a stiffness reduction and attenuation increase of the material, respectively. Furthermore, the damage tends to affect almost all the denominator coefficients a_k in amplitude, whereas additional coefficients appear at new positions (due to the symmetry break of the plate structure), thus reducing the sparsity $||a_k||_0$. Unfortunately, a deeper physical interpretation from the a_k-domain is not easily assessable.

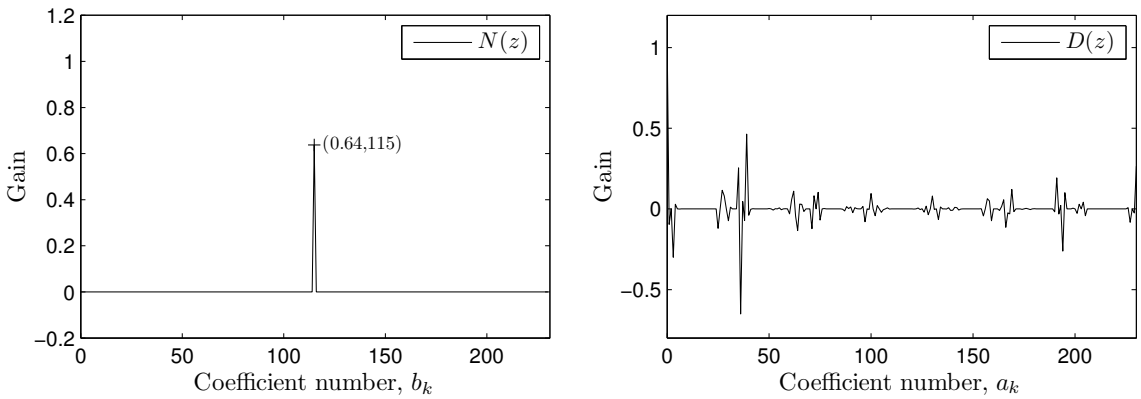

Figure 10.3: Representation of the numerator $N(z)$ (left) and denominator $D(z)$ (right) coefficients from the discrete-time transfer function $H^D(z)$ for a synthetically damaged specimen.

As commented in Section 7.4, the digital signal model enables to obtain the output signal $y(n)$ directly by filtering. Thus, Figure 10.4 compares the discrete time-domain signals obtained with the digital signal model (labeled as $y_{DSM}(n)$) and the TM formalism (labeled as $y_{TM}(n)$). The undamaged case is represented in the left figure (a), whereas the damaged one is depicted in the right figure (b). Note that the digital signal model provides results nearly identical to those obtained with the TM formalism, but in a simpler way.

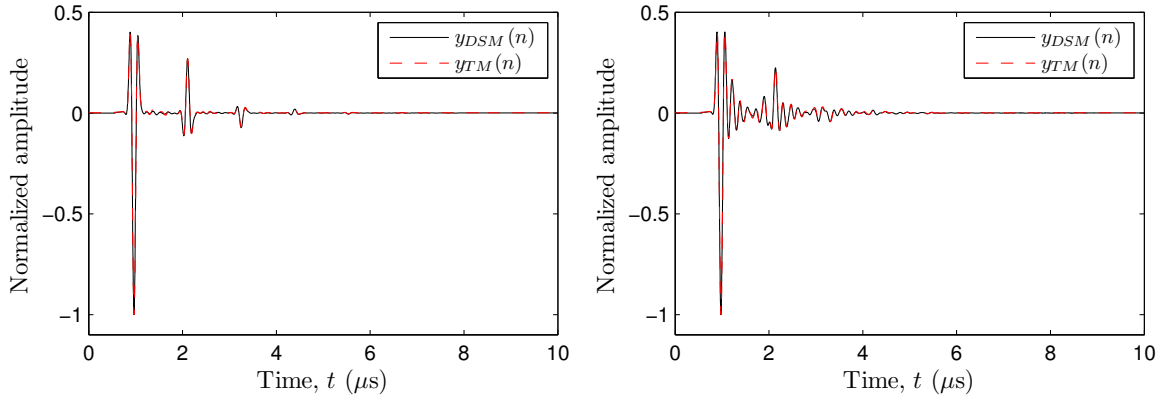

(a) Undamaged

(b) Damaged

Figure 10.4: (a) Time-domain signals $y_{DSM}(n)$ and $y_{TM}(n)$ obtained for the undamaged specimen through the digital signal model and the TM formalism, respectively. (b) Similar comparison for the damaged specimen.

Since a bare visual inspection of the time-domain signals does not enable us to detect discrepancies between both formalisms, a further comparison is performed in the frequency-domain. The spectrum of the output signal provided by the digital signal model can easily be obtained by evaluating z in the unitary circle, namely $Y(\omega) = H(\omega)X(\omega)$ with $H(\omega) = H^D(z)|_{z=e^{j\omega}}$. In contrast, the spectrum of the output signal obtained with the TM formalism is directly derived from Equation (6.22) in a sampled form $Y(\omega_k)$. The magnitude and phase spectra for the undamaged specimen are depicted in Figure 10.5, while Figure 10.6 shows them for the synthetically damaged specimen.

Those figures show that the TM formalism and the digital signal model provide again nearly identical results. However, the latter has the advantage that the computation of the frequency response is analytical and independent of the number of samples. Finally, the scarce discrepancies between both formalisms can be explained as follows: Actually, both methods deliver approximations of the underlying ideal spectrum of the output signal $Y_{ideal}(\omega)$. On the one hand, the sampled spectrum obtained with the TM formalism differs from the ideal one due to the inherent resolution loss of the DFT. The latter effect may be reduced by increasing the number of samples of the input signal (by zero-padding), at the cost of a higher computational resources (increased number of $\boldsymbol{P}^{(k)}$- and $\boldsymbol{T}^{(k)}$-matrices). On the other hand, the frequency response obtained with the digital signal model deviates also

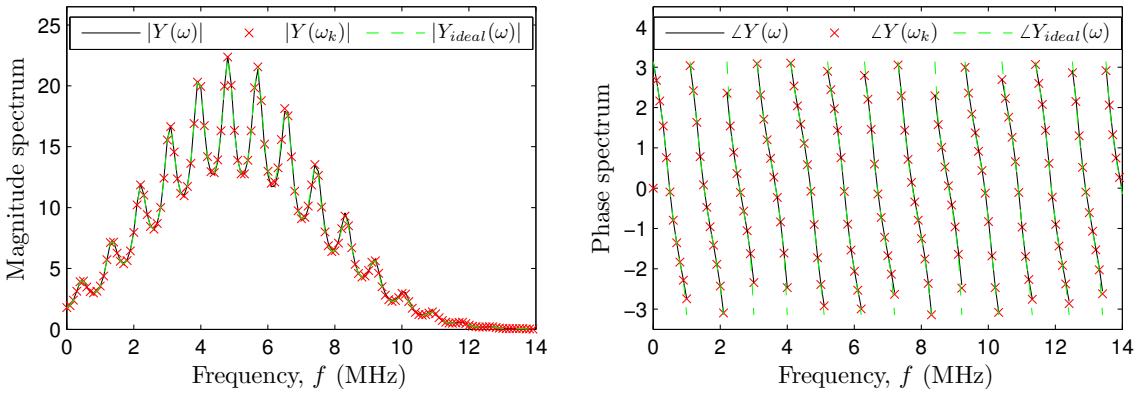

Figure 10.5: Analytical magnitude ($|Y(\omega)|$) and phase ($\angle Y(\omega)$) spectra obtained with the proposed digital signal model (continuous line) for the undamaged specimen, together with the sampled versions obtained with the TM formalism (discrete crosses).

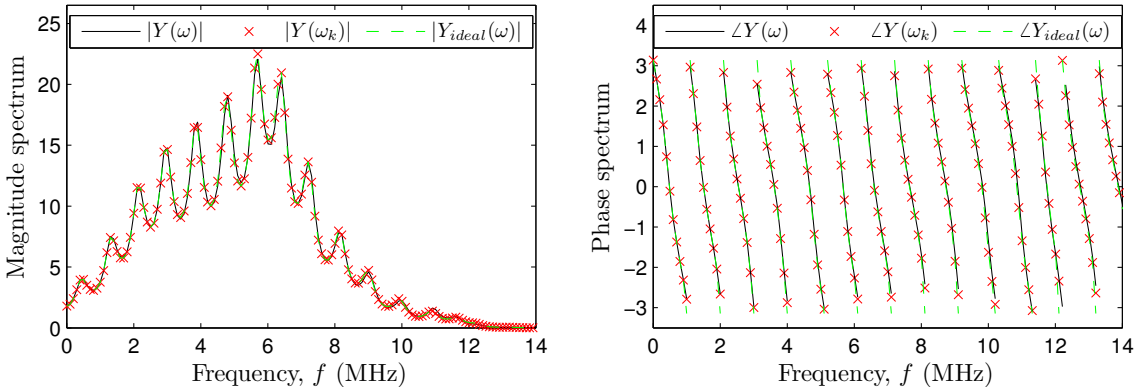

Figure 10.6: Analytical magnitude ($|Y(\omega)|$) and phase ($\angle Y(\omega)$) spectra obtained with the proposed digital signal model (continuous line) for the synthetically damaged specimen, together with the sampled versions obtained with the TM formalism (discrete crosses).

from the ideal one since the delays m_i are restricted to integer values. As mentioned in Section 7.4, increasing the sampling frequency or applying a fractional filter formalism helps to mitigate this problem. This also increases the computational cost but to a lesser extend than zero-padding in the TM formalism (only the input signals are longer, but the number of non-zero coefficients a_k remains constant).

10.2 Experimental validation

In the previous chapter, we already showed that the TM formalism and the digital modeling of the specimen were nearly equivalent. The present chapter aims at demonstrating the capability of the digital modeling of the specimen to predict the measurements obtained from several multilayered specimens (see Section 9.2.1). To evaluate the performance of that model, we propose to follow the next steps: Firstly, we need to determine the density of the single layers by measuring their volume and weight. The second tackled problem is

the calibration of the model with the signals experimentally obtained from the single layers. Then, the density and the values delivered by the calibration are used as input in the model to simulate the propagation through layered specimens. The key concept is to examine if the model can visually reproduce complex situations where numerous echoes overlap. A further criterium is to observe if the residuals contain components other than measurement noise [309]. Finally, some aspects related to the coefficients of the obtained digital filters are discussed.

The calibration is achieved by the matching procedure described in Section 9.3.1, in which two model parameters (the wave velocity and the attenuation coefficient) are adjusted with GA's to find the optimal model parameters characterizing the single layers. In this case, the minimization is a carried out in the time-domain. Basically, from the mechanical and geometrical properties, a discrete-time transfer function $H^D(z)$ can be obtained through Equation (7.25) for each single layer. Consequently, given a discrete-time input signal $x(n)$, the digital modeling of the specimen enables us to obtain the output signal $\tilde{y}(n)$ directly by filtering. Then, the latter is compared to the corresponding output signal $y(n)$ obtained experimentally. It is worth to mention that the input signal used here is not the synthetic one described in Figure 10.7, but an advanced version of the output signal measured in water (by removing the sample) depicted in Figure 9.3. Indeed, such a strategy allows us to take into account the transducers effect within the wave propagation simulation.

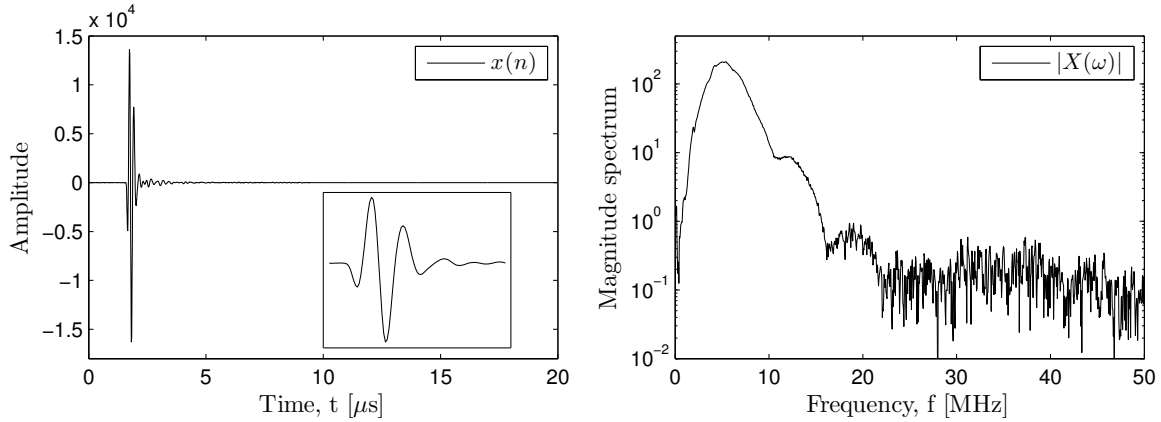

Figure 10.7: *Discrete-time input signal $x(n)$ (left) and its magnitude spectrum $|X(\omega)|$ (right) used as excitation for the synthetic layered specimens ($F_c = 5.5$ MHz). Note that the abscissas have been scaled with sampling frequency $F_s = 100$ MHz.*

Such calibration step has been applied to each measurement area and each frequency, and thus enables us to obtain statistically relevant range values for the mechanical properties of those single layers. The mean and standard deviation derived from those values, along with the density values, are summarized in Table 10.2. As can be observed, these values are in good agreement with those reported in Table 9.1. The values for specimens $S_{1,2}$, $S_{1,3}$ and $S_{1,5}$ are particularly close to those tabulated in the literature, whereas the values

for specimens $S_{1,1}$ and $S_{1,4}$ slightly differ from them. Nonetheless, one could have anticipated such discrepancy, since the density values for those specimens already indicated some divergence with respect to the expected values[1].

Specimen	Material	Density ρ [kg/m^3]	Wave velocity c_p [m/s]		Attenuation α [Np/m]	
			5.5 [MHz]	6 [MHz]	5.5 [MHz]	6 [MHz]
$S_{1,1}$	Aluminium^a	2876	6198 ± 8	6200 ± 9	49.0 ± 1.7	49.7 ± 1.4
$S_{1,2}$	Aluminium^b	2663	6382 ± 14	6377 ± 13	24.6 ± 0.2	24.3 ± 1.0
$S_{1,3}$	Brass	8626	4207 ± 12	4206 ± 14	23.0 ± 2.0	23.2 ± 2.0
$S_{1,4}$	PMMA^a	1168	2613 ± 3	2614 ± 2	105.8 ± 7.2	98.1 ± 5.0
$S_{1,5}$	PMMA^b	1195	2681 ± 4	2682 ± 2	69.4 ± 1.2	71.7 ± 1.1

Table 10.2: *Mechanical properties of the traditional materials obtained from the calibration procedure.*

Figure 10.8 depicts the resulting matching (for the optimal model parameters) between a measurement $y_{S_{1,j}}(n)$ and the numerically predicted model $\tilde{y}_{S_{1,j}}(n)$ for the single layers, $\forall j = 1, \ldots, 4$. As can be seen, fairly good matching is obtained.

The residuals $e_{S_{1,j}}(n)$ are plotted in Figure 10.9 to highlight which parts of the wave responses the model could not reproduce. As can be observed, there are two main sources of modeling error. The first one is common to all materials and is highly correlated to the signal echoes. This *approximation* error approximately amounts to 10% of the signal's amplitude, and can thus be considered as acceptable. It arises foremost from two factors: (1) the modeled signal can diverge from the experimental one since the delays m_i are restricted to integer values, and (2) the layers are idealized as homogeneous material (however, microheterogeneities might be present in the material, which are not contemplated in the model). The second error is common to all metals and can be considered as a *phenomenological* error. Indeed, some echoes with nearly constant amplitude (noticeable in the upper left plot of Figure 10.8) are definitely not present in the model. Those echoes are hypothesized to be transversal waves (S-waves) originated by longitudinal waves (P-waves) due to some superficial or contact effects (e.g. mode conversion due to a nonplanar water-specimen interface). It is therefore not surprising that the model does not reproduce them, since it has been developed to cope only with longitudinal waves. In any case, this *phenomenological* error has an even lower amplitude than the *approximation* one.

From the properties obtained in Table 10.2, a discrete-time transfer function $H^D(z)$ can directly be obtained for each multilayered configuration enumerated in Table 9.2. The resulting matching between a measurement $y_{S_{2,j}}(n)$ and the numerically predicted model $\tilde{y}_{S_{2,j}}(n)$

[1]Consequently, those results suggest that specimen $S_{1,1}$ probably is an alloy made of aluminum and some other metal. In the same vein, specimen $S_{1,4}$ might be a plastic material with nearly similar properties to PMMA (e.g. PEEK, etc.). Those differences are definitely not surprising, since the samples were obtained from residual laboratory materials, and in no case they discredit the results.

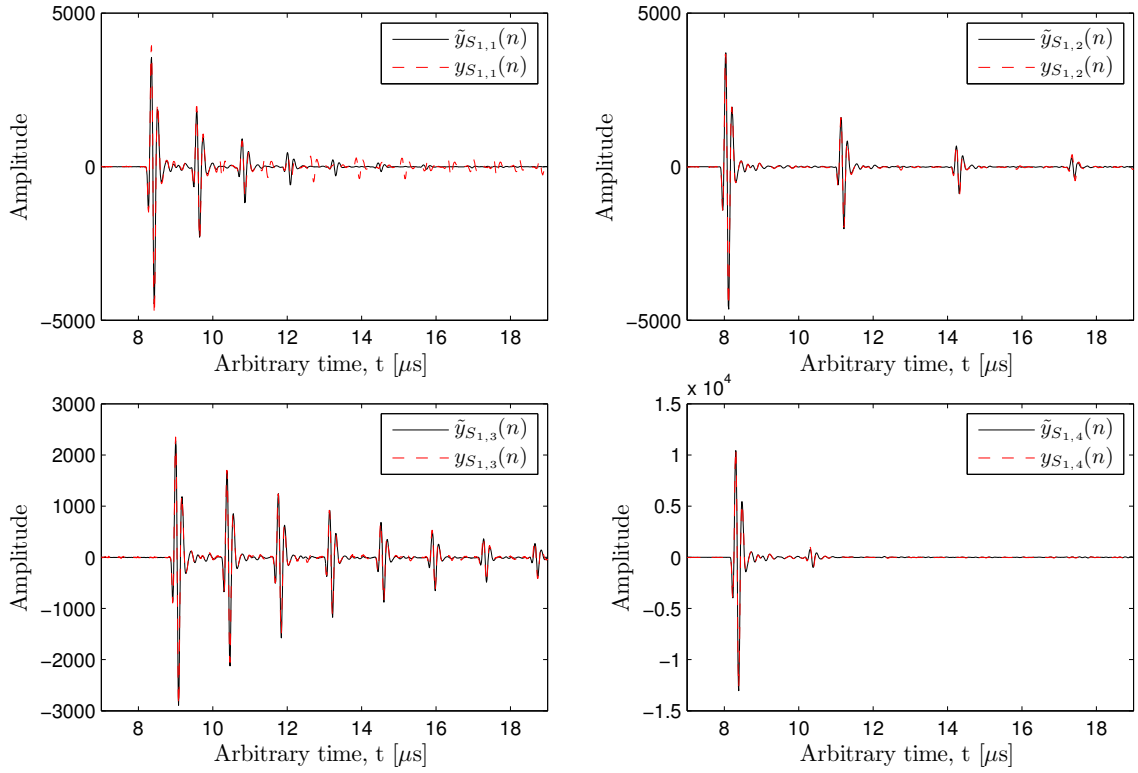

Figure 10.8: *Comparison between experimental measurements and signals predicted by the digital signal model for the single layers* $S_{1,j}$, $\forall i = 1, \ldots, 4$.

for the bi-layered specimens, $\forall j = 1, \ldots, 4$, is depicted in Figure 10.10. Note that the right plots represent the same specimens as in the left plots, but measured in their reverse side. Again, fairly good matching is obtained between the experimental and modeled signals. In addition, left and right plots are nearly similar and further support both the reproducibility of the experiment and the capability of the model to predict the measurements. The slight discrepancy in amplitude can be explained as follows: The layered specimens were disassembled and mounted again between each specific measurement, and this task possibly leads to slight changes in the contact pressure between the single layers, which in turn leads to a small alteration of the wave front amplitude. Finally, it is noteworthy that the transversal waves were almost completely filtered out by the plastic layer.

Figure 10.11 depicts the resulting matching between a measurement $y_{S_{3,j}}(n)$ and the numerically predicted model $\tilde{y}_{S_{3,j}}(n)$ for the three-layered specimens, $\forall j = 1, \ldots, 2$. The obtained matching between the experimental and modeled signals is reasonably good again. As for the bi-layered case, the right plot is again nearly identical to the left one, except for the slight amplitude difference. In such a configuration, the transversal waves are now totally absorbed by both plastic layers.

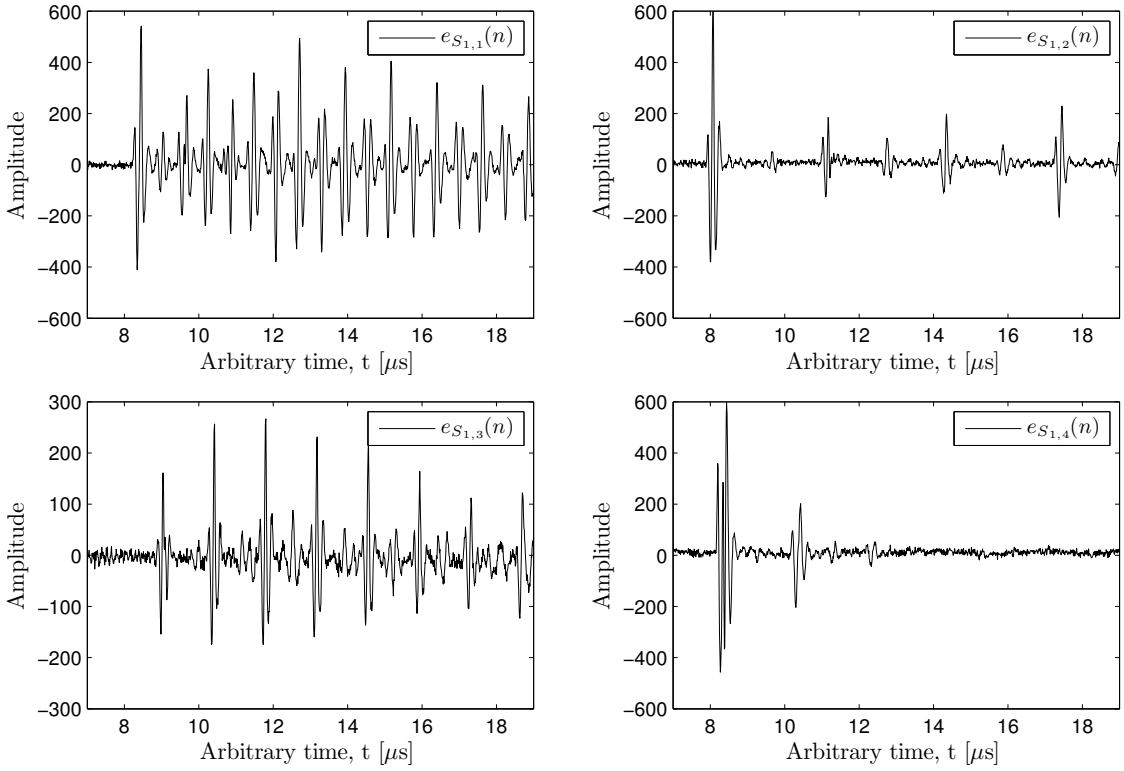

Figure 10.9: *Error between experimental measurements and signals predicted by the digital signal model for the single layers* $S_{1,j}$, $\forall i = 1, \ldots, 4$.

Finally, the resulting matching between a measurement $y_{S_{4,j}}(n)$ and the numerically predicted model $\tilde{y}_{S_{4,j}}(n)$ for the four-layered specimens, $\forall j = 1, \ldots, 4$, is depicted in Figure 10.12. In this case, the obtained matching between the experimental and modeled signals is remarkable, especially because in this situation, numerous and overlapped echoes are observable. This configuration definitely supports the potential of our model to face up complex wave responses originated from multilayered specimens.

A further inspection of the modeling error shows that the residuals $e_{S_{4,j}}(n)$ $(j = 1, 4)$ now only contain few components other than measurement noise, i.e. the *phenomenological* error has entirely disappeared and the *approximation* error has a more random distribution. One can thus conclude that this model can satisfactorily be used to describe multilayers.

Finally, the numerator $N(z)$ and denominator $D(z)$ coefficients of the discrete-time transfer function for the specimen $S_{4,4}$ is shown in Figure 10.14. As expected, the numerator consists of a single coefficient $b_0 = 0.0291$ at a sample-equivalent delay equal to the total thickness of the plate $\Lambda = 1315$, and the denominator is mostly composed of zeros (only 32 non-zero coefficients from 2631).

Although a rigorous physical interpretation from the a_k-domain is not easily assessable, it is noteworthy that the number of non-zero coefficients a_k is not directly related to the number of observable echoes in the wave response. Consequently, this model based on the physical properties of the layers seems to be more coherent than the proposals based on

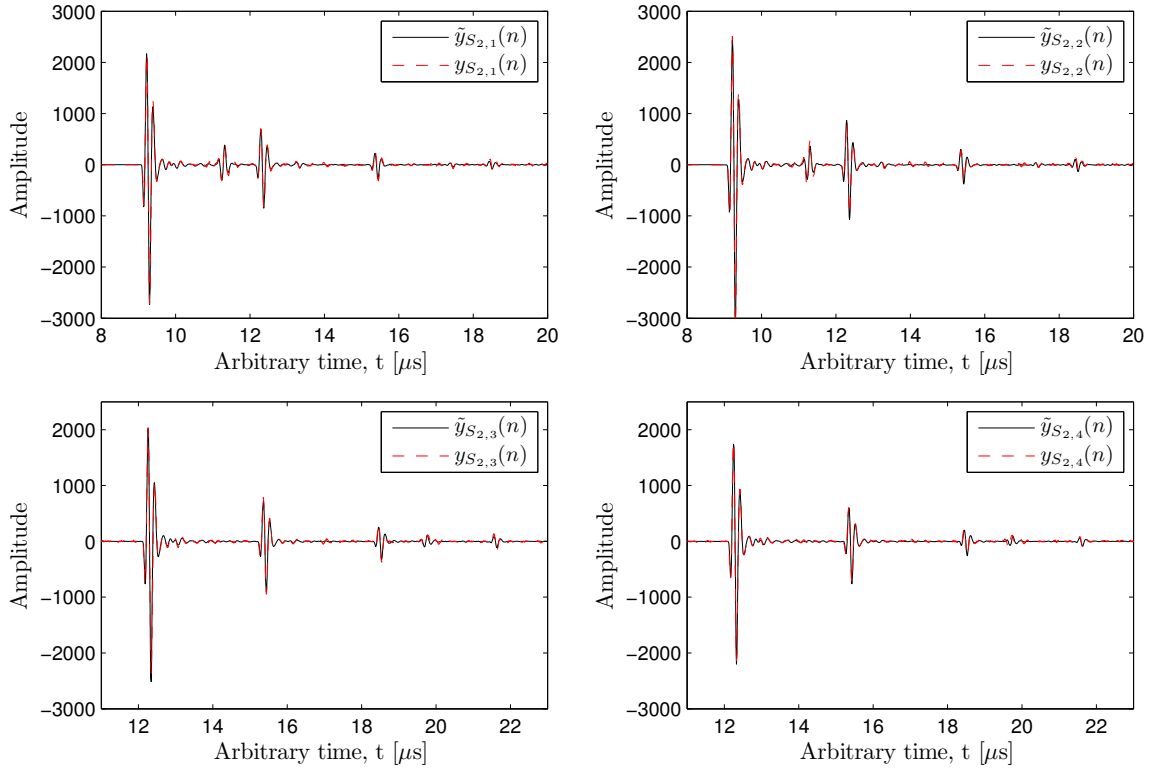

Figure 10.10: *Comparison between experimental measurements and signals predicted by the digital signal model for the bi-layered specimens* $S_{2,j}$, $\forall i = 1, \ldots, 4$.

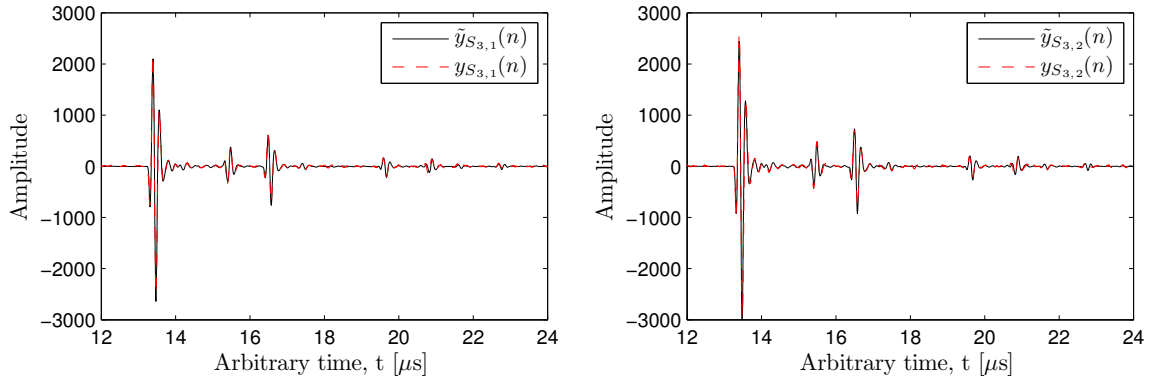

Figure 10.11: *Comparison between experimental measurements and signals predicted by the digital signal model for the three-layered specimens* $S_{3,j}$, $\forall i = 1, \ldots, 2$.

Bernoulli-Gaussian models, which assume that the output signal is made of superimposed Gaussian echoes that are time-shifted, amplitude-scaled, and noise-corrupted version of the input signal [111, 130]. In addition, those coefficients appear to follow a kind of repetitive pattern, since the coefficients distribution from coefficient a_{1227} is sign-changed and amplitude-reduced version of that starting at a_1.

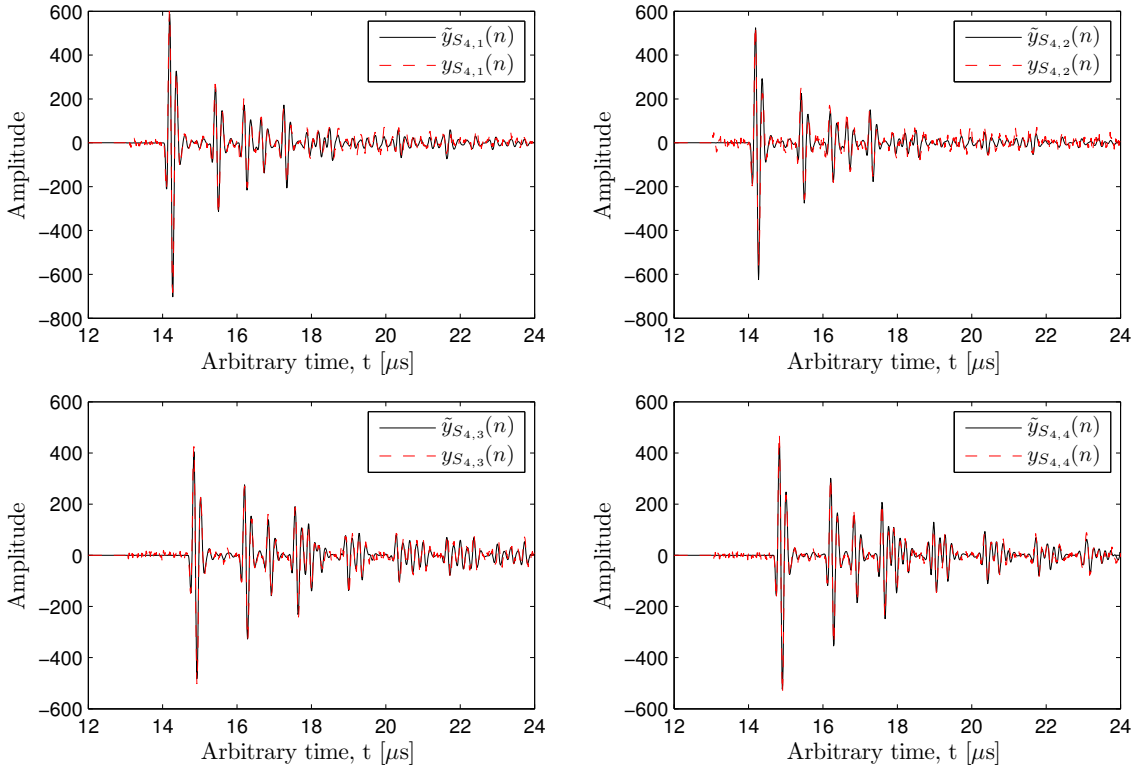

Figure 10.12: *Comparison between experimental measurements and signals predicted by the digital signal model for the four-layered specimens* $S_{4,j}$, $\forall i = 1, \ldots, 4$.

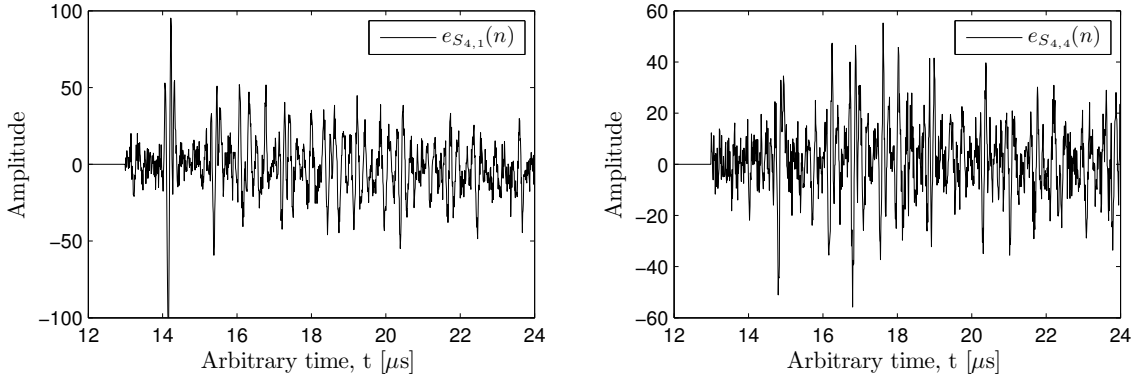

Figure 10.13: *Error between experimental measurements and signals predicted by the digital signal model for the four-layered specimens* $S_{4,j}$, $\forall i = 1, \ldots, 4$.

10.3 Discussion

Be aware the the TM formalism could also be applicable in principle, but its direct implementation has been found to suffer from numerical instabilities, particularly when considering layers of large thickness and high-frequency ultrasound (i.e. the large *frequency-thickness* products that arise in this formalism are usually referred to as the large "fd-problem" [78]). Indeed, the layered configurations presented here deal with relatively large layers, whereas the used frequencies are also relatively large (that is, the wave lengths corresponding to those frequencies are particularly small compared to the size of the layers). To evaluate the

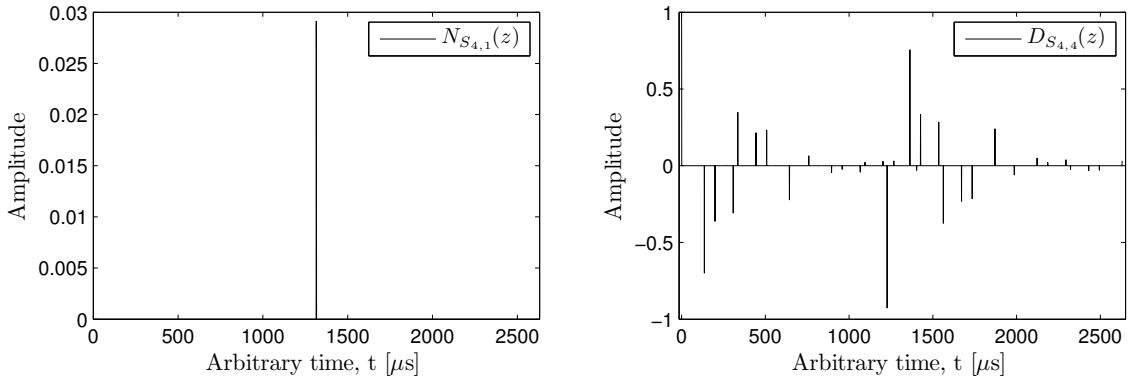

Figure 10.14: *Representation of the numerator $N(z)$ (left) and denominator $D(z)$ (right) coefficients from the discrete-time transfer function $H^D(z)$ for a four-layered specimen.*

applicability of the TM formalism in this case, let us consider the specimens $S_{1,1}$ and $S_{4,3}$, in order to cover a broad range of specimen's thicknesses. Figure 10.15 depicts the output signals $\hat{y}_{S_{1,1}}(n)$ and $\hat{y}_{S_{4,3}}(n)$ predicted by the TM formalism for a single layer and a four-layered specimen. As can be observed, both cases suffer from numerical instabilities, even when considering a single layer that is relatively thin. These anomalies are due to the poor conditioning of the transfer matrices when performing multiplications that combine both decaying and growing terms. In the first case (left plot), we represent the waveform obtained while considering only the stable frequencies (approximately up to 15 MHz). As can be seen, the resulting signal covers a coherent amplitude range, but the waveform is completely altered. In the second case (right plot), we represent again the waveform obtained while considering only the stable frequencies (approximately up to 10 MHz). In such a case, the signal is a sine-wave at a low-frequency, but with a huge amplitude.

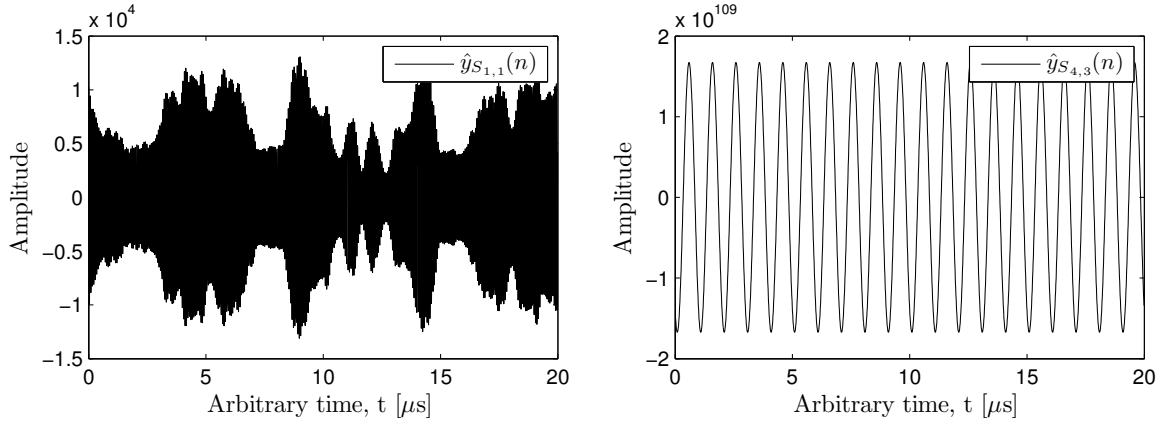

Figure 10.15: *Examples of numerical instabilities that may arise in the TM formalism in the case of large "fd-problems".*

As commented in Section 3.3.1, many modifications of the original TM approach and other slightly alternative methods have been proposed to palliate this precision problem. However, none of them is really efficient when dealing with complex problems (i.e. some

suffer from high computational resources, whereas others are limited to multilayered materials that consist of a reduced number of layers). To conclude, Table 10.3 summarizes the strengths and limitations of the digital signal model with respect to the original TM approach.

Models	Digital signal model	TM approach
Strengths	◦ Very-low complexity ◦ Valid for any number of layers ◦ Valid for absorbing layers ◦ Valid for layers of unequal wave-travel time ◦ Suitable for large "fd-problems" ◦ Enables to compute the underlying sparse transfer function	◦ Low complexity ◦ Valid for any number of layers ◦ Valid for absorbing layers ◦ Valid for layers of unequal wave-travel time
Limitations	◦ Limited to integer delays	◦ Depends on the input signal's appearance ◦ Depends on the number of samples of the input signal Unstable for large "fd-problems"

Table 10.3: *Strengths and limitations of the novel digital signal model.*

11

Robust parametrization for damage detection in CFRP plates

In this chapter, we propose three different signal modeling approaches for parametrizing ultrasonic signals and evaluate their discriminative capability for damage identification in CFRP plates.

11.1 Classical spectral estimation methods

In this section, some enhancements on the interpretation are done by adapting classical parametrization techniques to extract relevant features from the ultrasonic signals. Thus, a cepstral-based feature extractor is firstly designed and optimized by using a classification system based on *cepstral* distances. Then, this feature extractor is applied in an analysis-by-synthesis scheme which, by using a numerical model of the specimen, infers the values of the damage parameters.

11.1.1 Ultrasonic NDE framework

Signal acquisition and preprocessing

The specimen used here is that described in Section 9.2.2. After acquisition, the captured signals are preprocessed in order to provide a suitable representation of the ultrasonic signal. In a first step, the signals have been decimated at a sample frequency f_s of 20 MHz, in order to reduce part of the noise and focus on the frequency band of interest. Then, the signals have been multiplied by a Hamming window. In our case the window is foremost used to weight the signal samples over the time.

Damage detection and assessment

To design a signal processing system that provides a robust parametrization of the signals with a high discriminative capability between the different damage levels, a classification system based on *cepstral* distances has been developed. For an optimal use of the available data set, the training/test is performed using the *leaving-one-out* technique. Therefore, 39 signals are used to train a reference *cepstral* vector corresponding to a certain damage level, while the remaining signal is used for the test. Rotating the measurements enables us to train the system always with 39 signals, while testing it with $6 \times 40 = 240$ signals. The efficiency of the system is evaluated by defining a weighted error factor. Let the results of the test be a confusion table $R(i,j)$, with $i = 1, ..., 6$, where $R(i,j)$ represents the measurements number at damage level i that have been classified as a damage level j. The weighted error factor is then defined as,

$$w_{err}\,[\%] \quad = \quad 100 \times \frac{\sum_{i=1}^{6}\sum_{j=1}^{6} R(i,j) \cdot \frac{|i-j|}{3}}{240} \tag{11.1}$$

On the other hand, the goal of the NDE is to finally provide consistent damage information that characterize the specimen health state. To this end, the inverse problem strategy described in Section 9.3 is applied to find the values of the damage parameters $(\mathbf{p})$ that best fit the experimental measurements. For this experiment, the model used to idealize the experimental system describing the ultrasonic waves propagation in multilayered composites consists of the TM approach. The damage parameters identification is performed according to Fahim *et al.* [310], assuming that the damage in each layer, respectively in each interface, is strongly correlated with a reduction of the Young modulus. GA are applied as optimization algorithms.

11.1.2 Cepstral-based feature extractor design and optimization

Signal windowing

First, the selection of a suitable analysis window is considered. In this case, a classical Hamming window has been applied to the ultrasonic signals. As illustrated in figure 11.1, while in the original signal (left) predominates the first peak (wave front), the windowed signal (right) exhibits accentuated echoes amplitude, representative of the successive reflections of the transmitted pulse between the interface specimen/transducers.

Windowed signals are then transformed to the cepstral-domain. This experiment focuses on the *real cepstrum* $c(n)$, which is defined by means of the following expression:

$$\log|H(\omega)| \quad = \quad \sum_{n=-\infty}^{\infty} c(n) \cdot e^{j\omega n} \tag{11.2}$$

where $H(\omega)$ is the spectrum estimate. Preliminary experiments showed that the *complex cepstrum* do not provide any improvement, while its computation is cumbersome due to the unwrapping of the digital phase. Consequently, only the *real cepstrum* will be considered.

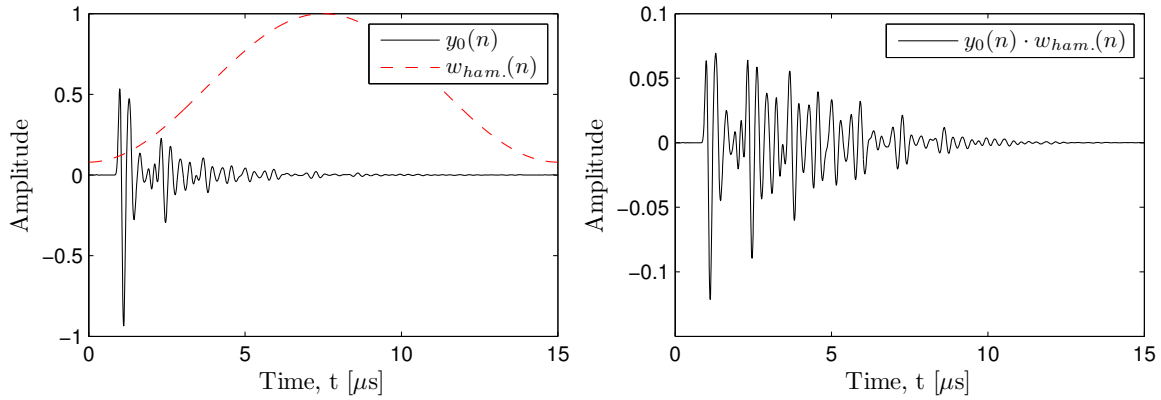

Figure 11.1: *Use of a temporal window to show off the echoes of the ultrasonic signal.*

In order to evaluate the effect of the analysis window and the damage discriminative capability, the following classification results have been compared: The signals obtained in the time-domain using an Euclidean distance (SIGNAL) with the ones obtained by the *real cepstrum* (CR) with an Euclidean (*cepstral*) distance using several lengths for the analysis window. Table 11.1 shows that the use of the Hamming windows improves the classification in comparison with the rectangular one, except for a window that amounts to 100 samples. It can be observed that the echoes are as important as the wave front for discriminating between the different damage level. Therefore, the echoes may be enhanced with a Hamming window, whose optimal longitude amounts to a range of $150 - 300$ samples.

	R-300	H-300	H-200	H-150	H-100
SIGNAL	32.50	26.25	26.11	26.94	30.55
CR	12.08	10.41	9.72	8.88	16.25

Table 11.1: Weighted error obtained for several analysis windows.

Spectrum smoothing

It is common to restrict the Euclidean distance to L *cepstral* coefficients. This process is called *liftering* and not only allows to reduce the number of *cepstral* components in computations but also corresponds to a smoothing of the spectrum, preserving its spectral envelope while removing the fine spectrum information. Applying windows different from the rectangular one also allows to weight the *cepstral*coefficients depending on their discriminative performance. Among them, we demonstrated that a *raised-sine* window can be successfully applied for damage classification using ultrasonic signals [311].

Alternatively we can also smooth the spectrum through signal modeling, based on the vision of the ultrasonic signal as a filter output, where the spectrum estimate is given by its frequency response. In particular, autoregressive (AR) processes are considered. All-pole filters have been found to provide a sufficiently accurate representation for many types of signals in many different applications [213], where as in NDE systems, the pursued information is hidden in a complex signal. If an all-pole model is assumed, an LPC (*linear predictive*

coding) spectrum estimate can be obtained. The expected effect of using a signal modeling that follows an all-pole representation is that the *cepstral* distance will be less sensitive to spurious variations of the spectrum. However, there are some uncertainties regarding this modeling: Determining the order p of the LPC analysis for ultrasonics is an open issue, which do not have an intrinsic meaning as in other applications. The goodness of this modeling will depend on whether or not an AR-modeling is consistent with the way in which the data is generated.

In this work, we have evaluated the effects of smoothing over the discriminative capability of the *cepstrum*. Both approaches, AR modeling and *liftering* have been jointly tested. In order to do this, an experiment has been developed, which consists of obtaining the weighted classification error for different LPC orders and *liftering* window lengths. This experiment will allow us to design an optimal LPC modeling and *liftering* of the ultrasonic signals. The corresponding (bidimensional) results are shown in figure 11.2.

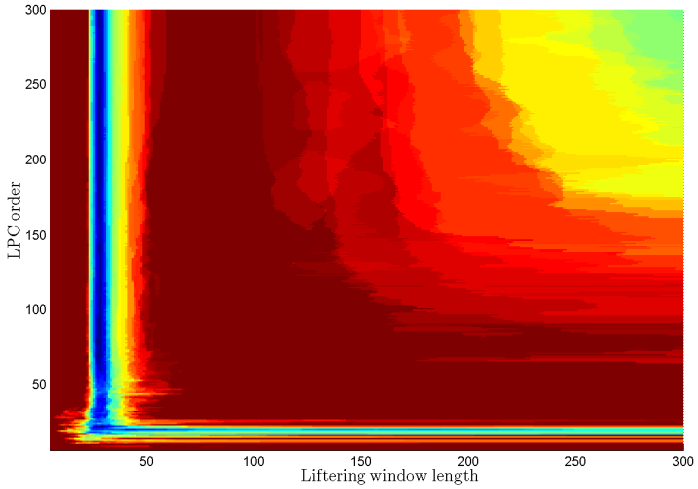

Figure 11.2: *Weighted error with respect to different prediction orders and* liftering *window lengths.*

The obtained results show a clear minimum for a *raised-sine liftering* window, whose length amounts to $28 - 29$ *cepstral* coefficients. Moreover, this minimum appears to be independent of the selected prediction orders, as long as it is high enough ($p > 20$). Therefore, the damage parameters reconstruction will be performed with a *raised-sine liftering* window of 28 samples and a prediction order of 28. It is worth to note that this number coincides with the echo time (in number of samples). This suggests that the *cepstrum* is, in some way, able to test the symmetry in the specimen (undamaged composite is symmetric). When the specimen is damaged, symmetry is usually broken, and a *liftering* window of echo length applied over the *cepstrum* is able to measure it.

11.1.3 Feature extractor validation

This section aims to validate the proposed methodology. The identification of the damage distribution is assessed by considering the following assumptions:

- The damage parameters evolution is monotonically dependent on the damage level.

- Damage, such as delamination, concentrates mostly in the last interfaces, and propagates then internally and nearly symmetrically.

Therefore, the configuration pattern for the damage parameters is restricted to 3 parameters: (p_1) denotes the Young modulus of the extremity layers, (p_2) the Young modulus of the extremity interface, and (p_3) the Young modulus of the middle interface, respectively. Each parameter is defined in a dimensionless and logarithmic scale, with respect to the undamaged state.

The robustness of the analysis-by-synthesis scheme is illustrated in figure 11.3, and compares the results obtained by performing the optimization directly on the time-domain signals with the ones obtained when the aforementioned *cepstral* parametrization is applied. The damage correlation parameters are plotted against the impact energy values. Each box has lines at the median value (red), at the lower and upper quartile values (blue), and whiskers at the minimum and maximum values (black). Outliers are represented by a red cross. In these plots a consistent decrease on the elastic modulus is expected as the damage energy increases.

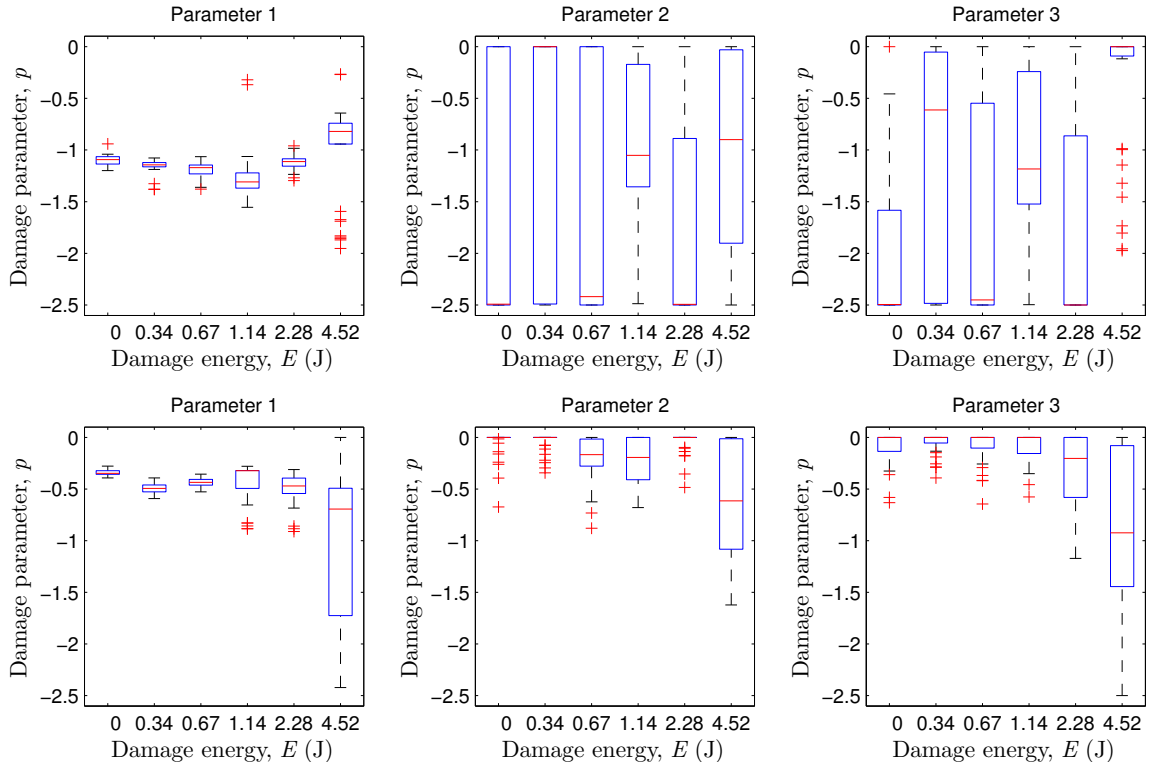

Figure 11.3: *Representation of the damage parameters evolution for simulations performed in the* time-domain *(first row), and* cepstral-domain *(second row).*

It results that the optimization performed in the cepstral-domain leads to a more consistent damage evolution than the one delivered by the time-domain solution. The reduced set of *cepstral* features improves the statistical distribution of the damage parameters: (1) The variability of the damage parameters at each damage level is drastically reduced. (2) The

median values of the damage parameters consistently decrease while increasing the damage level. A careful interpretation allows to observe that delamination (p_2) occur at early stage of the impact energy and increase with the damage level, while delamination (p_3) occur at some later stage of the impact energy, validating the aforementioned hypothesis.

11.1.4 Conclusions

This study shows the capability of the real LPC *cepstrum* to discriminate the damage level of a CFRP plate subjected to different impact energies. The discriminative performance of the proposed parametrization has been evaluated by a system based on *cepstral* distances that recognized the concrete damage level corresponding to a given test signal, leading to the following conclusions: (1) It has been demonstrated that it is necessary to include the wave echoes to perform the analysis. Consequently, they may be enhanced using a suitable analysis window. (2) The *cepstrum* is an appropriated domain to perform a feature extraction. This study has presented a *cepstral* coefficients selection based on the use of a simple *liftering* window with the appropriate size. Ongoing works may include the study of advanced extraction/selection techniques such as discriminative transformations of the feature space (LDA or PCA).

Finally, the *cepstral* parametrization has been inserted in a analysis-by-synthesis scheme, and allowed us to reconstruct consistently the damage parameters corresponding to different impact energies.

11.2 Heuristic sparse signal model

Signal processing has been proven to be an useful tool to characterize damaged materials under ultrasonic nondestructive evaluation. In this work, we hypothesize that the transfer function of multilayered materials for a through-transmission configuration can be represented as a classical all-pole model with sparse coefficients. To test this hypothesis, we propose an analysis-by-synthesis scheme which, by assuming an underlying sparse digital signal model of the specimen, infers the order and extent of the model parameters corresponding to a certain impact damage level. Then, we exploit the sparse structure of the obtained digital filter for practical NDE applications, with emphasis on impact damage identification of carbon-fiber rein- forced polymer plates.

This study presents a digital signal model H(z) to characterize the specimen being tested. An important point of this proposal is to provide a model with a small number of parameters, since low complexity models are desirable for fast, practical and accurate NDE systems. To this end, we assume that the model parameters have a particular sparse distribution, which may be inherently related to the material's mechanical and geometrical properties, and thus to its health state. This hypothesis is based on the conclusions from our previous work [10], where we introduced two different digital signal models based on a simplified physical analysis of the ultra- sonic wave propagation inside a CFRP plate. Results showed that *cepstra* extracted from these models, in which coefficients were distributed at several

lags, were more discriminative than other spectral estimation methods. In the present work, we propose an analysis- by-synthesis scheme, which compares the predicted signals with the ones obtained from laboratory experiments conducted on a CFRP plate [11]. In such a way, by means of a minimization procedure, we obtain the optimal order and extent of the model parameters, and thus show that a sparse signal model may be an useful tool to model wave propagation phenomena in multilayered materials. To our knowledge, our study draws for the first time a parallel between sparse signal modeling and its applications to ultrasonic NDE signal processing.

11.2.1 Material and methods

The proposed methodology consists of three elements: The (1) signal acquisition of the ultrasonic signals obtained from the wave interactions with a CFRP plate (i.e. the specimen tested is the CFRP symmetric plate described in Section 9.2.2), a (2) sparse signal model that idealizes the ultrasound-composite interactions, and is solved by the Prony's method, and an (3) analysis-by-synthesis scheme, which is used to predict the optimal coefficient positions corresponding to a certain damage level.

Sparse signal model

In this work, we propose a digital signal model for wave propagation in multilayered materials. A through-transmission configuration is adopted, representative of the successive reflections that suffer the transmitted signal between layers and specimen/transducers interfaces. In first place, the through-transmission configuration is considered as a discrete-time linear system. Thus, the material under investigation can be represented by a transfer function, which relates the discrete excitation and response signals [114]. Our proposal extends the intuitive physics-based all-pole signal model proposed by Fuentes *et al.* [312], solely inspired by concepts drawn from signal theory. In [312], the authors presented a simplified analysis of the complex wave propagation pattern within the plate, and showed that the model of the damaged specimen could be improved by including a fixed virtual interface which introduces a middle-term and long-term predictor, along with the typical short term predictor, in the transfer function. This model can effectively account for the multiple transmissions/reflections due to the multilayered structure and the damage. This sparse-like distribution of the model coefficients is exploited in our proposal.

However, it must be considered that the structural complexity of the material suggests that flaws may occur at different locations, and that a single virtual interface cannot account for all possible failure mechanisms. Moreover, a fixed interface does not respond to the phenomena associated with crack propagation due to increasing damage energies. Thus, it is reasonable to assume that a multilayered material can be modeled with a sparse transfer function, whose prediction coefficients behave dynamically, depending upon its damage state. We thus assume that the discrete-time transfer function $H(z)$, which represents a multilayered composite material in a through-transmission configuration, can be represented by

a delayed classical all-pole filter with sparse coefficients,

$$H(z) = \frac{bz^{-M}}{1 + \sum_{k=1}^{p} a_k z^{-k}} \tag{11.3}$$

where most of the coefficients a_k are zeros. The polynomial order p of the denominator is $2M$, where M corresponds to a sample delay equivalent to the time needed by the incident wave to cross the total thickness of the multilayered structure [312]. As experimentally observed, the numerator consists of a gain b plus a total thickness-equivalent sample delay M.

Analysis-by-synthesis scheme

The final goal of NDE systems is to provide consistent damage information that characterizes the specimen health state. Our proposal suggests that the underlying mechanical properties of the specimen are inherently associated to the sparse prediction coefficients a_k of the denominator in Equation (11.3). Thus, one may assume that damage will affect those coefficients both in amplitudes and positions. Provided the coefficient position vector $\boldsymbol{k}$, Prony's method allows us to obtain the optimal amplitudes for a filter with a given input/output signals. Unfortunately, there is no method that provides both optimal positions and amplitudes. Thus, we apply an analysis-by-synthesis scheme to find the values of the coefficient position vector $\boldsymbol{k}$ that best fit the experimental response signals $y^{(C)}(n)$, as depicted in Figure 11.4.

Given the transfer function $H^{(C)}(z)$ corresponding to a certain damage class $C \in [0-5]$, the excitation signal $x(n)$ applied to the specimen can be filtered, resulting in an approximation $y_H^{(C)}(n)$ of the experimental response signal $y^{(C)}(n)$ measured from the specimen, and corresponding to the same damage class C. Generally, the model coefficients are found such that the 2-norm of the residual $r(n)$ (the difference between the observed signal and the predicted one) is minimized. In this case, since $H^{(C)}(z)$ is an all-pole filter with sparse coefficients, we can reasonably assume that the optimal predictor is not the one that only minimizes the 2-norm but the one that also leaves the fewest non-zero prediction coefficients, i.e. the sparsest one. Sparsity is often measured as the cardinality, that is the so-called 0-norm [313, 314]. Thus, the specimen can be analyzed by defining a modeling error (or energy) in terms of the mean squared error between the actual response signal $y^{(C)}(n)$ and the modeled response $y_H^{(C)}(n)$, plus a sparsity term that accounts for the number of non-zeros coefficients in the transfer function,

$$f^{(C)} = ||\boldsymbol{r}^{(C)}||_2^2 + \varphi||\boldsymbol{a}^{(C)}||_0 \tag{11.4}$$

where φ is an empirical regularization term, defined so that the modeling error due to the sparsity term corresponds to a certain amount of the least squared error. It is noteworthy that setting $\varphi = 0$ leads to a standard linear prediction form. To account for all the N_r

measurement repetitions within a damage class C, a slightly different cost functional $g^{(C)}$ is introduced as,

$$g^{(C)} = \frac{1}{N_r} \sum_{i=1}^{N_r} f_i^{(C)} \tag{11.5}$$

Then, the parameters $\boldsymbol{k}$ that characterize the coefficient positions are found by a search algorithm that minimizes the cost functional $g^{(C)}$,

$$\hat{\boldsymbol{k}} = \arg\min_{\boldsymbol{k}} g^{(C)} \tag{11.6}$$

Binary genetic algorithms are applied to minimize Equation (11.6), and provide the analysis-by-synthesis optimal solution.

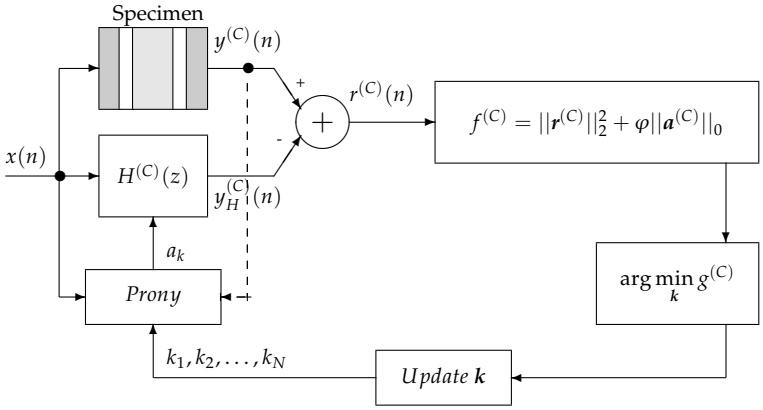

Figure 11.4: Analysis-by-synthesis scheme for a damage class C.

11.2.2 Experimental results

Analysis-by-synthesis solutions

This section presents the results obtained from the analysis-by-synthesis stage for the optimal position $\boldsymbol{k}$ of the prediction coefficient vector $\boldsymbol{a}$ corresponding to each damage class C. In order to reduce part of the noise and focus on the frequency band of interest, the experimental response signals $y(n)$ have been previously decimated to $F_s = 25$ MHz (250 samples). For the specimen tested, the resulting thickness equivalent sample delay is $M = 14$. The simulations have been performed for a wide range of regularization terms $\varphi \in [3 - 8] \cdot 10^{-5}$. Table 11.2 summarizes the optimal results.

Damage level	a_k-coefficient positions																											NZ
	1	2	3	4	5	6	7	8	9	10	11	12	13	14	15	16	17	18	19	20	21	22	23	24	25	26	27	28	
Damage 0	■	■	■	■	■	■	■	■	■	■	■	■	■			■										■		■	15
Damage 1	■	■	■	■	■	■	■	■	■		■	■	■	■		■	■						■					■	15
Damage 2	■	■	■	■			■	■	■	■	■	■		■	■			■						■		■		■	14
Damage 3	■	■	■	■			■	■	■	■		■	■	■		■					■							■	13
Damage 4	■	■		■	■	■	■		■	■	■	■		■	■			■				■	■					■	14
Damage 5	■	■		■	■		■	■	■				■	■	■	■	■	■		■	■			■	■	■	■	■	19

Table 11.2: Analysis-by-synthesis optimal solution for the positions of the non-zero coefficients a_k (indicated by grey cells), along with the number of non-zero (NZ) coefficients ($\varphi = 6e - 5$).

As can be observed, the coefficient position vector $\boldsymbol{k}$ changes slightly from one damage level to the next one. Some coefficients vanish and/or appear at new positions, due to the symmetry break of the plate structure. It is worth to point out that diagonal patterns which appear along increasing damage levels (e.g. from positions 13 to 18 and from 16 to 21) may be related to wave velocity reductions, i.e. to stiffness reduction of the specimen layers. Unfortunately, a direct physical interpretation from the a_k-domain is not easily assessable.

Damage recognition experiment

To evaluate the discriminative capability of the proposed model, a set of experiments have been carried out. For this task, a damage recognition system based on *cepstral* distances is developed. As in [311, 312], each experiment has been previously preprocessed with a Hamming window of 250 samples in the time-domain. The tested techniques employ the *real cepstrum* $c(n)$, which is defined as,

$$\log|H(\omega)| \quad = \quad \sum_{n=-\infty}^{\infty} c(n)e^{j\omega n} \tag{11.7}$$

where $H(\omega)$ is the spectrum estimate obtained from the signal model. Precisely, the way the spectrum is estimated characterizes each applied technique. Thus, the approach called *Real cepstrum* consists of using the periodogram obtained directly from the windowed signal, and corresponds to our baseline (i.e. non-parametric technique). The technique labeled as *LPC cepstrum* is based on the use of a standard all-pole model with order $p = 28$, as described in our previous works [311, 312]. Finally, the method named *Dynamic cesptrum* is based on the sparse signal model described by Equation (11.3), and whose coefficient positions $\boldsymbol{k}$ were determined according to the optimal results depicted in Table 11.2.

For an optimal use of the available data set, the training/test is performed using the *leaving-one-out* technique. Therefore, 9 signals are used to train a reference *cepstral* vector corresponding to a certain damage level, while the remaining signal is used for test. Rotating the measurements enables us to train the system always with 9 signals, while testing is performed over $6 \times 10 = 60$ signals. The performance of the system is measured through a weighted error factor. Let the results of the test be a confusion table $R(i, j)$, with $i, j = 1, \ldots, 6$, where $R(i, j)$ represents the number of measurements at damage level i that have been classified as a damage level j. The weighted error factor is then defined as,

$$w_{err}[\%] \quad = \quad 100 \times \frac{\sum_{i=1}^{6}\sum_{j=1}^{6} R(i,j) \cdot \frac{|i-j|}{3}}{60} \tag{11.8}$$

Thus, when the erroneously recognized class corresponds to a damage close to that of the correct class, the error has less influence on the error rate. Table 11.4 shows the results obtained for the different cepstrum-based techniques, along with our proposal. As can be observed, minimal weighted and absolute errors (1.67 % and 3 %, respectively) are obtained with the dynamic approach. It is also worth to note that a sparse modeling, with a lower

number of parameters, has a better discriminative capability than classical spectrum estimation approaches.

Cepstrum-based techniques	**Number of non-zero a_k**	**w_{err}** [%]	**err** [%]
Real cepstrum	–	8.33	23.33
LPC cepstrum	28	2.00	6.67
Dynamic cepstrum	$13-19$	1.67	3

Table 11.3: Classification errors for different cepstrum-based techniques.

11.2.3 Conclusions

This study shows the capability of a sparse signal modeling to discriminate the damage level of a CFRP plate subjected to different impact energies. First, an analysis-by-synthesis scheme has been proposed, to infer the order and extent of the model parameters corresponding to a certain impact damage level. Then, the performance of the proposed parametrization has been evaluated by a system based on *cepstral* distances that recognizes the specific damage level corresponding to a given test signal, leading to the following conclusions: (1) It has been demonstrated that modeling the complex wave propagation pattern using a sparse transfer function provides better results than other classical spectrum estimation techniques. (2) It has been shown that the prediction coefficients behave dynamically, depending upon the damage state of the material. Ongoing works may include a further study of the relation between the sparse prediction coefficients and the underlying material mechanical properties, in order to provide a consistent quantification of the damage parameters.

11.3 Physics-based sparse signal model

To evaluate the capability of the proposed model for damage discrimination, a set of experiments have been carried out. In the first experiment, a damage detection framework exploiting the convenient filter form provided by the digital signal model is proposed. In the second experiment, a damage identification system based on cepstral distances with an underlying model as in [312] is developed.

11.3.1 Damage detection evaluation

The nature of the proposed digital model, namely its all-pole structure, allows a simple and efficient use for industrial NDE applications. Ultrasonic response signals obtained from specimens can be whitened by inverse filtering, where the filter is computed from the material's properties provided by the manufacturer. While the inverse filtered response from the undamaged specimen is expected to be similar to the original excitation signal applied, the opposite is awaited for damaged specimens, due to the corresponding model mismatch, resulting in an effective damage detection procedure with a relatively low cost.

In this section, we evaluate this approach on the CFRP plate described in Section 9.2.2. Given the transfer function $H^D(z)$, which represents the undamaged multilayered composite material in a through-transmission configuration, the experimental response signal $y(n)$ can be whitened by inverse filtering, resulting in an approximation $\tilde{x}(n)$ of the original excitation signal $x(n)$ applied to the specimen. In general, it is not guaranteed that an inverse filter $H^{D^{-1}}(z)$ fulfill stability conditions. In our case, $H^D(z)$ is an all-pole filter, and thus the resulting inverse one is a finite impulse response (FIR) filter, which is inherently stable and can be computed straightforwardly. The specimen can then be classified by defining a modeling error in terms of the squared error between the actual excitation signal $x(n)$ and the inverse filter response $\tilde{x}(n)$,

$$\varepsilon_w \;=\; \sum_{n=0}^{N-1} e_w(n)^2 \;=\; \sum_{n=0}^{N-1} \left(\tilde{x}(n) - x(n)\right)^2 \tag{11.9}$$

where $e_w(n)$ denotes the whitening error. Figure 11.5 shows a diagram of the proposed scheme. It is expected that the experimental response signal obtained from an undamaged specimen $y_0(n)$ is well-approximated by the model, so it should be well-whitened, resulting in a low modeling error value ε_w. In contrast, the experimental response signal obtained from a damaged location $y_i(n) \in \{y_1(n), \ldots, y_5(n)\}$ is expected not to be well-whitened, leading to larger modeling error values.

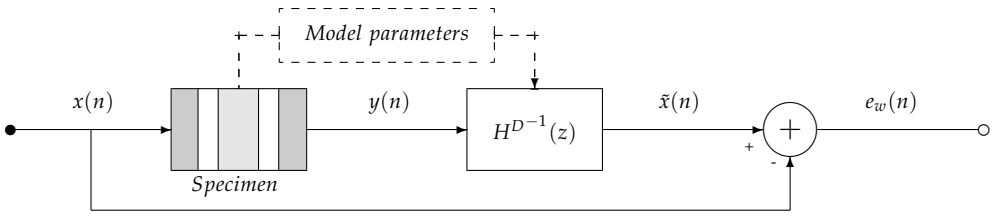

Figure 11.5: Diagram of the inverse filtering scheme proposed to compute the whitening error.

Nevertheless, the former damage detection framework still exhibits several drawbacks. First, the response signal energy decreases significantly as the impact energy increases. Thus, the modeling error ε_w alone is not as discriminative as initially expected. We get through this difficulty by introducing a relative modeling error $E_r = \varepsilon_w/\varepsilon_{nw}$, where ε_{nw} denotes the original response signal energy (non-whitened), that is $\varepsilon_{nw} = \sum_{n=0}^{N-1} y(n)^2$. Secondly, the damage information is mostly concentrated in the wave echoes (which represent successive wave transitions across the specimen) [311, 312], whereas the wave front remains almost unsensitive to damage. To account for this fact, temporal windowing $w(n)$ can be applied to the signals being compared, or more easily over the whitening error $e_w(n)$.

To evaluate the aforementioned damage detection framework, a model fitness measure is introduced as $\rho = 1/E_r$. Figure 11.6 shows the ρ-values obtained for the experimental data set, using five different temporal windows. The length of these windows was chosen so that the analysis focuses on the signal echoes. For this purpose, several rectangular

and Hamming windows were selected. The first window is a rectangular one of full signal length (RECT$^{(0)}$), whereas the other applied rectangular windows (RECT$^{(i)}$) depend on the specimen thickness Λ expressed in number of samples. To focus on the later echoes, 2Λ samples are successively removed from the analysis, that is, RECT$^{(1)}$ considers all the signal samples except the ones corresponding to the wave front, RECT$^{(2)}$ all the signal samples except the ones corresponding to the wave front and the first echo (a wave that crossed thrice the specimen), and so on. The last applied window is a Hamming window of signal length, used to enhance the echoes as in our previous studies [311, 312]. As can be observed, moderate and severe damage levels ($2-5$) are correctly discriminated by the proposed measure independently of the window used. The influence of the temporal windowing can be appreciated better for no and mild damage levels (0 and 1), which are, as expected, the most difficult cases to discriminate. By considering the complete signal (RECT$^{(0)}$), it is difficult to establish a clear threshold to discriminate between these levels. In contrast, removing the wave front (RECT$^{(1)}$) or enhancing the echoes (HAMM) by windowing provides significant improvements. Shifting the rectangular window on the later echoes (RECT$^{(2)}$) improves further the discrimination. Indeed, the proposed analysis provides the best results for this window, and a fitness threshold around 1.05 (see Figure 11.6), leading to 10% of type I errors and 0% of type II errors. Removing further echoes (RECT$^{(3)}$) makes the results worse. This could be explained because only a few samples, which suffer from severe quantization effects, are considered.

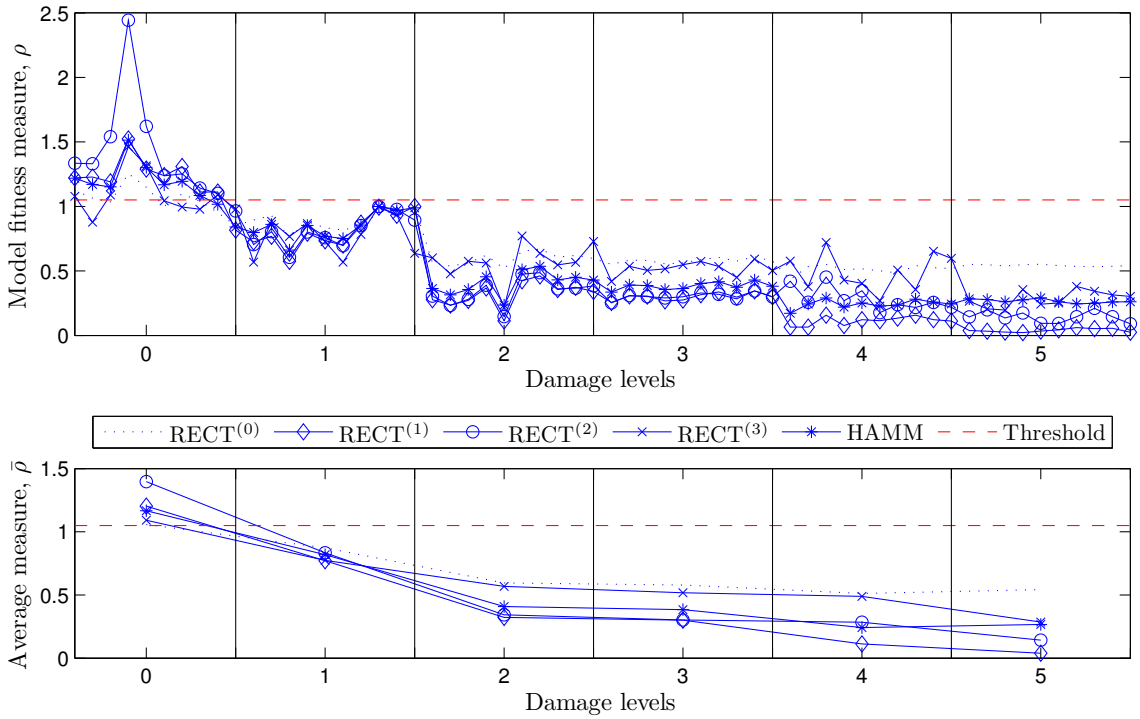

Figure 11.6: *Damage detection results obtained for several windows length and type.*

As can be seen, this experimental case study illustrates the potential of the proposed formalism, which achieves a very low complexity method for binary classification between damaged and undamaged specimens, using a sparse physics-based transfer function, analytically derived from the mechanical and geometrical properties of the material.

11.3.2 Damage identification evaluation

In this section, the proposed model is evaluated as underlying model in a damage recognition system based on cepstral distances [311, 312]. First, signals are preprocessed in order to reduce part of the noise and focus on the frequency band of interest. Thus, the sampling frequency is reduced to $F_s = 25$ MHz ($N = 250$ samples) by decimation and rectangular (R) or Hamming (H) windowing is applied over the resulting signals (the rectangular window corresponds to the best obtained window in the previous experiment). Damage classification is performed from Euclidean distances in the real cepstral-domain, where the real cepstrum $c(n)$ is defined as,

$$\log|H(\omega)| = \sum_{n=-\infty}^{\infty} c(n)e^{j\omega n} \tag{11.10}$$

where $H(\omega)$ is an estimate of the spectrum of the specimen under investigation. Non-parametric and parametric methods can be used in order to estimate this spectrum. In this work, the periodogram directly obtained from the windowed signal is employed as non-parametric technique, serving us as baseline (*FFT* technique). Parametric methods make use of an underlying model $H^D(z)$, whose parameters or coefficients must be estimated from the input/output signals. As a first parametric technique, we consider a short-term linear prediction model (LPC) consisting of a standard all-pole filter with order $p = 14$ (*LPC* tecnhique). This order p, and so the number of parameters, is chosen to correspond to the thickness-equivalent sample delay of the plate $\Lambda = 14$.

In our previous work [312], we presented a simplified analysis of the complex wave propagation pattern within the plate, and showed that this model could be improved for a damaged specimen by including a few coefficients which extends the specimen's transfer function with a middle and long-term predictors. This can alternatively be interpreted as a longer all-pole model with a sparse-like coefficient distribution. Thus, a second model is defined as an all-pole model of order $p = 28$, that is, twice the specimen's thickness expressed in samples, where the coefficients from positions 15 to 27 are forced to be zeros (*Simplified model 1*). The rest of coefficients (original LPC and 28^{th} ones) are obtained from the input/output signals by means of the Prony's method [214]. Additionally, we can define a third extended model, which also includes a middle-term coefficient placed at position 25 (*Simplified model 2*). The goal of this middle-term coefficient is to account for the damage by placing a fixed virtual interface in the plate [312]. However, it must be considered that the structural complexity of the material suggests that flaws may occur at different locations, and that a single virtual interface cannot account for all possible failure mechanisms. Therefore, in practice, the position of this interface must be determined empirically.

Instead of using a model based on a simplified analysis of the material, we can apply our proposed digital signal model to analytically derive the position and extent of the coefficients from the properties of the CFRP plate. The delays m_i of these sparse coefficients are fixed according to the positions obtained from the model for an undamaged specimen, assuming that damage affects mostly the gains of the sparse prediction coefficients a_k provided by the transfer function. The latter assumption implies that the changes caused in the signals due to damage should be absorbed by the gains at the fixed positions. Finally, a full LPC model with order $p = 28$ (maximum delay obtained in any previous model) is proposed for a fair comparison (*Full LPC*).

For an optimal use of the available data set, training/test is performed using the *leaving-one-out* technique. Therefore, 9 signals are used to train a reference cepstral vector corresponding to a certain damage level, while the remaining signal is used for the test. The accuracy of the system is evaluated by defining a weighted error factor [311, 312]. The test provides a confusion table $R(i, j)$ $(i, j = 1, \ldots, 6)$, where $R(i, j)$ represents the number of measurements at damage level i that have been classified as a damage level j. A weighted error rate is then defined as,

$$w_{err}[\%] \quad = \quad 100 \times \frac{\sum_{i=1}^{6} \sum_{j=1}^{6} R(i,j) \cdot \frac{|i-j|}{3}}{60} \tag{11.11}$$

Thus, when the erroneously recognized class corresponds to a damage close to that of the correct class, the error has less influence on the error rate. To evaluate the capability of the proposed classification system, cepstra are extracted from the aforementioned models. Table 11.4 shows the results obtained for these different cepstrum-based techniques, namely *FFT*, *LPC*, *Simplified model 1 (SM 1)*, *Simplified model 2 (SM 2)*, *Digital signal model (DSM)*, and *Full LPC*, and summarizes the position of the prediction coefficients corresponding to these models.

Cepstrum-based techniques	a_k-coefficient positions 1 2 3 4 5 6 7 8 9 10 11 12 13 14 15 16 17 18 19 20 21 22 23 24 25 26 27 28	NZ	$(N = 250)$ $w(n)$	w_{err} [%]
FFT		-	R	7.33
			H	8.33
LPC		14	R	9.33
			H	9.33
SM 1		15	R	8.00
			H	3.00
SM 2		16	R	7.67
			H	2.67
DSM		15	R	6.67
			H	**1.67**
Full LPC		28	R	6.67
			H	2.00

Table 11.4: Classification errors for different cepstrum-based techniques, along with the order and extend of the non-zero coefficients a_k (indicated by grey cells).

First, these results confirm that the modeling order p is tightly linked to twice the thickness-equivalent sample delay of the plate. Indeed, all the cesptra extracted from all-

pole models with $p = 28$ reduce drastically the weighted error compared to classical spectrum estimation methods (*LPC* and *FFT*). Adding a single middle and long-term prediction coefficients to a standard all-pole model (*Simplified models*) enables us to obtain cepstra that improve significantly the damage discrimination capability compared to the short-term *LPC* cepstrum. It is noteworthy that modeling the multilayered specimen with a short-term LPC model is equivalent to consider our material as a Goupillaud-type structure with $\Lambda = M = 14$. As can be observed, a sparse signal modeling whose coefficient positions are analytically obtained from the material's properties provides even better discrimination than those simplified sparse-like models. Even more remarkable is the fact that this sparse model with a reduced number of parameters yields better results than a LPC-model with the same modeling order (*Full LPC*). Concretely, minimal weighted error (1.67 %) is obtained with the digital signal modeling approach for signals that have been previously preprocessed with a Hamming window. As can be observed, rectangular windowing follows the same tendency albeit provides worse results, i.e. the resulting weighted errors are typically around $2 - 4$ times higher than the ones obtained with Hamming windowing (except for the *FFT* and *LPC* cepstra). Indeed, in contrast to the previous experiment where signals were only processed in the time-domain, the current evaluation involves spectrum estimates, where the rectangular windowing is usually avoided due to its poor performance.

11.3.3 Conclusions

This work shows the capability of a digital signal modeling approach which incorporates underlying mechanical concepts to identify damage in composite materials, particularly in a CFRP plate subjected to different impact energies. A set of experimental case studies has been proposed to evaluate the potential of the developed digital signal model in some practical NDE applications. In a first experiment, a damage detection evaluation has been carried out, showing that the digital filter represents an extremely fast and promising tool to discriminate damaged from undamaged specimens by inverse filtering. Indeed, this inverse filter is a sparse FIR filter, whose coefficients were directly obtained from the material's properties, without requiring any experimental calibration. In a second experiment, the discriminative performance of the proposed model has been evaluated by a system based on cepstral distances that recognizes the specific damage level corresponding to a given test signal. The damage levels have been identified with an accuracy of 98.37 % with a model that consists of 15 parameters, that is, half the amount of a full LPC model. It has been demonstrated that a sparse signal modeling with a reduced number of coefficients provides better results than other common spectrum estimation techniques. In contrast to standard or empirical models, the coefficients position and extent of our model are inherently linked to the material's properties (i.e. twice the thickness of the plate, stiffness, etc.), and thus to its health state.

Inverse filtering experiments for real-time monitoring of CFRP plates damaged by impact and fatigue with ultrasonic C-scan methods are currently under development at our

laboratory. Ongoing work includes further use of sparse signal models for ultrasonic NDE of materials, and particularly the use of a dynamic model with variable coefficients position and gain to improve the performance of damage recognition systems.

12

Probabilistic inverse problem for ultrasonic monitoring of tissue-engineered materials

The understanding of internal processes that affect the changes of consistency of soft tissue is a challenging problem. An ultrasound-monitoring Petri dish has been de- signed to monitor the evolution of relevant mechanical parameters during engineered tissue formation processes in real time. A better understanding of the measured ultrasonic signals required the use of numerical models of the ultrasound-tissue interactions. The extraction of relevant data and its evolution with sufficient sensitivity and accuracy is addressed by applying well-known signal processing techniques to both the experimental and numerically predicted measurements. In addition, a stochastic model-class selection formulation is used to rank which of the proposed interaction models are more plausible. The sensitivity of the system is first verified by monitoring a gelation process, as described in Section 12.1. Then, in Section 12.2, we expose the possibility of extending such a methodology for monitoring a fibrin-agarose based construct for artificial tissue development.

12.1 Monitoring of a gelation process

The proposed methodology combines four elements. (1) The signal acquisition of the ultrasonic signals obtained from the waves interaction with a sample of tissue, a (2) set of alternative attenuation models that simulate the ultrasound-tissue interaction, which is numerically solved by the transfer matrix formalism, a (3) stochastic model-class selection formulation used to rank which of the models parametrization are more plausible, and a (4)

NDE oriented signal processing framework that extract relevant features from both the experimental and numerically predicted signals. The latter is used to reconstruct the evolution of the relevant mechanical parameters during the culture reaction time.

The experimental system is idealized by a mathematical model of the propagation and interaction of the transmitted ultrasonic waves with all the parts of the system until they are received by the sensor. Several models are tested to idealize the removal of energy by dissipation or radiation. Three alternative damping models are used: (i) viscous, (ii) hysteretic, and (iii) proportional to integer time derivatives of the particle movement, based on their fractional time derivatives. The damping is defined in terms of the wave modulus M, which is modified from the undamped one M_0 to generate a dispersive one, which is a frequency-dependent complex modulus $M^*(\omega)$, where ω is the angular frequency if the modulus dispersion is represented by its frequency domain. The viscous model is defined in terms of the frequency-dependent loss factor η, obtained as the ratio between loss and storage moduli [315]. In this context, a specific view of hysteretic damping is taken, where it is expressed as a frequency-independent damping [225]. The last model, based on fractional time derivatives, leads to a damping function that may be expressed as a power law, and thus improves curve-fitting properties for relaxation [315, 225]. These models are selected according to their performance demonstrated in a previous study [316]. On one hand, the viscoelastic η and hysteretic ζ models are defined according to Maia *et al.* [317],

$$M^*(\omega) = M^0 \left(1 - i\omega\eta\right) \tag{12.1}$$

and

$$M^*(\omega) = M^0 \left(1 - i\zeta\right) \tag{12.2}$$

where η and ζ are the viscoelastic and hysteretic damping coefficients of tissue, respectively. On the other hand, the fractional time derivative damping is defined as,

$$M^*(\omega) = M^0 \frac{1 + b(i\omega)^\beta}{1 + a(i\omega)^\alpha} \tag{12.3}$$

The three models are summarized hereafter, highlighting the combination of the considered parameters,

Table 12.1: Combination of models.

Tag	Size	Parameters					
1	4	K^{tissue}	ζ	z^{ampl}	z^{time}		
2	4	K^{tissue}	η	z^{ampl}	z^{time}		
3	6	K^{tissue}	a	b	$\alpha = \beta$	z^{ampl}	z^{time}

where K^{tissue} denotes the Bulk modulus of tissue. The fractional derivative constants are defined as a, b, and $\alpha = \beta$. Two additional parameters z^{ampl} and z^{time} are introduced to control

the correction of the amplitude and the time-shift of the input signal in the culture, which corrects effects of temperature and other phenomena on the sensors, that affect attenuation and delay on the path from the electronics to the arrival of the signal at the culture specimen. The input signal $s^0(t)$ correction is defined by,

$$s^*(t) = z^{\text{ampl}} s^0(t + z^{\text{time}}) \tag{12.4}$$

The factor z^{ampl} corrects variations of the amplitude and phase of the excitation over the reaction process time, that may suffer the influence of several simultaneous factors including the temperature. Nonetheless, we assume that these factors can be summarized as a whole by introducing a phenomenological factor, labeled as z^{time}.

The mathematical model is approximated by a semi-analytical model of the wave interactions within multilayered materials based on the transfer matrix formalism (TMF) [224], describing the ultrasonic waves interactions between the Petri dish and the culture.

12.1.1 Measurements

The recorded signals by the ultrasound-monitored Petri dish every 250 seconds are shown in Figure 12.1, without and with specimen, respectively. No clear evolution is detectable by bare visual inspection of the signals. The recorded signals are mainly composed of three different waveforms (simplified paths of Fig. 1), namely (1) the wave front that propagates only through the PMMA layer (labeled as u_1), (2) a wave that crosses both the PMMA layer and the specimen (labeled as u_2), and (3) a wave echo produced by the former wave after crossing twice the specimen (labeled as u_3).

It is noteworthy that when the specimen is on place, the majority of the excitation signal (registered without specimen for calibration) is transmitted instead of reflected. Since the wavelength in gel is compatible with the layer thickness, the individual echoes generated by the multiple reflections inside the gel layer can be analyzed separately by signal processing.

12.1.2 Signal simulation

The transfer matrix formalism is used to generate sample signals, after calibrating the estimated parameters using the inverse problem, for the first signal (initial evolution time). Time-domain signals and magnitude spectra are shown in Figures 12.2-12.5 for the viscous model (case 2) at the initial time of the reaction process, respectively. In the lower figures, an analysis window (Hamming) has been applied to the signals, and classical and weighted residue definitions are considered, denoted as $\boldsymbol{r}_0$ and $\boldsymbol{r}_3$, respectively.

A significative ability to simulate the system can be observed visually. The influence of the signal windowing yields the following observations for the magnitude spectrum (Fig. 12.4-12.5): The envelope, that corresponds to the redundant character of the signal, remains almost unchanged. In contrast, the fine spectrum presents accentuated *peakiness* due to the enhanced echoes of the time-domain signals. In the time-domain, the classical residue $\boldsymbol{r_0}$ is strongly correlated with the signals themselves (Fig. 12.2), highlighting higher amplitude

where the signals energy is higher. However, the weighted residue $\boldsymbol{r_3}$ allows to remove some variability due to the measurements uncertainties (Fig. 12.3). Additionally, it enhances the signal parts containing information of the reaction process (here mainly the wave front), while allowing to remove the parts which are invariant to the process evolution (scattering parts). In the frequency-domain, the weighted residue allows to remove the frequency range being unsensitive to the reaction process, or being erroneous due to measurements noise. Thus, the resulting magnitude spectra of Fig. 12.5 show enhanced process information at certain frequencies, in contrast to the magnitude spectrum of Fig. 12.4.

12.1.3 Posterior probability of the model

The probability density function is computed for the viscous attenuation model, and some relevant samples issued from the results obtained in the previous section are shown in Figures 12.6-12.9. Since the PDF is a multidimensional function, without loss of generality, only a slice along two parameters is represented, namely the Bulk modulus of the tissue and the viscous damping coefficient.

The inspection of these plots reveals several local minima, valleys in the probability density function and variations of several orders of magnitude from good to bad model parameters. This implies a bad conditioning of the reconstruction inverse problem and justifies the use of advanced search algorithms such as genetic algorithms. Nonetheless, the use of a weighted residue definition enhance the slope of these local minima, and thus speed up the convergence of the search algorithm. It is noteworthy that the other attenuation models present similar trends. Additionally, some irrelevant samples issued from the cepstral analysis are illustrated in Figures 12.10-12.11.

The inspection of the plots obtained from the cepstral analysis reveals many local minima that approximately have the same values, leading to an ill-conditioned solution space.

12.1.4 Model class plausibility

The posterior probability $p(\mathcal{C})$ of every proposed model class $\mathcal{C} \in \mathfrak{C}$ is computed by Quasi Montecarlo integration using 2^{18} Sobol sampling points. Additionally, the estimation of Occam's factor, as well as the certainty metric $\overline{\sigma}$ are summarized in Tables 12.2-12.4 for time-domain signals, magnitude spectra and real cepstra, respectively.

The most plausible model class is shown to be 2, involving K^{tissue}, viscoelastic damping, and temperature and amplitude corrections. It is closely followed by class 1 (hysteretic damping), whereas class 3 does not provide results for all proposed signal processing techniques. The magnitude spectrum computed with weighted residue definitions $\boldsymbol{r}_1$ and $\boldsymbol{r}_3$ show significantly higher posterior probability $p(\mathcal{C})$ than the other domains of representation. The real cepstrum provides bad results as well for the posterior probability, which is consistent with the observations in the previous section. This evidence further supports the validity of the probabilistic formulation. Hence, the obtained equiprobable values demonstrate its insensitiveness with respect to the selected model classes.

Table 12.2: Plausibility of model classes. Time-domain.

Windowing	Residue	Model class	1	2	3
w_0	$\boldsymbol{r_0}$	$p(\mathcal{C})$ [%]	31.55	32.39	36.06
		Occam $[-log_{10}]$	2.24	4.10	1.90
		Certainty $[log_{10}]$	0.11	0.75	0.37
	$\boldsymbol{r_1}$	$p(\mathcal{C})$ [%]	33.33	33.33	33.33
		Occam $[-log_{10}]$	8.11	7.93	11.93
		Certainty $[log_{10}]$	1.69	1.66	1.97
	$\boldsymbol{r_3}$	$p(\mathcal{C})$ [%]	15.53	63.10	21.37
		Occam $[-log_{10}]$	7.34	9.95	14.78
		Certainty $[log_{10}]$	2.23	2.74	2.97
w_1	$\boldsymbol{r_0}$	$p(\mathcal{C})$ [%]	32.45	32.99	34.57
		Occam $[-log_{10}]$	7.14	6.50	7.44
		Certainty $[log_{10}]$	1.40	1.16	1.02
	$\boldsymbol{r_1}$	$p(\mathcal{C})$ [%]	33.33	33.33	33.33
		Occam $[-log_{10}]$	7.93	7.90	13.08
		Certainty $[log_{10}]$	1.83	1.95	∞
	$\boldsymbol{r_3}$	$p(\mathcal{C})$ [%]	34.81	31.57	33.62
		Occam $[-log_{10}]$	4.25	6.17	8.72
		Certainty $[log_{10}]$	1.39	1.79	1.45

The posterior probability $p(\mathcal{R})$ of every consistent residue definition $\mathcal{R} \in \mathfrak{R}$ is computed according to the posterior probability $p(\mathcal{C})$. Tables 12.5-12.6 summarized the obtained values together with the Occam's factor estimation and certainty metric, for the hysteretic and viscous damping, respectively.

The most plausible residue definition appears to be $\boldsymbol{r}_1$, which involves the inclusion of some prior information on the variance of the measurements over the temporal evolution of the reaction process, when the inverse problem is achieved in the frequency-domain. This ranking remains consistent independently of the model class. Signal windowing has a feeble influence on the results improvement.

12.1.5 Monitoring of evolution

The evolution of the relevant reconstructed mechanical parameters during the reaction process is shown in Figures 12.12-12.13 for the most relevant model class and residue definitions, respectively. The value of the reconstructed Bulk modulus at the beginning of the process approximately amounts to 2.385 [GPa]. Under the hypothesis that the gel layer is already in the gelation zone [318] at the initial process time (for such a thin specimen, the gel starts to gelify almost instantaneously), we suppose that the loss and storage moduli at the

Table 12.3: Plausibility of model classes. Magnitude spectrum.

Windowing	Residue	Model class	1	2	3
w_0	$\boldsymbol{r_0}$	$p(\mathcal{C})$ [%]	29.79	29.39	40.82
		Occam $[-log_{10}]$	0.09	-0.42	-5.17
		Certainty $[log_{10}]$	0.40	0.38	0.71
	$\boldsymbol{r_1}$	$p(\mathcal{C})$ [%]	49.94	50.06	-
		Occam $[-log_{10}]$	7.71	8.82	-
		Certainty $[log_{10}]$	1.52	1.63	-
	$\boldsymbol{r_3}$	$p(\mathcal{C})$ [%]	0.02	56.47	43.51
		Occam $[-log_{10}]$	4.84	5.88	22.37
		Certainty $[log_{10}]$	1.93	1.89	4.10
w_1	$\boldsymbol{r_0}$	$p(\mathcal{C})$ [%]	26.90	26.11	46.99
		Occam $[-log_{10}]$	2.47	1.82	-8.55
		Certainty $[log_{10}]$	0.08	0.08	-1.57
	$\boldsymbol{r_1}$	$p(\mathcal{C})$ [%]	49.98	50.02	-
		Occam $[-log_{10}]$	8.68	7.81	-
		Certainty $[log_{10}]$	1.80	1.49	-
	$\boldsymbol{r_3}$	$p(\mathcal{C})$ [%]	31.98	44.95	23.07
		Occam $[-log_{10}]$	5.11	4.77	16.15
		Certainty $[log_{10}]$	1.61	1.54	2.85

initial and end process times approximate the ones proposed by Wang *et al.* [318], namely $G_0'' = 1200$ [Pa], $G_0' = 80$ [Pa] and $G_{end}'' = 1800$ [Pa], $G_{end}' = 140$ [Pa], respectively. By making use of the following formula [225],

$$c_p = \sqrt{\frac{(K + \frac{4}{3}G)}{\rho}} \tag{12.5}$$

the wave velocity is found to be 1544 [m/s] at the initial time of the process. The latter is close to the value depicted by other authors for similar materials, among them Norisuye *et al.* [319]. Additionally, the last author suggests that the wave velocity suffers a reduction of around 3 % over the reaction process. Thus, thus Bulk modulus at the end of the process is found to be 2.272 [GPa] (diminution of 5 %), and is in agreement with the value obtained with the proposed formalism.

Some parameter evolutions reconstructed using residues and models with low plausibility (not shown in this paper for space constraints) show larger scattering and instabilities, consistently with the results in the two previous subsections. Those observations further supports the validity of the formulation and conclusions.

Table 12.4: Plausibility of model classes. Real cepstrum.

Windowing	Residue	Model class	1	2	3
w_0	$\boldsymbol{r_0}$	$p(\mathcal{C})$ [%]	33.33	33.33	33.34
		Occam $[-log_{10}]$	1.99	2.91	2.67
		Certainty $[log_{10}]$	0.53	0.45	0.08
	$\boldsymbol{r_1}$	$p(\mathcal{C})$ [%]	33.33	33.33	33.34
		Occam $[-log_{10}]$	8.23	8.51	10.95
		Certainty $[log_{10}]$	2.38	2.42	1.94
	$\boldsymbol{r_3}$	$p(\mathcal{C})$ [%]	33.33	33.33	33.34
		Occam $[-log_{10}]$	0.21	2.21	3.28
		Certainty $[log_{10}]$	0.12	0.31	0.32

Table 12.5: Plausibility of residue definitions. Time-domain.

Model	Window	Residue	$\boldsymbol{r}_0$	$\boldsymbol{r}_1$	$\boldsymbol{r}_2$	$\boldsymbol{r}_3$
1	w_0	$p(\mathcal{R})$ [%]	22.27	26.57	0	0
		Occam	2.24	8.11	-22.96	-7.34
		Certainty	0.11	1.68	-6.30	-2.23
	w_1	$p(\mathcal{R})$ [%]	24.56	26.57	0	0
		Occam	7.14	7.93	-19.54	-4.25
		Certainty	1.40	1.83	-5.40	-1.39
2	w_0	$p(\mathcal{R})$ [%]	22.64	26.31	0	0
		Occam	4.10	7.93	-23.77	-9.95
		Certainty	0.74	1.66	-6.25	-2.74
	w_1	$p(\mathcal{C})$ [%]	24.72	26.31	0	0
		Occam	6.50	7.90	-20.30	-6.17
		Certainty	1.16	1.95	-5.38	-1.79

12.1.6 Conclusions

A numerical method to determine the elastic and dynamic energy dissipation properties during a gelation process has been developed by combining the solution of a probabilistic inverse problem with signal processing techniques, applying genetic algorithms to minimize a cost functional, and using a semi-analytical model of the interaction between ultrasonic waves and tissue.

The proposed model-class and residue selection and their subjacent class plausibility have enabled to rank both the models and the suitable residue definitions according to their compatibility with the observations. The resulting trade-off between model simplicity and fitting to observations have demonstrated that the viscous damping models, combined with

Table 12.6: Plausibility of residue definitions. Magnitude spectrum.

Model	Window	Residue	r_0	r_1	r_2	r_3
1	w_0	$p(\mathcal{R})$ [%]	5.87	38.87	0	0
		Occam	0.09	7.71	-14.49	-4.84
		Certainty	-0.40	1.52	-3.98	-1.93
	w_1	$p(\mathcal{R})$ [%]	15.64	39.61	0	0
		Occam	2.47	8.68	-11.81	-5.11
		Certainty	0.08	1.80	-3.40	-1.61
2	w_0	$p(\mathcal{R})$ [%]	5.82	39.12	0	0
		Occam	-0.42	8.82	-14.87	-5.88
		Certainty	-0.38	1.63	-4.00	-1.89
	w_1	$p(\mathcal{C})$ [%]	15.25	39.81	0	0
		Occam	1.82	7.81	-12.02	-4.77
		Certainty	0.08	1.49	-3.35	-1.55

some prior information on the measurements variance over the reaction process evolution, are feasible to characterize the complex evolution of the process.

The reconstructed model parameters highlight the following statements. For the viscoelastic models, the Bulk modulus consistently decreases while increasing the damping coefficient. Therefore, both parameters may be associated to the same phenomena, but a careful interpretation has not been carried out at that time. The evolution of the model parameters has a stronger slope during the first 200-300 seconds of the reaction process, and remain almost constant afterwards. This trend validates the observations done *in situ* where the gelation occurred during the first $3-5$ minutes. Consequently, the proposed methodology demonstrates capability to discriminate the process during its early solidification phase. For a better understanding of the ultrasonic tissue monitoring, *in vitro* studies on real tissue combined with histological studies may be conducted.

12.2 Monitoring of a fibrin-agarose based construct for artificial tissue development

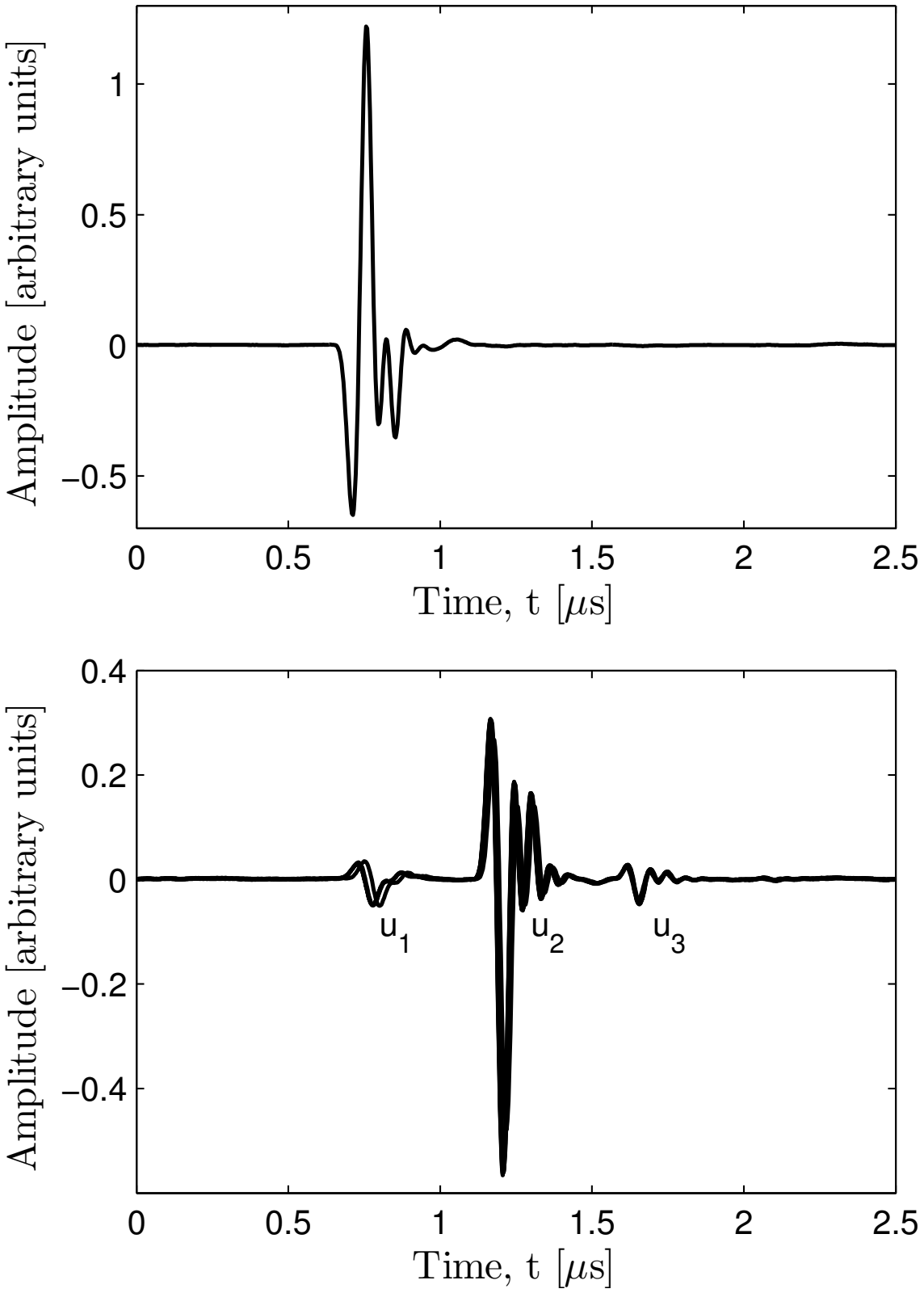

Figure 12.1: Signals sample: sequence of signals without specimen (above); signal with specimen registered every 250 seconds (below).

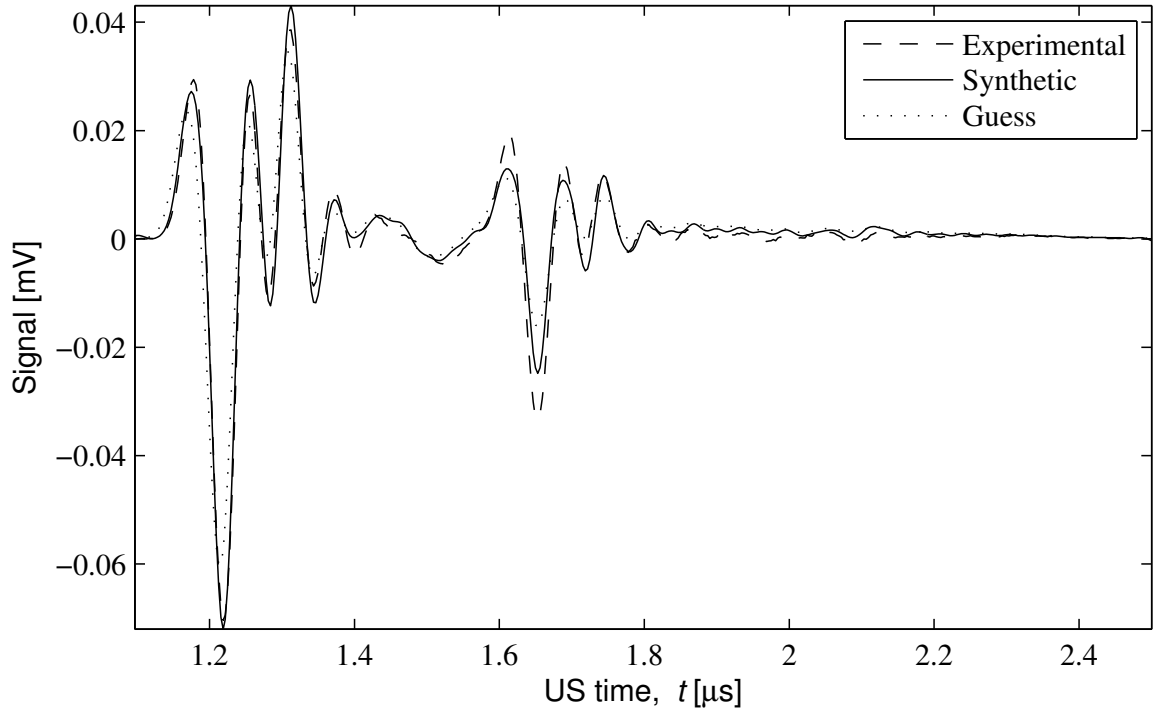

Figure 12.2: Example of fitting of experimental and simulated observations. Viscous model. Time-domain. Residue r_0.

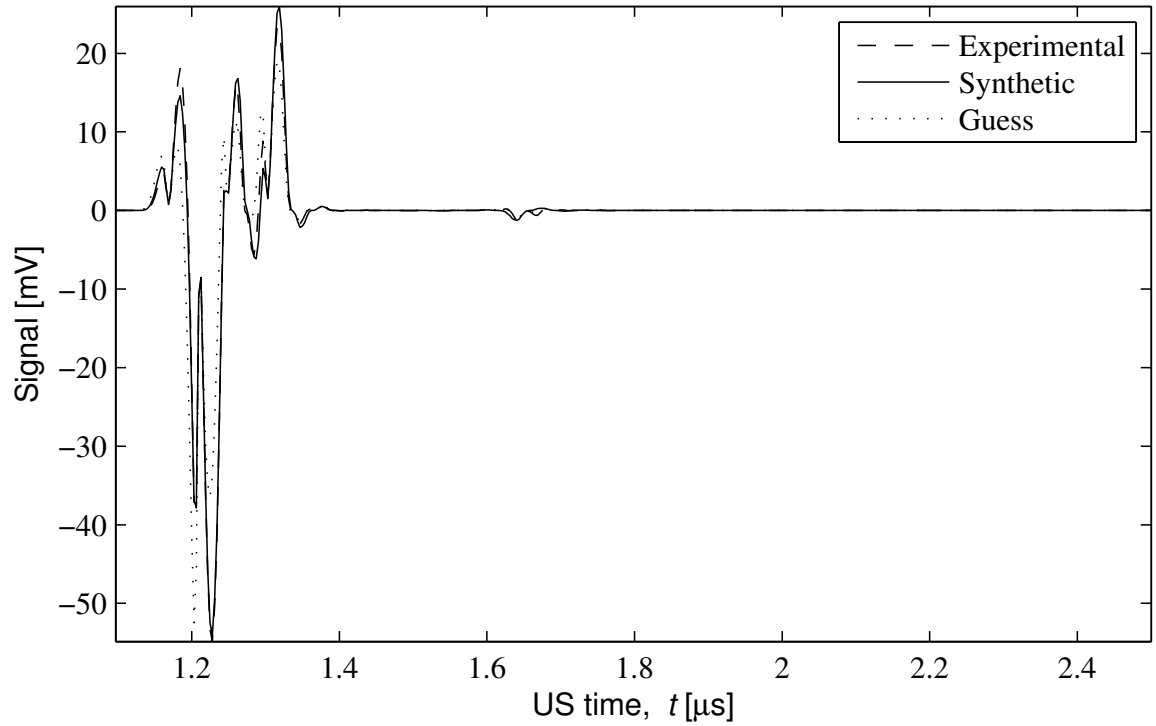

Figure 12.3: Example of fitting of experimental and simulated observations. Viscous model. Time-domain. Residue r_3.

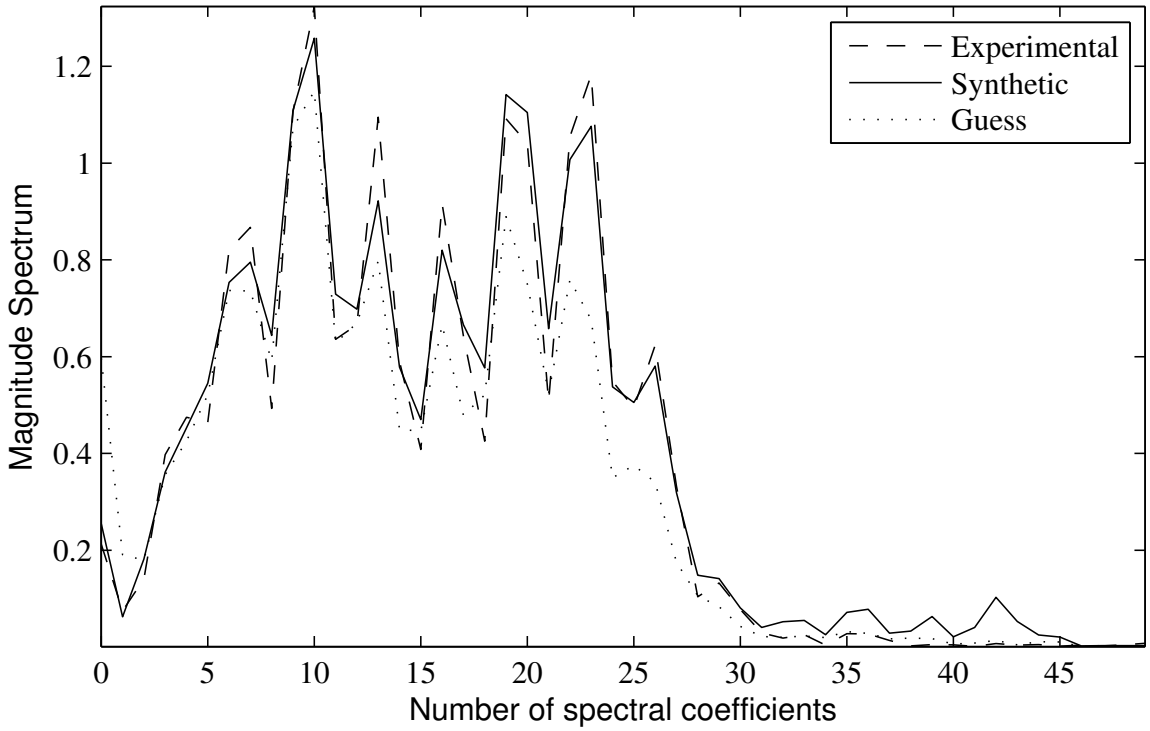

Figure 12.4: Example of fitting of experimental and simulated observations. Viscous model. Magnitude-spectrum. Residue r_0.

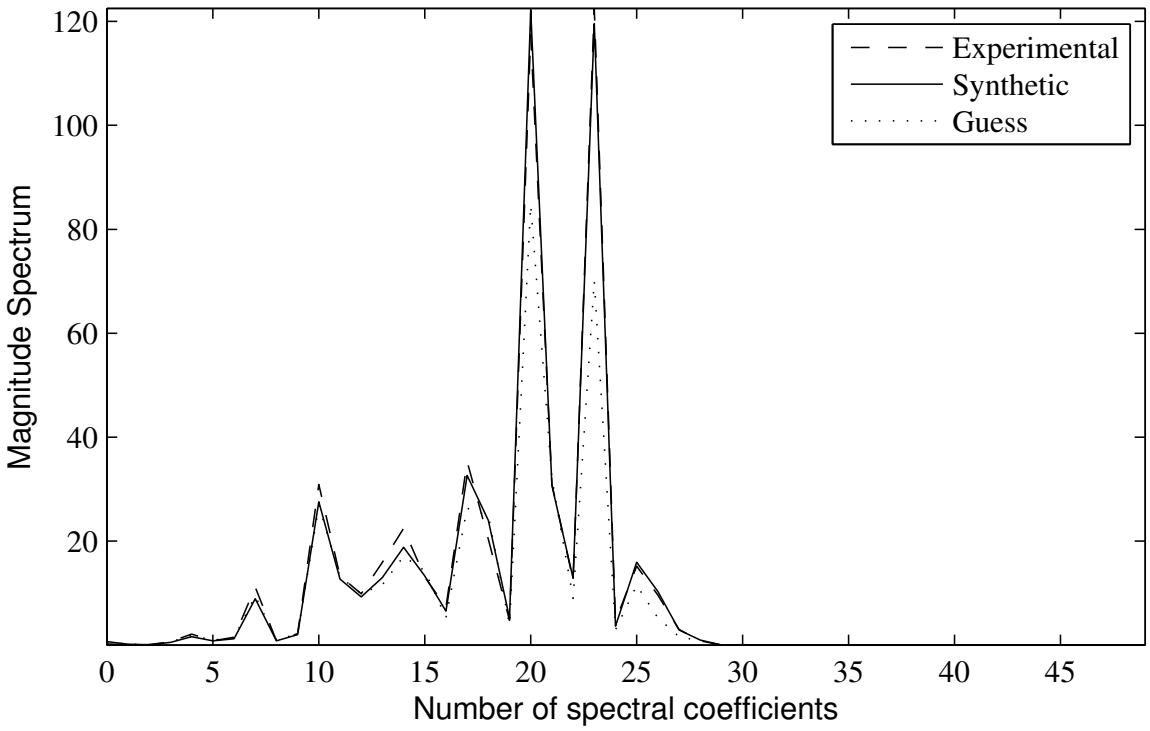

Figure 12.5: Example of fitting of experimental and simulated observations. Viscous model. Magnitude-spectrum. Residue r_3.

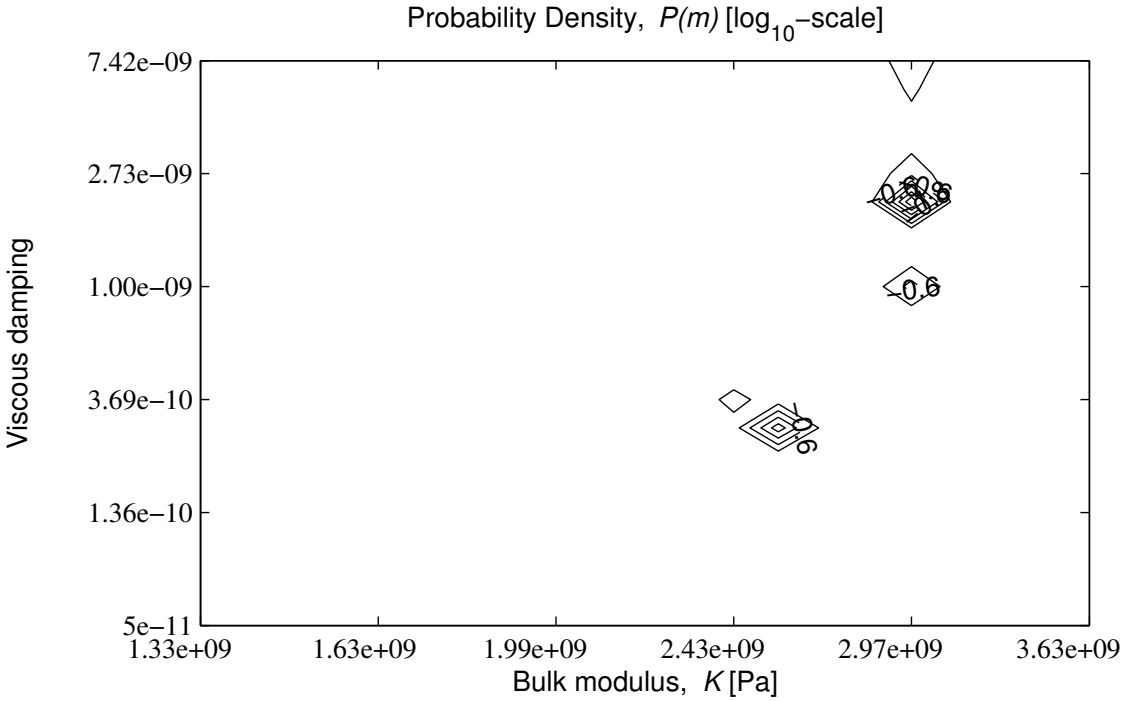

Figure 12.6: Posterior probability of the model. Slice along two parameters. Viscous model. Time-domain. Residue r_0.

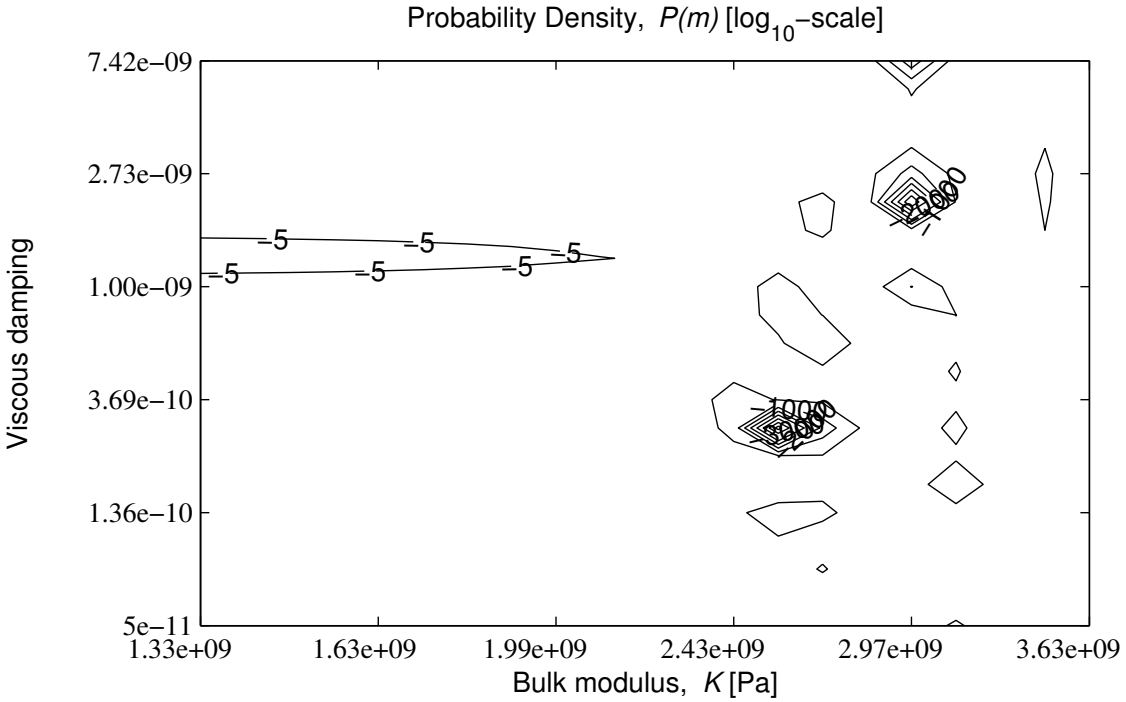

Figure 12.7: Poste1ior probability of the model. Slice along two parameters. Viscous model. Time-domain. Residue r_3.

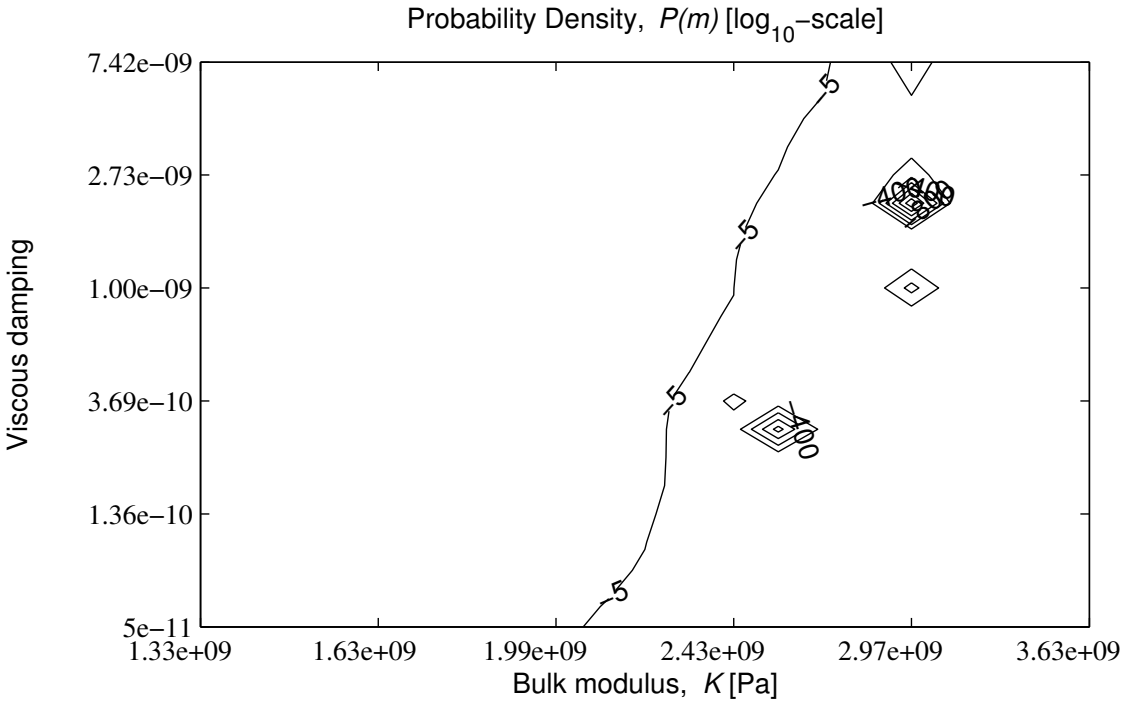

Figure 12.8: Posterior probability of the model. Slice along two parameters. Viscous model. Magnitude-spectrum. Residue $\boldsymbol{r}_0$.

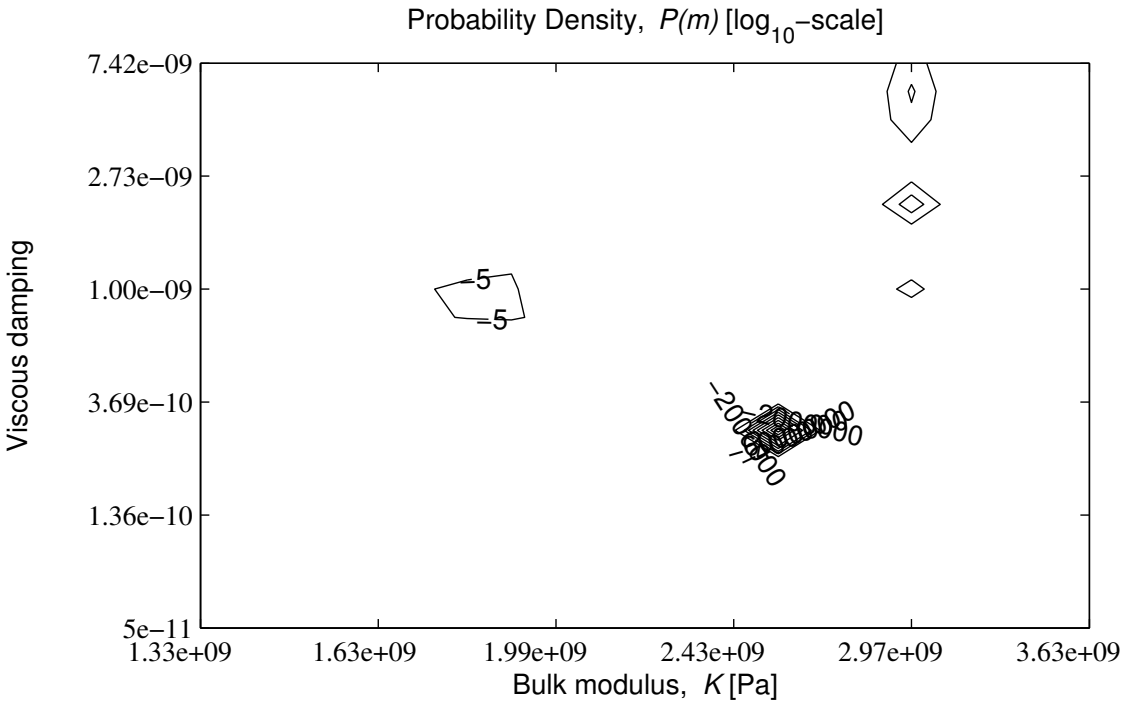

Figure 12.9: Posterior probability of the model. Slice along two parameters. Viscous model. Magnitude-spectrum. Residue $\boldsymbol{r}_3$.

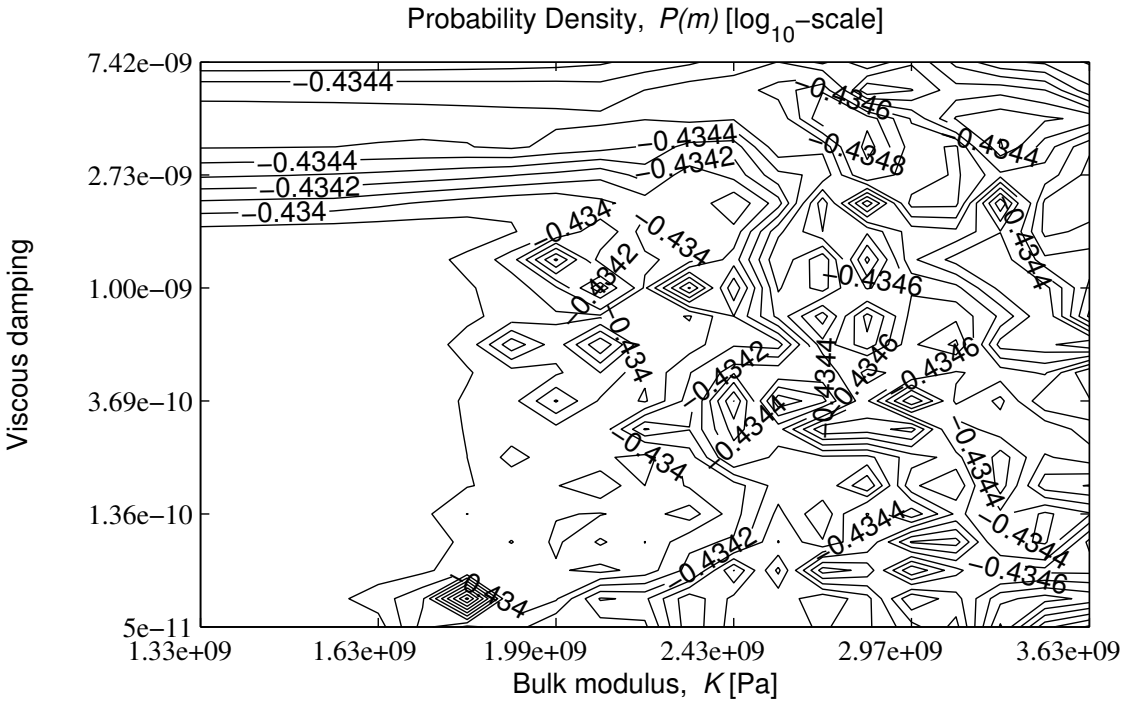

Figure 12.10: Posterior probability of the model. Slice along two parameters. Viscous model. Real cepstrum. Residue r_0.

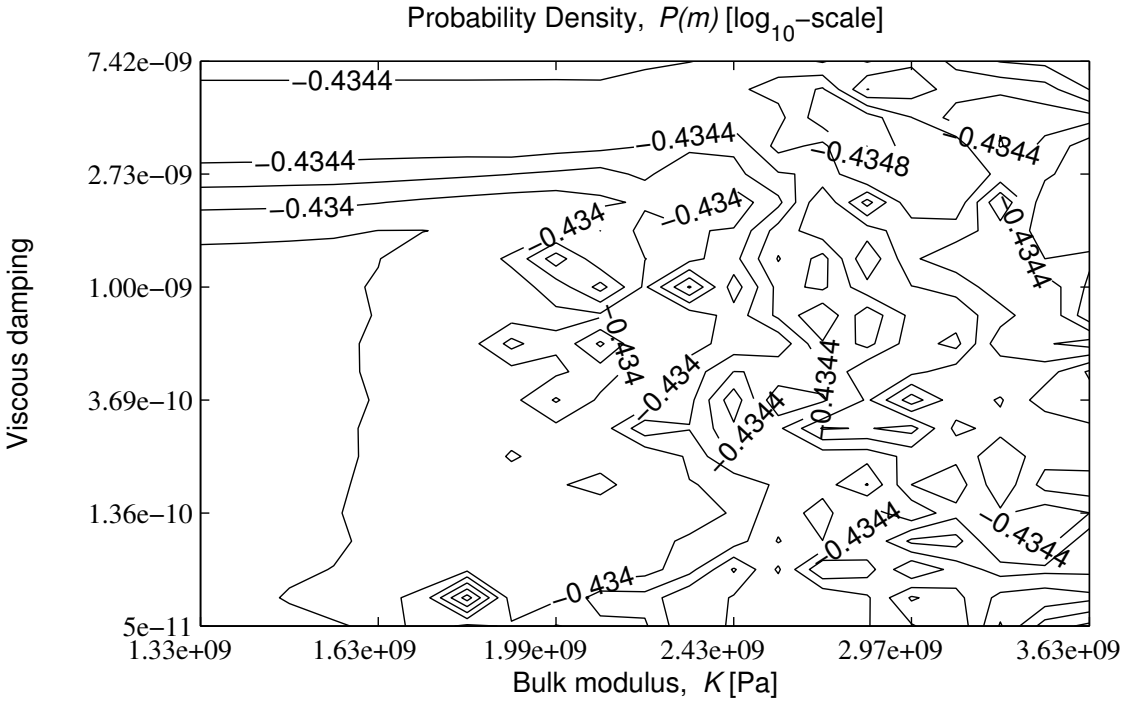

Figure 12.11: Posterior probability of the model. Slice along two parameters. Viscous model. Real cepstrum. Residue r_3.

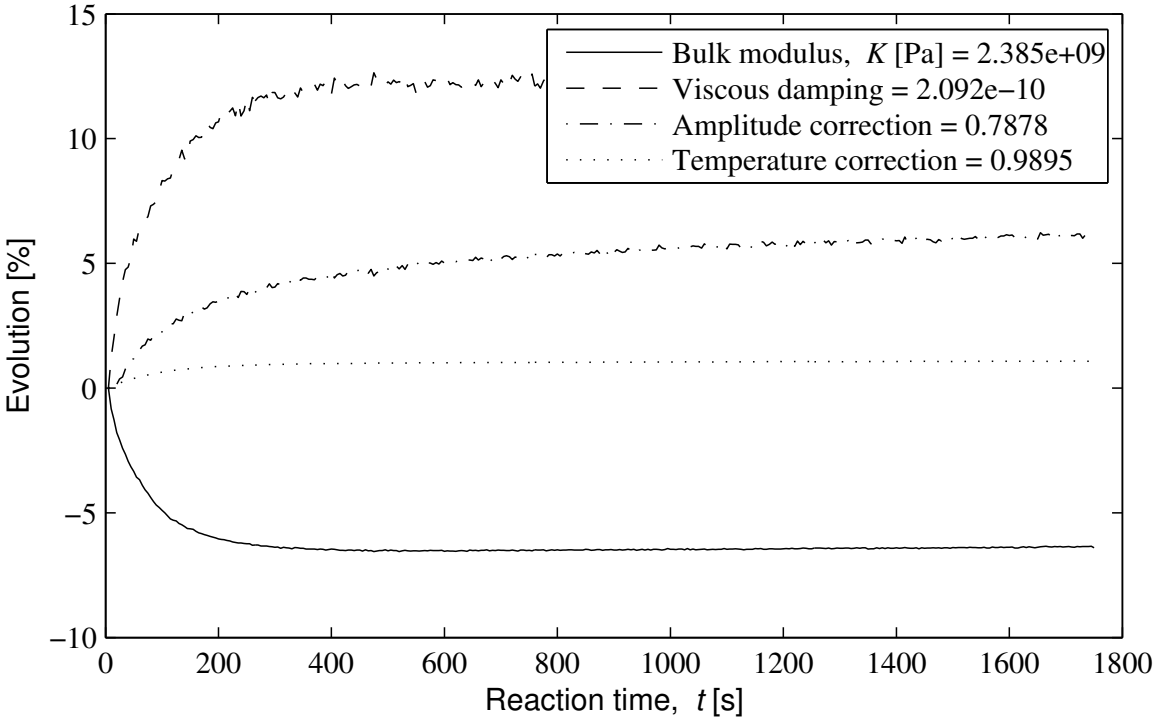

Figure 12.12: Evolution of model parameters during reaction. Viscoelastic model. Time-domain. Classical residue. Without signal windowing.

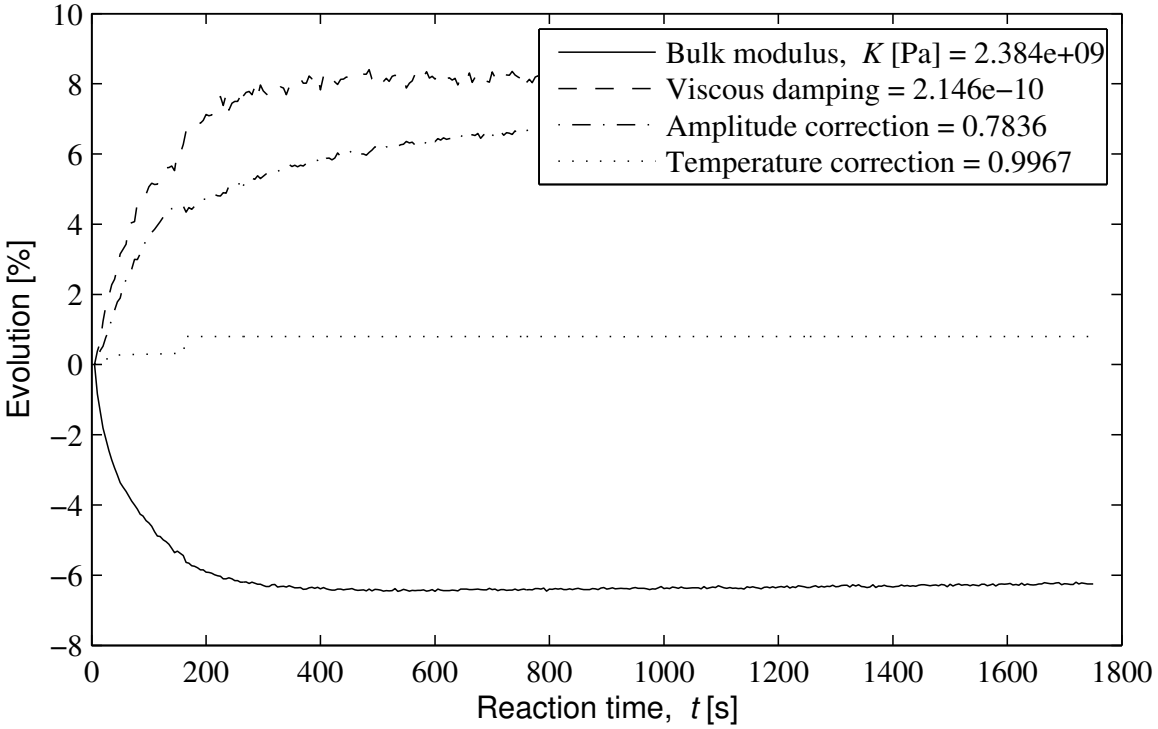

Figure 12.13: Evolution of model parameters during reaction. Viscoelastic model. Magnitude spectrum. Weighted residue. Signal windowing.

13

A nonlinear through-transmission finite-amplitude method for bone damage assessment

This chapter aims at measuring the effective material nonlinearity β using a finite-amplitude through-transmission nonlinear method, also called harmonic generation technique. Since a major practical difficulty of the second harmonic generation technique relies on the existence of nonlinear distortions from the electronic devices, a semi-analytical approach is proposed to extract the intrinsic material nonlinearity, by separating the nonlinear contributions from the immersion medium, the transducers and the electronics. Laboratory experiments were conducted on a bovine cortical bone sample, and on other materials with increasing structural complexity for validation. The correlations between cracks density and the ultrasonic properties (velocity, attenuation and nonlinearity) are investigated, and the results are contrasted against other available NDE techniques.

13.1 Postprocessing method

The measurements procedure consists of four steps. Initially, the response signal was measured in water at two different positions corresponding to locations ahead of and at the back of the specimen (steps ① and ②). Then, the response signals were measured with the specimen *in situ* along the scanning area at both frequencies (steps ③ and ④).

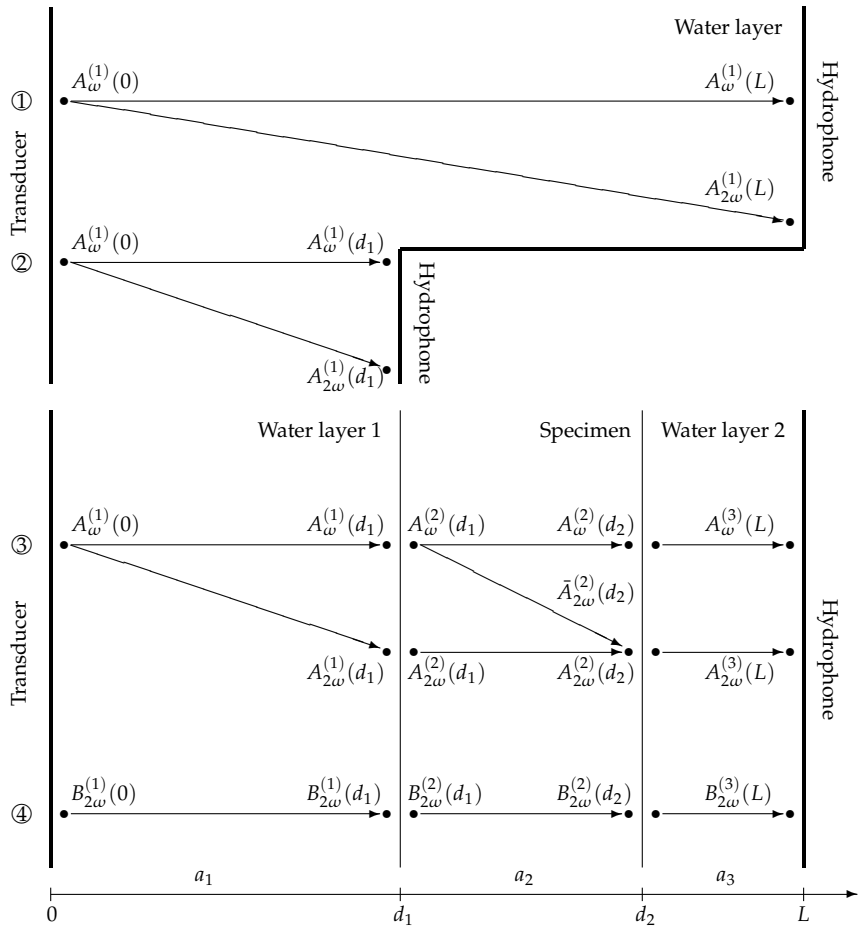

Figure 13.1: Semi-analytical approach used to extract the linear and nonlinear material's properties from the measurements.

In order to reconstruct the linear and nonlinear material's properties of the specimen under inspection, a semi-analytical approach is proposed by considering the following assumptions: (i) the attenuation in the water layers is negligible, (ii) the thickness a_3 of water layer 2 is small, and thus the nonlinearity can be assumed not to accumulate over this distance (i.e. $\beta_w^{(3)} \approx 0$) [285], (iii) only second harmonics are considered, and thus frequency-mixing effects due to higher-order harmonics are negligible, and (iv) the density of the specimen is assumed to be constant. The measurements procedure along with the semi-analytical approach are summarized in Figure 13.1.

The wave velocity c_s of the specimen can be calculated by cross-correlating the windowed waveforms in water and in the specimen at a distance L from the transducer, characterized by the amplitudes $A_\omega^{(1)}(L)$ and $A_\omega^{(3)}(L)$. The attenuation coefficients (expressed in [dB/cm/MHz]) of the specimen at the central frequencies ω and 2ω can be obtained by comparing the measurements in water ahead of the specimen with the ones in the specimen

as,

$$\alpha_1 = 20\frac{\log\left(\frac{A_\omega^{(1)}(d_1)T_{sw}T_{ws}}{A_\omega^{(3)}(L)}\right)}{a_2 f_c} \quad , \quad \alpha_2 = 20\frac{\log\left(\frac{B_{2\omega}^{(1)}(d_1)T_{sw}T_{ws}}{B_{2\omega}^{(3)}(L)}\right)}{2a_2 f_c} \tag{13.1}$$

where T_{ws} and T_{sw} denote the transmission coefficients from water to specimen, and specimen to water, respectively. The second harmonics amplitude can be written down as,

$$\begin{aligned} A_{2\omega}^{(3)}(L) &= \left(A_{2\omega}^{(2)}(d_2) + \bar{A}_{2\omega}^{(2)}(d_2)\right) T_{sw} \\ &= \left(A_{2\omega}^{(2)}(d_1)e^{-\alpha_2 a_2} + \bar{A}_{2\omega}^{(2)}(d_2)\right) T_{sw} \\ &= \left(A_{2\omega}^{(1)}(d_1)e^{-\alpha_2 a_2}T_{ws} + \bar{A}_{2\omega}^{(2)}(d_2)\right) T_{sw} \end{aligned} \tag{13.2}$$

By applying Equation (4.21), the intrinsic nonlinear parameter β_s of the specimen can be obtained as,

$$\beta_s = \frac{4c_s^2\bar{A}_{2\omega}^{(2)}(d_2)}{\omega^2 a_2\left(A_\omega^{(2)}(d_2)\right)^2} = \frac{4c_s^2\left(A_{2\omega}^{(3)}(L)T_{sw} - A_{2\omega}^{(1)}(d_1)e^{-\alpha_2 a_2}T_{ws}T_{sw}^2\right)}{\omega^2 a_2\left(A_\omega^{(3)}(L)\right)^2} \tag{13.3}$$

It is noteworthy that, in the proposed form, this solution accounts for both the specimen attenuation and the impedance losses due to the immersion medium. Alternatively, the effective nonlinear parameter β_{obs} is also computed, which is directly extracted from the observed fundamental and second harmonics.

$$\beta_{obs} = \frac{4c_{obs}^2 A_{2\omega}^{(3)}(L)}{\omega^2 L\left(A_\omega^{(3)}(L)\right)^2} \tag{13.4}$$

where c_{obs} is the effective wave velocity obtained by applying classical mixing rules,

$$c_{obs} = \frac{d_w + d_s}{\frac{d_w}{c_w} + \frac{d_s}{c_s}} \tag{13.5}$$

where d_i and c_i, with $i = w, s$ denote the thickness and wave velocity of the immersion medium and specimen, respectively.

13.2 Validation

The semi-analytical approach together with the experimental methodology defined above are applied to a set of specimens composed of increasingly complex materials in order to validate the method.

Figure 13.2 shows the time-domain signals and magnitude spectra of the ultrasonic signals measured with and without the PMMA sample in the acoustic path by using the finite-amplitude through-transmission method. The time-domain signals distortions are shown

to increase along the acoustic path in the direction of increasing damage level. A direct interpretation of the nonlinearity variation is not feasible in the frequency-domain, since the second harmonic peaks measured with the specimen in-place are affected by the nonlinear contribution of water. Nonetheless, the second harmonic peak values measured on the damaged area appear to be higher than the ones measured on the undamaged area.

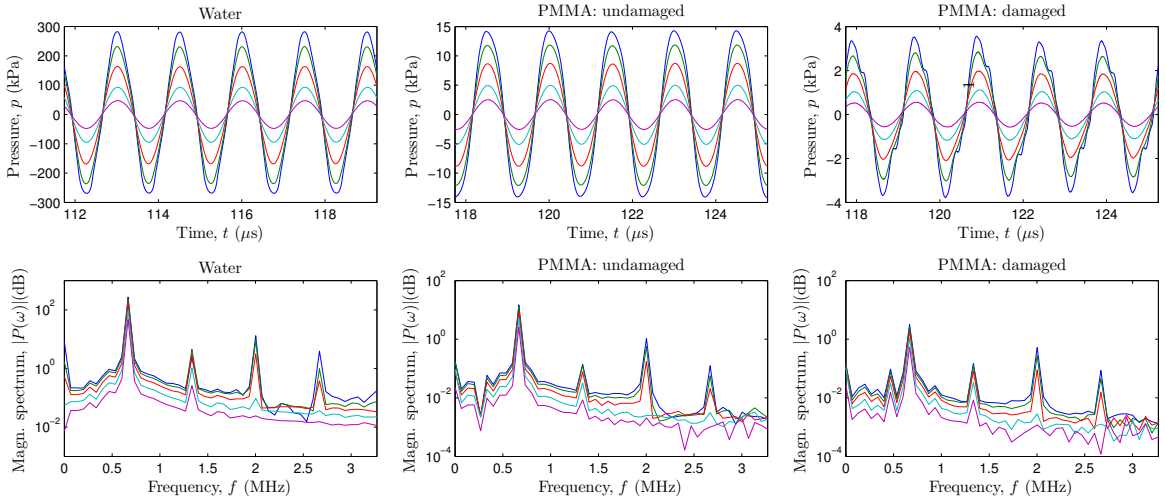

Figure 13.2: Time-domain signals and magnitude spectra of the ultrasonic signals measured with and without the PMMA sample in the acoustic path.

The wave velocity, attenuation, effective nonlinearity, and PMMA nonlinearity maps obtained for the scanned areas are depicted in Figure 13.3. The wave velocity c_p is observed to decrease as the holes density increases. However, the latter acoustic property only provides a kind of global information about areas of higher/lower density, nonetheless without achieving an accurate localization and quantification of the holes themselves. In contrast, the attenuation coefficient α and effective nonlinear parameter β_{obs} provide more fine information about the damage type and location. It is worth to point out that the intrinsic nonlinear parameter β of the material enhance the previous observations.

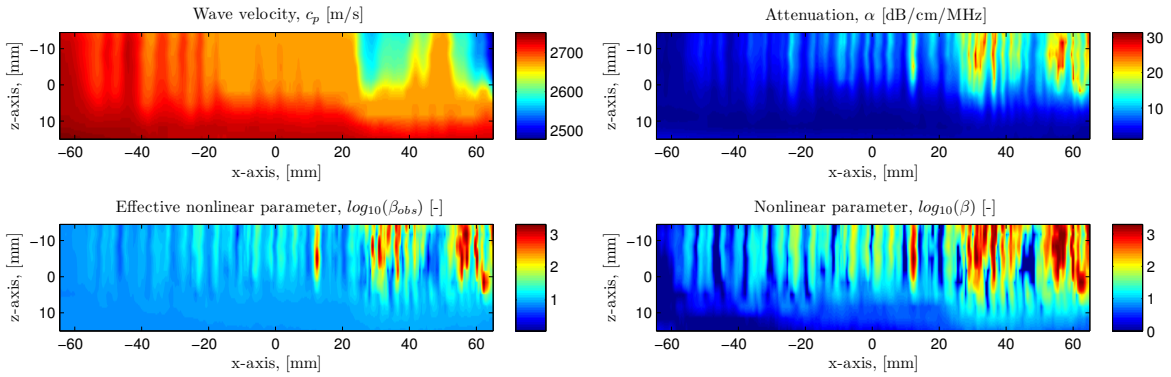

Figure 13.3: Results obtained for the PMMA beam: Wave velocity c_p, attenuation coefficient α, effective nonlinear parameter β_{obs}, and nonlinear parameter β.

Figure 13.4 shows the linear and nonlinear material properties as a function of the drilled holes density. The squares represent the experimental measurements averaged each 7.5 millimeters (whose values correspond to the mean values of the map columns of Figure 13.3), whereas the solid line represents the linear regression fit to the measurements. The wave velocity and attenuation coefficient show high r-values (-0.94 and 0.92, respectively) with the drilled hole density. A slightly higher correlation is obtained between the drilled hole density and the nonlinear parameter β ($r = 0.95$).

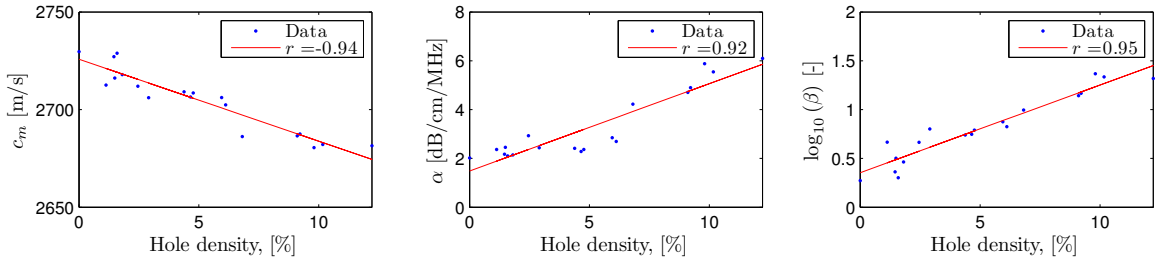

Figure 13.4: Linear and nonlinear material properties as a function of the drilled holes density.

The Pearson's correlation coefficients r obtained between the drilled hole density and the ultrasonic properties (c_p, α, and β) for the PMMA sample are summarized in Table 13.1, along with correlations between pairs of the ultrasonic properties ($p < 10^{-8}$ for all).

Parameter	Density	c_p	α	β
Density	1	-0.94	0.92	0.95
c_p		1	0.91	-0.98
α			1	0.91
β				1

Table 13.1: Pearson's correlation r between drill density and ultrasonic properties.

Alternatively, Table 13.2 shows the univariate and the multivariate regression models that predict the hole density from the ultrasonic properties.

Dependent variable	Independent variable	R^2
Drill density	c_p	0.88
	α	0.85
	β	0.91
	c_p, α	0.90
	c_p, β	0.91
	α, β	0.92
	c_p, α, β	0.93

Table 13.2: Univariate and multivariate regression models that predict the drill density from the ultrasonic properties.

The best univariate predictor of the hole density is proved to be β, which provides an adjusted squared correlation coefficient $R^2 = 0.91$. The multivariate regressions substantially increase R^2 over the univariate regression, when including c_p and/or α within the models.

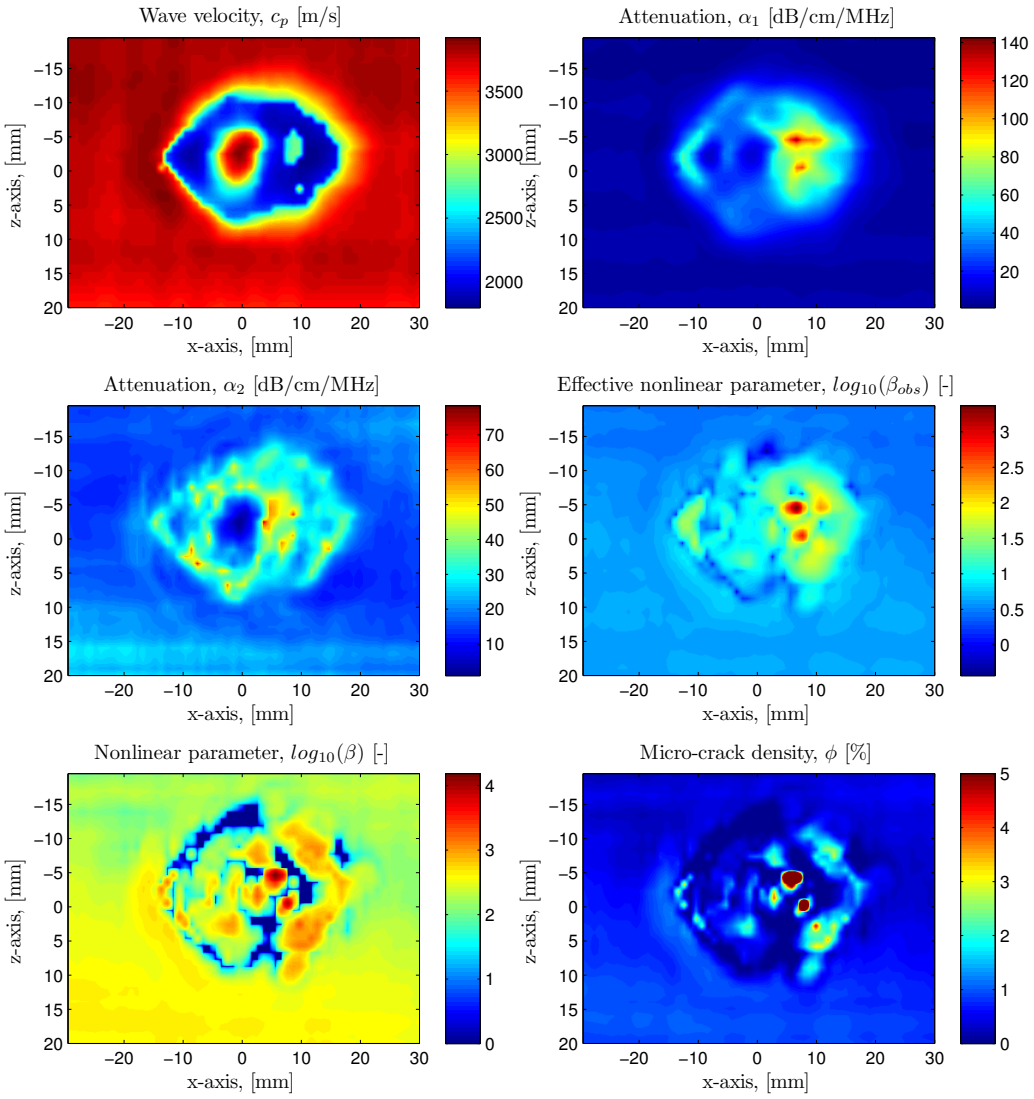

Figure 13.5: Results obtained for the CFRP plate: Wave velocity c_p, attenuation coefficients α_1 and α_2, effective nonlinear parameter β_{obs}, and nonlinear parameter β, along with the micro-crack density ϕ.

These results strengthen the previous observations, namely that the nonlinear parameter β may have potential, along with the linear ultrasonic properties c_p and α to characterize damaged materials.

Figure 13.5 depicts the wave velocity, attenuation coefficients, effective nonlinearity, and CFRP nonlinearity maps obtained for the scanned areas. As expected, the wave velocity c_p is found to decrease around the impacted zone. As observed in the case of the PMMA, the attenuation coefficients α_1 and α_2, and the effective nonlinear parameter β_{obs} enables us to obtain further information about the damage type (matrix cracking, delaminations, etc.) and projected location. Again, the intrinsic nonlinear parameter of the material provides

enhanced information, in the sense that it could be complemented with that of the linear properties.

The micro-crack density ϕ is calculated from the equation provided by Rus *et al.* [320], and contrasted against experimental values obtained from an X-ray image. On the one hand, three damage areas (A_1, A_2, and A_3) were selected from the X-ray image and the number of (micro-)cracks were counted over those areas to determine the density. On the other hand, the ϕ-values obtained numerically were averaged over the corresponding areas, as depicted in Figure 13.6. The micro-cracks densities obtained experimentally for the three areas are $[\phi_1, \phi_2, \phi_3]_{exp} = [0.85, 0.95, 0.78]\%$, and are of the same order of magnitude as those obtained numerically ($[\phi_1, \phi_2, \phi_3]_{num} = [0.78, 0.99, 0.42]\%$).

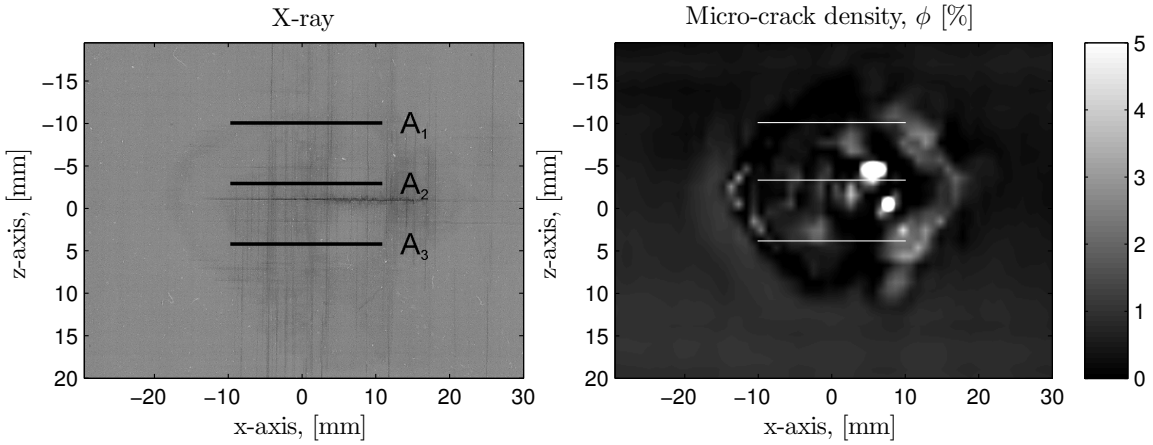

Figure 13.6: Experimentally obtained and numerically predicted micro-cracks densities.

13.3 Bone damage assessment

The time-domain signals and magnitude spectra of the ultrasonic signals measured with and without the bone sample in the acoustic path by using the finite-amplitude through-transmission method are depicted in Figure 13.7. As observed for other materials, the time-domain signal nonlinear distortions increase with the specimen in the acoustic path (and more when a damaged area is scanned). Again, the second harmonic peak values measured on the damaged area are consistently observed to be significantly higher than the ones measured on the undamaged area.

Figure 13.8 depicts the wave velocity, attenuation coefficients, effective nonlinearity, and bone nonlinearity maps obtained for the scanned areas. The wave velocity c_p remains significantly constant (the variations are mainly due to the intrinsic inhomogeneous bone properties). As observed in the aforementioned cases, the attenuation coefficients α_1 and α_2, and the effective nonlinear parameter β_{obs} allows to obtain further information about the bone structure (such as apposition lines, which appear concentrically) and damages. The intrinsic nonlinear parameter of the material consistently provides enhanced structural information.

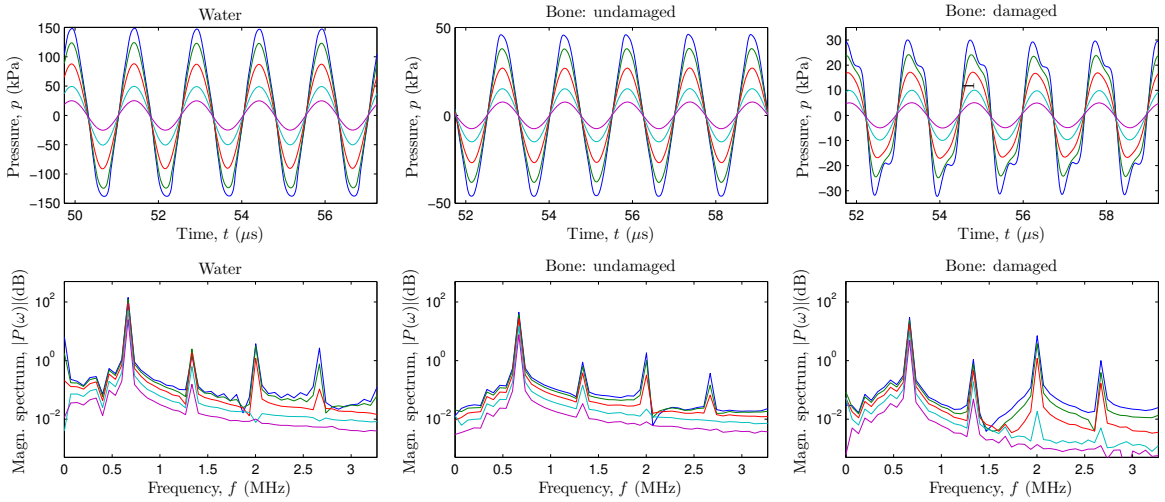

Figure 13.7: Time-domain signals and magnitude spectra of the ultrasonic signals measured with and without the PMMA sample in the acoustic path.

Table 13.3 summarizes the obtained results, providing a range of values for the undamaged and damaged specimens. The interval values indicate the changes from undamaged to damage state, whereas interval values between squared brackets indicate the variations within the sample (for the case of bone sample only, since its structure cannot be considered homogeneous).

Material	Wave velocity c_p $[m/s]$	Attenuation α $[dB/cm/MHz]$	Nonlinearity β $[-]$
Water	1500	0.002	4.6
PMMA	2740-2480	0.8-12	10-1000
CFRP	3500-2000	2-70	390-1600
Cortical bone	[3300-4000]	[5-8]	[100-300]

Table 13.3: Mechanical properties of the considered materials.

Those results can also be compared to literature values when available. The β values for water and PMMA are in reasonable agreement with measurements previously obtained by other authors, where they usually amount to around $\beta_{water} \in [3-6]$ [321, 283, 210] and $\beta_{pmma} \in [9-15]$ [322, 283], respectively. The β values for the CFRP plate is hardly comparable, since it may strongly depend upon the manufacture process, on the properties of each component, and on the laminate stacking sequence. The linear properties of the cortical bone sample are in good agreement with that provided by Laugier and Haïat [323]. To our knowledge, the intrinsic β value for the cortical bone sample has never been reported before. The microstructure of cortical bone is considerably different as that of trabecular bone, but it is reasonable to expect that the nonlinearity of dense trabecular bone could be of the same order of magnitude than that of cortical bone, as a first approximation. Indeed, the β values for the cortical bone sample fall within the range of those reported by some authors for dense trabecular bone samples [283, 285].

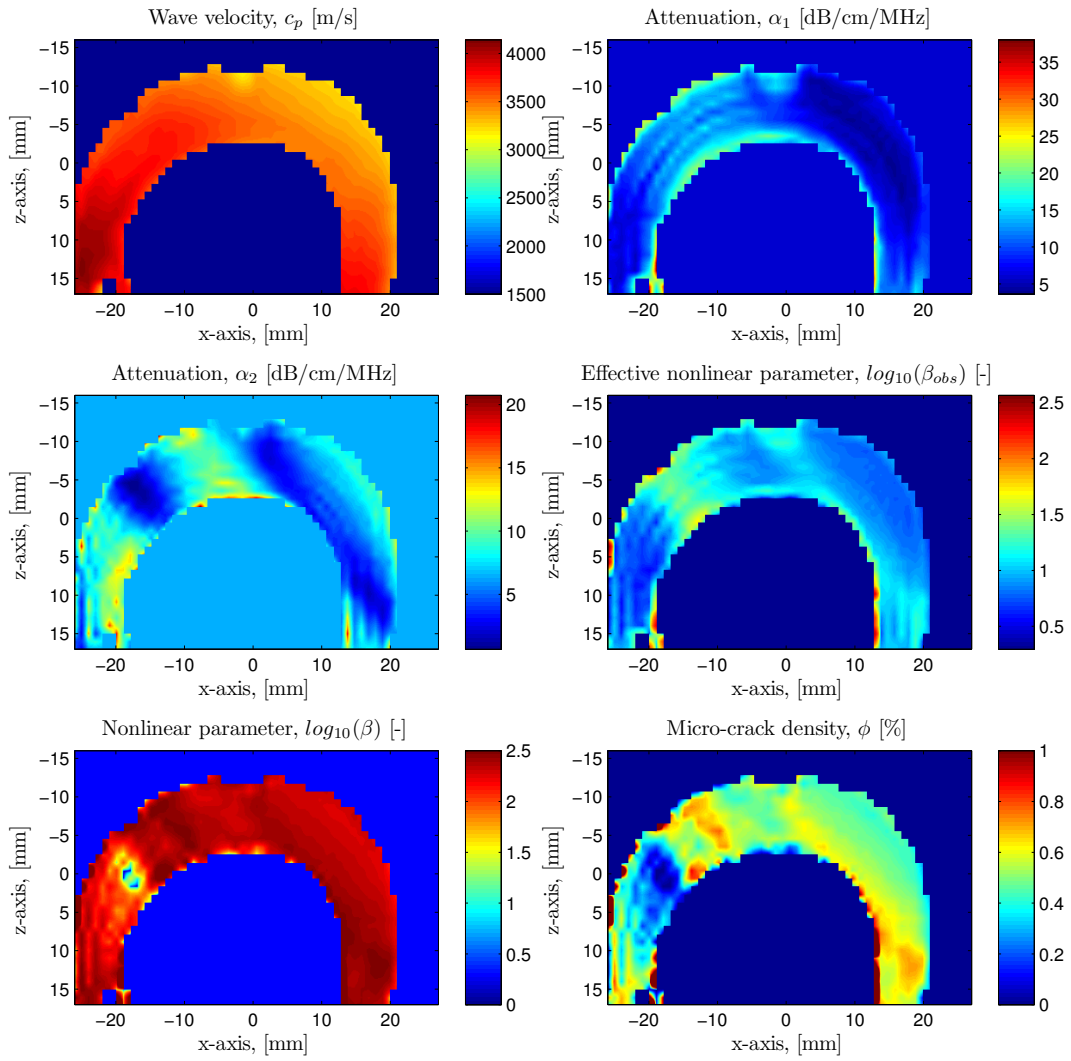

Figure 13.8: Results obtained for the bone sample: Wave velocity c_p, attenuation coefficients α_1 and α_2, effective nonlinear parameter β_{obs}, and nonlinear parameter β, along with the micro-crack density ϕ.

13.4 Conclusions

The present study investigates the feasibility of the nonlinear finite-ampli-tude through-transmission method for cortical bone damage assessment in vitro. A semi-analytical model has been proposed to extract the nonlinear parameter of first-order β from the measurements. In addition, to understand the relationship between nonlinearity and fracture risk, a homogenization formulation including the clapping contact mechanism has been developed in Part I to hypothesize a relationship with the density of microcracks. This parameter has been successfully related to damage, and appears consistent with other nondestructive damage assessment techniques. The results are validated on materials with increasing structural complexity. This work suggests that β may have potential, along with the linear ultrasonic properties c_p and α, for bone damage assessment and fracture risk prediction.

Part V

CONCLUSIONS AND FUTURE WORKS

14

Conclusions and future works

This chapter presents the most relevant conclusions of the obtained results, along with a discussion regarding the exposed contributions. In addition, some future works currently under development at our laboratory are commented.

Ultrasonic wave modeling

In this thesis, we presented a signal modeling framework for wave propagation in multilayered materials, which is based on concepts drawn from lattice filter theory. The underlying methodology is based on a physical analysis of the ultrasound-material interactions, and provides a further understanding of the relationship between the material properties and the model parameters. First, an analogy between the signal modeling approach and the Transfer Matrix formalism has been established, highlighting the strength and limitations of both methods. Then, a theoretical formalism has been proposed, which efficiently extends the classical recursive framework for Goupillaud-type media to any multilayered structures. The resulting formalism has demonstrated that a through-transmission setup for ultrasonic wave propagation in multilayered structures can be modeled as a classical all-pole filter with sparse coefficients. Ongoing theoretical work includes further exploitation of concepts drawn from signal theory to study the wave propagation phenomena within multilayered structure under conditions less restrictive than those used here, such as oblique incidence of the emitted wave or other layer properties as frequency-dependent attenuation.

In addition, both the digital signal model and the TM formalism were extended to account for nonlinear constitutive behavior. Concretely, the NTM formalism was successfully developed and demonstrated its potential for ultrasonic wave propagation in multilayered

structures. In contrast, the nonlinear digital signal model, in its proposed form lacks of practical applicability. future research in that vein should be conducted, especially on the feasibility of ex- pressing the nonlinear frequency response as a discrete-time transfer function, along with the possibility of representing some missing physical components into the network diagram. Finding a discrete-time transfer function that approximates the nonlinear frequency response for the frequency range of interest in a suitable way is particularly challenging, since the resulting filter of first-order might have a huge number of coefficients.

Signal processing and feature extraction

This work shows the capability of a digital signal modeling approach which incorporates underlying mechanical concepts to identify damage in composite materials, particularly in a CFRP plate subjected to different impact energies. A set of experimental case studies has been proposed to evaluate the potential of the developed digital signal model in some practical NDE applications. In a first experiment, a damage detection evaluation has been carried out, showing that the digital filter represents an extremely fast and promising tool to discriminate damaged from undamaged specimens by inverse filtering. Indeed, this inverse filter is a sparse FIR filter, whose coefficients were directly obtained from the material?s properties, without requiring any experimental calibration. In a second experiment, the discrimnative performance of the proposed model has been evaluated by a system based on *cepstral* distances that recognizes the specific damage level corresponding to a given test signal. The damage levels have been identified with an accuracy of 98.37 % with a model that consists of 15 parameters, that is, half the amount of a full LPC model. It has been demonstrated that a sparse signal modeling with a reduced number of coefficients provides better results than other common spectrum estimation techniques. In contrast to standard or empirical models, the coefficients position and extent of our model are inherently linked to the material?s properties (i.e. twice the thickness of the plate, stiffness, etc.), and thus to its health state.

Inverse filtering experiments for real-time monitoring of CFRP plates damaged by impact and fatigue with ultrasonic C-scan methods are currently under development at our laboratory. Ongoing work includes further use of sparse signal models for ultrasonic NDE of materials, and particularly the use of a dynamic model with variable coefficients position and gain to improve the performance of damage recognition systems.

Model-based estimation procedure

The presented monitoring technique achieves for the first time the reconstruction of multiple damages in CFRP plates from a single measurement. The methodology is physics-based through a computational models of ultrasound-pathology interactions. In contrast to other studies, the damage is not identified by considering the time-of-flight or the broadband ultrasound attenuation, but by reconstructing the complete waveform. Moreover, the damage multiplicity does not only appear at several locations (layers) but simultaneously in different

forms (layer degradation and interlaminar debonding). For a better understanding of the damage mechanisms, further investigations may be conducted by validating our proposal with other NDE techniques, such as X-ray.

A numerical method to determine the elastic and dynamic energy dissipation properties during tissue-engineered processes has been developed by combining the solution of a probabilistic inverse problem with signal processing techniques, applying genetic algorithms to minimize a cost function, and using a semi-analytical model of the interaction between ultrasonic waves and tissue. The proposed model-class and residue selection and their underlying class plausibility have enabled ranking of both the models and the suitable residue definitions according to their compatibility with the observations. The resulting trade-off between model simplicity and fitting to observations has demonstrated that the viscous damping models, combined with some prior information on the measurements variance over the reaction process evolution, are feasible to characterize the complex evolution of the process. For a better understanding of ultrasonic tissue monitoring, further *in vitro* studies on real tissue combined with histological studies may be conducted.

Nonlinear ultrasound

The finite-amplitude through-transmission method is a relatively straight-forward technique to measure the second harmonic peak, and thus obtain nonlinear parameters of a material. The low complexity of the experimental installation could make of this method a low-cost and valuable technology for in-vivo diagnostic applications. Nonetheless, a practical extraction of the second harmonic requires efforts in minimizing the nonlinear distortions from electronic devices and in optimizing the reproducibility of the experiment. Indeed, several factors such as the size of the gap between the specimen and the hydrophone or the geometrical dispersion of the transducers (inherently related to the focal distance) may have a drastic influence on the measured β, and should be analyzed carefully. The proposed semi-analytical model offers an efficient way to extract the intrinsic nonlinear parameters from the observed signals. However, a sensitivity study should be performed to assess the influence of independent variables such as specimen density and thickness, on its performance. Moreover, this simple model should be improved to take into account higher-order nonlinearities or even nonclassical behavior such as hysteresis. Although the understanding of the influence of odd harmonics is beyond the scope of the present study, it is noteworthy that an increase of the third harmonics (and probably higher-order ones) at high energy levels could be detectable.

Despite those restrictions, it has been demonstrated that (i) the nonlinear parameters increase in a logarithmic way with respect to increasing damage, (ii) the effective nonlinear parameter provides information nearly similar to that offered by the attenuation coefficient, and is thus totally ineffective from a practical point of view, and that (iii) in contrast to the previous effective property, the nonlinear parameter extracted from the semi-analytical delivers valuable and complementary information to the linear mechanical properties. This

last property could turn nonlinear ultrasonics a feasible and sensitive diagnostic fracture risk assessment tool.

15

Conclusiones y trabajos futuros

Este capítulo presenta las conclusiones más relevantes acerca de los resultados obtenidos junto con la discusión sobre las contribuciones expuestas. Asimismo se comentarán algunos trabajos que actualmente están en desarrollo en nuestro laboratorio.

Modelos de propagación de la onda ultrasónica

En esta tesis, presentamos un procedimiento de modelado de la señal para la propagación de ondas en materiales estratificados basado en conceptos inspirados por la teoría de filtros en celosía. La metodología subyacente se basa en un análisis físico de las interacciones de las señales ultrasónicas con el material, y proporciona una mejor comprensión de las relaciones entre las propiedades del material y los parámetros del modelo. En primer lugar, se ha establecido una analogía entre el planteamiento del modelado de señal y el formalismo de la Matriz de Transferencia, señalando las ventajas y las limitaciones de ambos métodos. En segundo lugar, se ha propuesto un formalismo teórico, el cual amplía de forma eficiente el planteamiento clásico recursivo para los materiales del tipo Goupillaud para cualquier estructura estratificada. El formalismo resultante ha demostrado que un dispositivo de transmisión para la propagación de ondas ultrasónicas en materiales estratificados puede ser modelado como un filtro todo-polo clásico con coeficientes *sparse*. Los trabajos teóricos futuros incluirán una exploración más avanzada de los conceptos inspirados desde la teoría de la señal para el estudio del fenómeno de la propagación de ondas en estructuras estratificadas bajo condiciones menos restrictivas que las que han sido usadas en el caso que se presenta, como por ejemplo incidencias oblicuas de la onda emitida u otras propiedades de las capas como una atenuación dependiente de la frecuencia.

Por otra parte, tanto el modelado de señal digital como el formalismo *TM* han sido ampliados para tener en cuenta el comportamiento constitutivo no lineal. Concretamente, el formalismo *NTM* ha proporcionado resultados satisfactorios. En cambio, el modelado digital de señal no lineal, en la forma propuesta carece de aplicabilidad práctica. Las próximas investigaciones que deberán realizarse en ese sentido consideran la factibilidad de expresar la respuesta en frecuencia no lineal como una función de transferencia en tiempo discreto, junto con la posibilidad de representar algunas componentes físicas ausentes en el diagrama de cuate puertos. Sería además un desafío encontrar una función de transferencia en tiempo discreto con una forma adecuada que aproxime la respuesta en frecuencia no lineal para el rango de frecuencia de interés, ya que el filtro de primer orden resultante puede tener un enorme número de coeficientes.

Procesado de señal y extracción de características

Este trabajo muestra la capacidad de un planteamiento de modelado digital de señal que incorpora conceptos subyacentes de mecánica para identificar el daño en materiales compuestos, particularmente en una placa de fibra de carbono sometida a diferentes energías de impactos. Hemos estudiado un conjunto de casos experimentales para evaluar el potencial del modelado digital de señal desarrollado en algunas aplicaciones de evaluación no destructiva ultrasónica. En un primer experimento, se ha llevado a cabo una evaluación de detección de daños, que nos muestra que el filtro digital representa una herramienta extremamente rápida y prometedora para discriminar los especímenes dañados de los no dañados por el uso de un filtro inverso. En efecto, este filtro inverso es un filtro *sparse FIR*, cuyos coeficientes han sido obtenidos directamente de las propiedades del material sin que haya sido necesario realizar ningún tipo de calibración experimental. En el segundo experimento, la capacidad para discriminar daños del modelo propuesto ha sido evaluada por un sistema basado en distancias *cepstrales* que reconoce el nivel específico de daño correspondiente a una señal de test dada. El nivel de daño ha sido identificado con una precisión de 98.37% con un modelo que consiste en 15 parámetros, lo que significa la mitad de la cantidad de un modelo *LPC* completo. Se ha demostrado que un modelo de señal *sparse*, con un reducido número de coeficientes, proporciona mejores resultados que otras técnicas de estimación de espectros comunes. En contraste con los modelos empíricos o estándar, las posiciones y las extensiones de los coeficientes de nuestro modelo están inherentemente vinculadas con las propiedades del material (por ejemplo el doble del grosor de la placa, la rigidez, etc.), y por tanto a su estado de salud.

Los experimentos con filtros inversos para monitorizar en tiempo real placas de fibra de carbón dañadas por impacto y fatiga con métodos de ultrasonidos C-scan están siendo desarrollados en nuestro laboratorio. Los trabajos en curso tienen previsto un uso más amplio del modelo de señal *sparse* para la evaluación no destructiva ultrasónica de materiales, y particularmente el uso de un modelo dinámico con coeficientes de posición variable para tratar de mejorar los sistemas de reconocimiento de daños.

Procedimiento de estimación basado en modelos

La técnica de monitorización presentada permite lograr por primera vez la reconstrucción de múltiples daños en placas de fibra de carbono a partir de una sola medida. Esta metodología está basada en la física a través de un modelo computacional de las interacciones de los ultrasonidos con la patología. A diferencia de otros estudios, las patologías no se identifican considerando el tiempo de vuelo o la atenuación ultrasónica de banda ancha, sino que se identifican reconstruyendo la forma de onda completa. Además, los múltiples daños no solo aparecen en posiciones distintas del material (capas), sino más bien simultáneamente de forma distinta (degradación de las capas o despegamiento interlaminar). Para una mejor comprensión de los mecanismos de daño, las futuras investigaciones deberán orientarse hacia la validación de nuestra propuesta con otras técnicas no destructivas, como los rayos X.

Se ha desarrollado un modelo numérico para determinar la elasticidad y las propiedades dinámicas de disipación de la energía durante los procesos evolutivos de cultivos tisulares, combinando la solución de un problema inverso probabilístico con las técnicas de procesado de señal, aplicando algoritmos genéticos para minimizar la función de coste, y usando un modelo semi-analítico de interacción de las ondas ultrasónicas con el tejido. La selección de modelo y de residuo propuesta y la plausibilidad de clase subyacente nos ha permitido clasificar las definiciones de modelos y de residuos respecto a su compatibilidad con las observaciones. En consecuencia, el compromiso entre la simplicidad del modelo y su adaptación a las observaciones ha demostrado que el modelo de atenuación viscosa, combinado con alguna información *a priori* sobre la varianza de las medidas a lo largo del proceso de evolución, son factibles para caracterizar la compleja evolución del proceso. Para una mejor comprensión de la monitorización ultrasónica del tejido deberán realizarse otros estudios *in vitro* en tiempo real.

Ultrasonidos no lineales

El método de amplitud finita en transmisión es una técnica relativamente directa para medir el pico del segundo armónico, y así obtener los parámetros no lineales del material. La baja complejidad del montaje experimental hace de ese método un candidato óptimo para el desarrollo de una tecnología de bajo coste eficaz para aplicaciones de diagnostico in vivo. No obstante, a nivel practico, una extracción del segundo armónico requiere un particular esfuerzo a la hora de minimizar las distorsiones no lineales del dispositivo electrónico y de optimizar la reproducibilidad del experimento. De hecho, ciertos factores como el tamaño del hueco entre el espécimen y el hidrófono o la dispersión geométrica de los transductores (intrínsecamente relacionadas con la distancia focal) pueden tener una influencia drástica sobre el parámetro no lineal medido, y por tanto tienen que ser analizados detenidamente. El modelo semi-analítico propuesto ofrece una vía eficiente para extraer los parámetros no lineales intrínsecos de las señales observadas. Por tanto, deberá realizarse un estudio de sensibilidad para averiguar la influencia de variables independientes como la densidad

o el espesor del espécimen sobre el comportamiento del modelo. Además, este modelo básico debería ser ampliado para tener en cuenta no linealidades de orden superior o comportamiento no clásico (histeresis). Aunque la comprensión de la influencia de armónicos impares no esta contemplado en este estudio, cabe destacar que un incremento del tercer armónico (y probablemente de los de orden superior) a niveles de energía elevados pueda ser perceptible.

A pesar de esas restricciones, hemos demostrado que (i) los parámetros no lineales crecen con un comportamiento logarítmico conforme crece el daño; (ii) el parámetro no lineal efectivo proporciona información aproximadamente similar a la proporcionada por el coeficiente de atenuación, y por tanto es inútil considerarlo en la práctica; y (iii) al contrario de la propiedad efectiva mencionada anteriormente, el parámetro no lineal extraído mediante el modelo semi-analítico nos proporciona una información valiosa y complementaria a las propiedades mecánicas lineales. Esa última propiedad nos sugiere que los ultrasonidos no lineales puedan ser una herramienta de diagnostico viable y sensible para evaluar el riesgo de fractura.

Part VI

APPENDICES

A

Derivation of the TM method

This appendix presents a step-by-step derivation of the TM method, by providing the reader the complete equations for establishing the discontinuity and propagation matrices.

A.1 Discontinuity matrix

The continuity of displacement and stress across an arbitrary interface $x = d_i$ ($i = 1, \ldots, M$) is carefully analyzed. The first condition of Equation (6.4) leads to,

$$u_i^f(d_i, \Omega) + u_i^b(d_i, \Omega) \quad = \quad u_{i+1}^f(d_i, \Omega) + u_{i+1}^b(d_i, \Omega) \tag{A.1}$$

whereas the second condition can be written down as,

$$E_i \left[\frac{\partial u_i^f(x, \Omega)}{\partial x} + \frac{\partial u_i^b(x, \Omega)}{\partial x} \right] \Bigg|_{x=d_i} \quad = \quad E_{i+1} \left[\frac{\partial u_{i+1}^f(x, \Omega)}{\partial x} + \frac{\partial u_{i+1}^b(x, \Omega)}{\partial x} \right] \Bigg|_{x=d_i} \tag{A.2}$$

yielding,

$$-jE_i \frac{\Omega}{c_i} \left[u_i^f(d_i, \Omega) - u_i^b(d_i, \Omega) \right] \quad = \quad -jE_{i+1} \frac{\Omega}{c_{i+1}} \left[u_{i+1}^f(d_i, \Omega) - u_{i+1}^b(d_i, \Omega) \right] \tag{A.3}$$

By multiplying Equation (A.3) by the factor $\frac{jc_{i+1}}{\Omega E_{i+1}}$ and adding it to Equation (A.1), an expression for the forward-propagating part of the wave displacement in layer $i+1$ as function

of the forward- and backward-propagating parts of the wave displacement in layer i can be obtained as,

$$u_{i+1}^{f}(d_i,\Omega) = \frac{1}{2}\left(1+\frac{Z_i}{Z_{i+1}}\right)u_i^{f}(d_i,\Omega)+\frac{1}{2}\left(1-\frac{Z_i}{Z_{i+1}}\right)u_i^{b}(d_i,\Omega) \tag{A.4}$$

where $Z_j = \rho_j c_j = E_j/c_j$ denotes the acoustic impedance of a layer j. An expression for the backward-propagating part of the wave displacement in layer $i+1$ can be found accordingly as,

$$u_{i+1}^{b}(d_i,\Omega) = \frac{1}{2}\left(1-\frac{Z_i}{Z_{i+1}}\right)u_i^{f}(d_i,\Omega)+\frac{1}{2}\left(1+\frac{Z_i}{Z_{i+1}}\right)u_i^{b}(d_i,\Omega) \tag{A.5}$$

From Equations (A.4)-(A.5), one can easily recover the discontinuity matrix presented in Equation (6.6).

A.2 Propagation matrix

The derivation of the propagation matrix is trivial. In linear acoustics, it is well-known that the forward- and backward propagating parts do not interact with each others. Thus, considering an harmonic wave propagating in the same homogeneous layer i from position $x = d_{i-1}$ to position $x = d_i$, its transformed displacement at the respective locations can be expressed as,

$$\begin{bmatrix} A_i e^{-j\frac{\Omega}{c_i}d_i} \\ B_i e^{j\frac{\Omega}{c_i}d_i} \end{bmatrix} = \begin{pmatrix} p_i & 0 \\ 0 & p_i^{-1} \end{pmatrix} \begin{bmatrix} A_i e^{-j\frac{\Omega}{c_i}d_{i-1}} \\ B_i e^{j\frac{\Omega}{c_i}d_{i-1}} \end{bmatrix} \tag{A.6}$$

where $p_i = e^{-j\frac{\Omega}{c_i}(d_i-d_{i-1})}$. By inserting the layer's thickness $a_i = d_i - d_{i-1}$, one directly retrieves the propagation matrix presented in Equation (6.8).

B

Outline of the signal modeling approach

This appendix describes in details the demonstrations necessary for establishing the signal modeling approach, and the subsequent digital signal model.

B.1 Distributive property

Equation (7.17) can be proven by deduction. Let us show that Equation (7.17) is correct for $M = 2$, and can thus be extrapolated to an arbitrary number of layers M.

$$\begin{aligned}
&\prod_{i=0}^{M-1} \begin{pmatrix} G_{M-i}^{(A)} e^{-j\omega m_{M-i}} & G_{M-i}^{(B)} e^{j\omega m_{M-i}} \\ G_{M-i}^{(C)} e^{-j\omega m_{M-i}} & G_{M-i}^{(D)} e^{j\omega m_{M-i}} \end{pmatrix} = \begin{pmatrix} G_2^{(A)} e^{-j\omega m_2} & G_2^{(B)} e^{j\omega m_2} \\ G_2^{(C)} e^{-j\omega m_2} & G_2^{(D)} e^{j\omega m_2} \end{pmatrix} \cdot \begin{pmatrix} G_1^{(A)} e^{-j\omega m_1} & G_1^{(B)} e^{j\omega m_1} \\ G_1^{(C)} e^{-j\omega m_1} & G_1^{(D)} e^{j\omega m_1} \end{pmatrix} = \\
&\begin{pmatrix} G_2^{(A)} G_1^{(A)} e^{-j\omega(m_1+m_2)} + G_2^{(B)} G_1^{(C)} e^{-j\omega(m_1-m_2)} & G_2^{(A)} G_1^{(B)} e^{j\omega(m_1-m_2)} + G_2^{(B)} G_1^{(D)} e^{j\omega(m_1+m_2)} \\ G_2^{(C)} G_1^{(A)} e^{-j\omega(m_1+m_2)} + G_2^{(D)} G_1^{(C)} e^{-j\omega(m_1-m_2)} & G_2^{(C)} G_1^{(B)} e^{j\omega(m_1-m_2)} + G_2^{(D)} G_1^{(D)} e^{j\omega(m_1+m_2)} \end{pmatrix} = \\
&\begin{pmatrix} G_2^{(A)} G_1^{(A)} e^{-j\omega(m_1+m_2)} & G_2^{(B)} G_1^{(D)} e^{j\omega(m_1+m_2)} \\ G_2^{(C)} G_1^{(A)} e^{-j\omega(m_1+m_2)} & G_2^{(D)} G_1^{(D)} e^{j\omega(m_1+m_2)} \end{pmatrix} + \begin{pmatrix} G_2^{(B)} G_1^{(C)} e^{-j\omega(m_1-m_2)} & G_2^{(A)} G_1^{(B)} e^{j\omega(m_1-m_2)} \\ G_2^{(D)} G_1^{(C)} e^{-j\omega(m_1-m_2)} & G_2^{(C)} G_1^{(B)} e^{j\omega(m_1-m_2)} \end{pmatrix} = \\
&\begin{pmatrix} \bar{G}_1^{(A)} e^{-j\omega\bar{m}_1} & \bar{G}_1^{(B)} e^{j\omega\bar{m}_1} \\ \bar{G}_1^{(C)} e^{-j\omega\bar{m}_1} & \bar{G}_1^{(D)} e^{j\omega\bar{m}_1} \end{pmatrix} + \begin{pmatrix} \bar{G}_2^{(A)} e^{-j\omega\bar{m}_2} & \bar{G}_2^{(B)} e^{j\omega\bar{m}_2} \\ \bar{G}_2^{(C)} e^{-j\omega\bar{m}_2} & \bar{G}_2^{(D)} e^{j\omega\bar{m}_2} \end{pmatrix} = \sum_{k=1}^{2^{M-1}} \begin{pmatrix} \bar{G}_k^{(A)} e^{-j\omega\bar{m}_k} & \bar{G}_k^{(B)} e^{j\omega\bar{m}_k} \\ \bar{G}_k^{(C)} e^{-j\omega\bar{m}_k} & \bar{G}_k^{(D)} e^{j\omega\bar{m}_k} \end{pmatrix}
\end{aligned} \tag{B.1}$$

where the group delays $\bar{m}_k$, with $k \in \{1, 2\}$, are obtained as a linear combination of the group delays m_{M-i}, namely $\bar{m}_1 = m_1 + m_2$ and $\bar{m}_2 = m_1 - m_2$. On the other hand, the gains labeled with an overscore result from multiplicative combinations of the original gains,

namely:

$$\begin{array}{cccc} \bar{G}_1^{(A)} = G_2^{(A)} G_1^{(A)} & , & \bar{G}_1^{(B)} = G_2^{(B)} G_1^{(D)} & , & \bar{G}_1^{(C)} = G_2^{(C)} G_1^{(A)} & , & \bar{G}_1^{(D)} = G_2^{(D)} G_1^{(D)} \\ \bar{G}_2^{(A)} = G_2^{(B)} G_1^{(C)} & , & \bar{G}_2^{(B)} = G_2^{(A)} G_1^{(B)} & , & \bar{G}_2^{(C)} = G_2^{(D)} G_1^{(C)} & , & \bar{G}_2^{(D)} = G_2^{(C)} G_1^{(B)} \end{array} \tag{B.2}$$

B.2 General form

Equation (7.20) can be proven by induction. Thus, assuming that Equation (7.20) is correct for $(M-1)$ layers (the hypothesis is correct and trivial for $M=1$), by multiplying it by another transfer matrix for a layer M, the obtained product may retain the same form with $(M-1)$ increased to M. Hence,

$$\begin{aligned} \boldsymbol{u}_{M+1}(z) &= \frac{G_{\alpha_M} z^{-m_M}}{(1+G_{r_M})} \begin{pmatrix} 1 & G_{r_M} G_{\alpha_M}^{-2} z^{2m_M} \\ G_{r_M} & G_{\alpha_M}^{-2} z^{2m_M} \end{pmatrix} \left(\prod_{i=1}^{M-1} \frac{G_{\alpha_i} z^{-m_i}}{(1+G_{r_i})} \right) \begin{pmatrix} P_{M-1}(G_\alpha, z) & \left(\prod_{i=1}^{M-1} G_{\alpha_i}^{-2} z^{2m_i} \right) Q_{M-1}(G_\alpha^{-1}, z^{-1}) \\ Q_{M-1}(G_\alpha, z) & \left(\prod_{i=1}^{M-1} G_{\alpha_i}^{-2} z^{2m_i} \right) P_{M-1}(G_\alpha^{-1}, z^{-1}) \end{pmatrix} \boldsymbol{u}_1(z) \\ &= \left(\prod_{i=1}^{M} \frac{G_{\alpha_i} z^{-m_i}}{(1+G_{r_i})} \right) \begin{pmatrix} P_{M-1}(G_\alpha, z) + G_{r_M} G_{\alpha_M}^{-2} z^{2m_M} Q_{M-1}(G_\alpha, z) & \left(\prod_{i=1}^{M} G_{\alpha_i}^{-2} z^{2m_i} \right) \left(G_{r_M} P_{M-1}(G_\alpha^{-1}, z^{-1}) + G_{\alpha_M}^2 z^{-2m_M} Q_{M-1}(G_\alpha^{-1}, z^{-1}) \right) \\ G_{r_M} P_{M-1}(G_\alpha, z) + G_{\alpha_M}^{-2} z^{2m_M} Q_{M-1}(G_\alpha, z) & \left(\prod_{i=1}^{M} G_{\alpha_i}^{-2} z^{2m_i} \right) \left(P_{M-1}(G_\alpha^{-1}, z^{-1}) + G_{r_M} G_{\alpha_M}^2 z^{-2m_M} Q_{M-1}(G_\alpha^{-1}, z^{-1}) \right) \end{pmatrix} \boldsymbol{u}_1(z) \\ &= \left(\prod_{i=1}^{M} \frac{G_{\alpha_i} z^{-m_i}}{(1+G_{r_i})} \right) \begin{pmatrix} P_M(G_\alpha, z) & \left(\prod_{i=1}^{M} G_{\alpha_i}^{-2} z^{2m_i} \right) Q_M(G_\alpha^{-1}, z^{-1}) \\ Q_M(G_\alpha, z) & \left(\prod_{i=1}^{M} G_{\alpha_i}^{-2} z^{2m_i} \right) P_M(G_\alpha^{-1}, z^{-1}) \end{pmatrix} \boldsymbol{u}_1(z) \end{aligned} \tag{B.3}$$

where it can be seen that the scaling factor is of the same form with $(M-1)$ changed to M.

B.3 Iterative application

The relationship of Equation (7.23) can be obtained by making use of the recursive scheme described by the polynomial expressions of Equation (7.21),

$$\begin{aligned} & P_M(G_\alpha, z) P_M(G_\alpha^{-1}, z^{-1}) - Q_M(G_\alpha, z) Q_M(G_\alpha^{-1}, z^{-1}) \\ = \; & \left(P_{M-1}(G_\alpha, z) P_{M-1}(G_\alpha^{-1}, z^{-1}) - Q_{M-1}(G_\alpha, z) Q_{M-1}(G_\alpha^{-1}, z^{-1}) \right) (1 - G_{r_M}^2) \\ = \; & \dots \\ = \; & \left(P_1(G_\alpha, z) P_1(G_\alpha^{-1}, z^{-1}) - Q_1(G_\alpha, z) Q_1(G_\alpha^{-1}, z^{-1}) \right) (1 - G_{r_M}^2) \dots (1 - G_{r_2}^2) \end{aligned} \tag{B.4}$$

Given the initial conditions of the recursion $P_1(G_\alpha, z) = P_1(G_\alpha^{-1}, z^{-1}) = 1$ and $Q_1(G_\alpha, z) = Q_1(G_\alpha^{-1}, z^{-1}) = G_{r_1}$ yields an iterative application,

$$P_M(G_\alpha, z) P_M(G_\alpha^{-1}, z^{-1}) - Q_M(G_\alpha, z) Q_M(G_\alpha^{-1}, z^{-1}) \;=\; \prod_{i=1}^{M} (1 - G_{r_i}^2) \tag{B.5}$$

which, in analogy to the energy conservation principle, says that for each frequency ω, the energy flowing through the i^{th} layer equals the energy flowing through the $i+1^{th}$ layer.

C

Derivation of the NTM method

This appendix presents a step-by-step derivation of the NTM formalism. First, the obtaining of the elements of the first-order discontinuity and propagation matrices is described (see Equations (8.6) and (8.10)). In a second part, the identities used in Equation (8.17) are proven.

C.1 First-order discontinuity matrix

The continuity of displacement $u^{(1)}(d_i, \Omega)$ and stress $\sigma^{(1)}(d_i, \Omega)$ across an arbitrary interface $x = d_i$ ($i = 1, \ldots, M$) for the first-order perturbation solution is carefully analyzed. For sake of notation simplicity, the argument (d_i, Ω) is omitted along the derivation. The first condition, $u_i^{(1)} = u_{i+1}^{(1)}$ leads to,

$$u_i^{(1),f} + u_i^{(1),b} \quad = \quad u_{i+1}^{(1),f} + u_{i+1}^{(1),b} \tag{C.1}$$

whereas the second condition, $\sigma_i^{(1)} = \sigma_{i+1}^{(1)}$, which can also be written down as,

$$E_i \left[\frac{\partial u_i^{(1)}}{\partial x} + \beta_i \left(\frac{\partial u_i^{(0)}}{\partial x} \right)^2 \right] \Bigg|_{x=d_i} \quad = \quad E_{i+1} \left[\frac{\partial u_{i+1}^{(1)}}{\partial x} + \beta_{i+1} \left(\frac{\partial u_{i+1}^{(0)}}{\partial x} \right)^2 \right] \Bigg|_{x=d_i} \tag{C.2}$$

yields,

$$-2j\frac{\Omega}{c_i}E_i\left(u_i^{(1),f}-u_i^{(1),b}\right)-\frac{1}{2}\beta_i\left(\frac{\Omega}{c_i}\right)^2E_i\left(\left[u_i^{(0),f}\right]^2+\left[u_i^{(0),b}\right]^2-4u_i^{(0),f}u_i^{(0),b}\right)=$$
$$-2j\frac{\Omega}{c_{i+1}}E_{i+1}\left(u_{i+1}^{(1),f}-u_{i+1}^{(1),b}\right)-\frac{1}{2}\beta_{i+1}\left(\frac{\Omega}{c_{i+1}}\right)^2E_{i+1}\left(\left[u_{i+1}^{(0),f}\right]^2+\left[u_{i+1}^{(0),b}\right]^2-4u_{i+1}^{(0),f}u_{i+1}^{(0),b}\right) \tag{C.3}$$

By combining Equation (C.1) with Equation (C.3), an expression for the forward-propagating part of the first-order wave displacement in layer $i+1$ as function of the forward- and backward-propagating parts of the first-order wave displacement in layer i can be found as,

$$\begin{aligned}u_{i+1}^{(1),f} &= \frac{1}{2}\left(1+\frac{Z_i}{Z_{i+1}}\right)u_i^{(1),f}+\frac{1}{2}\left(1-\frac{Z_i}{Z_{i+1}}\right)u_i^{(1),b}\\ &- \frac{j}{4}\beta_i\frac{\Omega}{c_i}\frac{Z_i}{Z_{i+1}}\left(\left[u_i^{(0),f}\right]^2+\left[u_i^{(0),b}\right]^2-4u_i^{(0),f}u_i^{(0),b}\right)\\ &+ \frac{j}{4}\beta_{i+1}\frac{\Omega}{c_{i+1}}\left(\left[u_{i+1}^{(0),f}\right]^2+\left[u_{i+1}^{(0),b}\right]^2-4u_{i+1}^{(0),f}u_{i+1}^{(0),b}\right)\end{aligned} \tag{C.4}$$

Nonetheless, the last term of Equation (C.4) still depends on properties of layer $i+1$. A way to get around it is the use of the linear relations provided by the continuity of displacement and stress for the zero-order solution (see Equations (A.4)-(A.5)). Hence, an expression for the square of the forward-propagating part of the zero-order wave displacement in layer $i+1$ can be found as,

$$\begin{aligned}\left[u_{i+1}^{(0),f}\right]^2 &= \underbrace{\left(\frac{1}{2}\left(1+\frac{Z_i}{Z_{i+1}}\right)\right)^2}_{\mathcal{D}_{i,11}^2}\left[u_i^{(0),f}\right]^2+\underbrace{\left(\frac{1}{2}\left(1-\frac{Z_i}{Z_{i+1}}\right)\right)^2}_{\mathcal{D}_{i,12}^2}\left[u_i^{(0),b}\right]^2\\ &+ \underbrace{\frac{1}{2}\left(1-\left(\frac{Z_i}{Z_{i+1}}\right)^2\right)}_{2\mathcal{D}_{i,11}\mathcal{D}_{i,12}}u_i^{(0),f}u_i^{(0),b}\end{aligned} \tag{C.5}$$

An expression for the square of the backward-propagating part of the zero-order wave displacement in layer $i+1$ can be found accordingly as,

$$\begin{aligned}\left[u_{i+1}^{(0),b}\right]^2 &= \underbrace{\left(\frac{1}{2}\left(1-\frac{Z_i}{Z_{i+1}}\right)\right)^2}_{\mathcal{D}_{i,12}^2}\left[u_i^{(0),f}\right]^2+\underbrace{\left(\frac{1}{2}\left(1+\frac{Z_i}{Z_{i+1}}\right)\right)^2}_{\mathcal{D}_{i,11}^2}\left[u_i^{(0),b}\right]^2\\ &+ \underbrace{\frac{1}{2}\left(1-\left(\frac{Z_i}{Z_{i+1}}\right)^2\right)}_{2\mathcal{D}_{i,11}\mathcal{D}_{i,12}}u_i^{(0),f}u_i^{(0),b}\end{aligned} \tag{C.6}$$

Following the same scheme enables us to find out an expression for the mixed-propagating part of the zero-order wave displacement in layer $i+1$ as,

$$u_{i+1}^{(0),f}u_{i+1}^{(0),b} = \underbrace{\frac{1}{4}\left(1-\left(\frac{Z_i}{Z_{i+1}}\right)^2\right)}_{\mathcal{D}_{i,11}\mathcal{D}_{i,12}}\left(\left[u_i^{(0),f}\right]^2+\left[u_i^{(0),b}\right]^2\right)+\underbrace{\frac{1}{2}\left(1+\left(\frac{Z_i}{Z_{i+1}}\right)^2\right)}_{\mathcal{D}_{i,11}^2+\mathcal{D}_{i,12}^2}u_i^{(0),f}u_i^{(0),b} \tag{C.7}$$

Hence, by inserting Equation (C.5)-(C.7) into Equation (C.4), an expression for the forward-propagating part of the first-order wave displacement in layer $i+1$ can be found as,

$$\begin{aligned} u_{i+1}^{(1),f} &= \underbrace{\frac{1}{2}\left(1+\frac{Z_i}{Z_{i+1}}\right)}_{\mathcal{D}_{i,11}}u_i^{(1),f}+\underbrace{\frac{1}{2}\left(1-\frac{Z_i}{Z_{i+1}}\right)}_{\mathcal{D}_{i,12}}u_i^{(1),b} \\ &- \underbrace{\frac{j}{4}\left(\beta_i\frac{\Omega}{c_i}\frac{Z_i}{Z_{i+1}}+\frac{1}{2}\beta_{i+1}\frac{\Omega}{c_{i+1}}\left(1-3\left(\frac{Z_i}{Z_{i+1}}\right)^2\right)\right)}_{-\mathcal{D}_{i,41}(\Omega)}\left(\left[u_i^{(0),f}\right]^2+\left[u_i^{(0),b}\right]^2\right) \\ &+ \underbrace{j\left(\beta_i\frac{\Omega}{c_i}\frac{Z_i}{Z_{i+1}}-\frac{1}{4}\beta_{i+1}\frac{\Omega}{c_{i+1}}\left(1+3\left(\frac{Z_i}{Z_{i+1}}\right)^2\right)\right)}_{\mathcal{D}_{i,43}(\Omega)}u_i^{(0),f}u_i^{(0),b} \end{aligned} \tag{C.8}$$

An expression for the backward-propagating part of the first-order wave displacement in layer $i+1$ can be found accordingly as,

$$\begin{aligned} u_{i+1}^{(1),b} &= \underbrace{\frac{1}{2}\left(1-\frac{Z_i}{Z_{i+1}}\right)}_{\mathcal{D}_{i,12}}u_i^{(1),f}+\underbrace{\frac{1}{2}\left(1+\frac{Z_i}{Z_{i+1}}\right)}_{\mathcal{D}_{i,11}}u_i^{(1),b} \\ &+ \underbrace{\frac{j}{4}\left(\beta_i\frac{\Omega}{c_i}\frac{Z_i}{Z_{i+1}}+\frac{1}{2}\beta_{i+1}\frac{\Omega}{c_{i+1}}\left(1-3\left(\frac{Z_i}{Z_{i+1}}\right)^2\right)\right)}_{-\mathcal{D}_{i,41}(\Omega)}\left(\left[u_i^{(0),f}\right]^2+\left[u_i^{(0),b}\right]^2\right) \\ &- \underbrace{j\left(\beta_i\frac{\Omega}{c_i}\frac{Z_i}{Z_{i+1}}-\frac{1}{4}\beta_{i+1}\frac{\Omega}{c_{i+1}}\left(1+3\left(\frac{Z_i}{Z_{i+1}}\right)^2\right)\right)}_{\mathcal{D}_{i,43}(\Omega)}u_i^{(0),f}u_i^{(0),b} \end{aligned} \tag{C.9}$$

From those expressions, on can easily retrieve the first-order discontinuity matrix of Equation (8.6), and the linear and nonlinear frequency-dependent elements detailed in Equations (8.7)-(8.8).

C.2 First-order propagation matrix

The derivation of the first-order propagation matrix is not as trivial as for the linear case. Indeed, in nonlinear acoustics, the nonlinear terms (e.g. second harmonics) are generated by frequency-mixing of the fundamental waves, and forward- and backward propagating

parts also can interact with each others. Thus, considering an harmonic wave propagating in the same nonlinear homogeneous layer i from position $x = d_{i-1}$ to position $x = d_i$, its transformed displacement at the respective locations can be expressed as,

$$\begin{bmatrix} \left(A_i e^{-j\frac{\Omega}{c_i}d_i}\right)^2 \\ \left(B_i e^{j\frac{\Omega}{c_i}d_i}\right)^2 \\ A_i B_i \\ \left(\bar{A}_i + \frac{1}{2}\beta_i\left(\frac{\Omega}{c_i}\right)^2 d_i A_i^2\right) e^{-2j\frac{\Omega}{c_i}d_i} \\ \left(\bar{B}_i + \frac{1}{2}\beta_i\left(\frac{\Omega}{c_i}\right)^2 d_i B_i^2\right) e^{2j\frac{\Omega}{c_i}d_i} \end{bmatrix} = \begin{pmatrix} p_i & 0 & 0 & 0 & 0 \\ 0 & p_i^{-1} & 0 & 0 & 0 \\ 0 & 0 & 1 & 0 & 0 \\ \eta_i(\Omega)p_i & 0 & 0 & p_i & 0 \\ 0 & \eta_i(\Omega)p_i^{-1} & 0 & 0 & p_i^{-1} \end{pmatrix} \begin{bmatrix} \left(A_i e^{-j\frac{\Omega}{c_i}d_{i-1}}\right)^2 \\ \left(B_i e^{j\frac{\Omega}{c_i}d_{i-1}}\right)^2 \\ A_i B_i \\ \left(\bar{A}_i + \frac{1}{2}\beta_i\left(\frac{\Omega}{c_i}\right)^2 d_{i-1} A_i^2\right) e^{-2j\frac{\Omega}{c_i}d_{i-1}} \\ \left(\bar{B}_i + \frac{1}{2}\beta_i\left(\frac{\Omega}{c_i}\right)^2 d_{i-1} B_i^2\right) e^{2j\frac{\Omega}{c_i}d_{i-1}} \end{bmatrix} \tag{C.10}$$

where $p_i = e^{-2j\frac{\Omega}{c_i}(d_i - d_{i-1})}$ and $\eta_i(\Omega) = \frac{1}{2}\beta_i\left(\frac{\Omega}{c_i}\right)^2 (d_i - d_{i-1})$. By inserting the layer's thickness $a_i = d_i - d_{i-1}$, one can recover the first-order propagation matrix presented in Equation (8.10). It can be shown that the first-order propagation matrix provided by Yun *et al.* [208], i.e.:

$$\boldsymbol{\mathcal{P}}_i^{Yun}(2\Omega) = \begin{pmatrix} p_i & 0 & 0 & 0 & 0 \\ 0 & p_i^{-1} & 0 & 0 & 0 \\ 0 & 0 & 1 & 0 & 0 \\ p_i & 0 & 0 & \eta_i(\Omega)p_i & 0 \\ 0 & p_i^{-1} & 0 & 0 & \eta_i(\Omega)p_i^{-1} \end{pmatrix}, \tag{C.11}$$

cannot deliver the correct relations between the wave displacements at locations d_i and d_{i-1}.

C.3 First-order transfer matrix

The identities used in Equation (8.17) can be proven by induction. Thus, assuming that Equation (8.17) is correct for $(M-1)$ nonlinear layers, by multiplying it by another first-order transfer matrix for a layer M, the obtained product may retain the same form with $(M-1)$ increased to M. As can be observed in Equation (8.11), this hypothesis is correct and trivial for $M=1$.

$$
\begin{aligned}
\boldsymbol{\mathcal{T}}^{(1)}(\Omega) = \boldsymbol{\mathcal{T}}^{(1)}_{M}(\Omega)\boldsymbol{\mathcal{T}}^{(1)}_{M-1}(\Omega) = &\begin{pmatrix}
\mathcal{D}^2_{M,11}e^{-2j\frac{\Omega}{c_M}a_M} & \mathcal{D}^2_{M,12}e^{2j\frac{\Omega}{c_M}a_M} & 2\mathcal{D}_{M,11}\mathcal{D}_{M,12} & 0 & 0 \\
\mathcal{D}^2_{M,12}e^{-2j\frac{\Omega}{c_M}a_M} & \mathcal{D}^2_{M,11}e^{2j\frac{\Omega}{c_M}a_M} & 2\mathcal{D}_{M,11}\mathcal{D}_{M,12} & 0 & 0 \\
\mathcal{D}_{M,11}\mathcal{D}_{M,12}e^{-2j\frac{\Omega}{c_M}a_M} & \mathcal{D}_{M,11}\mathcal{D}_{M,12}e^{2j\frac{\Omega}{c_M}a_M} & \mathcal{D}^2_{M,11}+\mathcal{D}^2_{M,12} & 0 & 0 \\
(\mathcal{D}_{M,41}(\Omega)+\eta_M(\Omega)\mathcal{D}_{M,11})\,e^{-2j\frac{\Omega}{c_M}a_M} & (\mathcal{D}_{M,41}(\Omega)+\eta_M(\Omega)\mathcal{D}_{M,12})\,e^{2j\frac{\Omega}{c_M}a_M} & -\mathcal{D}_{M,43}(\Omega) & \mathcal{D}_{M,11}e^{-2j\frac{\Omega}{c_M}a_M} & \mathcal{D}_{M,12}e^{2j\frac{\Omega}{c_M}a_M} \\
(-\mathcal{D}_{M,41}(\Omega)+\eta_M(\Omega)\mathcal{D}_{M,12})\,e^{-2j\frac{\Omega}{c_M}a_M} & (-\mathcal{D}_{M,41}(\Omega)+\eta_M(\Omega)\mathcal{D}_{M,11})\,e^{2j\frac{\Omega}{c_M}a_M} & \mathcal{D}_{M,43}(\Omega) & \mathcal{D}_{M,12}e^{-2j\frac{\Omega}{c_M}a_M} & \mathcal{D}_{M,11}e^{2j\frac{\Omega}{c_M}a_M}
\end{pmatrix}\cdot \\
&\begin{pmatrix}
\mathcal{T}^{(1)}_{M-1,11}(\Omega) & \mathcal{T}^{(1)}_{M-1,12}(\Omega) & 2\sqrt{\mathcal{T}^{(1)}_{M-1,11}(\Omega)\mathcal{T}^{(1)}_{M-1,12}(\Omega)} & 0 & 0 \\
\mathcal{T}^{(1)}_{M-1,12}(-\Omega) & \mathcal{T}^{(1)}_{M-1,11}(-\Omega) & 2\sqrt{\mathcal{T}^{(1)}_{M-1,11}(-\Omega)\mathcal{T}^{(1)}_{M-1,12}(-\Omega)} & 0 & 0 \\
\sqrt{\mathcal{T}^{(1)}_{M-1,11}(\Omega)\mathcal{T}^{(1)}_{M-1,12}(-\Omega)} & \sqrt{\mathcal{T}^{(1)}_{M,11}(-\Omega)\mathcal{T}^{(1)}_{M-1,12}(\Omega)} & \sqrt{\mathcal{T}^{(1)}_{M-1,11}(\Omega)\mathcal{T}^{(1)}_{M-1,11}(-\Omega)}+\sqrt{\mathcal{T}^{(1)}_{M-1,12}(\Omega)\mathcal{T}^{(1)}_{M-1,12}(-\Omega)} & 0 & 0 \\
\mathcal{T}^{(1)}_{M-1,41}(\Omega) & \mathcal{T}^{(1)}_{M-1,42}(\Omega) & \mathcal{T}^{(1)}_{M-1,43}(\Omega) & \sqrt{\mathcal{T}^{(1)}_{M-1,11}(2\Omega)} & \sqrt{\mathcal{T}^{(1)}_{M-1,12}(2\Omega)} \\
\mathcal{T}^{(1)}_{M-1,42}(-\Omega) & \mathcal{T}^{(1)}_{M-1,41}(-\Omega) & \mathcal{T}^{(1)}_{M-1,43}(-\Omega) & \sqrt{\mathcal{T}^{(1)}_{M-1,12}(-2\Omega)} & \sqrt{\mathcal{T}^{(1)}_{M-1,11}(-2\Omega)}
\end{pmatrix} = \\
&\begin{pmatrix}
\mathcal{T}^{(1)}_{11}(\Omega) & \mathcal{T}^{(1)}_{12}(\Omega) & 2\sqrt{\mathcal{T}^{(1)}_{11}(\Omega)\mathcal{T}^{(1)}_{12}(\Omega)} & 0 & 0 \\
\mathcal{T}^{(1)}_{12}(-\Omega) & \mathcal{T}^{(1)}_{11}(-\Omega) & 2\sqrt{\mathcal{T}^{(1)}_{11}(-\Omega)\mathcal{T}^{(1)}_{12}(-\Omega)} & 0 & 0 \\
\sqrt{\mathcal{T}^{(1)}_{11}(\Omega)\mathcal{T}^{(1)}_{12}(-\Omega)} & \sqrt{\mathcal{T}^{(1)}_{M,11}(-\Omega)\mathcal{T}^{(1)}_{12}(\Omega)} & \sqrt{\mathcal{T}^{(1)}_{11}(\Omega)\mathcal{T}^{(1)}_{11}(-\Omega)}+\sqrt{\mathcal{T}^{(1)}_{12}(\Omega)\mathcal{T}^{(1)}_{12}(-\Omega)} & 0 & 0 \\
\mathcal{T}^{(1)}_{41}(\Omega) & \mathcal{T}^{(1)}_{42}(\Omega) & \mathcal{T}^{(1)}_{43}(\Omega) & \sqrt{\mathcal{T}^{(1)}_{11}(2\Omega)} & \sqrt{\mathcal{T}^{(1)}_{12}(2\Omega)} \\
\mathcal{T}^{(1)}_{42}(-\Omega) & \mathcal{T}^{(1)}_{41}(-\Omega) & \mathcal{T}^{(1)}_{43}(-\Omega) & \sqrt{\mathcal{T}^{(1)}_{12}(-2\Omega)} & \sqrt{\mathcal{T}^{(1)}_{11}(-2\Omega)}
\end{pmatrix}
\end{aligned}
\tag{C.12}
$$

We will show hereafter that the 19 non-zero elements of the matrix described in Equation (8.16) can be related to the 5 independent elements that arise in the resulting matrix of Equation (C.12). The elements of the first row of that matrix can be written down as,

$$
\begin{aligned}
\mathcal{T}^{(1)}_{11}(\Omega) &= \mathcal{D}^2_{M,11}e^{-2j\frac{\Omega}{c_M}a_M}\mathcal{T}^{(1)}_{M-1,11}(\Omega) + \mathcal{D}^2_{M,12}e^{2j\frac{\Omega}{c_M}a_M}\mathcal{T}^{(1)}_{M-1,12}(-\Omega) \\
&+ 2\mathcal{D}_{M,11}\mathcal{D}_{M,12}\sqrt{\mathcal{T}^{(1)}_{M-1,11}(\Omega)\mathcal{T}^{(1)}_{M-1,12}(-\Omega)} \\
&= \left(\mathcal{D}_{M,11}e^{-j\frac{\Omega}{c_M}a_M}\sqrt{\mathcal{T}^{(1)}_{M-1,11}(\Omega)} + \mathcal{D}_{M,12}e^{j\frac{\Omega}{c_M}a_M}\sqrt{\mathcal{T}^{(1)}_{M-1,12}(-\Omega)}\right)^2,
\end{aligned}
\tag{C.13}
$$

$$
\begin{aligned}
\mathcal{T}^{(1)}_{12}(\Omega) &= \mathcal{D}^2_{M,11}e^{-2j\frac{\Omega}{c_M}a_M}\mathcal{T}^{(1)}_{M-1,12}(\Omega) + \mathcal{D}^2_{M,12}e^{2j\frac{\Omega}{c_M}a_M}\mathcal{T}^{(1)}_{M-1,11}(-\Omega) \\
&+ 2\mathcal{D}_{M,11}\mathcal{D}_{M,12}\sqrt{\mathcal{T}^{(1)}_{M-1,11}(-\Omega)\mathcal{T}^{(1)}_{M-1,12}(\Omega)} \\
&= \left(\mathcal{D}_{M,11}e^{-j\frac{\Omega}{c_M}a_M}\sqrt{\mathcal{T}^{(1)}_{M-1,12}(\Omega)} + \mathcal{D}_{M,12}e^{j\frac{\Omega}{c_M}a_M}\sqrt{\mathcal{T}^{(1)}_{M-1,11}(-\Omega)}\right)^2,
\end{aligned}
\tag{C.14}
$$

and

$$\begin{aligned}
\mathcal{T}_{13}^{(1)}(\Omega) &= 2\mathcal{D}_{M,11}^{2} e^{-2j\frac{\Omega}{c_M}a_(M)} \sqrt{\mathcal{T}_{M-1,11}^{(1)}(\Omega)\mathcal{T}_{M-1,12}^{(1)}(\Omega)} \\
&+ 2\mathcal{D}_{M,12}^{2} e^{2j\frac{\Omega}{c_M}a_(M)} \sqrt{\mathcal{T}_{M-1,11}^{(1)}(-\Omega)\mathcal{T}_{M-1,12}^{(1)}(-\Omega)} \\
&+ 2\mathcal{D}_{M,11}\mathcal{D}_{M,12}\left(\sqrt{\mathcal{T}_{M-1,11}^{(1)}(\Omega)\mathcal{T}_{M-1,11}^{(1)}(-\Omega)} + \sqrt{\mathcal{T}_{M-1,12}^{(1)}(\Omega)\mathcal{T}_{M-1,12}^{(1)}(-\Omega)}\right) \\
&= 2\left(\mathcal{D}_{M,11}e^{-j\frac{\Omega}{c_M}a_M}\sqrt{\mathcal{T}_{M-1,11}^{(1)}(\Omega)} + \mathcal{D}_{M,12}e^{j\frac{\Omega}{c_M}a_M}\sqrt{\mathcal{T}_{M-1,12}^{(1)}(-\Omega)}\right) \\
&\cdot \quad \left(\mathcal{D}_{M,11}e^{-j\frac{\Omega}{c_M}a_M}\sqrt{\mathcal{T}_{M-1,12}^{(1)}(\Omega)} + \mathcal{D}_{M,12}e^{j\frac{\Omega}{c_M}a_M}\sqrt{\mathcal{T}_{M-1,11}^{(1)}(-\Omega)}\right) \\
&= 2\sqrt{\mathcal{T}_{11}^{(1)}(\Omega)\mathcal{T}_{12}^{(1)}(\Omega)}.
\end{aligned} \tag{C.15}$$

As can be observed, the $\mathcal{T}_{13}^{(1)}(\Omega)$-element of the first-order transfer matrix can be expressed by means of the elements $\mathcal{T}_{11}^{(1)}(\Omega)$ and $\mathcal{T}_{12}^{(1)}(\Omega)$. Following this reasoning for the second and third rows enables us to find other elements of that matrix, which also dependent upon those two elements. Hence,

$$\begin{aligned}
\mathcal{T}_{21}^{(1)}(\Omega) &= \mathcal{D}_{M,12}^{2} e^{-2j\frac{\Omega}{c_M}a_M}\mathcal{T}_{M-1,11}^{(1)}(\Omega) + \mathcal{D}_{M,11}^{2} e^{2j\frac{\Omega}{c_M}a_M}\mathcal{T}_{M-1,12}^{(1)}(-\Omega) \\
&+ 2\mathcal{D}_{M,11}\mathcal{D}_{M,12}\sqrt{\mathcal{T}_{M-1,11}^{(1)}(\Omega)\mathcal{T}_{M-1,12}^{(1)}(-\Omega)} \\
&= \left(\mathcal{D}_{M,12}e^{-j\frac{\Omega}{c_M}a_M}\sqrt{\mathcal{T}_{M-1,11}^{(1)}(\Omega)} + \mathcal{D}_{M,11}e^{j\frac{\Omega}{c_M}a_M}\sqrt{\mathcal{T}_{M-1,12}^{(1)}(-\Omega)}\right)^2 \\
&= \mathcal{T}_{12}^{(1)}(-\Omega),
\end{aligned} \tag{C.16}$$

$$\begin{aligned}
\mathcal{T}_{22}^{(1)}(\Omega) &= \mathcal{D}_{M,12}^{2} e^{-2j\frac{\Omega}{c_M}a_M}\mathcal{T}_{M-1,12}^{(1)}(\Omega) + \mathcal{D}_{M,11}^{2} e^{2j\frac{\Omega}{c_M}a_M}\mathcal{T}_{M-1,11}^{(1)}(-\Omega) \\
&+ 2\mathcal{D}_{M,11}\mathcal{D}_{M,12}\sqrt{\mathcal{T}_{M-1,11}^{(1)}(-\Omega)\mathcal{T}_{M-1,12}^{(1)}(\Omega)} \\
&= \left(\mathcal{D}_{M,12}e^{-j\frac{\Omega}{c_M}a_M}\sqrt{\mathcal{T}_{M-1,12}^{(1)}(\Omega)} + \mathcal{D}_{M,11}e^{j\frac{\Omega}{c_M}a_M}\sqrt{\mathcal{T}_{M-1,11}^{(1)}(-\Omega)}\right)^2 \\
&= \mathcal{T}_{11}^{(1)}(-\Omega),
\end{aligned} \tag{C.17}$$

$$
\begin{aligned}
\mathcal{T}_{23}^{(1)}(\Omega) &= 2\mathcal{D}_{M,12}^2 e^{-2j\frac{\Omega}{c_M}a_(M)}\sqrt{\mathcal{T}_{M-1,11}^{(1)}(\Omega)\mathcal{T}_{M-1,12}^{(1)}(\Omega)} \\
&+ 2\mathcal{D}_{M,11}^2 e^{2j\frac{\Omega}{c_M}a_(M)}\sqrt{\mathcal{T}_{M-1,11}^{(1)}(-\Omega)\mathcal{T}_{M-1,12}^{(1)}(-\Omega)} \\
&+ 2\mathcal{D}_{M,11}\mathcal{D}_{M,12}\left(\sqrt{\mathcal{T}_{M-1,11}^{(1)}(\Omega)\mathcal{T}_{M-1,11}^{(1)}(-\Omega)}+\sqrt{\mathcal{T}_{M-1,12}^{(1)}(\Omega)\mathcal{T}_{M-1,12}^{(1)}(-\Omega)}\right) \\
&= 2\left(\mathcal{D}_{M,12}e^{-j\frac{\Omega}{c_M}a_M}\sqrt{\mathcal{T}_{M-1,11}^{(1)}(\Omega)}+\mathcal{D}_{M,11}e^{j\frac{\Omega}{c_M}a_M}\sqrt{\mathcal{T}_{M-1,12}^{(1)}(-\Omega)}\right) \\
&\cdot \quad \left(\mathcal{D}_{M,12}e^{-j\frac{\Omega}{c_M}a_M}\sqrt{\mathcal{T}_{M-1,12}^{(1)}(\Omega)}+\mathcal{D}_{M,11}e^{j\frac{\Omega}{c_M}a_M}\sqrt{\mathcal{T}_{M-1,11}^{(1)}(-\Omega)}\right) \\
&= 2\sqrt{\mathcal{T}_{11}^{(1)}(-\Omega)\mathcal{T}_{12}^{(1)}(-\Omega)},
\end{aligned}
\tag{C.18}
$$

$$
\begin{aligned}
\mathcal{T}_{31}^{(1)}(\Omega) &= \mathcal{D}_{M,11}\mathcal{D}_{M,12}e^{-2j\frac{\Omega}{c_M}a_M}\mathcal{T}_{M-1,11}^{(1)}(\Omega)+\mathcal{D}_{M,11}\mathcal{D}_{M,12}e^{2j\frac{\Omega}{c_M}a_M}\mathcal{T}_{M-1,12}^{(1)}(-\Omega) \\
&+ \left(\mathcal{D}_{M,11}^2+\mathcal{D}_{M,12}^2\right)\sqrt{\mathcal{T}_{M-1,11}^{(1)}(\Omega)\mathcal{T}_{M-1,12}^{(1)}(-\Omega)} \\
&= \left(\mathcal{D}_{M,11}e^{-j\frac{\Omega}{c_M}a_M}\sqrt{\mathcal{T}_{M-1,11}^{(1)}(\Omega)}+\mathcal{D}_{M,12}e^{j\frac{\Omega}{c_M}a_M}\sqrt{\mathcal{T}_{M-1,12}^{(1)}(-\Omega)}\right) \\
&\cdot \quad \left(\mathcal{D}_{M,12}e^{-j\frac{\Omega}{c_M}a_M}\sqrt{\mathcal{T}_{M-1,11}^{(1)}(\Omega)}+\mathcal{D}_{M,11}e^{j\frac{\Omega}{c_M}a_M}\sqrt{\mathcal{T}_{M-1,12}^{(1)}(-\Omega)}\right) \\
&= \sqrt{\mathcal{T}_{11}^{(1)}(\Omega)\mathcal{T}_{12}^{(1)}(-\Omega)},
\end{aligned}
\tag{C.19}
$$

$$
\begin{aligned}
\mathcal{T}_{32}^{(1)}(\Omega) &= \mathcal{D}_{M,11}\mathcal{D}_{M,12}e^{-2j\frac{\Omega}{c_M}a_M}\mathcal{T}_{M-1,12}^{(1)}(\Omega)+\mathcal{D}_{M,11}\mathcal{D}_{M,12}e^{2j\frac{\Omega}{c_M}a_M}\mathcal{T}_{M-1,11}^{(1)}(-\Omega) \\
&+ \left(\mathcal{D}_{M,11}^2+\mathcal{D}_{M,12}^2\right)\sqrt{\mathcal{T}_{M-1,11}^{(1)}(-\Omega)\mathcal{T}_{M-1,12}^{(1)}(\Omega)} \\
&= \left(\mathcal{D}_{M,12}e^{-j\frac{\Omega}{c_M}a_M}\sqrt{\mathcal{T}_{M-1,12}^{(1)}(\Omega)}+\mathcal{D}_{M,11}e^{j\frac{\Omega}{c_M}a_M}\sqrt{\mathcal{T}_{M-1,11}^{(1)}(-\Omega)}\right) \\
&\cdot \quad \left(\mathcal{D}_{M,11}e^{-j\frac{\Omega}{c_M}a_M}\sqrt{\mathcal{T}_{M-1,12}^{(1)}(\Omega)}+\mathcal{D}_{M,12}e^{j\frac{\Omega}{c_M}a_M}\sqrt{\mathcal{T}_{M-1,11}^{(1)}(-\Omega)}\right) \\
&= \sqrt{\mathcal{T}_{11}^{(1)}(-\Omega)\mathcal{T}_{12}^{(1)}(\Omega)},
\end{aligned}
\tag{C.20}
$$

and

$$\begin{aligned}
\mathcal{T}_{33}^{(1)}(\Omega) &= 2\mathcal{D}_{M,11}\mathcal{D}_{M,12}e^{-2j\frac{\Omega}{c_M}a_M}\sqrt{\mathcal{T}_{M-1,11}^{(1)}(\Omega)\mathcal{T}_{M-1,12}^{(1)}(\Omega)} \\
&+ 2\mathcal{D}_{M,11}\mathcal{D}_{M,12}e^{2j\frac{\Omega}{c_M}a_M}\sqrt{\mathcal{T}_{M-1,11}^{(1)}(-\Omega)\mathcal{T}_{M-1,12}^{(1)}(-\Omega)} \\
&+ \left(\mathcal{D}_{M,11}^2+\mathcal{D}_{M,12}^2\right)\left(\sqrt{\mathcal{T}_{M-1,11}^{(1)}(\Omega)\mathcal{T}_{M-1,11}^{(1)}(-\Omega)}+\sqrt{\mathcal{T}_{M-1,12}^{(1)}(\Omega)\mathcal{T}_{M-1,12}^{(1)}(-\Omega)}\right) \\
&= \left(\mathcal{D}_{M,11}e^{-j\frac{\Omega}{c_M}a_M}\sqrt{\mathcal{T}_{M-1,11}^{(1)}(\Omega)}+\mathcal{D}_{M,12}e^{j\frac{\Omega}{c_M}a_M}\sqrt{\mathcal{T}_{M-1,12}^{(1)}(-\Omega)}\right) \\
&\cdot \left(\mathcal{D}_{M,12}e^{-j\frac{\Omega}{c_M}a_M}\sqrt{\mathcal{T}_{M-1,12}^{(1)}(\Omega)}+\mathcal{D}_{M,11}e^{j\frac{\Omega}{c_M}a_M}\sqrt{\mathcal{T}_{M-1,11}^{(1)}(-\Omega)}\right) \\
&+ \left(\mathcal{D}_{M,11}e^{-j\frac{\Omega}{c_M}a_M}\sqrt{\mathcal{T}_{M-1,12}^{(1)}(\Omega)}+\mathcal{D}_{M,12}e^{j\frac{\Omega}{c_M}a_M}\sqrt{\mathcal{T}_{M-1,11}^{(1)}(-\Omega)}\right) \\
&\cdot \left(\mathcal{D}_{M,12}e^{-j\frac{\Omega}{c_M}a_M}\sqrt{\mathcal{T}_{M-1,11}^{(1)}(\Omega)}+\mathcal{D}_{M,11}e^{j\frac{\Omega}{c_M}a_M}\sqrt{\mathcal{T}_{M-1,12}^{(1)}(-\Omega)}\right) \\
&= \sqrt{\mathcal{T}_{11}^{(1)}(\Omega)\mathcal{T}_{11}^{(1)}(-\Omega)}+\sqrt{\mathcal{T}_{12}^{(1)}(\Omega)\mathcal{T}_{12}^{(1)}(-\Omega)}.
\end{aligned} \tag{C.21}$$

This reasoning can be further applied to the lower-right elements of the fourth and fifth rows, leading to:

$$\begin{aligned}
\mathcal{T}_{44}^{(1)}(\Omega) &= \mathcal{D}_{M,11}e^{-2j\frac{\Omega}{c_M}a_M}\sqrt{\mathcal{T}_{M-1,11}^{(1)}(2\Omega)}+\mathcal{D}_{M,12}e^{2j\frac{\Omega}{c_M}a_M}\sqrt{\mathcal{T}_{M-1,12}^{(1)}(-2\Omega)} \\
&= \sqrt{\mathcal{T}_{11}^{(1)}(2\Omega)},
\end{aligned} \tag{C.22}$$

$$\begin{aligned}
\mathcal{T}_{45}^{(1)}(\Omega) &= \mathcal{D}_{M,11}e^{-2j\frac{\Omega}{c_M}a_M}\sqrt{\mathcal{T}_{M-1,12}^{(1)}(2\Omega)}+\mathcal{D}_{M,12}e^{2j\frac{\Omega}{c_M}a_M}\sqrt{\mathcal{T}_{M-1,11}^{(1)}(-2\Omega)} \\
&= \sqrt{\mathcal{T}_{12}^{(1)}(2\Omega)},
\end{aligned} \tag{C.23}$$

$$\begin{aligned}
\mathcal{T}_{54}^{(1)}(\Omega) &= \mathcal{D}_{M,12}e^{-2j\frac{\Omega}{c_M}a_M}\sqrt{\mathcal{T}_{M-1,11}^{(1)}(2\Omega)}+\mathcal{D}_{M,11}e^{2j\frac{\Omega}{c_M}a_M}\sqrt{\mathcal{T}_{M-1,12}^{(1)}(-2\Omega)} \\
&= \sqrt{\mathcal{T}_{12}^{(1)}(-2\Omega)},
\end{aligned} \tag{C.24}$$

and

$$\begin{aligned}
\mathcal{T}_{55}^{(1)}(\Omega) &= \mathcal{D}_{M,12}e^{-2j\frac{\Omega}{c_M}a_M}\sqrt{\mathcal{T}_{M-1,12}^{(1)}(2\Omega)}+\mathcal{D}_{M,11}e^{2j\frac{\Omega}{c_M}a_M}\sqrt{\mathcal{T}_{M-1,11}^{(1)}(-2\Omega)} \\
&= \sqrt{\mathcal{T}_{11}^{(1)}(-2\Omega)},
\end{aligned} \tag{C.25}$$

Finally, the remaining six elements of the fourth and fifth rows which explicitly contain the nonlinear terms can obviously not be directly related to those two elements, and they thus keep their original denomination. Nevertheless, some relations can be established between

them. To this end, let us consider the three first elements of the fourth row. Hence,

$$\begin{aligned}\mathcal{T}_{41}^{(1)}(\Omega) &= (\mathcal{D}_{M,41}(\Omega)+\eta_M(\Omega)\mathcal{D}_{M,11})\,e^{-2j\frac{\Omega}{c_M}a_M}\mathcal{T}_{M-1,11}^{(1)}(\Omega)\\ &+ (\mathcal{D}_{M,41}(\Omega)+\eta_M(\Omega)\mathcal{D}_{M,12})\,e^{2j\frac{\Omega}{c_M}a_M}\mathcal{T}_{M-1,12}^{(1)}(-\Omega)\\ &+ \mathcal{D}_{M,11}e^{-2j\frac{\Omega}{c_M}a_M}\mathcal{T}_{M-1,41}^{(1)}(\Omega)+\mathcal{D}_{M,12}e^{2j\frac{\Omega}{c_M}a_M}\mathcal{T}_{M-1,42}^{(1)}(-\Omega)\\ &- \mathcal{D}_{M,43}(\Omega)\sqrt{\mathcal{T}_{M-1,11}^{(1)}(\Omega)\mathcal{T}_{M-1,12}^{(1)}(-\Omega)},\end{aligned} \tag{C.26}$$

$$\begin{aligned}\mathcal{T}_{42}^{(1)}(\Omega) &= (\mathcal{D}_{M,41}(\Omega)+\eta_M(\Omega)\mathcal{D}_{M,11})\,e^{-2j\frac{\Omega}{c_M}a_M}\mathcal{T}_{M-1,12}^{(1)}(\Omega)\\ &+ (\mathcal{D}_{M,41}(\Omega)+\eta_M(\Omega)\mathcal{D}_{M,12})\,e^{2j\frac{\Omega}{c_M}a_M}\mathcal{T}_{M-1,11}^{(1)}(-\Omega)\\ &+ \mathcal{D}_{M,11}e^{-2j\frac{\Omega}{c_M}a_M}\mathcal{T}_{M-1,42}^{(1)}(\Omega)+\mathcal{D}_{M,12}e^{2j\frac{\Omega}{c_M}a_M}\mathcal{T}_{M-1,41}^{(1)}(-\Omega)\\ &- \mathcal{D}_{M,43}(\Omega)\sqrt{\mathcal{T}_{M-1,11}^{(1)}(-\Omega)\mathcal{T}_{M-1,12}^{(1)}(\Omega)},\end{aligned} \tag{C.27}$$

and

$$\begin{aligned}\mathcal{T}_{43}^{(1)}(\Omega) &= 2\,(\mathcal{D}_{M,41}(\Omega)+\eta_M(\Omega)\mathcal{D}_{M,11})\,e^{-2j\frac{\Omega}{c_M}a_M}\sqrt{\mathcal{T}_{M-1,11}^{(1)}(\Omega)\mathcal{T}_{M-1,12}^{(1)}(\Omega)}\\ &+ 2\,(\mathcal{D}_{M,41}(\Omega)+\eta_M(\Omega)\mathcal{D}_{M,12})\,e^{2j\frac{\Omega}{c_M}a_M}\sqrt{\mathcal{T}_{M-1,11}^{(1)}(-\Omega)\mathcal{T}_{M-1,12}^{(1)}(-\Omega)}\\ &+ \mathcal{D}_{M,11}e^{-2j\frac{\Omega}{c_M}a_M}\mathcal{T}_{M-1,43}^{(1)}(\Omega)+\mathcal{D}_{M,12}e^{2j\frac{\Omega}{c_M}a_M}\mathcal{T}_{M-1,43}^{(1)}(-\Omega)\\ &- \mathcal{D}_{M,43}(\Omega)\left(\sqrt{\mathcal{T}_{M-1,11}^{(1)}(\Omega)\mathcal{T}_{M-1,11}^{(1)}(-\Omega)}+\sqrt{\mathcal{T}_{M-1,12}^{(1)}(\Omega)\mathcal{T}_{M-1,12}^{(1)}(-\Omega)}\right).\end{aligned} \tag{C.28}$$

By making use of the identities $-\mathcal{D}_{i,41}(\Omega) = \mathcal{D}_{i,41}(-\Omega)$, $-\mathcal{D}_{i,43}(\Omega) = \mathcal{D}_{i,43}(-\Omega)$, and $\eta_i(\Omega) = \eta_i(-\Omega)$, $\forall i$, the three first elements of the fifth row can be written down as follows,

$$\begin{aligned}\mathcal{T}_{51}^{(1)}(\Omega) &= (-\mathcal{D}_{M,41}(\Omega)+\eta_M(\Omega)\mathcal{D}_{M,12})\,e^{-2j\frac{\Omega}{c_M}a_M}\mathcal{T}_{M-1,11}^{(1)}(\Omega)\\ &+ (-\mathcal{D}_{M,41}(\Omega)+\eta_M(\Omega)\mathcal{D}_{M,11})\,e^{2j\frac{\Omega}{c_M}a_M}\mathcal{T}_{M-1,12}^{(1)}(-\Omega)\\ &+ \mathcal{D}_{M,12}e^{-2j\frac{\Omega}{c_M}a_M}\mathcal{T}_{M-1,41}^{(1)}(\Omega)+\mathcal{D}_{M,11}e^{2j\frac{\Omega}{c_M}a_M}\mathcal{T}_{M-1,42}^{(1)}(-\Omega)\\ &+ \mathcal{D}_{M,43}(\Omega)\sqrt{\mathcal{T}_{M-1,11}^{(1)}(\Omega)\mathcal{T}_{M-1,12}^{(1)}(-\Omega)}\\ &= \mathcal{T}_{42}^{(1)}(-\Omega),\end{aligned} \tag{C.29}$$

$$\begin{aligned}\mathcal{T}_{52}^{(1)}(\Omega) &= (-\mathcal{D}_{M,41}(\Omega)+\eta_M(\Omega)\mathcal{D}_{M,12})\,e^{-2j\frac{\Omega}{c_M}a_M}\mathcal{T}_{M-1,12}^{(1)}(\Omega)\\ &+ (-\mathcal{D}_{M,41}(\Omega)+\eta_M(\Omega)\mathcal{D}_{M,11})\,e^{2j\frac{\Omega}{c_M}a_M}\mathcal{T}_{M-1,11}^{(1)}(-\Omega)\\ &+ \mathcal{D}_{M,12}e^{-2j\frac{\Omega}{c_M}a_M}\mathcal{T}_{M-1,42}^{(1)}(\Omega)+\mathcal{D}_{M,11}e^{2j\frac{\Omega}{c_M}a_M}\mathcal{T}_{M-1,41}^{(1)}(-\Omega)\\ &+ \mathcal{D}_{M,43}(\Omega)\sqrt{\mathcal{T}_{M-1,11}^{(1)}(-\Omega)\mathcal{T}_{M-1,12}^{(1)}(\Omega)}\\ &= \mathcal{T}_{41}^{(1)}(-\Omega),\end{aligned} \tag{C.30}$$

and

$$\begin{aligned}
\mathcal{T}_{53}^{(1)}(\Omega) &= 2\left(-\mathcal{D}_{M,41}(\Omega)+\eta_M(\Omega)\mathcal{D}_{M,12}\right)e^{-2j\frac{\Omega}{c_M}a_M}\sqrt{\mathcal{T}_{M-1,11}^{(1)}(\Omega)\mathcal{T}_{M-1,12}^{(1)}(\Omega)} \\
&+ 2\left(-\mathcal{D}_{M,41}(\Omega)+\eta_M(\Omega)\mathcal{D}_{M,11}\right)e^{2j\frac{\Omega}{c_M}a_M}\sqrt{\mathcal{T}_{M-1,11}^{(1)}(-\Omega)\mathcal{T}_{M-1,12}^{(1)}(-\Omega)} \\
&+ \mathcal{D}_{M,12}e^{-2j\frac{\Omega}{c_M}a_M}\mathcal{T}_{M-1,43}^{(1)}(\Omega)+\mathcal{D}_{M,11}e^{2j\frac{\Omega}{c_M}a_M}\mathcal{T}_{M-1,43}^{(1)}(-\Omega) \\
&+ \mathcal{D}_{M,43}(\Omega)\left(\sqrt{\mathcal{T}_{M-1,11}^{(1)}(\Omega)\mathcal{T}_{M-1,11}^{(1)}(-\Omega)}+\sqrt{\mathcal{T}_{M-1,12}^{(1)}(\Omega)\mathcal{T}_{M-1,12}^{(1)}(-\Omega)}\right). \\
&= \mathcal{T}_{43}^{(1)}(-\Omega).
\end{aligned} \tag{C.31}$$

From those expressions, we recover all the identities used in Equation (8.17), and show that the 19 non-zero elements of the first-order transfer matrix $\boldsymbol{\mathcal{T}}^{(1)}(\Omega)$ can be expressed using only five elements, namely $\mathcal{T}_{11}^{(1)}(\Omega)$, $\mathcal{T}_{12}^{(1)}(\Omega)$, $\mathcal{T}_{41}^{(1)}(\Omega)$, $\mathcal{T}_{42}^{(1)}(\Omega)$, and $\mathcal{T}_{43}^{(1)}(\Omega)$.

C.4 Relation between the zero and first-order transfer matrices

Let us here show that the system that span the upper left 3×3 sub-matrix of $\mathcal{T}^{(1)}(\Omega)$ in Equation (8.17) corresponds to a quadratic form of the linear transfer matrix. To this end, let us first assume that the linear transfer matrix is correct for $(M-1)$ layers, and thus by multiplying it by another transfer matrix for a layer M, the obtained product may retain the same form with $(M-1)$ increased to M. Then, we will compare the obtained elements to those derived in Appendix C.3.

$$\begin{aligned}
\boldsymbol{\mathcal{T}}^{(0)}(\Omega)=\boldsymbol{\mathcal{T}}_{M}^{(0)}(\Omega)\boldsymbol{\mathcal{T}}_{M-1}^{(0)}(\Omega) &= \begin{pmatrix} \mathcal{D}_{M,11}e^{-j\frac{\Omega}{c_i}a_i} & \mathcal{D}_{M,12}e^{j\frac{\Omega}{c_i}a_i} \\ \mathcal{D}_{M,12}e^{-j\frac{\Omega}{c_i}a_i} & \mathcal{D}_{M,11}e^{j\frac{\Omega}{c_i}a_i} \end{pmatrix}\cdot\begin{pmatrix} \mathcal{T}_{M-1,11}^{(0)}(\Omega) & \mathcal{T}_{M-1,12}^{(0)}(\Omega) \\ \mathcal{T}_{M-1,12}^{(0)}(-\Omega) & \mathcal{T}_{M-1,11}^{(0)}(-\Omega) \end{pmatrix} \\
&= \begin{pmatrix} \mathcal{T}_{11}^{(0)}(\Omega) & \mathcal{T}_{12}^{(0)}(\Omega) \\ \mathcal{T}_{12}^{(0)}(-\Omega) & \mathcal{T}_{11}^{(0)}(-\Omega) \end{pmatrix}
\end{aligned} \tag{C.32}$$

The resulting elements can be written down as,

$$\begin{aligned}
\mathcal{T}_{11}^{(0)}(\Omega) &= \mathcal{D}_{M,11}e^{-j\frac{\Omega}{c_M}a_M}\mathcal{T}_{M-1,11}^{(0)}(\Omega)+\mathcal{D}_{M,12}e^{j\frac{\Omega}{c_M}a_M}\mathcal{T}_{M-1,12}^{(0)}(-\Omega) \\
&= \mathcal{D}_{M,11}e^{-j\frac{\Omega}{c_M}a_M}\sqrt{\mathcal{T}_{M-1,11}^{(1)}(\Omega)}+\mathcal{D}_{M,12}e^{j\frac{\Omega}{c_M}a_M}\sqrt{\mathcal{T}_{M-1,12}^{(1)}(-\Omega)} \\
&= \sqrt{\mathcal{T}_{11}^{(1)}(\Omega)},
\end{aligned} \tag{C.33}$$

$$\begin{aligned}
\mathcal{T}_{12}^{(0)}(\Omega) &= \mathcal{D}_{M,11}e^{-j\frac{\Omega}{c_M}a_M}\mathcal{T}_{M-1,12}^{(0)}(\Omega)+\mathcal{D}_{M,12}e^{j\frac{\Omega}{c_M}a_M}\mathcal{T}_{M-1,11}^{(0)}(-\Omega) \\
&= \mathcal{D}_{M,11}e^{-j\frac{\Omega}{c_M}a_M}\sqrt{\mathcal{T}_{M-1,12}^{(1)}(\Omega)}+\mathcal{D}_{M,12}e^{j\frac{\Omega}{c_M}a_M}\sqrt{\mathcal{T}_{M-1,11}^{(1)}(-\Omega)} \\
&= \sqrt{\mathcal{T}_{12}^{(1)}(\Omega)},
\end{aligned} \tag{C.34}$$

$$\begin{aligned}
\mathcal{T}_{21}^{(0)}(\Omega) &= \mathcal{D}_{M,12}e^{-j\frac{\Omega}{c_M}a_M}\mathcal{T}_{M-1,11}^{(0)}(\Omega) + \mathcal{D}_{M,11}e^{j\frac{\Omega}{c_M}a_M}\mathcal{T}_{M-1,12}^{(0)}(-\Omega) \\
&= \mathcal{D}_{M,12}e^{-j\frac{\Omega}{c_M}a_M}\sqrt{\mathcal{T}_{M-1,11}^{(1)}(\Omega)} + \mathcal{D}_{M,11}e^{j\frac{\Omega}{c_M}a_M}\sqrt{\mathcal{T}_{M-1,12}^{(1)}(-\Omega)} \\
&= \mathcal{T}_{12}^{(0)}(-\Omega) \\
&= \sqrt{\mathcal{T}_{12}^{(1)}(-\Omega)},
\end{aligned} \tag{C.35}$$

and

$$\begin{aligned}
\mathcal{T}_{22}^{(0)}(\Omega) &= \mathcal{D}_{M,12}e^{-j\frac{\Omega}{c_M}a_M}\mathcal{T}_{M-1,12}^{(0)}(\Omega) + \mathcal{D}_{M,11}e^{j\frac{\Omega}{c_M}a_M}\mathcal{T}_{M-1,11}^{(0)}(-\Omega) \\
&= \mathcal{D}_{M,12}e^{-j\frac{\Omega}{c_M}a_M}\sqrt{\mathcal{T}_{M-1,12}^{(1)}(\Omega)} + \mathcal{D}_{M,11}e^{j\frac{\Omega}{c_M}a_M}\sqrt{\mathcal{T}_{M-1,11}^{(1)}(-\Omega)} \\
&= \mathcal{T}_{11}^{(0)}(-\Omega) \\
&= \sqrt{\mathcal{T}_{11}^{(1)}(-\Omega)}.
\end{aligned} \tag{C.36}$$

As can be observed, comparing these elements to those derived in Equations (D.2)-(D.6) enable us to show that Equation (8.21) is a quadratic form of the expression delivered by Equation (6.14).

D

Outline of the nonlinear signal modeling

The identities used in Equation (8.37) can be proven by induction. Thus, assuming that Equation (8.37) is correct for $(M-1)$ layers, by multiplying it by another frequency response of first-order for a layer M, the obtained product may retain the same form with $(M-1)$ increased to M. As can be observed in Equation (8.31), this hypothesis is correct and trivial for $M = 1$ since $H_i^{NL}(\omega) = H_i^{NL}(-\omega)$.

$$\boldsymbol{T}^{(1)}(\omega) = \boldsymbol{T}_M^{(1)}(\omega)\boldsymbol{T}_{M-1}^{(1)}(\omega) = \begin{pmatrix} D_{M,11}^2 e^{-2j\omega m_M} & D_{M,12}^2 e^{2j\omega m_M} & 2D_{M,11}D_{M,12} & 0 & 0 \\ D_{M,12}^2 e^{-2j\omega m_M} & D_{M,11}^2 e^{2j\omega m_M} & 2D_{M,11}D_{M,12} & 0 & 0 \\ D_{M,11}D_{M,12}e^{-2j\omega m_M} & D_{M,11}D_{M,12}e^{2j\omega m_M} & D_{M,11}^2 + D_{M,12}^2 & 0 & 0 \\ D_{M,11}H_M^{NL}(\omega)e^{-2j\omega m_M} & D_{M,12}H_M^{NL}(\omega)e^{2j\omega m_M} & 0 & D_{M,11}e^{-2j\omega m_M} & D_{M,12}e^{2j\omega m_M} \\ D_{M,12}H_M^{NL}(\omega)e^{-2j\omega m_M} & D_{M,11}H_M^{NL}(\omega)e^{2j\omega m_M} & 0 & D_{M,12}e^{-2j\omega m_M} & D_{M,11}e^{2j\omega m_M} \end{pmatrix} \cdot$$

$$\begin{pmatrix} T_{M-1,11}^{(1)}(\omega) & T_{M-1,12}^{(1)}(\omega) & 2\sqrt{T_{M-1,11}^{(1)}(\omega)T_{M-1,12}^{(1)}(\omega)} & 0 & 0 \\ T_{M-1,12}^{(1)}(-\omega) & T_{M-1,11}^{(1)}(-\omega) & 2\sqrt{T_{M-1,11}^{(1)}(-\omega)T_{M-1,12}^{(1)}(-\omega)} & 0 & 0 \\ \sqrt{T_{M-1,11}^{(1)}(\omega)T_{M-1,12}^{(1)}(-\omega)} & \sqrt{T_{M,11}^{(1)}(-\omega)T_{M-1,12}^{(1)}(\omega)} & \sqrt{T_{M-1,11}^{(1)}(\omega)T_{M-1,11}^{(1)}(-\omega)} + \sqrt{T_{M-1,12}^{(1)}(\omega)T_{M-1,12}^{(1)}(-\omega)} & 0 & 0 \\ T_{M-1,41}^{(1)}(\omega) & T_{M-1,42}^{(1)}(\omega) & T_{M-1,43}^{(1)}(\omega) & \sqrt{T_{M-1,11}^{(1)}(2\omega)} & \sqrt{T_{M-1,12}^{(1)}(2\omega)} \\ T_{M-1,42}^{(1)}(-\omega) & T_{M-1,41}^{(1)}(-\omega) & T_{M-1,43}^{(1)}(-\omega) & \sqrt{T_{M-1,12}^{(1)}(-2\omega)} & \sqrt{T_{M-1,11}^{(1)}(-2\omega)} \end{pmatrix} =$$

$$\begin{pmatrix} T_{11}^{(1)}(\omega) & T_{12}^{(1)}(\omega) & 2\sqrt{T_{11}^{(1)}(\omega)T_{12}^{(1)}(\omega)} & 0 & 0 \\ T_{12}^{(1)}(-\omega) & T_{11}^{(1)}(-\omega) & 2\sqrt{T_{11}^{(1)}(-\omega)T_{12}^{(1)}(-\omega)} & 0 & 0 \\ \sqrt{T_{11}^{(1)}(\omega)T_{12}^{(1)}(-\omega)} & \sqrt{T_{M,11}^{(1)}(-\omega)T_{12}^{(1)}(\omega)} & \sqrt{T_{11}^{(1)}(\omega)T_{11}^{(1)}(-\omega)} + \sqrt{T_{12}^{(1)}(\omega)T_{12}^{(1)}(-\omega)} & 0 & 0 \\ T_{41}^{(1)}(\omega) & T_{42}^{(1)}(\omega) & T_{43}^{(1)}(\omega) & \sqrt{T_{11}^{(1)}(2\omega)} & \sqrt{T_{12}^{(1)}(2\omega)} \\ T_{42}^{(1)}(-\omega) & T_{41}^{(1)}(-\omega) & T_{43}^{(1)}(-\omega) & \sqrt{T_{12}^{(1)}(-2\omega)} & \sqrt{T_{11}^{(1)}(-2\omega)} \end{pmatrix} \tag{D.1}$$

We will show hereafter that the 19 non-zero elements of the matrix described in Equation (8.28) can be related to the 5 independent elements that arise in the resulting matrix of Equa-

tion (D.1). The elements of the first row of that matrix can be written down as,

$$\begin{aligned} T_{11}^{(1)}(\omega) &= D_{M,11}^2 e^{-2j\omega m_M} T_{M-1,11}^{(1)}(\omega) + D_{M,12}^2 e^{2j\omega m_M} T_{M-1,12}^{(1)}(-\omega) \\ &+ 2D_{M,11}D_{M,12}\sqrt{T_{M-1,11}^{(1)}(\omega)T_{M-1,12}^{(1)}(-\omega)} \\ &= \left(D_{M,11}e^{-j\omega m_M}\sqrt{T_{M-1,11}^{(1)}(\omega)} + D_{M,12}e^{j\omega m_M}\sqrt{T_{M-1,12}^{(1)}(-\omega)}\right)^2, \end{aligned} \tag{D.2}$$

$$\begin{aligned} T_{12}^{(1)}(\omega) &= D_{M,11}^2 e^{-2j\omega m_M} T_{M-1,12}^{(1)}(\omega) + D_{M,12}^2 e^{2j\omega m_M} T_{M-1,11}^{(1)}(-\omega) \\ &+ 2D_{M,11}D_{M,12}\sqrt{T_{M-1,11}^{(1)}(-\omega)T_{M-1,12}^{(1)}(\omega)} \\ &= \left(D_{M,11}e^{-j\omega m_M}\sqrt{T_{M-1,12}^{(1)}(\omega)} + D_{M,12}e^{j\omega m_M}\sqrt{T_{M-1,11}^{(1)}(-\omega)}\right)^2, \end{aligned} \tag{D.3}$$

and

$$\begin{aligned} T_{13}^{(1)}(\omega) &= 2D_{M,11}^2 e^{-2j\omega m_M}\sqrt{T_{M-1,11}^{(1)}(\omega)T_{M-1,12}^{(1)}(\omega)} \\ &+ 2D_{M,12}^2 e^{2j\omega m_M}\sqrt{T_{M-1,11}^{(1)}(-\omega)T_{M-1,12}^{(1)}(-\omega)} \\ &+ 2D_{M,11}D_{M,12}\left(\sqrt{T_{M-1,11}^{(1)}(\omega)T_{M-1,11}^{(1)}(-\omega)} + \sqrt{T_{M-1,12}^{(1)}(\omega)T_{M-1,12}^{(1)}(-\omega)}\right) \\ &= 2\left(D_{M,11}e^{-j\omega m_M}\sqrt{T_{M-1,11}^{(1)}(\omega)} + D_{M,12}e^{j\omega m_M}\sqrt{T_{M-1,12}^{(1)}(-\omega)}\right) \\ &\cdot \left(D_{M,11}e^{-j\omega m_M}\sqrt{T_{M-1,12}^{(1)}(\omega)} + D_{M,12}e^{j\omega m_M}\sqrt{T_{M-1,11}^{(1)}(-\omega)}\right) \\ &= 2\sqrt{T_{11}^{(1)}(\omega)T_{12}^{(1)}(\omega)}. \end{aligned} \tag{D.4}$$

As can be observed, the $T_{13}^{(1)}(\omega)$-element of the frequency response of first-order can be expressed by means of the elements $T_{11}^{(1)}(\omega)$ and $T_{12}^{(1)}(\omega)$. Following this reasoning for the second and third rows enables us to find other elements of that matrix, which also dependent upon those two elements. Hence,

$$\begin{aligned} T_{21}^{(1)}(\omega) &= D_{M,12}^2 e^{-2j\omega m_M} T_{M-1,11}^{(1)}(\omega) + D_{M,11}^2 e^{2j\omega m_M} T_{M-1,12}^{(1)}(-\omega) \\ &+ 2D_{M,11}D_{M,12}\sqrt{T_{M-1,11}^{(1)}(\omega)T_{M-1,12}^{(1)}(-\omega)} \\ &= \left(D_{M,12}e^{-j\omega m_M}\sqrt{T_{M-1,11}^{(1)}(\omega)} + D_{M,11}e^{j\omega m_M}\sqrt{T_{M-1,12}^{(1)}(-\omega)}\right)^2 \\ &= T_{12}^{(1)}(-\omega), \end{aligned} \tag{D.5}$$

$$
\begin{aligned}
T_{22}^{(1)}(\omega) &= D_{M,12}^2 e^{-2j\omega m_M} T_{M-1,12}^{(1)}(\omega) + D_{M,11}^2 e^{2j\omega m_M} T_{M-1,11}^{(1)}(-\omega) \\
&+ 2D_{M,11}D_{M,12}\sqrt{T_{M-1,11}^{(1)}(-\omega)T_{M-1,12}^{(1)}(\omega)} \\
&= \left(D_{M,12}e^{-j\omega m_M}\sqrt{T_{M-1,12}^{(1)}(\omega)} + D_{M,11}e^{j\omega m_M}\sqrt{T_{M-1,11}^{(1)}(-\omega)}\right)^2 \\
&= T_{11}^{(1)}(-\omega),
\end{aligned}
\tag{D.6}
$$

$$
\begin{aligned}
T_{23}^{(1)}(\omega) &= 2D_{M,12}^2 e^{-2j\omega m_M}\sqrt{T_{M-1,11}^{(1)}(\omega)T_{M-1,12}^{(1)}(\omega)} \\
&+ 2D_{M,11}^2 e^{2j\omega m_M}\sqrt{T_{M-1,11}^{(1)}(-\omega)T_{M-1,12}^{(1)}(-\omega)} \\
&+ 2D_{M,11}D_{M,12}\left(\sqrt{T_{M-1,11}^{(1)}(\omega)T_{M-1,11}^{(1)}(-\omega)} + \sqrt{T_{M-1,12}^{(1)}(\omega)T_{M-1,12}^{(1)}(-\omega)}\right) \\
&= 2\left(D_{M,12}e^{-j\omega m_M}\sqrt{T_{M-1,11}^{(1)}(\omega)} + D_{M,11}e^{j\omega m_M}\sqrt{T_{M-1,12}^{(1)}(-\omega)}\right) \\
&\cdot \left(D_{M,12}e^{-j\omega m_M}\sqrt{T_{M-1,12}^{(1)}(\omega)} + D_{M,11}e^{j\omega m_M}\sqrt{T_{M-1,11}^{(1)}(-\omega)}\right) \\
&= 2\sqrt{T_{11}^{(1)}(-\omega)T_{12}^{(1)}(-\omega)},
\end{aligned}
\tag{D.7}
$$

$$
\begin{aligned}
T_{31}^{(1)}(\omega) &= D_{M,11}D_{M,12}e^{-2j\omega m_M}T_{M-1,11}^{(1)}(\omega) + D_{M,11}D_{M,12}e^{2j\omega m_M}T_{M-1,12}^{(1)}(-\omega) \\
&+ \left(D_{M,11}^2 + D_{M,12}^2\right)\sqrt{T_{M-1,11}^{(1)}(\omega)T_{M-1,12}^{(1)}(-\omega)} \\
&= \left(D_{M,11}e^{-j\omega m_M}\sqrt{T_{M-1,11}^{(1)}(\omega)} + D_{M,12}e^{j\omega m_M}\sqrt{T_{M-1,12}^{(1)}(-\omega)}\right) \\
&\cdot \left(D_{M,12}e^{-j\omega m_M}\sqrt{T_{M-1,11}^{(1)}(\omega)} + D_{M,11}e^{j\omega m_M}\sqrt{T_{M-1,12}^{(1)}(-\omega)}\right) \\
&= \sqrt{T_{11}^{(1)}(\omega)T_{12}^{(1)}(-\omega)},
\end{aligned}
\tag{D.8}
$$

$$
\begin{aligned}
T_{32}^{(1)}(\omega) &= D_{M,11}D_{M,12}e^{-2j\omega m_M}T_{M-1,12}^{(1)}(\omega) + D_{M,11}D_{M,12}e^{2j\omega m_M}T_{M-1,11}^{(1)}(-\omega) \\
&+ \left(D_{M,11}^2 + D_{M,12}^2\right)\sqrt{T_{M-1,11}^{(1)}(-\omega)T_{M-1,12}^{(1)}(\omega)} \\
&= \left(D_{M,12}e^{-j\omega m_M}\sqrt{T_{M-1,12}^{(1)}(\omega)} + D_{M,11}e^{j\omega m_M}\sqrt{T_{M-1,11}^{(1)}(-\omega)}\right) \\
&\cdot \left(D_{M,11}e^{-j\omega m_M}\sqrt{T_{M-1,12}^{(1)}(\omega)} + D_{M,12}e^{j\omega m_M}\sqrt{T_{M-1,11}^{(1)}(-\omega)}\right) \\
&= \sqrt{T_{11}^{(1)}(-\omega)T_{12}^{(1)}(\omega)},
\end{aligned}
\tag{D.9}
$$

and

$$\begin{aligned}
T_{33}^{(1)}(\omega) &= 2D_{M,11}D_{M,12}e^{-2j\omega m_M}\sqrt{T_{M-1,11}^{(1)}(\omega)T_{M-1,12}^{(1)}(\omega)} \\
&+ 2D_{M,11}D_{M,12}e^{2j\omega m_M}\sqrt{T_{M-1,11}^{(1)}(-\omega)T_{M-1,12}^{(1)}(-\omega)} \\
&+ \left(D_{M,11}^2 + D_{M,12}^2\right)\left(\sqrt{T_{M-1,11}^{(1)}(\omega)T_{M-1,11}^{(1)}(-\omega)} + \sqrt{T_{M-1,12}^{(1)}(\omega)T_{M-1,12}^{(1)}(-\omega)}\right) \\
&= \left(D_{M,11}e^{-j\omega m_M}\sqrt{T_{M-1,11}^{(1)}(\omega)} + D_{M,12}e^{j\omega m_M}\sqrt{T_{M-1,12}^{(1)}(-\omega)}\right) \\
&\cdot \left(D_{M,12}e^{-j\omega m_M}\sqrt{T_{M-1,12}^{(1)}(\omega)} + D_{M,11}e^{j\omega m_M}\sqrt{T_{M-1,11}^{(1)}(-\omega)}\right) \\
&+ \left(D_{M,11}e^{-j\omega m_M}\sqrt{T_{M-1,12}^{(1)}(\omega)} + D_{M,12}e^{j\omega m_M}\sqrt{T_{M-1,11}^{(1)}(-\omega)}\right) \\
&\cdot \left(D_{M,12}e^{-j\omega m_M}\sqrt{T_{M-1,11}^{(1)}(\omega)} + D_{M,11}e^{j\omega m_M}\sqrt{T_{M-1,12}^{(1)}(-\omega)}\right) \\
&= \sqrt{T_{11}^{(1)}(\omega)T_{11}^{(1)}(-\omega)} + \sqrt{T_{12}^{(1)}(\omega)T_{12}^{(1)}(-\omega)}.
\end{aligned} \tag{D.10}$$

This reasoning can be further applied to the lower-right elements of the fourth and fifth rows, leading to:

$$\begin{aligned}
T_{44}^{(1)}(\omega) &= D_{M,11}e^{-2j\omega m_M}\sqrt{T_{M-1,11}^{(1)}(2\omega)} + D_{M,12}e^{2j\omega m_M}\sqrt{T_{M-1,12}^{(1)}(-2\omega)} \\
&= \sqrt{T_{11}^{(1)}(2\omega)},
\end{aligned} \tag{D.11}$$

$$\begin{aligned}
T_{45}^{(1)}(\omega) &= D_{M,11}e^{-2j\omega m_M}\sqrt{T_{M-1,12}^{(1)}(2\omega)} + D_{M,12}e^{2j\omega m_M}\sqrt{T_{M-1,11}^{(1)}(-2\omega)} \\
&= \sqrt{T_{12}^{(1)}(2\omega)},
\end{aligned} \tag{D.12}$$

$$\begin{aligned}
T_{54}^{(1)}(\omega) &= D_{M,12}e^{-2j\omega m_M}\sqrt{T_{M-1,11}^{(1)}(2\omega)} + D_{M,11}e^{2j\omega m_M}\sqrt{T_{M-1,12}^{(1)}(-2\omega)} \\
&= \sqrt{T_{12}^{(1)}(-2\omega)},
\end{aligned} \tag{D.13}$$

and

$$\begin{aligned}
T_{55}^{(1)}(\omega) &= D_{M,12}e^{-2j\omega m_M}\sqrt{T_{M-1,12}^{(1)}(2\omega)} + D_{M,11}e^{2j\omega m_M}\sqrt{T_{M-1,11}^{(1)}(-2\omega)} \\
&= \sqrt{T_{11}^{(1)}(-2\omega)},
\end{aligned} \tag{D.14}$$

Finally, the remaining six elements of the fourth and fifth rows which explicitly contain the nonlinear terms can obviously not be directly related to those two elements, and they thus keep their original denomination. Nevertheless, some relations can be established between

them. To this end, let us consider the three first elements of the fourth row. Hence,

$$\begin{aligned} T_{41}^{(1)}(\omega) &= D_{M,11}H_M^{NL}(\omega)e^{-2j\omega m_M}T_{M-1,11}^{(1)}(\omega) + D_{M,12}H_M^{NL}(\omega)e^{2j\omega m_M}T_{M-1,12}^{(1)}(-\omega) \\ &+ D_{M,11}e^{-2j\omega m_M}T_{M-1,41}^{(1)}(\omega) + D_{M,12}e^{2j\omega m_M}T_{M-1,42}^{(1)}(-\omega), \end{aligned} \tag{D.15}$$

$$\begin{aligned} T_{42}^{(1)}(\omega) &= D_{M,11}H_M^{NL}(\omega)e^{-2j\omega m_M}T_{M-1,12}^{(1)}(\omega) + D_{M,12}H_M^{NL}(\omega)e^{2j\omega m_M}T_{M-1,11}^{(1)}(-\omega) \\ &+ D_{M,11}e^{-2j\omega m_M}T_{M-1,42}^{(1)}(\omega) + D_{M,12}e^{2j\omega m_M}T_{M-1,41}^{(1)}(-\omega), \end{aligned} \tag{D.16}$$

and

$$\begin{aligned} T_{43}^{(1)}(\omega) &= 2D_{M,11}H_M^{NL}(\omega)e^{-2j\omega m_M}\sqrt{T_{M-1,11}^{(1)}(\omega)T_{M-1,12}^{(1)}(\omega)} \\ &+ 2D_{M,12}H_M^{NL}(\omega)e^{2j\omega m_M}\sqrt{T_{M-1,11}^{(1)}(-\omega)T_{M-1,12}^{(1)}(-\omega)} \\ &+ D_{M,11}e^{-2j\omega m_M}T_{M-1,43}^{(1)}(\omega) + D_{M,12}e^{2j\omega m_M}T_{M-1,43}^{(1)}(-\omega). \end{aligned} \tag{D.17}$$

By making use of the identities $-D_{i,41}(\omega) = D_{i,41}(-\omega)$, $-D_{i,43}(\omega) = D_{i,43}(-\omega)$, and $H_i^{NL}(\omega) = H_i^{NL}(-\omega)$, $\forall i$, the three first elements of the fifth row can be written down as follows,

$$\begin{aligned} T_{51}^{(1)}(\omega) &= D_{M,12}H_M^{NL}(\omega)e^{-2j\omega m_M}T_{M-1,11}^{(1)}(\omega) + D_{M,11}H_M^{NL}(\omega)e^{2j\omega m_M}T_{M-1,12}^{(1)}(-\omega) \\ &+ D_{M,12}e^{-2j\omega m_M}T_{M-1,41}^{(1)}(\omega) + D_{M,11}e^{2j\omega m_M}T_{M-1,42}^{(1)}(-\omega) \\ &= T_{42}^{(1)}(-\omega), \end{aligned} \tag{D.18}$$

$$\begin{aligned} T_{52}^{(1)}(\omega) &= D_{M,12}H_M^{NL}(\omega)e^{-2j\omega m_M}T_{M-1,12}^{(1)}(\omega) + D_{M,11}H_M^{NL}(\omega)e^{2j\omega m_M}T_{M-1,11}^{(1)}(-\omega) \\ &+ D_{M,12}e^{-2j\omega m_M}T_{M-1,42}^{(1)}(\omega) + D_{M,11}e^{2j\omega m_M}T_{M-1,41}^{(1)}(-\omega) \\ &= T_{41}^{(1)}(-\omega), \end{aligned} \tag{D.19}$$

and

$$\begin{aligned} T_{53}^{(1)}(\omega) &= 2D_{M,12}H_M^{NL}(\omega)e^{-2j\omega m_M}\sqrt{T_{M-1,11}^{(1)}(\omega)T_{M-1,12}^{(1)}(\omega)} \\ &+ 2D_{M,11}H_M^{NL}(\omega)e^{2j\omega m_M}\sqrt{T_{M-1,11}^{(1)}(-\omega)T_{M-1,12}^{(1)}(-\omega)} \\ &+ D_{M,12}e^{-2j\omega m_M}T_{M-1,43}^{(1)}(\omega) + D_{M,11}e^{2j\omega m_M}T_{M-1,43}^{(1)}(-\omega) \\ &= T_{43}^{(1)}(-\omega). \end{aligned} \tag{D.20}$$

From those expressions, we recover all the identities used in Equation (8.37), and show that the 19 non-zero elements of the frequency response of first-order $\boldsymbol{T}^{(1)}(\omega)$ can be expressed using only five elements, namely $T_{11}^{(1)}(\omega)$, $T_{12}^{(1)}(\omega)$, $T_{41}^{(1)}(\omega)$, $T_{42}^{(1)}(\omega)$, and $T_{43}^{(1)}(\omega)$.

E

Contributions

The outcomes from this dissertation and other contributions of the PhD fellow are partially reflected in the refereed journals and conference proceedings listed below.

- Refereed journal publications:
  - N. Bochud and G. Rus, Probabilistic inverse problem to characterize tissue-equivalent material mechanical properties, *IEEE Transactions on Ultrasonics, Ferroelectrics and Frequency Control (Special Issue: Novel Embedded Systems for Ultrasonic Imaging and Signal)*, 59(7):1443–1456, 2012 (Journal ranking: SCI – 1.822; 7/31 (Q_1): Acoustics; cited by 1).
  - A. Fahim, R. Gallego, N. Bochud, and G. Rus, Model-based damage reconstruction in composites from ultrasound transmission, *Composites Part B: Engineering*, 45(1):50–62, 2013 (Journal ranking: SCI – 2.143; 7/90 (Q_1): Multi. Eng.; cited by 3).
  - N. Bochud, A. Gomez, G. Rus, and A. Peinado, A sparse digital signal model for ultrasonic nondestructive evaluation of composite materials, *Submitted to IEEE Transactions on Ultrasonics, Ferroelectrics, and Frequency Control (under review)*, 2014 (Journal ranking: SCI – 1.822; 7/31 (Q_1): Acoustics).
  - L. Peralta, N. Bochud, and G. Rus, Mechanical characterization of cervical tissue by ultrasound, *Submitted to the Journal of the Mechanical Behavior of Biomedical Materials (under review)*, 2014 (Journal ranking: SCI – 2.368; 25/79 (Q_2): Biomed. Eng.).

- G. Rus, J. Melchor, N. Bochud, L. Peralta, and W.J. Parnell, A micro-mechanical approach for nonlinear quantitative ultrasound, *Submitted to Ultrasonics (under review)*, 2014 (Journal ranking: SCI – 2.018; 5/31 (Q_1): Acoustics).

- Relevant conference proceedings:
  - N. Bochud, A. Fahim, A. Gomez, and G. Rus, Impact damage characterization in composites using signal processing techniques, *Procedia Engineering of the The Twelfth East Asia-Pacific Conference on Structural Engineering and Construction*, 14:169–176, Hong-Kong, January 2011.
  - N. Bochud, A. Gomez, G. Rus, J. L. Carmona, and A. Peinado, Robust parametrization for non- destructive evaluation of composites using ultrasonic signals, *IEEE International Conference on Acoustics Speech, and Signal Processing*, p. 1789–1792, Praga, May 2011 (cited by 6).
  - B. Fuentes, J. L. Carmona, N. Bochud, A. Gomez, and A. Peinado, Model-based cepstral analysis for ultrasonic non-destructive evaluation of composites, *IEEE International Conference on Acoustics Speech, and Signal Processing*, p. 1717–1720, Tokyo, March 2012 (cited by 3).
  - G. Rus, N. Bochud, J. Melchor, M. Alaminos, and A. Campos, Dispersive model selection and reconstruction for tissue culture ultrasonic monitoring, *International Congress on Ultrasonics*, p. 375–378, Gdansk, September 2012.
  - N. Bochud, A. Gomez, G. Rus, and A. Peinado, Sparse signal model for ultrasonic nondestructive evaluation of CFRP plates, *IEEE International Conference on Acoustics Speech, and Signal Processing*, p. 2844–2847, Vancouver, May 2013.

References

[1] M.J.S. Lowe. Matrix techniques for modeling ultrasonic waves in multilayered media. *IEEE Transactions on Ultrasonics, Ferroelectrics and Frequency Control*, 42(4):525–542, 1995.

[2] M.G. Messineo, G.L. Frontini, G.E. Elicabe, and L. Gaete-Garretón. Equivalent ultrasonic impedance in multilayer media. a parameter estimation problem. *Inverse Problems in Science and Engineering*, pages 1–20, 2013.

[3] M. Rielly, V. Humphrey, and F. Duck. A theoretical and experimental investigation of nonlinear ultrasound propagation through tissue mimicking fluids. In *IEEE Ultrasonics Symposium*, volume 2, pages 1355–1358, 2000.

[4] E.R. Hughes, T.G. Leighton, G.W. Petley, and P.R. White. Ultrasonic propagation in cancellous bone: A new stratified model. *Ultrasound in Medicine & Biology*, 25(5):811–821, 1999.

[5] W. Lin, Y.-X. Qin, and C. Rubin. Ultrasonic wave propagation in trabecular bone predicted by the stratified model. *Annals of biomedical engineering*, 29(9):781–790, 2001.

[6] G.-M. Zhang and D.M. Harvey. Contemporary ultrasonic signal processing approaches for nondestructive evaluation of multilayered structures. *Nondestructive Testing and Evaluation*, 27(1):1–27, 2012.

[7] J.D. Achenbach. Quantitative nondestructive evaluation. *International Journal of Solids and Structures*, 37(1):13–27, 2000.

[8] A. Tarantola. *Inverse Problem Theory*. SIAM, 2005.

[9] S. Kubo. Classification of inverse problems arising in field problems and their treatments. In *IUTAM Symposium Tokyo/Japan, 1993*, 1993.

[10] G.P. Singh and S. Udpa. The role of digital signal processing in ndt. *NDT international*, 19(3):125–132, 1986.

[11] T. Wang, J. Saniie, and X. Jin. Analysis of low-order autoregressive models for ultrasonic grain signal characterization. *IEEE Transactions on Ultrasonics, Ferroelectrics and Frequency Control*, 38(2):116–124, 1991.

[12] R. Prakash. Non-destructive testing of composites. *Composites*, 11(4):217–224, 1980.

[13] G.-M. Zhang, C.-Z. Zhang, and D.M. Harvey. Sparse signal representation and its applications in ultrasonic nde. *Ultrasonics*, 52:351–363, 2011.

[14] Q. Shen, M. Omar, and S. Dongri. Ultrasonic nde techniques for impact damage inspection on cfrp laminates. *Journal of materials science research*, 1(1):1–15, 2011.

[15] V.K. Kinra and C. Zhu. Ultrasonic nondestructive evaluation of thin (sub-wavelength) coatings. *The Journal of the Acoustical Society of America*, 93:2454–1467, 1993.

[16] T.C. Hanshaw, C.S. Hsu, and M.J. Anderson. Analysis of ultrasonic non destructive evaluation data using singular value decomposition of the hankel data matrix. In *American Control Conference*, volume 5, pages 3672–3677, 2001.

[17] S.P. Neal and D.O. Thompson. The measurement and analysis of acoustic noise as a random variable in ultrasonic nondestructive evaluation. *The Journal of the Acoustical Society of America*, 86:S94, 1989.

[18] A. Grennberg and M. Sandell. Estimation of subsample time delay differences in narrowband ultrasonic echoes using the hilbert transform correlation. *IEEE Transactions on Ultrasonics, Ferroelectrics and Frequency Control*, 41(5):588–595, 1994.

[19] M.A.G Izquierdo, M.G. Hernández, and J.J. Anaya. Time-varying prediction filter for structural noise reduction in ultrasonic nde. *Ultrasonics*, 44:e1001–e1005, 2006.

[20] S.P. Neal, P.L. Speckman, and M.A. Enright. Flaw signature estimation in ultrasonic nondestructive evaluation using the wiener filter with limited prior information. *IEEE Transactions on Ultrasonics, Ferroelectrics and Frequency Control*, 40(4):347–353, 1993.

[21] S.-K. Sin and C.-H. Chen. A comparison of deconvolution techniques for the ultrasonic nondestructive evaluation of materials. *IEEE Transactions on Image Processing*, 1(1):3–10, 1992.

[22] S.-C. Wooh and C. Wei. Cepstrum-based deconvolution of ultrasonic pulse-echo signals from laminated composite materials. In *Proceedings of the 12th Engineering Mechanics Conference*, pages 1–4, 1998.

[23] A.K. Nandi, D. Mampel, and B. Roscher. Blind deconvolution of ultrasonic signals in nondestructive testing applications. *IEEE Transactions on Signal Processing*, 45(5):1382–1390, 1997.

[24] L. Ghouti and C.H. Chen. Deconvolution of ultrasonic nondestructive evaluation signals using higher-order statistics. In *IEEE International Conference on Acoustics, Speech, and Signal Processing*, volume 3, pages 1457–1460, 1999.

[25] A. Abbate, J. Koay, J. Frankel, S.C. Schroeder, and P. Das. Signal detection and noise suppression using a wavelet transform signal processor: application to ultrasonic flaw detection. *IEEE Transactions on Ultrasonics, Ferroelectrics and Frequency Control*, 44(1):14–26, 1997.

[26] M.A. Malik and J. Saniie. Generalized time-frequency representation of ultrasonic signals. In *IEEE Ultrasonics Symposium*, pages 691–695, 1993.

[27] M. Rodriguez, L. Vergara, and J. Morales. Real-time prototype for microcracks detection on ceramic materials. In *International Symposium on Time-Frequency and Time-Scale Analysis*, pages 469–472, 1996.

[28] G. Wu, J. Su, D. Zhu, H. Gou, W. Sheng, and Y. Li. Ultrasonic nde of thin composite plate based on an enhanced wigner-ville distribution. In *17th World Conference on Nondestructive Testing, Shanghai, China*, 2008.

[29] N.M. Bilgutay, V.L. Newhouse, and E.S. Furgason. Flaw visibility enhancement by split-spectrum processing techniques. In *IEEE Ultrasonics Symposium*, pages 878–883, 1981.

[30] N. Bilgutay, J. Popovics, S. Popovics, and M. Karaoguz. Recent developments in concrete nondestructive evaluation. In *International Conference on Acoustics, Speech, and Signal Processing*, volume 6, pages 3393–3396, 2001.

[31] A. Benammar, R. Drai, and A. Guessoum. Detection of delamination defects in cfrp materials using ultrasonic signal processing. *Ultrasonics*, 48(8):731–738, 2008.

[32] S.C. Ng, N. Ismail, A. Ali, B. Sahari, J.M. Yusof, and B.W. Chu. Non-destructive inspection of multi-layered composite using ultrasonic signal processing. In *IOP Conference Series: Materials Science and Engineering*, volume 17.

[33] A. Messina. Detecting damage in beams through digital differentiator filters and continuous wavelet transforms. *Journal of sound and vibration*, 272(1):385–412, 2004.

[34] W.-X. Yang, J.B. Hull, and M.D. Seymour. A contribution to the applicability of complex wavelet analysis of ultrasonic signals. *NDT & E International*, 37(6):497–504, 2004.

[35] K. Harrouche, J.M. Rouvaen, M. Ouaftouh, M. Ourak, and F. Haine. Signal-processing methods for analysing the structure of carbon-epoxy-resin composite materials. *Measurement Science and Technology*, 11(3):285—-290, 2000.

[36] S. Legendre, J. Goyette, and D. Massicotte. Ultrasonic nde of composite material structures using wavelet coefficients. *NDT & E International*, 34(1):31–37, 2001.

[37] I.M. Johnstone and B.W. Silverman. Wavelet threshold estimators for data with correlated noise. *Journal of the Royal Statistical Society: Series B (Statistical Methodology)*, 59(2):319–351, 1997.

[38] G.-M. Zhang, D.M. Harvey, and D.R. Braden. Signal denoising and ultrasonic flaw detection via overcomplete and sparse representations. *The Journal of the Acoustical Society of America*, 124:2963–2972.

[39] J. Guo, J. Wu, X. Yang, and G. Liu. Ultrasonic nondestructive signals processing based on matching pursuit with gabor dictionary. *Chinese Journal of Mechanical Engineering*, 24(4):591–595, 2011.

[40] F. Boßmann, G. Plonka, T. Peter, O. Nemitz, and T. Schmitte. Sparse deconvolution methods for ultrasonic ndt. *Journal of Nondestructive Evaluation*, 31(3):225–244, 2012.

[41] T. Olofsson and T. Stepinski. Minimum entropy deconvolution of pulse-echo signals acquired from attenuative layered media. *The Journal of the Acoustical Society of America*, 109:2831–2839.

[42] C. Soussen, J. Idier, E. Carcreff, L. Simon, and C. Potel. Ultrasonic non destructive testing based on sparse deconvolution. In *Journal of Physics: Conference Series*, volume 353, page 012018, 2012.

[43] T.J. Case and R.C. Waag. Flaw identification from time and frequency features of ultrasonic waveforms. *IEEE Transactions on Ultrasonics, Ferroelectrics and Frequency Control*, 43(4):592–600, 1996.

[44] J.E. Michaels, A.C. Cobb, and T.E. Michaels. A comparison of feature-based classifiers for ultrasonic structural health monitoring. In *NDE for Health Monitoring and Diagnostics*, pages 363–374, 2004.

[45] A. Peinado and J.C. Segura. *Speech recognition over digital channels*. John Wiley & Sons, 2006.

[46] Á. de la Torre, A.M. Peinado, A.J. Rubio, V.E. Sánchez, and J.E. Díaz. An application of minimum classification error to feature space transformations for speech recognition. *Speech Communication*, 20(3):273–290, 1996.

[47] A. de la Torre, A.M. Peinado, A.J. Rubio, and V. Sánchez. A dfe-based algorithm for feature selection in speech recognition. In *IEEE International Conference on Acoustics, Speech, and Signal Processing*, volume 2, pages 1519–1522, 1997.

[48] E. Meyer and T. Tuthill. Bayesian classification of ultrasound signals using wavelet coefficients. In *IEEE National Aerospace and Electronics Conference*, volume 1, pages 240–243, 1995.

[49] M. Khelil, M. Boudraa, A. Kechida, and R. Drai. Classification of defects by the svm method and the principal component analysis (pca). *Transactions on Engineering, Computing and Technology*, 9:226–231, 2005.

[50] P. Ramuhalli, J. Kim, L. Udpa, and S.S. Udpa. Multichannel signal processing methods for ultrasonic nondestructive evaluation. In *Sensor Array and Multichannel Signal Processing Workshop Proceedings, 2002*, pages 229–233, 2002.

[51] A. Salazar, R. Miralles, A. Parra, L. Vergara, and J. Gosalbez. Ultrasonic signal processing for archaeological ceramic restoration. In *IEEE International Conference on Acoustics, Speech and Signal Processing*, volume 3, pages 1160–1163, 2006.

[52] A. Salazar, J. Gosálbez, J. Igual, R. Llinares, and L. Vergara. Two applications of independent component analysis for non-destructive evaluation by ultrasounds. In *Independent Component Analysis and Blind Signal Separation*, pages 406–413. 2006.

[53] M. Cabrera, X. Castell, and R. Montoliu. Crack detection system based on spectral analysis of a ultrasonic resonance signals. In *IEEE International Conference on Acoustics, Speech, and Signal Processing*, volume 2, pages 605–608, 2003.

[54] R. Miralles, J. Morales, and L. Vergara. An industrial application of signal processing: ceramic microcrack detection. In *IEEE International Conference on Acoustics, Speech, and Signal Processing*, volume 4, pages 2271–2274, 1999.

[55] A. Masnata and M. Sunseri. Neural network classification of flaws detected by ultrasonic means. *NDT & E International*, 29(2):87–93, 1996.

[56] F. Hägglund, J. Martinsson, and J.E. Carlson. Flaw detection in layered media based on parametric modeling of overlapping ultrasonic echoes. In *IEEE Ultrasonics Symposium*, pages 136–139, 2006.

[57] F. Hägglund, J.E. Carlson, and T. Andersson. Ultrasonic classification of thin layers within multi-layered materials. *Measurement Science and Technology*, 21(1):1–10, 2009.

[58] L. Brekhovskikh. *Waves in layered media*. Academic Press, NY, 1960.

[59] Y.-H. Pao, W.-Q. Chen, and X.-Y. Su. The reverberation-ray matrix and transfer matrix analyses of unidirectional wave motion. *Wave Motion*, 44(6):419–438, 2007.

[60] E.L. Adler. Matrix methods applied to acoustic waves in multilayers. *IEEE Transactions on Ultrasonics, Ferroelectrics and Frequency Control*, 37(6):485–490, 1990.

[61] W.T. Thomson. Transmission of elastic waves through a stratified solid medium. *Journal of Applied Physics*, 21(2):89–93, 1950.

[62] N.A. Haskell. The dispersion of surface waves on multilayered media. *Bulletin of the Seismological Society of America*, 43(1):17–34, 1953.

[63] F. Gilbert and G.E. Backus. Propagator matrices in elastic wave and vibration problems. *Geophysics*, 31(2):326–332, 1966.

[64] W.R. Scott and P.F. Gordon. Ultrasonic spectrum analysis for nondestructive testing of layered composite materials. *The Journal of the Acoustical Society of America*, 62:108–116, 1977.

[65] D.L. Folds and C.D. Loggins. Transmission and reflection of ultrasonic waves in layered media. *The Journal of the Acoustical Society of America*, 62:1102–1109, 1977.

[66] P. Cervanka and P. Challande. A new efficient algorithm to compute the exact reflection and transmission factors for plane waves in layered absorbing media (liquids and solids). *The Journal of the Acoustical Society of America*, 89:1579–1589, 1991.

[67] D. Lévesque and L. Piché. A robust transfer matrix formulation for the ultrasonic response of multilayered absorbing media. *The Journal of the Acoustical Society of America*, 92:452–467, 1992.

[68] A.H. Nayfeh. The general problem of elastic wave propagation in multilayered anisotropic media. *Journal of the Acoustical Society of America*, 89(4):1521–1531, 1991.

[69] B. Hosten and M. Castaings. Transfer matrix of multilayered absorbing and anisotropic media. measurements and simulations of ultrasonic wave propagation through composite materials. *The Journal of the Acoustical Society of America*, 94:1488–1495, 1993.

[70] A.H. Nayfeh. *Wave propagation in layered anisotropic media: With application to composites*. North-Holland, 1995.

[71] W. Huang, S.I. Rokhlin, and Y.J. Wang. Effect of fibre-matrix interphase on wave propagation along, and scattering from, multilayered fibers in composites. transfer matrix approach. *Ultrasonics*, 33(5):365–375, 1995.

[72] W. Huang and S.I. Rokhlin. Generalized self-consistent model for composites with functionally graded and multilayered interphases. transfer matrix approach. *Mechanics of materials*, 22(3):219–247, 1996.

[73] A.K. Vashishth and P. Khurana. Waves in stratified anisotropic poroelastic media: a transfer matrix approach. *Journal of sound and vibration*, 277(1):239–275, 2004.

[74] M. Schoenberg. Wave propagation in alternating solid and fluid layers. *Wave motion*, 6(3):303–320, 1984.

[75] C. Potel and J.-F. de Belleval. Propagation in an anisotropic periodically multilayered medium. *The Journal of the Acoustical Society of America*, 93:2669–2677, 1993.

[76] S.E. Hanneman and V.K. Kinra. A new technique for ultrasonic nondestructive evaluation of adhesive joints: Part i. theory. *Experimental mechanics*, 32(4):323–331, 1992.

[77] V.K. Kinra and V.R. Iyer. Ultrasonic measurement of the thickness, phase velocity, density or attenuation of a thin-viscoelastic plate. part i: The forward problem. *Ultrasonics*, 33(2):95–109, 1995.

[78] J.W. Dunkin. Computation of modal solutions in layered, elastic media at high frequencies. *Bulletin of the Seismological Society of America*, 55(2):335–358, 1965.

[79] T. Kundu and A.K. Mal. Elastic waves in a multilayered solid due to a dislocation source. *Wave Motion*, 7(5):459–471, 1985.

[80] *Transmission coefficient of multilayered absorbing anisotropic media. A solution to the numerical limitations of the Thomson-Haskell method. Application to composite materials*, 1993.

[81] M. Castaings and B. Hosten. Delta operator technique to improve the thomson-haskell-method stability for propagation in multilayered anisotropic absorbing plates. *The Journal of the Acoustical Society of America*, 95:1931–1941, 1994.

[82] E.L. Tan. A concise and efficient scattering matrix formalism for stable analysis of elastic wave propagation in multilayered anisotropic solids. *Ultrasonics*, 41(3):229–236, 2003.

[83] B. Hosten. Bulk heterogeneous plane waves propagation through viscoelastic plates and stratified media with large values of frequency domain. *Ultrasonics*, 29(6):445–450, 1991.

[84] K. Balasubramaniam. On a numerical truncation approximation algorithm for transfer matrix method. *The Journal of the Acoustical Society of America*, 107:1053–1056, 2000.

[85] L. Knopoff. A matrix method for elastic wave problems. *Bulletin of the Seismological Society of America*, 54(1):431–438, 1964.

[86] H. Schmidt and F.B. Jensen. A full wave solution for propagation in multilayered viscoelastic media with application to gaussian beam reflection at fluid–solid interfaces. *The Journal of the Acoustical Society of America*, 77:813–825.

[87] H. Schmidt and G. Tango. Efficient global matrix approach to the computation of synthetic seismograms. *Geophysical Journal International*, 84(2):331–359, 1986.

[88] A.K. Mal. Wave propagation in layered composite laminates under periodic surface loads. *Wave Motion*, 10(3):257–266, 1988.

[89] E. Kausel and J.M. Roësset. Stiffness matrices for layered soils. *Bulletin of the Seismological Society of America*, 71(6):1743–1761, 1981.

[90] L. Wang and S.I. Rokhlin. Stable reformulation of transfer matrix method for wave propagation in layered anisotropic media. *Ultrasonics*, 39(6):413–424, 2001.

[91] S.I. Rokhlin and L. Wang. Stable recursive algorithm for elastic wave propagation in layered anisotropic media: Stiffness matrix method. *The Journal of the Acoustical Society of America*, 112:822–834, 2002.

[92] L. Wang and S.I. Rokhlin. Recursive asymptotic stiffness matrix method for analysis of surface acoustic wave devices on layered piezoelectric media. *Applied physics letters*, 81(21):4049–4051, 2002.

[93] L. Wang and S.I. Rokhlin. Modeling of wave propagation in layered piezoelectric media by a recursive asymptotic method. *IEEE Transactions on Ultrasonics, Ferroelectrics and Frequency Control*, 51(9):1060–1071, 2004.

[94] K. Balasubramaniam, V. Mukundan, and M.V. Reddy. A comparison of ultrasonic wave reflection/transmission models from isotropic multilayered structures by transfer-matrix and stiffness-matrix recursive algorithms. In *AIP Conference Proceedings*, volume 657, pages 1095–1102, 2003.

[95] E.L. Tan. Hybrid compliance-stiffness matrix method for stable analysis of elastic wave propagation in multilayered anisotropic media. *The Journal of the Acoustical Society of America*, 119:45–53, 2006.

[96] J.F. Claerbout. *Fundamentals of Geophysical Data Processing, with applications to petroleum prospecting*. Blackwell Scientific Publications, 1985.

[97] G.S. Kino. *Acoustic waves: devices, imaging, and analog signal processing*, volume 107. Prentice-Hall Englewood Cliffs, NJ, 1987.

[98] D. Sjöberg. Analysis of wave propagation in stratified structures using circuit analogues, with application to electromagnetic absorbers. *European Journal of Physics*, 29(4):721–734, 2008.

[99] *Circuit analogs for wave propagation in stratified structures*, 2010.

[100] S.R. Ghorayeb, E. Maione, and Va. La Magna. Modeling of ultrasonic wave propagation in teeth using pspice: a comparison with finite element models. *IEEE Transactions on Ultrasonics, Ferroelectrics and Frequency Control*, 48(4):1124–1131, 2001.

[101] R. Challis, F. Blarel, M. Unwin, J. Paul, and X. Guo. Models of ultrasonic wave propagation in epoxy materials. *IEEE Transactions on Ultrasonics, Ferroelectrics and Frequency Control*, 56(6):1225–1237, 2009.

[102] M. Vogt and H. Ermert. Scattering parameters measurement for the determination of layered media properties with 25 mhz ultrasound. In *IEEE Ultrasonics Symposium*, pages 1402–1405, 2006.

[103] S.J. Orfanidis. Electromagnetic waves and antennas. 2008.

[104] P.L. Goupillaud. An approach to inverse filtering of near-surface layer effects from seismic records. *Geophysics*, 26(6):754–760, 1961.

[105] R.J. Freemantle, R.E. Challis, and J.D.H White. A z-transform technique for thin-layer reverberation cancellation applied to ultrasonic ndt of adhered structures. In *Advanced Techniques for Collection and Interpretation of NDT Data*, pages 1–7, 1994.

[106] A.P. Velo, G.A. Gazonas, and T. Ameya. z-transform methods for the optimal design of one-dimensional layered elastic media. *SIAM Journal on Applied Mathematics*, 70(3):762–788, 2009.

[107] G.A. Gazonas and A.P. Velo. Analytical solutions for the resonance response of goupillaud-type elastic media using z-transform methods. *Wave Motion*, doi: 10.1016/j.wavemoti.2011.08.002, 2011.

[108] J.J. Kormylo and J.M. Mendel. Maximum-likelihood seismic deconvolution. *IEEE Transactions on Geoscience and Remote Sensing*, (1):72–82, 1983.

[109] F. Champagnat, Y. Goussard, and J. Idier. Unsupervised deconvolution of sparse spike trains using stochastic approximation. *IEEE Transactions on Signal Processing*, 44(12):2988–2998, 1996.

[110] T. Olofsson and T. Stepinski. Maximum a posteriori deconvolution of sparse ultrasonic signals using genetic optimization. *Ultrasonics*, 37(6):423–432, 1999.

[111] R. Demirli and J. Saniie. Model-based estimation of ultrasonic echoes. part i: Analysis and algorithms. *IEEE Transactions on Ultrasonics, Ferroelectrics and Frequency Control*, 48(3):787–802, 2001.

[112] W. Liang and P.-W. Que. Maximum non-gaussianity parameters estimation of ultrasonic echoes and its application in ultrasonic non-destructive evaluation. *Measurement Science and Technology*, 18(12):3743–3750, 2007.

[113] F. Hägglund, J. Martinsson, J.E. Carlson, and C. Carlander. Model-based characterization of thin layers using pulse-echo ultrasound. In *International Congress on Ultrasonics*, volume 1562, pages 9–12, 2007.

[114] F. Hagglund, J. Martinsson, and J.E. Carlson. Model-based estimation of thin multilayered media using ultrasonic measurements. *Ultrasonics, Ferroelectrics and Frequency Control, IEEE Transactions on*, 56(8):1689–1702, 2009.

[115] J. Martinsson, F. Hägglund, and J.E. Carlson. Complete post-separation of overlapping ultrasonic signals by combining hard and soft modeling. *Ultrasonics*, 48(5):427–443, 2008.

[116] J.E. Dennis and R.B. Schnabel. *Numerical methods for unconstrained optimization and nonlinear equations*, volume 16. SIAM, 1983.

[117] G. Rus and R. Gallego. Optimization algorithms for identification inverse problems with the boundary element method. *Engineering Analysis with Boundary Elements*, 26(4):315–327, 2002.

[118] S.M. Kay. Fundamentals of statistical signal processing: Estimation theory. 1993.

[119] D.W. Marquardt. An algorithm for least-squares estimation of nonlinear parameters. *Journal of the Society for Industrial & Applied Mathematics*, 11(2):431–441, 1963.

[120] J.E. Dennis and J.J. Moré. A characterization of superlinear convergence and its application to quasi-newton methods. *Mathematics of Computation*, 28(126):549–560, 1974.

[121] V.K. Kinra, P.T. Jaminet, C. Zhu, and V.R. Iyer. Simultaneous measurement of the acoustical properties of a thin-layered medium: The inverse problem. *The Journal of the Acoustical Society of America*, 95:3059–3074, 1994.

[122] V.K. Kinra and V.R. Iyer. Ultrasonic measurement of the thickness, phase velocity, density or attenuation of a thin-viscoelastic plate. part ii: The inverse problem. *Ultrasonics*, 33(2):111–122, 1995.

[123] M.J. Maron and R.J. Lopez. *Numerical analysis: a practical approach*. Macmillan New York, 1982.

[124] K. Balasubramaniam and S.C. Whitney. Ultrasonic through-transmission characterization of thick fibre-reinforced composites. *Ndt & E International*, 29(4):225–236, 1996.

[125] B.A. Auld. *Acoustic fields and waves in solids*, volume 1. Wiley New York, 1973.

[126] K. Balasubramaniam and N.S. Rao. Inversion of composite material elastic constants from ultrasonic bulk wave phase velocity data using genetic algorithms. *Composites Part B: Engineering*, 29(2):171–180, 1998.

[127] M. Feder and E. Weinstein. Parameter estimation of superimposed signals using the em algorithm. *IEEE Transactions on Acoustics, Speech and Signal Processing*, 36(4):477–489, 1988.

[128] R. Demirli and J. Saniie. Parameter estimation of multiple interfering echoes using the sage algorithm. In *IEEE Ultrasonics Symposium*, volume 1, pages 831–834, 1998.

[129] I. Ziskind and M. Wax. Maximum likelihood localization of multiple sources by alternating projection. *IEEE Transactions on Acoustics, Speech and Signal Processing*, 36(10):1553–1560, 1988.

[130] R. Demirli and J. Saniie. Model-based estimation of ultrasonic echoes. part ii: Nondestructive evaluation applications. *IEEE Transactions on Ultrasonics, Ferroelectrics and Frequency Control*, 48(3):803–811, 2001.

[131] C.F. Wu. On the convergence properties of the em algorithm. *The Annals of Statistics*, 11(1):95–103, 1983.

[132] P.J. Chung and J.F. Bohme. Comparative convergence analysis of em and sage algorithms in doa estimation. *IEEE Transactions on Signal Processing*, 49(12):2940–2949, 2001.

[133] P. Guillaume and R. Pintelon. A gauss-newton-like optimization algorithm for "weighte" nonlinear least-squares problems. *IEEE Transactions on Signal Processing*, 44(9):2222–2228, 1996.

[134] R. Pintelon and J. Schoukens. *System identification: a frequency domain approach*. John Wiley & Sons, 2001.

[135] R. Fletcher. *Practical methods of optimization*. John Wiley & Sons, 2013.

[136] J. Kormylo and J. Mendel. Maximum likelihood detection and estimation of bernoulli-gaussian processes. *IEEE Transactions on Information Theory*, 28(3):482–488, 1982.

[137] M. Lavielle. Bayesian deconvolution of bernoulli-gaussian processes. *Signal processing*, 33(1):67–79, 1993.

[138] A.E. Yagle and R.R. Joshi. Maximum likelihood estimation with side information of a 1-d discrete layered medium from its noisy impulse reflection response. *IEEE Transactions on Signal Processing*, 48(7):1975–1983, 2000.

[139] H.L. Taylor, S.C. Banks, and J.F. McCoy. Deconvolution with the l_1 norm. *Geophysics*, 44(1):39–52, 1979.

[140] D.A. Lorenz and D. Tredel. Greedy deconvolution of point-like objects. In *Signal Processing with Adaptive Sparse Structured Representations (SPARSE workshop)*, pages 1–5, 2009.

[141] M. Elad. *Sparse and redundant representations: from theory to applications in signal and image processing*. Springer, 2010.

[142] S.G. Mallat and Z. Zhang. Matching pursuits with time-frequency dictionaries. *IEEE Transactions on Signal Processing*, 41(12):3397–3415, 1993.

[143] N. Ruiz-Reyes, P. Vera-Candeas, J. Curpian-Alonso, R. Mata-Campos, and J.C. Cuevas-Martinez. New matching pursuit-based algorithm for snr improvement in ultrasonic ndt. *NDT & E International*, 38(6):453–458, 2005.

[144] N. Ruiz-Reyes, P. Vera-Candeas, J. Curpian-Alonso, J.C. Cuevas-Martinez, and J.L. Blanco-Claraco. High-resolution pursuit for detecting flaw echoes close to the material surface in ultrasonic ndt. *NDT & E International*, 39(6):487–492, 2006.

[145] E. Mor, A. Azoulay, and M. Aladjem. A matching pursuit method for approximating overlapping ultrasonic echoes. *IEEE Transactions on Ultrasonics, Ferroelectrics and Frequency Control*, 57(9):1996–2004, 2010.

[146] J.A. Tropp. Greed is good: Algorithmic results for sparse approximation. *IEEE Transactions on Information Theory*, 50(10):2231–2242, 2004.

[147] T. Peter, D. Potts, and M. Tasche. Nonlinear approximation by sums of exponentials and translates. *SIAM Journal on Scientific Computing*, 33(4):1920–1947, 2011.

[148] J.L. Beck and K.-V. Yuen. Model selection using response measurements: Bayesian probabilistic approach. *Journal of Engineering Mechanics*, 130(2):192–203, 2004.

[149] T.E. Matikas. Damage characterization and real-time health monitoring of aerospace materials using innovative nde tools. *Journal of Materials Engineering and Performance*, 19(5):751–760, 2010.

[150] R.J. Zemp, J. Tavakkoli, and R.S.C. Cobbold. Modeling of nonlinear ultrasound propagation in tissue from array transducers. *The Journal of the Acoustical Society of America*, 113:139–152, 2003.

[151] K. Hokstad. Nonlinear and dispersive acoustic wave propagation. *Geophysics*, 69(3):840–848, 2004.

[152] D.O. Breazeale, M. .and Thompson. Finite-amplitude ultrasonic waves in aluminum. *Applied Physics Letters*, 3(5):77–78, 1963.

[153] R.A. Guyer and P.A. Johnson. Nonlinear mesoscopic elasticity: Evidence for a new class of materials. *Physics today*, 52:30, 1999.

[154] L.A. Ostrovsky and P.A. Johnson. Dynamic nonlinear elasticity in geomaterials. *Rivista del nuovo cimento*, 24(7):1–46, 2001.

[155] L.D. Landau and E.M. Lifshitz. *Theory of Elasticity*. Pergamon press, Oxford, 1959.

[156] R.A. Guyer and P.A. Johnson. *Nonlinear mesoscopic elasticity: the complex behavior of rocks, soil, concrete*. John Wiley & Sons, 2009.

[157] R.A. Guyer, J. TenCate, and P. Johnson. Hysteresis and the dynamic elasticity of consolidated granular materials. *Physical review letters*, 82(16):3280–3283, 1999.

[158] J.A. TenCate, E. Smith, and R.A. Guyer. Universal slow dynamics in granular solids. *Physical review letters*, 85(5):1020–1023, 2000.

[159] L.K. Zarembo and V. I. Timoshenko. Nonlinear acoustics. *Moscow University*, 1, 1984.

[160] Y. Zheng, R.G. Maev, and I.Y. Solodov. Nonlinear acoustic applications for material characterization: A review. *Canadian Journal of Physics*, 77(12):927–967, 2000.

[161] R.T. Beyer. Nonlinear acoustics (naval sea system commands). *Washington DC*, 1974.

[162] L. Germain and J.D.N. Cheeke. Generation and detection of high-order harmonics in liquids using a scanning acoustic microscope. *The Journal of the Acoustical Society of America*, 83:942–949, 1988.

[163]

[164] A. Hikata, B.B. Chick, and C. Elbaum. Effect of dislocations on finite amplitude ultrasonic waves in aluminum. *Applied Physics Letters*, 3(11):195–197, 1963.

[165] L.K. Zarembo and V.A. Krasil'Nikov. Nonlinear phenomena in the propagation of elastic waves in solids. *Physics-Uspekhi*, 13(6):778–797, 1971.

[166] J. Philip and M.A. Breazeale. Temperature variation of some combinations of third-order elastic constants of silicon between 300 and 3°k. *Journal of Applied Physics*, 52(5):3383–3387, 1981.

[167] N. Ichida, T. Sato, and M. Linzer. Imaging the nonlinear ultrasonic parameter of a medium. *Ultrasonic Imaging*, 5(4):295–299, 1983.

[168] W.K. Law, L.A. Frizzell, and F. Dunn. Comparison of thermodynamic and finite amplitude methods of b/a measurement in biological materials. *The Journal of the Acoustical Society of America*, 74:1295–1297, 1983.

[169] X.-F. Gong, Z.-M. Zhu, T. Shi, and J.-H. Huang. Determination of the acoustic nonlinearity parameter in biological media using fais and itd methods. *The Journal of the Acoustical Society of America*, 86:1, 1989.

[170] J.A. TenCate, K.E.A Van Den Abeele, T.J. Shankland, and P.A. Johnson. Laboratory study of linear and nonlinear elastic pulse propagation in sandstone. *The Journal of the Acoustical Society of America*, 100:1383–1391, 1996.

[171] M.F. Hamilton and D.T. Blackstock. *Nonlinear acoustics*. Acoustical Society of America, 1998.

[172] R.N. Thurston and M.J. Shapiro. Interpretation of ultrasonic experiments on finite-amplitude waves. *The Journal of the Acoustical Society of America*, 41:1112–1125, 1967.

[173] R.B. Thompson, O. Buck, and D.O. Thompson. Higher harmonics of finite amplitude ultrasonic waves in solids. *The Journal of the Acoustical Society of America*, 59:1087–1094, 1976.

[174] D. Zhang, X.-F. Gong, and B. Zhang. Second harmonic sound field after insertion of a biological tissue sample. *The Journal of the Acoustical Society of America*, 111:45–48.

[175] X.-F. Zhu, L. Zhou, D. Zhang, and X.-F. Gong. Nonlinear propagation of focused ultrasound in layered biological tissues based on angular spectrum approach. *Chinese Physics*, 14(8):1594–1599, 2005.

[176] B.J. Landsberger and M.F. Hamilton. Second-harmonic generation in sound beams reflected from, and transmitted through, immersed elastic solids. *The Journal of the Acoustical Society of America*, 109:488–500, 2001.

[177] O. Bou Matar, M. Vila, and F.V. Meulen. Experimental and numerical study of the insert-substitution method: application to the measurement of the nonlinear parameter β of solids. In *IEEE Ultrasonics Symposium*, volume 1, pages 709–712, 2001.

[178] G.D. Meegan Jr, P.A. Johnson, R.A. Guyer, and K.R. McCall. Observations of nonlinear elastic wave behavior in sandstone. *The Journal of the Acoustical Society of America*, 94:3387–3391, 1993.

[179] R.A. Guyer, K.R. McCall, and K.E.A. Van Den Abeele. Slow elastic dynamics in a resonant bar of rock. *Geophysical research letters*, 25(10):1585–1588, 1998.

[180]

[181] K.R. McCall. Theoretical study of nonlinear elastic wave propagation. *Journal of Geophysical Research*, 99(B2):2591–2600, 1994.

[182] K.E.A Van Den Abeele and P.A. Johnson. Elastic pulsed wave propagation in media with second- or higher-order nonlinearity. part ii. simulation of experimental measurements on berea sandstone. *Journal of the Acoustical Society of America*, 99–105(6), 1996.

[183] K.R. McCall and R.A. Guyer. Equation of state and wave propagation in hysteretic nonlinear elastic materials. *Journal of Geophysical Research*, 99(B12):23887–23897, 1994.

[184]

[185] V. Aleshin, V. Gusev, and V.Y.U. Zaitsev. Propagation of acoustics waves of nonsimplex form in a material with hysteretic quadratic nonlinearity: analysis and numerical simulations. *Journal of Computational Acoustics*, 12(3):319–354, 2004.

[186] E. Barbieri, M. Meo, and U. Polimeno. Nonlinear wave propagation in damaged hysteretic materials using a frequency domain-based pm space formulation. *International Journal of Solids and Structures*, 46(1):165–180, 2009.

[187] P. Antonaci, C.L.E. Bruno, A.S. Gliozzi, and M. Scalerandi. Evolution of damage-induced nonlinearity in proximity of discontinuities in concrete. *International Journal of Solids and Structures*, 47(11):1603–1610, 2010.

[188] J.H. Cantrell and W.T. Yost. Effect of precipitate coherency strains on acoustic harmonic generation. *Journal of applied physics*, 81(7):2957–2962.

[189]

[190] A.M. Sutin. Nonlinear acoustic nondestructive testing of cracks. *The Journal of the Acoustical Society of America*, 99:2539, 1996.

[191] A.M. Sutin and V.E. Nazarov. Nonlinear acoustic methods of crack diagnostics. *Radiophysics and quantum electronics*, 38(3-4):109–120, 1995.

[192] L.K. Zarembo, V.A. Krasil'nikov, and I.E. Shkol'nik. Nonlinear acoustics in a problem of diagnosing the strength of solids. *Strength of Materials*, 21(11):1544–1551, 1989.

[193] C.L.E. Bruno, A.S. Gliozzi, M. Scalerandi, and P. Antonaci. Analysis of elastic nonlinearity using the scaling subtraction method. *Physical Review B*, 79(6):1–13, 2009.

[194] J.K. Na, W.T. Yost, and J.H. Cantrell. Variation of sound velocity in fatigued aluminum 2024-t4 as a function of hydrostatic pressure. pages 2075–2082, 1993.

[195] J.H. Cantrell and W.T. Yost. Acoustic harmonic generation from fatigue-induced dislocation dipoles. *Philosophical magazine A*, 69(2):315–326, 1994.

[196] I.Y. Solodov. Ultrasonics of non-linear contacts: propagation, reflection and ndeapplications. *Ultrasonics*, 36(1):383–390, 1998.

[197] D. Donskoy, A. Sutin, and A. Ekimov. Nonlinear acoustic interaction on contact interfaces and its use for nondestructive testing. *Ndt & E International*, 34(4):231–238, 2001.

[198] I.Y. Solodov, N. Krohn, and G. Busse. Can: an example of nonclassical acoustic nonlinearity in solids. *Ultrasonics*, 40(1):621–625, 2002.

[199] J.M. Richardson. Harmonic generation at an unbounded interface. part i. planar interface between semi-infinite elastic media. *International Journal of Engineering Science*, 17.

[200] S. Zhou and Y. Shui. Nonlinear reflection of bulk acoustic waves at an interface. *Journal of applied physics*, 72(11):5070–5080, 1992.

[201] S. Zhou, W. Jiang, and Y. Shui. Nonlinear bulk acoustic waves in anisotropic solids: Propagation, generation, and reflection. *Journal of applied physics*, 78(1):39–46, 1995.

[202] C. Pecorari. An extension of the spring model to nonlinear interfaces. In *AIP Conference Proceedings*, volume 657, pages 49–56, 2003.

[203] C. Pecorari. Nonlinear interaction of plane ultrasonic waves with an interface between rough surfaces in contact. *The Journal of the Acoustical Society of America*, 113:3065–3072, 2003.

[204] A. Berezovski, M. Berezovski, and J. Engelbrecht. Numerical simulation of nonlinear elastic wave propagation in piecewise homogeneous media. *Materials Science and Engineering: A*, 418(1):364–369, 2006.

[205] P.P. Delsanto, S. Hirsekorn, V. Agostini, R. Loparco, and A. Koka. Modeling the propagation of ultrasonic waves in the interface region between two bonded elements. *Ultrasonics*, 40(1):605–610, 2002.

[206] M. Rothenfusser, M. Mayr, and J. Baumann. Acoustic nonlinearities in adhesive joints. *Ultrasonics*, 38(1):322–326, 2000.

[207] R. Williams, E. Cherin, T. Y.J. Lam, J. Tavakkoli, R.J. Zemp, and F.S. Foster. Nonlinear ultrasound propagation through layered liquid and tissue-equivalent media: computational and experimental results at high frequency. *Physics in medicine and biology*, 51(22):5809–5824, 2006.

[208] Y. Yun, G.Q. Miao, P. Zhang, K. Huang, and R.J. Wei. Nonlinear acoustic wave propagating in one-dimensional layered system. *Physics Letters A*, 343(5):351–358, 2005.

[209] K.F. Graff. *Wave Motion in Elastic Solids*. Dover publications, 1975.

[210] C. Pantea, C.F. Osterhoudt, and D.N. Sinha. Determination of acoustical nonlinear parameter β of water using the finite amplitude method. *Ultrasonics*, 53(5):1012–1019.

[211] A.V. Oppenheim and R.W. Schafer. *Discrete-time signal processing*, volume 5. Prentice-Hall, Upper Saddle River, New Jersey, 1989.

[212] F.J. Harris. On the use of windows for harmonic analysis with the discrete fourier transform.

[213] M.H. Hayes. *Statistical digital signal processing and modeling*. John Wiley & Sons, 1996.

[214] J.G. Proakis and D.G. Manolakis. *Digital Signal Processing: Principles, Algorithms, and Applications*. Prentice-Hall, International, Inc., New Jersey, 1996.

[215] A.V. Oppenheim and R.W. Schafer. From frequency to quefrency: A history of the cepstrum. *IEEE Signal Processing Magazine*, 21(5):95–106, 2004.

[216] J.S. Lim and A.V. Oppenheim. *Advanced Topics in Signal Processing*. Prentice Hall, Englewood Cliffs, New Jersey, 1988.

[217] S.T. Kaplan and T.J. Ulrych. Phase unwrapping: A review of methods and a novel technique. In *CSPG CSEG Convention*, pages 534–537, 2007.

[218] B.P. Bogert, M.J.R. Healy, and J.W. Tukey. The quefrency alanysis of time series for echoes: Cepstrum, pseudo-autocovariance, cross-cepstrum and saphe cracking. In *Proceedings of the Symposium on Time Series Analysis*, pages 209–243, 1963.

[219] D.G. Childers, D.P. Skinner, and R.C. Kemerait. The cepstrum: A guide to processing. 65(10):1428–1443, 1977.

[220] Y. Tohkura. A weighted cepstral distance measure for speech recognition. 35(10):1414–1422, 1987.

[221] J.-C. Junqua and H. Wakita. A comparative study of cepstral lifters and distance measures for all-pole models of speech in noise. In *IEEE International Conference on Acoustics, Speech and Signal Processing*, pages 476–479, 1989.

[222] B.-H. Juang, L. Rabiner, and J. Wilpon. On the use of bandpass liftering in speech recognition. 35(7):947–954, 1987.

[223] A.M. Gómez, A.M. Peinado, V. Sánchez, and A.J. Rubio. Recognition of coded speech transmitted over wireless channels. *IEEE Transactions on Wireless Communications*, 5(9):2555–2562, 2006.

[224] N. Cretu and G. Nita. Pulse propagation in finite elastic inhomogeneous media. *Computational materials science*, 31(3):329–336, 2004.

[225] R. Lake. *Viscoelastic materials*. Cambridge University Press, 2009.

[226] S. Treitel and E.A. Robinson. Seismic wave propagation in layered media in terms of communication theory. *Geophysics*, 31(1):17–32, 1966.

[227] V. Valimaki and T.I. Laakso. Principles of fractional delay filters. In *IEEE International Conference on Acoustics, Speech, and Signal Processing*, volume 6, pages 3870–3873, Istanbul, March 2000.

[228] W.R. Sutton. Strategic positioning in composites for global competitiveness. *Moving Forward With 50 Years of Leadership in Advanced Materials*, 39:2373–2384, 1994.

[229] C.E. Bakis, L.C. Bank, V.L. Brown, E. Cosenza, J.F. Davalos, J.J. Lesko, A. Machida, S.H. Rizkalla, and T.C. Triantafillou. Fiber-reinforced polymer composites for construction-state-of-the-art review. *Journal of Composites for Construction*, 6(2):73–87, 2002.

[230] L.C. Hollaway. A review of the present and future utilization of frp composites in the civil infrastructure with reference to their important in-service properties. *Construction and Building Materials*, 24(12):2419–2445, 2010.

[231] R.D. Jamison. The role of microdamage in tensile failure of graphite/epoxy laminates. *Composites Science and Technology*, 24(2):83–99, 1985.

[232] W.J. Cantwell and J. Morton. The impact resistance of composite materials - a review. *composites*, 22(5):347–362, 1991.

[233] S. Abrate. Impact on laminated composites: recent advances. *Applied Mechanics Reviews*, 47:517, 1994.

[234] A. Ruosi, M. Valentino, G. Peluso, and G. Pepe. Analysis of low-velocity impact damage in reinforced carbon fiber composites by hts-squid magnetometers. *Applied Superconductivity, IEEE Transactions on*, 11(1):1172–1175, 2001.

[235] F. Aymerich and S. Meili. Ultrasonic evaluation of matrix damage in impacted composite laminates. *Composites Part B: Engineering*, 31(1):1–6, 2000.

[236] R. Olsson, M.V. Donadon, and B.G. Falzon. Delamination threshold load for dynamic impact on plates. *International journal of solids and structures*, 43(10):3124–3141, 2006.

[237] T. Mitrevski, I.H. Marshall, and R. Thomson. The influence of impactor shape on the damage to composite laminates. *Composite structures*, 76(1):116–122, 2006.

[238] R. Talreja. Damage and fatigue in composites–a personal account. *Composites Science and Technology*, 68(13):2585–2591, 2008.

[239] M. Rheinfurth, N. Kosmann, D. Sauer, G. Busse, and K. Schulte. Lamb waves for non-contact fatigue state evaluation of composites under various mechanical loading conditions. *Composites Part A: Applied Science and Manufacturing*, 43(8):1203–1211, 2012.

[240] H. Schmutzler, M. Alder, N. Kosmann, H. Wittich, and K. Schulte. Degradation monitoring of impact damaged cfrp under fatigue loading with pulse phase thermography. *Preprint*, pages 1–26, 2013.

[241] A. Rotem and H.G. Nelson. Failure of a laminated composite under tension - compression fatigue loading. *Composites Science and Technology*, 36(1):45–62, 1989.

[242] A. Tropis, M. Thomas, J.L. Bounie, and P. Lafon. Certification of the composite outer wing of the atr72. *Proceedings of the Institution of Mechanical Engineers, Part G: Journal of Aerospace Engineering*, 209(4):327–339, 1995.

[243] T.E. Serdinak. Post-impact fatigue of cross-plied, through-the-thickness reinforced carbon/epoxy composites. *NASA STI/Recon Technical Report N*, 95:31419.

[244] N. Uda, K. Ono, and K. Kunoo. Compression fatigue failure of cfrp laminates with impact damage. *Composites Science and Technology*, 69(14):2308–2314, 2009.

[245] A.S. Chen, D.P. Almond, and B. Harris. Impact damage growth in composites under fatigue conditions monitored by acoustography. *International journal of fatigue*, 24(2):257–261, 2002.

[246] D.D. Symons and G. Davis. Fatigue testing of impact-damaged t300/914 carbon-fibre-reinforced plastic. *Composites science and technology*, 60(3):379–389, 2000.

[247] A. Gagel, D. Lange, and K. Schulte. On the relation between crack densities, stiffness degradation, and surface temperature distribution of tensile fatigue loaded glass-fibre non-crimp-fabric reinforced epoxy. *Composites Part A: Applied Science and Manufacturing*, 37(2):222–228, 2006.

[248] K. Harri, P. Guillaume, and S. Vanlanduit. On-line damage detection on a wing panel using transmission of multisine ultrasonic waves. *NDT & E International*, 41(4):312–317, 2008.

[249] S.-C. Wooh and I.M. Daniel. Three-dimensional ultrasonic imaging of defects and damage in composite materials. *Materials Evaluation*, 52(10), 1994.

[250] M.V. Hosur, C.R.L. Murthy, T.S. Ramamurthy, and A. Shet. Estimation of impact-induced damage in cfrr laminates through ultrasonic imaging. *NDT & E International*, 31(5):359–374, 1998.

[251] M.R. Gorman. Ultrasonic polar backscatter imaging of transverse matrix cracks. *Journal of composite materials*, 25(11):1499–1514, 1991.

[252] K.V. Steiner, R.F. Eduljee, X. Huang, and J.W. Gillespie Jr. Ultrasonic nde techniques for the evaluation of matrix cracking in composite laminates. *Composites science and technology*, 53(2):193–198, 1995.

[253] Langer R. and Vacanti J.P. Tissue engineering. *Science*, 260(5110):920–926, 1993.

[254] R. Archer and D.J. Williams. Why tissue engineering needs process engineering. *Nature biotechnology*, 23(11):1353–1355, 2005.

[255] M.L. Mather, S.P. Morgan, and J.A. Crowe. Meeting the needs of monitoring in tissue engineering. *Regenerative Medicine*, 2(2):145–160, 2007.

[256] K. Kim, C.G. Jeong, and S.J. Hollister. Non-invasive monitoring of tissue scaffold degradation using ultrasound elasticity imaging. *Acta biomaterialia*, 4(4):783–790, 2008.

[257] RM. Williams, W.R. Zipfel, and W.W. Webb. Multiphoton microscopy in biological research. *Current opinion in chemical biology*, 5(5):603–608, 2001.

[258] K. König, K. Schenke-Layland, I. Riemann, and U.A. Stock. Multiphoton autofluorescence imaging of intratissue elastic fibers. *Biomaterials*, 26(5):495–500, 2005.

[259] W. Sun, A. Darling, B. Starly, and J. Nam. Computer-aided tissue engineering: overview, scope and challenges. *Biotechnology and Applied Biochemistry*, 39(1):29–47, 2004.

[260] K.Y. Lee and D.J. Mooney. Hydrogels for tissue engineering. *Chemical reviews*, 101(7):1869–1880, 2001.

[261] N.E. Fedorovich, J. Alblas, J.R. de Wijn, W.E. Hennink, A.J. Verbout, and W.J.A Dhert. Hydrogels as extracellular matrices for skeletal tissue engineering: state-of-the-art and novel application in organ printing. *Tissue engineering*, 13(8):1905–1925, 2007.

[262] E.J. Orwin, M.L. Borene, and A. Hubel. Biomechanical and optical characteristics of a corneal stromal equivalent. *Journal of biomechanical engineering*, 125(4):439–444, 2003.

[263] M. Ahearne, Y. Yang, A.J. El Haj, K.Y. Then, and K.-K. Liu. Characterizing the viscoelastic properties of thin hydrogel-based constructs for tissue engineering applications. *Journal of the Royal Society Interface*, 2(5):455–463, 2005.

[264] Y. Yang, P.O. Bagnaninchi, M. Ahearne, R.K. Wang, and K.-K. Liu. A novel optical coherence tomography-based micro-indentation technique for mechanical characterization of hydrogels. *Journal of The Royal Society Interface*, 4(17):1169–1173, 2007.

[265] K. Hattori, Y. Takakura, H. Ohgushi, T. Habata, K. Uematsu, M. Takenaka, and K. Ikeuchi. Which cartilage is regenerated, hyaline cartilage or fibrocartilage? non-invasive ultrasonic evaluation of tissue-engineered cartilage. *Rheumatology*, 43(9):1106–1108, 2004.

[266] K. Hattori, Y. Takakura, H. Ohgushi, T. Habata, K. Uematsu, and K. Ikeuchi. Novel ultrasonic evaluation of tissue-engineered cartilage for large osteochondral defects – non-invasive judgment of tissue-engineered cartilage. *Journal of orthopaedic research*, 23(5):1179–1183, 2005.

[267] M.A. Rice, K.R. Waters, and K.S. Anseth. Ultrasound monitoring of cartilaginous matrix evolution in degradable peg hydrogels. *Acta biomaterialia*, 5(1):152–161, 2009.

[268] S. Kreitz, G. Dohmen, S. Hasken, T. Schmitz-Rode, P. Mela, and S. Jockenhoevel. Non-destructive method to evaluate the collagen content of fibrin-based tissue engineered structures via ultrasound. *Tissue Engineering Part C: Methods*, 17(10):1021–1026, 2011.

[269] S.L. Hui, C.W. Slemenda, and C.C. Johnston Jr. Age and bone mass as predictors of fracture in a prospective study. *Journal of clinical investigation*, 81(6):1804–1809, 1988.

[270] P.D. Delmas and E. Seeman. Changes in bone mineral density explain little of the reduction in vertebral or nonvertebral fracture risk with anti-resorptive therapy. *Bone*, 34(4):599–604, 2004.

[271] C.F. Njeh, C.M. Boivin, and C.M. Langton. The role of ultrasound in the assessment of osteoporosis: a review. *Osteoporosis International*, 7(1):7–22, 1997.

[272] M.L. Bouxsein. Bone quality: where do we go from here? *Osteoporosis international*, 14(5):118–127, 2003.

[273] B. Borah, G.J. Gross, T.E. Dufresne, T.S. Smith, M.D. Cockman, P.A. Chmielewski, M.W. Lundy, J.R. Hartke, and E.W. Sod. Three-dimensional microimaging (mrμi and

μct), finite element modeling, and rapid prototyping provide unique insights into bone architecture in osteoporosis. *The anatomical record*, 265(2):101–110, 2001.

[274] P. Ross, C. Huang, J. Davis, K. Imose, J. Yates, J. Vogel, and R. Wasnich. Predicting vertebral deformity using bone densitometry at various skeletal sites and calcaneus ultrasound. *Bone*, 16(3):325–332, 1995.

[275] P. Zioupos. Accumulation of in-vivo fatigue microdamage and its relation to biomechanical properties in ageing human cortical bone. *Journal of microscopy*, 201(2):270–278, 2001.

[276] D. Burr. Microdamage and bone strength. *Osteoporosis International*, 14:67–72, 2003.

[277] K.E.A. Van Den Abeele, A. Sutin, J. Carmeliet, and P.A. Johnson. Micro-damage diagnostics using nonlinear elastic wave spectroscopy (news). *Ndt & E International*, 34(4):239–248, 2001.

[278] L. Hoff, K.G. Oygarden, E.K. Hagen, and J.A. Falch. Diagnosis of osteoporosis using nonlinear ultrasound. In *IEEE Symposium on Ultrasonics*, volume 1, pages 1010–1013, 2003.

[279] H.E. Engan, K.A. Ingebrigtsen, K.G. Oygarden, E.K. Hagen, and L. Hoff. Nonlinear ultrasound detection of osteoporosis. In *IEEE Ultrasonics Symposium*, pages 2096–2099, 2006.

[280] M. Muller, A. Sutin, R. Guyer, M. Talmant, P. Laugier, and P.A. Johnson. Nonlinear resonant ultrasound spectroscopy (nrus) applied to damage assessment in bone. *The Journal of the Acoustical Society of America*, 118:3946–3952, 2005.

[281] M. Muller, D. Mitton, M. Talmant, P. Johnson, and P. Laugier. Nonlinear ultrasound can detect accumulated damage in human bone. *Journal of biomechanics*, 41(5):1062–1068, 2008.

[282] S. Haupert, G. Renaud, J. Riviere, M. Talmant, P.A. Johnson, and P. Laugier. High-accuracy acoustic detection of nonclassical component of material nonlinearity. *The Journal of the Acoustical Society of America*, 130(5):2654–2661, 2011.

[283] G. Renaud, S. Calllé, J.-P. Remenieras, and M. Defontaine. Exploration of trabecular bone nonlinear elasticity using time-of-flight modulation. *IEEE Transactions on Ultrasonics, Ferroelectrics and Frequency Control*, 55(7):1497–1507, 2008.

[284] H. Moreschi, S. Callé, S. Guerard, D. Mitton, G. Renaud, and M. Defontaine. Monitoring trabecular bone microdamage using a dynamic acousto-elastic testing method. *Proceedings of the Institution of Mechanical Engineers, Part H: Journal of Engineering in Medicine*, 225(3):282–295, 2011.

[285] K.I. Lee. Feasibility of bone assessment by using the nonlinear parameter in trabecular bone. *Journal of the Korean Physical Society*, 62(8):1108–1113, 2013.

[286] J. Rivière, S. Haupert, P. Laugier, and P.A. Johnson. Nonlinear ultrasound: Potential of the cross-correlation method for osseointegration monitoring. *The Journal of the Acoustical Society of America*, 132(3):EL202–EL207, 2012.

[287] J. Rivière, S. Haupert, P. Laugier, T.J. Ulrich, P.-Y. Le Bas, and P.A. Johnson. Time reversed elastic nonlinearity diagnostic applied to mock osseointegration monitoring applying two experimental models. *The Journal of the Acoustical Society of America*, 131:1922–1927.

[288] J.E. Carlson, J. Van Deventer, A. Scolan, and C. Carlander. Frequency and temperature dependence of acoustic properties of polymers used in pulse-echo systems. In *IEEE Symposium on Ultrasonics*, volume 1, pages 885–888, 2003.

[289] S.T Moe, K.I Draget, G. Skjåk-Bræ, and O. Simdsrød. Temperature dependence of the elastic modulus of alginate gels. *Carbohydrate polymers*, 19(4):279–284.

[290] K.-I. Kawabata, Y. Waki, T. Matsumura, and S.-I. Umemura. Tissue mimicking phantom for ultrasonic elastography with finely adjustable elastic and echographic properties. In *IEEE Ultrasonics Symposium*, volume 2, pages 1502–1505, 2004.

[291] S.A. Goss, R.L. Johnston, and F. Dunn. Comprehensive compilation of empirical ultrasonic properties of mammalian tissues. *The Journal of the Acoustical Society of America*, 64:423–457, 1978.

[292] R. Ortega, A. Téllez, L. Leija, and A. Vera. Measurement of ultrasonic properties of muscle and blood biological phantoms. *Physics Procedia*, 3(1):627–634, 2010.

[293] A.C. Ximenes Oliveira. *Estudio de la expresión génica en la enfermedad periodontal y obtención de un modelo de matriz biológica descelularizada para la regeneración tisular guiada*. PhD Thesis, Universidad de Granada, 2013.

[294] G. Holzer, G. von Skrbensky, L.A. Holzer, and W. Pichl. Hip fractures and the contribution of cortical versus trabecular bone to femoral neck strength. *Journal of Bone and Mineral Research*, 24(3):468–474, 2009.

[295] R. Zebaze, A. Ghasem-Zadeh, A. Bohte, S. Iuliano-Burns, M. Mirams, R.I. Price, E.J. Mackie, and E. Seeman. Intracortical remodeling and porosity in the distal radius and post-mortem femurs of women: a cross-sectional study. *The Lancet*, 375(9727):1729–1736, 2010.

[296] Q. Grimal, J. Grondin, S. Guérard, R. Barkmann, K. Engelke, C.-C. Glüer, and P.l Laugier. Quantitative ultrasound of cortical bone in the femoral neck predicts femur strength: Results of a pilot study. *Journal of Bone and Mineral Research*, 28(2):302–312, 2013.

[297] A.M. Krivtsov and M. Wiercigroch. Nonlinear dynamics of percussive drilling of hard materials. In *ASME Design Engineering Technical Conferences*, pages 1–6, 1999.

[298] P. Manogg. Investigation of the rupture of a plexiglas plate by means of an optical method involving high-speed filming of the shadows originating around holes drilled in the plate. *International Journal of Fracture Mechanics*, 2(4):604–613, 1966.

[299] J.S. Knopp, J.C. Aldrin, and P. Misra. Considerations in the validation and application of models for eddy current inspection of cracks around fastener holes. *Journal of Nondestructive Evaluation*, 25(3):123–137, 2006.

[300] R. Gallego and G. Rus. Identification of cracks and cavities using the topological sensitivity boundary integral equation. *Computational Mechanics*, 33(2):154–163, 2004.

[301] R. Gallego, L. Comino, and A. Ruiz-Cabello. Material constant sensitivity boundary integral equation for anisotropic solids. *International journal for numerical methods in engineering*, 66(12):1913–1933, 2006.

[302] S.-Y. Lee and S.-C. Wooh. Waveform-based identification of structural damage using the combined finite element method and microgenetic algorithms. *Journal of Structural Engineering*, 131(9):1464–1472, 2005.

[303] D.E. Goldberg and M.P. Samtni. Engineering optimization via the genetic algorithms. *Computers and Structures*, 40:1321–1327, 1991.

[304] G. Rus, R. Palma, and J.L. Pérez-Aparicio. Optimal measurement setup for damage detection in piezoelectric plates. *International Journal of Engineering Science*, 47(4):554–572, 2009.

[305] H.E. Kyburg. *Probability and inductive logic*. Macmillan London, 1970.

[306] H. Jeffrey. Theory of probability. *Clarendon Press, Oxford*, 1961.

[307] R.T. Cox. *The algebra of probable inference*. Johns Hopkins Press Baltimore, 1961.

[308] S.W. Huang and P.C. Li. Binary code design for high-frequency ultrasound. *IEEE Transactions on Ultrasonics, Ferroelectrics and Frequency Control*, 54(5):947–956, 2007.

[309] L. Ljung. *System identification: theory for the user*.

[310] A.A. Fahim, R. Gallego, N. Bochud, and G. Rus. Model-based damage reconstruction in composites from ultrasound transmission. *Composites Part B: Engineering*, 45(1):50–62, 2012.

[311] N. Bochud, A.M. Gomez, G. Rus, J.L. Carmona, and A.M. Peinado. Robust parametrization for non-destructive evaluation of composites using ultrasonic signals. In *International Conference on Acoustics, Speech and Signal Processing*, pages 1789–1792, Prague, May 2011.

[312] B. Fuentes, J.L. Carmona, N. Bochud, A.M. Gomez, and A.M. Peinado. Model-based cepstral analysis for ultrasonic non-destructive evaluation of composites. In *IEEE International Conference on Acoustics, Speech and Signal Processing*, pages 1717–1720, Kyoto, March 2012.

[313] D. Giacobello, M.G. Christensen, M.N. Murthi, S.H. Jensen, and M. Moonen. Sparse linear prediction and its applications to speech processing. *IEEE Transactions on Audio, Speech, and Language Processing*, 20(5):1644–1657, 2012.

[314] J. Koloda, A.M. Peinado, and V. Sánchez. Speech reconstruction by sparse linear prediction. In *Advances in Speech and Language Technologies for Iberian Languages*, pages 247–256, 2012.

[315] L. Gaul. The influence of damping on waves and vibrations. *Mechanical systems and signal processing*, 13(1):1–30, 1999.

[316] G. Rus, N. Bochud, J. Melchor, M. Alaminos, and A. Campos. Dispersive model selection and reconstruction for tissue culture ultrasonic monitoring. In *AIP Conference Proceedings*, volume 1433, pages 375–378, 2012.

[317] N.M.M. Maia, J.M.M. Silva, and A.M.R. Ribeiro. On a general model for damping. *Journal of Sound and Vibration*, 218(5):749–767, 1998.

[318] Y.Z. Wang, X.F. Zhang, and J.X. Zhang. New insight into kinetics behavior of the structural formation process in agar gelation. *Rheologica Acta*, 52(1):39–48, 2011.

[319] T. Norisuye, A. Strybulevych, M. Scanlon, and J. Page. Ultrasonic investigation of the gelation process of poly (acrylamide) gels. In *Macromolecular symposia*, volume 242, pages 208–215, 2006.

[320] G. Rus, . Melchor, J, N. Bochud, L. Peralta, and W.J. Parnell. New insight into kinetics behavior of the structural formation process in agar gelation. *Submitted to Ultrasonics (under review)*, 2014.

[321] W.N. Cobb. Finite amplitude method for the determination of the acoustic nonlinearity parameter b/a. *The Journal of the Acoustical Society of America*, 73:1525–1531, 1983.

[322] R.M. D'Angelo, K.W. Winkler, T.J. Plona, B.J. Landsberger, and D.L. Johnson. Test of hyperelasticity in highly nonlinear solids: Sedimentary rocks. *Physical review letters*, 93(21):1–4, 2004.

[323] P. Laugier and G. Haïat. *Bone quantitative ultrasound*. Springer, 2011.